JUSTUS-LIEBIG-
UNIVERSITÄT
GIESSEN

Properties Of Heavy-Light Four-Quark States From Functional Methods

Dissertation

zur Erlangung des akademischen Grades eines
Doktors der Naturwissenschaften (Dr. rer. nat.)

Joshua Hoffer

Januar 2025

Institut für Theoretische Physik
Fachbereich 07:
Mathematik und Informatik, Physik, Geographie
Justus-Liebig-Universität Giessen

Erstgutachter und Betreuer:	Prof. Dr. Christian S. Fischer
Zweitgutachter:	Prof. Dr. Marc Wagner

"In physics, you don't have to go around making trouble for yourself - nature does it for you."

Frank A. Wilczek

Abstract

In this work we study the properties – specifically mass spectra and internal structure – of exotic mesons in the charmonium and bottomonium energy regions. Most of these mesons are deemed candidates for four-quark states featuring two heavy and two light quarks. For our calculations, we employ the functional framework of Dyson-Schwinger and Bethe-Salpeter equations (DSEs and BSEs) using a four-quark formulation. We begin by solving the quark DSEs for different quark flavours and calculating mass spectra from several two-body meson and diquark BSEs. These results serve as input for the four-quark BSE, the central object of this work. Using a physically motivated Ansatz, we describe the heavy-light four-quark states in terms of all possible internal two-quark groupings and the attractive and repulsive forces between them. We compare the mass spectra obtained using only the attractive and the attractive plus repulsive components to experimental measurements or theoretical predictions. In this way, we are able to assess the importance of repulsive forces for our description. Furthermore, we are able to investigate the favoured internal structure of the four-quark states by calculating the contribution of each internal component to the total normalization.

We observe that the inclusion of the repulsive forces leads to a much better agreement of our calculated mass spectra with the observed experimental spectra for the hidden-charm and hidden-bottom four-quark states. For the open-flavour four-quark states with total spin $J = 1$, the effect of including the repulsive forces is found to be especially significant, rendering our masses for the T^-_{bb}, $T^-_{bb\bar{s}}$, T_{bc} and $T_{cc}(3875)^+$ in quantitative agreement with predictions from the literature. Regarding the internal structure, we see that most of the investigated hidden-flavour four-quark states are purely dominated by the respective lightest internal heavy-light meson-meson components. The $J^{PC} = 1^{+-}$, including the $T_{c\bar{c}1}(3900)$ and $T_{b\bar{b}1}(10610)$, and the 0^{-+} channel show a very different picture, however, with a strong tendency towards a dominant hadro-quarkonium component. In all cases, the contribution coming from the diquark-antidiquark pairings is almost negligible. For the open-flavour states, we observe an interesting trend when considering the binding energy of the states with respect to the lowest heavy-light meson-meson threshold. For very shallow bound states, e.g., T^+_{cc} and T_{bc}, the corresponding heavy-light meson-meson component is found to be dominating. However, the deeper the state is bound, e.g., $T^-_{bb\bar{s}}$ and T^-_{bb}, the stronger the contribution coming from the diquark-antidiquark pairings becomes.

Kurzzusammenfassung

In dieser Arbeit untersuchen wir die Eigenschaften – insbesondere Massenspektren und innere Struktur – von exotischen Mesonen in den Charmonium- und Bottomonium-Energiebereichen. Die meisten dieser Mesonen gelten als Kandidaten für Vier-Quark-Zustände mit zwei schweren und zwei leichten Quarks. Für unsere Untersuchungen verwenden wir eine Kombination aus Dyson-Schwinger- und Bethe-Salpeter-Gleichungen (DSEs und BSEs) in einer Vier-Quark-Formulierung. Wir beginnen mit der Lösung der Quark-DSEs für verschiedene Quark-Flavours und berechnen Massenspektren von mehreren Zweikörper-Meson und Diquark BSEs. Diese Ergebnisse dienen als Input für die Vier-Quark-BSE, die zentrale Gleichung dieser Arbeit. Unter Verwendung eines physikalisch motivierten Ansatzes beschreiben wir die schwer-leichten Vier-Quark-Zustände mit allen möglichen internen Zwei-Quark-Gruppierungen und den anziehenden und abstoßenden Kräfte zwischen ihnen. Wir vergleichen die Massenspektren, die wir entweder nur unter Verwendung der anziehenden oder der anziehenden plus abstoßenden Komponenten erhalten haben, mit experimentellen Messungen oder theoretischen Vorhersagen. Auf diese Weise können wir die Bedeutung der abstoßenden Kräfte für unsere Beschreibung beurteilen. Darüber hinaus können wir die bevorzugte innere Struktur der Vier-Quark-Zustände untersuchen, indem wir den Beitrag jeder inneren Komponente zur Gesamtnormierung berechnen.

Wir stellen fest, dass die Einbeziehung der abstoßenden Kräfte zu einer viel besseren Übereinstimmung unserer berechneten Massenspektren mit den beobachteten experimentellen Spektren für die Vier-Quark-Zustände mit versteckter Charm und versteckter Bottomness führt. Für die Vier-Quark-Zustände mit offener Flavour-Ladung und Gesamtspin J=1 ist der Effekt der Einbeziehung der Abstoßungskräfte besonders signifikant, wodurch unsere Massen für T^-_{bb}, $T^-_{bb\bar{s}}$, T_{bc} und $T_{cc}(3875)^+$ quantitativ mit den Vorhersagen aus der Literatur übereinstimmen. Was die interne Struktur betrifft, sehen wir, dass die meisten der untersuchten Vier-Quark-Zustände mit versteckten Flavour-Ladungen rein von der zugehörigen leichtesten internen schwer-leichten Meson-Meson-Komponenten dominiert werden. Der $J^{PC} = 1^{+-}$, einschließlich der $T_{c\bar{c}1}(3900)$ und $T_{b\bar{b}1}(10610)$, und der 0^{-+} Kanal zeigen ein ganz anderes Bild, mit einer starken Tendenz zu einer dominanten Hadro-Quarkonium-Komponente. Alle diese Zustände weisen verschwindend kleine Diquark-Antidiquark-Komponenten auf. Für die Zustände mit offener Flavour-Ladung beobachten wir einen interessanten Trend, wenn wir die Bindungsenergie der Zustände in Bezug auf die niedrigste schwer-leichte Meson-Meson-Schwelle betrachten. Für sehr schwach gebundene Zustände, zum Beispiel T^+_{cc} und T_{bc}, zeigt sich die entsprechende schwer-leichte Meson-Meson-Komponente als dominant. Je tiefer jedoch der Zustand gebunden ist, zum Beispiel $T^-_{bb\bar{s}}$ und T^-_{bb}, desto stärker wird der Beitrag, der von den (schwer-schwer)(leicht-leicht) Diquark-Antidiquark-Paarungen kommt.

Frequently-Used Abbreviations and Acronyms

To make the text more concise, we used many abbreviations throughout this work. All of them are defined upon their first occurrence or when they are reintroduced after some time. A comprehensive list is provided in the following for a quick overview.

BSA	Bethe-Salpeter amplitude
BSE	Bethe-Salpeter equation
BSM	beyond standard model
BSWF	Bethe-Salpeter wave function
DCSB	dynamical chiral symmetry breaking
DSE	Dyson-Schwinger equation
EFT	effective field theory
EVC	eigenvalue curve
FYE	Faddeev-Yakubovsky equation
GMOR	Gell-Mann-Oakes-Renner relation
IR	infrared
MT	Maris-Tandy
NCC	norm contribution curve
NCQMEC	norm contribution quark mass evolution curve
n**PI**	n-particle irreducible
PDG	Particle Data Group
QCD	quantum chromodynamics
QED	quantum electrodynamics
QFT	quantum field theory
QMEC	(Current-)quark mass evolution curve
SPM	Schlessinger-Point-Method
SU(N)	special unitary group of degree N
TBMPP	two-body momentum partitioning parameters
U(N)	unitary group of degree N
UV	ultraviolet

Contents

Rest of this page intentionally left blank.

Chapter 1

Introduction

To the best of our current knowledge, there are four fundamental forces which govern the observed phenomena in our universe: *electromagnetism*, *weak interaction*, *strong interaction* and *gravitation*. Electromagnetism describes the forces between electrically charged particles such as protons and electrons. The acting range is in principle infinite, but the strength decreases rapidly with increasing distance. The weak interaction governs the processes of nuclear decays and can only be observed on subatomic length scales. The strong interaction binds together the atomic nuclei and is responsible for generating about 99% of the directly observable mass in the universe. It acts only on subatomic length scales, but does not decrease with increasing distance, instead approaching a non-zero value. In its acting radius it is the strongest known force in the universe. Lastly, gravitation is the force governing the dynamics of macroscopic objects like planets, galaxies or everyday objects. This force is by far the weakest in its acting radius, which is infinitely large, and cannot be shielded.

The first three forces are all well described in terms of fermionic particles, i.e., electrons, protons, quarks, etc., with half-integer spin, talking to each other via the exchange of bosonic particles, i.e., photons, W- and Z-bosons and gluons, which have integer spin and are the respective force carriers. Currently, the most successful way to describe the behaviour of particles and their interactions mathematically is using the framework of *quantum field theories* (QFTs), where the particles are seen as manifestations of underlying fields. The QFT describing the effects of the electromagnetic interactions is called quantum electrodynamics (QED), first formulated by Shin'ichirō Tomonaga, Julian Schwinger and Richard P. Feynman [1–4]. The coupling 'constant' of QED, i.e., the measure of the importance of the interactions between the particles, is very small for the energy scales of interest, which allows QED to be treated using perturbation theory. This means that the processes can be calculated directly to very high accuracy. The theory of QED is often combined with the theory of weak interaction, proposed by Sheldon Glashow, Steven Weinberg and Abdus Salam [5–7], into a QFT called electroweak theory (EWT). The QFT describing the theory of strong interactions, i.e., quantum chromodynamics (QCD), formulated by Harald Fritsch and Heinrich Leutwyler in collaboration with Murray Gell-Mann [8], presents a totally different picture. Here, the coupling is only small enough for high energies (or small distances), where it approaches zero, to allow the theory to be treated using perturbation theory. This property is called *asymptotic freedom* [9, 10]. For small energies (or large distances) the coupling is too strong for perturbation theory to work, presenting enormous technical and conceptual challenges for theoretical physicists

all over the world. The combination of these three QFTs forms the Standard Model of particle physics, the most successful theory of nature to date.

The only force not part of the Standard Model is gravitation, as its formulation in terms of a robust quantum theory is still subject to current research. Instead, this force is described in terms of the (classical) geometric theory of general relativity (GR), which to this day has withstood any experimental test. This theory works very well for phenomena involving large distances. However, this force is irrelevant for particle physics. Coming up with a robust quantum formulation of gravitation and unifying the description of all forces into one theory is the field of current active research in the "beyond standard model" (BSM) community.

1.1 QCD, Quarks and Hadrons

For the thesis at hand, we neglect QED, EWT and gravity and focus purely on the theory of strong interaction. The fundamental fermionic particles of QCD – *quarks* (q) and *antiquarks* ($\bar{q}$) – were first introduced by Murray Gell-Mann [11] and independently by George Zweig [1] [12, 13]. As of today, we have found six different types of quarks – also referred to as *flavours*: *up* (u), *down* (d), *strange* (s), *charm* (c), *bottom* (b) (also often called *beauty*) and *top* (t). Over time, it was discovered that additional to having a fractional electric charge, $+2e/3$ for "up"-like quarks (u, c, t) and $-1e/3$ for "down"-like quarks (d, s, b), with e the elementary charge, quarks need to carry another type of charge, which can be characterized by three different values [14, 15]. In a loose analogy to the three fundamental colours (red, green, blue), this additional charge is commonly referred to as *colour charge*. This is also where the name quantum chromodynamics comes from (Greek: *chrōma*="colour"). Because we do not have one charge like in QED, but three, QCD is a non-Abelian gauge theory with the underlying symmetry group of SU(3). In contrast to QED, also the exchange bosons – which for QCD are called *gluons* (g) – carry a colour charge. This leads to them being able to interact with each other, as well as with the quarks.

Using the quarks and gluons as building blocks for hadrons, we find that only states for which "adding up" the (anti)colours of the constituents to give a "colourless" or "white" (red + green + blue, colour + anticolour) combination yield hadrons observable in nature. When trying to separate a quark from such a colourless state, the potential energy increases by virtue of the strong force increasing with larger distances, leading to quark-antiquark production. This in turn ensures the two resulting states to be colourless. This implies that coloured objects are not observable, which is a phenomenon known as (*colour*) *confinement*. It leads to the formation of bound states using specific configurations of quarks and gluons. The two simplest configurations are mesons as quark-antiquark ($q\bar{q}$) states and baryons consisting of three quarks (qqq) (e.g., protons and neutrons). Based on this, quarks need to have a baryon number (B) of $B_q = 1/3$. Consequently, antiquarks have $B_{\bar{q}} = -1/3$ and gluons have $B_g = 0$. Thus, a more general classification scheme is to identify bosonic mesons as states with baryon number $B = 0$ and fermionic baryons with baryon number $B = 1$. Apart from the conventional $q\bar{q}$ mesons and qqq baryons, one can construct states

[1] Who initially called them "aces".

with other compositions, which are commonly referred to as *exotic* hadrons. The most prominent are *four-quark states* ($qq\bar{q}\bar{q}$), *hybrids* having a quark-antiquark pair and a gluon ($q\bar{q}g$) and *glueballs*, which consist of at least two gluons ($gg[g\ldots]$). There are also states with even higher number of (anti)quarks like pentaquarks, a system of four quarks and an antiquark ($qqqq\bar{q}$) or hexaquarks, which consist of six quarks. States with even more quark content, while theoretically possible, are not likely to occur as standalone states in nature. The wave function for such a state can, however, potentially appear as part of the superposition of wave functions for a given state, e.g., bosonic hadrons can have $q\bar{q}$ and four-quark components as well as hybrid or glueball components as long as the different components have the same quantum numbers as the full hadron.

The notion of these states being exotic comes from the fact, that the non-relativistic quark model [11–13] cannot explain states with certain quantum numbers or with net-electric charges using conventional $q\bar{q}$ mesons. A more natural description of these states comes from considering an "exotic" composition – as given above – or the inclusion of relativistic effects. For an extensive overview over multiquark states from a theoretical and experimental perspective, see [16–18].

Instead of combining a quark and an antiquark to form a $q\bar{q}$ meson, one can also combine two quarks to form a coloured qq state named a *diquark*. Because they are coloured objects, and thus per definition non-observable, they can only occur in higher bound states or resonances, e.g., in four-quark states, and can be understood more as an auxiliary tool.

This thesis will investigate the properties of four-quark states containing at least two heavy quarks like charm and bottom.

1.2 Motivation

Light scalar nonet. Although hadrons with exotic quark content, e.g., $qq\bar{q}\bar{q}$ and $qqqq\bar{q}$, were proposed in the original formulation of the quark model [11–13], there was no necessity to use such quark configurations to explain the properties of the hadrons at the time. However, this all changed with the observation of the scalar ($J^{PC} = 0^{++}$) $f_0(500)/\sigma$ meson with a mass of ~ 650 MeV [19] (now $400 - 550$ MeV [20]). In the non-relativistic quark model the relation $P = (-1)^{L+1}$ holds, to determine the parity (P) from the orbital angular momentum (L). Consequently, states with $P = -1$ (pseudoscalar 0^{-+} and vector 1^{--}) are s-wave ($L = 0$) and states with $P = +1$ (scalar 0^{++} and axialvector $1^{+\pm}$) are considered p-wave ($L = 1$)[2]. The energy contributions coming from the orbital angular momentum should force the p-wave states to be heavier than the s-wave states. Therefore, the σ meson is expected to be heavier than the ρ meson (1^{--}) in the $q\bar{q}$ picture. Instead, an inverse mass ordering is observed, as $m_\sigma < m_\rho$. Considering the whole light scalar nonet, we find that in the $q\bar{q}$ picture, the $a_0(980)$ states should be mass degenerate with the $f_0(500)$ because of the same quark content and the $f_0(980)$ should have $s\bar{s}$ quark content and be much heavier. Instead, the $a_0(980)$ is found almost mass degenerate with the $f_0(980)$ and the $f_0(500)$ is found much lighter. All of the inconsistencies above can be remedied, by

[2] For the mesons with $J \leq 1$.

considering the light scalar mesons as having a $qq\bar{q}\bar{q}$ quark content. This was first suggested 1977 by Robert J. Jaffe [21].

Heavy-flavour spectra. The non-relativistic constituent quark models work very well for mesons containing heavy quarks, as here the non-relativistic approach is reasonable. For a long time, all the known states in the charm and bottom region could be well described by considering them as $c\bar{c}$ and $b\bar{b}$ states respectively. That is, until the $\chi_{c1}(3872)$ (originally named $X(3872)$) was discovered by the Belle Collaboration [22] in 2003. This state has quantum numbers $0(1^{++})$ [23, 24] and cannot be explained as a pure $c\bar{c}$ state. One reason for this is, that the first observed final state already features a pure $c\bar{c}$ state, i.e., $J/\psi\pi^+\pi^-$. Furthermore, the low decay width of $\Gamma = 1.19 \pm 0.21$ MeV together with the closeness to the $D\bar{D}^*$ threshold suggests a four-quark nature with quark content $cq\bar{q}\bar{c}$. This discovery was the start to exotic hadron spectroscopy as we know it today. Over the following decades many more exotic hadrons were measured and classified, see [20] for an overview of the spectra in the charmonium and bottomonium region. Initially, the states with non-zero electric charge were labelled with the letter Z, vector states were termed with the letter Y and the rest with the letter X and the mass given in parentheses. Especially the discovery of states with electric charge (Z) eliminated any doubts regarding the existence of exotic mesons consisting of at least four quarks. Note, that the PDG recently changed the naming scheme and now denotes states with minimal quark content $qq\bar{q}\bar{q}$ with the letter T (for tetraquark)[3], see [20] for details. We will use the latter naming scheme throughout this thesis.

So far, all observed four-quark candidates with zero flavour charge, i.e., states with quark content $Qq\bar{q}\bar{Q}$ with $Q \in \{c, b\}$ and $q \in \{u, d, s\}$, are resonances decaying predominantly via strong interaction, with decay widths ranging from a few to a few hundred MeV [20]. The same cannot be said about four-quark candidates with non-zero flavour charge, i.e., states with $QQ'\bar{q}\bar{q}'$ [4] where $Q, Q' \in \{c, b\}$ and $\bar{q}, \bar{q}' \in \{\bar{u}, \bar{d}, \bar{s}\}$. Here, the states are expected to be bound if the heavy quark pair (QQ') is sufficiently heavy and the mass of the antiquark pair sufficiently light [25–29]. In this case, the QQ' pair effectively behaves like a point-like $\bar{\mathbf{3}}_\mathbf{c}$ (colour-antitriplet) antiquark, resulting in a binding mechanism similar to that of a heavy-light baryon. The only experimentally identified state of this kind is the $T_{cc}(3875)^+$ discovered at LHCb in 2022 [30, 31], which has a suggested quark content of $cc\bar{u}\bar{d}$. This state is extremely shallow, with a binding energy of $-273(61)$ keV with respect to the D^0D^{*+} threshold, and with $410(165)$ keV it has an extremely narrow decay width. Following the argument from above, the states with heavier QQ' pair should be possibly deeply bound. Indeed, theoretical predictions for the binding energy of the $bb\bar{u}\bar{d}$ state, called T^-_{bb}, yield values around $-(100 - 200)$ MeV with respect to the $\bar{B}\bar{B}^*$ threshold. For the $bb\bar{u}\bar{s}$, termed $T^-_{bb\bar{s}}$, the binding energy is predicted to be in the range $-(30 - 100)$ MeV. For both, see [32–37] and references therein.

[3] The quark content (other than u/d), the spin and the electric charge are denoted as super- and subscripts. A $Qu\bar{d}\bar{Q}'$ state (Q, Q' denoting heavy quarks) with spin J, electric charge c and mass M would be denoted as $T_{Q\bar{Q}'J}(M)^c$.

[4] Note, that when only considering the strong interactions, as done in this work, $QQ'\bar{q}\bar{q}'$ and $\bar{Q}\bar{Q}'qq'$ is equivalent

Internal structure. When investigating hadrons containing four quarks, it is natural to think about what the preferred arrangement of the quarks inside might be. Considering a four-quark state with generic quark content $Q_1Q_2\bar{Q}_3\bar{Q}_4$ one can identify four different possibilities:

1. *Compact four-quark state*: Here the four quarks all interact strongly with each other and are bunched tightly together with no apparent clusterings.
2. *Meson-meson*: In this picture, two (heavy-light) mesons with quark content $(Q_1\bar{Q}_i)(Q_2\bar{Q}_j)$ $(i,j=3,4)$ constitute a composite state, which can be either bound or resonant. If the mass of this state is slightly below the threshold of the two mesons making it up, this state is called a *meson-molecule*, see, e.g., [16, 38] and references therein for a general overview of these states.
3. *Hadro-quarkonium*: This type of clustering is a special case of the meson-meson picture, only relevant for heavy-light states with quark content $Q_1Q_2\bar{Q}_3\bar{Q}_4 = Qq\bar{q}\bar{Q}$. The two mesons have quark content $(Q\bar{Q})$ and $(q\bar{q})$. In analogy to the picture of the atom, the heavy $Q\bar{Q}$ pair forms the core and sits at the centre, while the light $q\bar{q}$ pair orbits around it. For a review regarding the importance of this picture for the charmonium spectrum see [39].
4. *Diquark-antidiquark*: Here we have a diquark (Q_1Q_2) and an antidiquark $(\bar{Q}_3\bar{Q}_4)$ being tightly bound by the colour force to form a spatially compact four-quark state. This kind of clustering is generally referred to as *tetraquark* in the literature [21]. For a pedagogic introduction of this picture and its application to multiquark states see, e.g., [17].

The first configuration (1.) will not be considered in this work, for reasons explained later on. For a comprehensive overview of the whole topic we refer to the recent review [40]. Different theoretical approaches mostly utilize one of the above possibilities to describe four-quark states. Thus, for a lot of measured states there is no final agreement between the different approaches regarding the internal structure. The PANDA experiment at FAIR (once finished) will be able to measure line shapes of exotic hadrons, which would provide important information to shed some light on the internal structure, see, e.g., [41] for further information.

1.3 Theory and Experiment

In physics, there is generally an effective synergy between theory and experiment. Theorists are coming up with theories and models to describe the processes of nature and look at the experimental results for verification of their calculations, while experimentalists analyse the measured data and look towards the theories for the underlying mechanism. It therefore comes to no surprise, that this is also the case for elementary particle and hadron physics. Groups of experimental physicists all around the world work on conceptualizing and building experimental apparatus at the various particle accelerator facilities to measure and analyse the properties of matter. On the other side, theorists work on finding an appropriate mathematical description of hadrons that can be used to reproduce the experimental

results and make predictions for future experiments, e.g., suggest energy scales at which the experimentalists should look for multiquark states. See, e.g., Ref. [40] for a recent overview of this interplay.

Experiments

In this section, we want to shortly outline the biggest experiments investigating exotic hadrons. Experiments especially suited to investigate heavy-flavour exotica are so called B-factories, which are designed to produce a large number of B-mesons via the decay of the $\Upsilon(4S)$, which is a $b\bar{b}$ state almost exclusively decaying to $B\bar{B}$ [20].

Belle (II). The Belle (II) is a B-factory experiment at the (Super)KEKB accelerator in Japan. The new flagship accelerator does e^-e^+-collision at extremely high luminosities. With the $\chi_{c1}(3872)$ (formerly known as the $X(3872)$) the collaboration famously reported the first heavy-light four-quark candidate and first ever measured exotic hadron in 2003 [22]. This discovery kicked off a new era of hadron physics and the Belle collaboration reported the finding of many additional exotic hadrons, e.g., the $\chi_{c0}(3915)$ [42], the majority of the $T_{c\bar{c}(\dots)J}$ states and the only verified four-quark candidates in the bottom spectrum, i.e., the $T_{b\bar{b}1}(10610)$ and $T_{b\bar{b}1}(10650)^+$ [43]. At the time of writing, the collaboration consists of 122 institutes from 27 countries [44].

LHCb. The LHCb (large Hadron Collider beauty) is an experiment at CERN which is dedicated to heavy-flavour physics, see [45] for details. It is not commonly referred to as B-factory due to it being not solely concerned with the study of b-quark particles. It is responsible for the discovery of many exotic hadrons in the last decade. Starting with the $P_{c\bar{c}}(4380)^+$, $P_{c\bar{c}}(4450)$ [46, 47] in 2015, LHCb discovered all of the known pentaquark candidates to date. It was also here, that the quantum numbers of the $\chi_{c1}(3872)$ four-quark state were determined [23, 24]. Furthermore, the four-quark candidates containing a $c\bar{c}$ pair and at least one antistrange ($\bar{s}$) quark, i.e., $\chi_{c1}(4274)$, $\chi_{c0}(4500)$, $\chi_{c0}(4700)$ [48], $X(4630)$, $\chi_{c1}(4685)$, $T_{c\bar{c}\bar{s}1}(4000)$ and $T_{c\bar{c}\bar{s}1}(4220)^+$ [49] were found at LHCb. The collaboration reported an all charm ($cc\bar{c}\bar{c}$) candidate termed $T_{cc\bar{c}\bar{c}}(6900)^0$ [50]. The most recent observation was the first ever doubly-charmed four-quark state candidate named $T_{cc}(3875)^+$ [30, 31]. Today, the LHCb collaboration consists of 73 institutes in 12 countries [51].

BES III. The Beijing Spectrometer III (BES III) is also an e^-e^+-collider, but with the focus to study states involving charm quarks. Most notably, they first discovered the state known now as $T_{c\bar{c}1}(3900)$ [52], as well as confirmed many other exotic candidates. At the time of writing, the BSE III collaboration consists of 85 institutes from 17 countries [53].

PANDA. The PANDA (antiProton ANnihilation at DArmstadt) is an experiment planned at the FAIR facility in Darmstadt. It will use proton-antiproton annihilation to study multiple aspects of hadron physics, like hadron spectroscopy, hadrons in medium and the structure of nuclei. Of special importance for this work is the focus of investigating the

charmonium states and the possibility to measure the line shapes of four-quark candidates in this energy range. This would allow to make statements about the internal structure. An overview of the planned physics programme in Phase One can be found in [41].

Notable discontinued experiments. There have been many experiments in the past searching for and reporting four-quark candidates, which have, however, been discontinued. Examples include the CDF and DØ experiments at Fermilab, reporting the $\chi_{c1}(4140)$ [54] (called $Y(4140)$ when discovered) and the $T_{b\bar{s}}(5568)^{\pm}$ [55] (originally $X(5568)^{\pm}$) respectively, the latter of which is still not seen at any other experiment. Also the BaBar experiment, which was a B-factory at the SLAC collider searching for four-quark candidates.

Theoretical approaches and current status

In this section we want to provide an overview over the most important theoretical approaches used to study four-quark states. We will only discuss the basic ideas and refer the interested reader to [56] for a more detailed overview. All of the methods below come with their strengths and weaknesses and ideally are used complementary to each other.

(Constituent) Quark Models. As mentioned earlier, the quark model was initially invented to classify conventional mesons and baryons in the 1960s, but is still in use to this day. The quarks in this model are quite heavy, having an effective mass, allowing the systems to be treated with a non-relativistic Schrödinger equation for spin-spin interactions. Different aspects of the internal dynamics are captured by using different potentials, see [57] for a pedagogical introduction. The model works best for hadrons with heavy quarks, as there the non-relativistic approach is reasonable. The model, by construction, breaks down when one wants to consider four-quark states. This can be remedied by combining the quarks to form diquarks and antidiquarks as effective degrees of freedom, see Refs. [58–60] for recent reviews using diquark-antidiquark models to investigate heavy-flavour four-quark states.

Lattice QCD. Treating QCD on a lattice is one of the most rigorous and widely trusted methods for studying four-quark states because it provides results directly from first principles of quantum chromodynamics. This numerical approach discretizes spacetime on a lattice, allowing QCD calculations to be performed non-perturbatively. It is particularly useful for determining the binding energies, spatial structures, and decay properties of tetraquarks. Lattice QCD has been essential in validating the existence of four-quark states and estimating their masses. We refer the interested reader to [61] for a pedagogical introduction to lattice QCD and [62, 63] for recent overviews of the status and technical challenges regarding the study of heavy-flavour four-quark states.

Functional framework (DSE/BSE). The combination of Dyson-Schwinger equations (DSEs), which are coupled systems of different one-particle irreducible Green's functions

and Bethe-Salpeter equations (BSEs) provides a non-perturbative and fully relativistic framework to study the properties of hadrons. Since the DSEs of different Green's functions are coupled, inserting them into each other yields an infinite tower of integral equations, which however encapsulates the full dynamics of QCD. In practice, one either iteratively solves a suitably truncated closed system of self-consistent DSEs or applies effective models. The solutions are used as input for the BSEs, which are relativistic hadronic bound state equations derived from full $2n$-quark Green's functions. This framework has proven to be a powerful toolbox to study properties of conventional mesons and baryons [64, 65] and exotic hadrons [66–68]. See also [69] for a pedagogical introduction and [70] for a recent review of four-quark states. An obvious weakness of this framework is the uncertainties regarding the error estimation.

Effective Field Theories (EFTs). EFTs simplify the study of four-quark states by focusing on the relevant degrees of freedom at particular energy scales, making them ideal for low-energy or heavy-quark systems. EFTs, such as heavy-quark effective theory (HQET) or non-relativistic QCD (NRQCD), incorporate symmetries like heavy-quark spin and flavour symmetry. These symmetries allow systematic expansions in powers of momenta or quark masses, enabling precise calculations of the dynamics and decays of four-quark states. Using the famous Weinberg compositeness criterion [71, 72], one can also make statements about the internal structure for hadronic molecule candidates, cf., e.g., [16]. See [56] and references therein for an extensive introduction to the field.

QCD sum rules. This method bridges QCD theory with experimental observables and is particularly valuable for making model-independent predictions about the properties of four-quark states. Using operator product expansion and QCD vacuum condensates, QCD sum rules relate the masses, decay constants, and other properties of four-quark states to integrals over spectral functions. This approach is versatile and has been applied to both stable and unstable tetraquark states. We point the interested reader to [73] and the comprehensive list of references therein for a thorough introduction to the subject.

Current theoretical status. Generally, using theoretical approaches provides the possibility to systematically vary parameters such as the quark mass and the coupling. The different theoretical approaches outlined above mostly utilize one of the possible internal clusterings listed in Section 1.2 to describe four-quark states. Most quark model calculations resort to a description in terms of a diquark-antidiquark pair, while EFTs often use the meson-molecule picture, especially for systems close to two-meson thresholds like the $\chi_{c1}(3872)$ or $T_{cc}(3875)^+$. However, this a priori choice of an internal configuration introduces an obvious bias towards the state being dominated by the chosen internal clustering.

Since hadrons are quantum states, the superposition of all three possible internal configurations (interactions 2.-4. listed in Section 1.2) should provide a complete description of four-quark candidates and allow to make more accurate statements about the internal structure. This has successfully been done in the functional framework of Dyson-

Schwinger/Bethe-Salpeter equations for certain charmonium-like four-quark states [67, 74, 75]. Here, there is no a priori bias towards any preferred internal clustering and the equation dynamically decides which internal quark configuration it likes best. For example, the $\chi_{c1}(3872)$ and $T_{cc}(3875)^+$ were found to predominantly be a $D\bar{D}^*$ and DD^* molecule respectively. A very prominent and strong tool to calculate observables from first principles is lattice QCD. The operator basis for the lattice calculation also includes operators describing all three possible internal configurations. A recent overview how the internal structure can be determined from lattice calculations are given in [62, 76]. A comprehensive list and discussion of recent lattice results for open-flavour four-quark states can be found in [63].

Overall, we see that the results coming from the different theoretical approaches are very diverse when it comes to the favoured internal configurations. Each of these methods is faced with their own technical and conceptual challenges. Thus, it might take a few more years before the results from the different methods can be compared on a quantitative level and common conclusions can be drawn.

1.4 Outline

The central goal of this thesis is to investigate the mass spectra and internal structure of heavy-light four-quark states in the charm and bottom region. To this end, we employ a functional framework, which is able to describe the four-quark states in its entirety, i.e., including all the possible internal quark configurations. To our knowledge, our framework is the only covariant one, which is able to consider the superposition of all important compositions (meson-meson, hadro-quarkonium, diquark-antidiquark and possible quark-antiquark components) without a priori bias.

This framework has been successfully applied in the past to investigate the light scalar nonet [77] and certain hidden- and open-flavour four-quark states in the charm region [78, 79]. While previous works only consider attractive forces between the internal clusters, we extend this to also include repulsive forces. Using this extended basis, we reanalyse the results for four-quark states with total spin $J = 0, 1$ in the charm region and extend our considerations to four-quark states in the bottom region. Furthermore, we explore a novel method to investigate the internal structure of the four-quark states by considering the norm contributions of the different internal clusters.

This thesis is structured as follows. In the beginning, we will shortly outline the underlying theory of QCD to lay the foundation of this work. Building on that, we will briefly review correlation functions in general, before deriving and discussing the quark Dyson-Schwinger equation (DSE) in Chapter 3. In Chapter 4, we will first derive the homogeneous meson Bethe-Salpeter/Faddeev-Yakubovsky equation (BSE/FYE) in a general way, before considering the special case of the two-quark BSE and its solution. Having done that, we will discuss the main equation of this work, i.e., the four-quark FYE, and its intricacies in Chapter 5. Then, we present our results for the mass spectra of hidden- and open-flavour four-quark states and discuss the importance of attractive and repulsive colour channels. We then introduce a novel method to investigate the internal structure

and present our obtained results for the dominant internal structure of the aforementioned exotic hadrons. In the end, final conclusions will be drawn.

Chapter 2

Quantum Chromodynamics

The best theory we currently have to describe the theory of strong interactions is Quantum Chromodynamics (QCD). It is a non-Abelian quantum field theory which describes the *colour force* binding its fundamental fields, i.e., (anti)quark- and gluon fields, into colourless hadrons (mesons, baryons, tetraquarks, pentaquarks, glueballs, etc.). Furthermore, it can also describe the binding of these hadrons into nuclei. As the focus of this work is to investigate the properties of hadrons, it is useful to provide a short overview of the properties of QCD.

We will shortly lay out the mathematical structure of QCD and then discuss of its most important symmetries and phenomenological aspects. All of the topics are kept at an overview level, as they are readily accessible in great detail in many standard QFT textbooks, e.g., [80–85].

2.1 Mathematical formulation of QCD

The fundamental ideas of Quantum Chromodynamics have been laid out in Chapter 1. It is a Yang-Mills theory based on the symmetry group $\mathrm{SU}(N_c)$, with $N_c = 3$ being the number of colour charges realized in nature.

The most basic quantity of a quantum theory is the *Lagrangian* or *Lagrangian density* $\mathcal{L}$. We can obtain the Lagrangian density of QCD, by requiring the fields of the theory, i.e., the quark (ψ) and antiquark ($\bar{\psi}$) fields, to transform invariantly under the symmetry group $\mathrm{SU}(3)$. The symmetry transformations in this context are *local*, i.e., they depend on the spacetime position x. If we recall, that every element U of the group $\mathrm{SU}(N)$ can be written as an exponential map of the generators t and a transformation or gauge parameter α, which can be chosen appropriately, then the $\mathrm{SU}(3)$ *local* symmetry transformation of the quark and antiquark spinors reads

$$\psi_i(x) \longrightarrow U_{ij}(x)\psi^j(x) = \exp\left(i\alpha_a(x)t^a_{ij}\right)\psi^j(x)\,, \tag{2.1}$$

$$\bar{\psi}_i(x) \longrightarrow \bar{\psi}^j(x)\left(U^{-1}\right)_{ji}(x)\,, \tag{2.2}$$

where the $i, j = 1, \ldots, N_c$ represent the colour indices of the fundamental ($\mathbf{3}$) representation while the $a = 1, \ldots, N_c^2 - 1$ denotes the colour index of the adjoint ($\bar{\mathbf{8}}$) representation. For better readability, we will drop the fundamental colour indices and the spacetime arguments and assume them to be present implicitly.

Being based on the symmetry group SU(3) renders QCD a *non-Abelian* Yang-Mills theory, i.e., the generators of the group do not commute. Instead, they fulfil the commutation relations

$$[t^a, t^b] = if^{ab}{}_c t^c \,, \tag{2.3}$$

which is the *Lie bracket* of the associated *Lie algebra* $\mathfrak{su}(3)$. The f^{abc} are the structure constants of $\mathfrak{su}(3)$ and a, b, c are again adjoint colour indices. A detailed discussion of the group SU(N) and its algebra $\mathfrak{su}(N)$ is given in Appendix A.3.

As established in Chapter 1, quarks are fermions, i.e., spin-1/2 particles. The Lagrangian density for free fermions in Euclidean spacetime reads $\mathcal{L}_{\text{Dirac}} = \bar{\psi}(\not{\partial} + m)\psi$. It is easy to see, that the massterm of $\mathcal{L}_{\text{Dirac}}$ is invariant under the transformations in Eq. (2.1). However, the kinetic term is not. To render this term invariant, one replaces the partial derivative with the *covariant derivative*

$$D_\mu := \partial_\mu + igA^a_\mu t_a \,, \tag{2.4}$$

which transforms accordingly. This change introduces the *gluon field* A^a_μ and the *strong coupling constant* g; μ denotes a Lorentz index. Consequently, the covariant derivative introduces and governs the interactions between quarks and gluons. The colour index a for the gluon field indicates that there are in total 8 gauge bosons in QCD.

As a direct consequence of the replacement $\not{\partial} \to \not{D}$ in $\mathcal{L}_{\text{Dirac}}$ we get the transformation properties of the gluon field:

$$A_\mu \longrightarrow A'_\mu = UA_\mu U^\dagger + \frac{i}{g} \cdot U\left(\partial_\mu U^\dagger\right) \,, \tag{2.5}$$

where we have used the abbreviation $A_\mu := A^a_\mu t_a$.

With the purely fermionic part settled, we turn our attention to the pure gauge part. In gauge theories, e.g., QED, the gauge part is expressed in terms of the *field strength tensor* F. Due to the non-Abelian nature of SU(3), the field strength tensor has to take the following form to ensure the correct transformation behaviour of the Lagrangian

$$F^a_{\mu\nu} = \partial_\mu A^a_\nu - \partial_\nu A^a_\mu - g f^a{}_{bc} A^b_\mu A^c_\nu \,. \tag{2.6}$$

The first two terms are identical to the QED case and the last term is due to the non-commutative behaviour of the generators of SU(3). This last term implies the existence of gluon self-interaction, i.e., three- and four-gluon vertices. This is a major difference to photons in QED, which cannot interact with themselves.

In total, the Lagrangian density of QCD in Euclidean spacetime reads

$$\mathcal{L}_{\text{QCD}} = \sum_f \bar{\psi}_f(\not{D} + m_f)\psi_f - \frac{1}{4} \cdot F^a_{\mu\nu} F_a^{\mu\nu} \,. \tag{2.7}$$

The sum index denotes the quark flavours of QCD $f \in \{u, d, s, c, b, t\}$ and the m_f are the

corresponding current-quark masses.

It is straightforward to check, that the Lagrangian density in Eq. (2.7) is invariant under the transformations Eqs. (2.1) and (2.5). The integral of the Lagrangian density over spacetime yields the QCD action

$$S_{\mathrm{QCD}}[\psi, \bar{\psi}, A_\mu] = \int \mathrm{d}^4x \, \mathcal{L}_{\mathrm{QCD}}[\psi, \bar{\psi}, A_\mu] \,, \tag{2.8}$$

which is the essential quantity in the partition function $\mathcal{Z}$ in its path-integral formulation:

$$\mathcal{Z}_{\mathrm{QCD}}[\psi, \bar{\psi}, A_\mu] = \int \mathcal{D}[\psi, \bar{\psi}, A_\mu] \, \exp\Big(- S_{\mathrm{QCD}}[\psi, \bar{\psi}, A_\mu]\Big) \,, \tag{2.9}$$

with the classical action S_{QCD} in the exponent of the partition function. Integrating over all field configurations leads to the inclusion of all possible quantum fluctuations around the classical action. The partition function in Eq. (2.9) implicitly contains the Lagrangian and thus one could obtain every interesting quantity from it. There is, however, a fundamental problem. In Eq. (2.9) the $\mathcal{D}A$ integrates over all possible field configurations, which includes also field configurations that are equivalent via the gauge transformations of Eq. (2.5). This overcounting of equivalent gauge field configurations renders the gluon propagator ill-defined.

To remedy this situation one needs to single out exactly one field configuration among all the equivalent ones. This can be achieved by using *gauge fixing*. More precisely one uses the well-known (*DeWitt-*)*Faddeev-Popov procedure* [86–88]. It needs to be remarked here, that even this procedure is not without flaws as by means of *Gribov copies* the possibility of overcounting the equivalent gauge field configurations is always present.[1] A pedagogical discussion of the gauge fixing procedure and its ambiguities can be found in Appendix B.3 in [93]. An alternative approach to deal with the overcounting issue is to discretize spacetime and formulate QCD in terms of a *lattice field theory*. Here gauge fixing is not strictly necessary, but can be done to compare to results from other approaches. A broad and very pedagogical introduction and overview of lattice QCD and its intricacies is given in [61].

As the framework used in this thesis is a continuum field theory we apply the Faddeev-Popov procedure and arrive at the gauge-fixed QCD Lagrangian, which serves as the basis for all the derivations and investigations throughout this work:

$$\mathcal{L}_{\mathrm{QCD}} = \sum_f \bar{\psi}_f(\not{D} + m_f)\psi_f - \frac{1}{4} \cdot F^a_{\mu\nu} F_a^{\mu\nu} - \frac{(\partial_\mu A_a^\mu)^2}{2\xi} + i\left(\partial_\mu \bar{c}^a\right)\left(D^\mu_{ab} c^b\right) \,. \tag{2.10}$$

The gauge fixing procedure introduces the auxiliary fields $\bar{c}^a$ and c^a, which are called the *Faddeev-Popov ghosts*. They are complex scalar fields, i.e., have spin zero, but are Grassmann-

[1] We note, that for the energy regions we are interested in the effect is negligibly small [89–91]. Hence, the source of error on observable quantities is negligible compared to other error sources, see, e.g., [92]. We therefore neglect their importance for this work.

valued and thus fulfil anticommutation relations. Note, that in contrast to the quark fields ψ and $\bar{\psi}$ the ghost fields c^a and $\bar{c}^a$ are **not** related to one another via charge conjugation. This leads to a violation of the *spin-statistics theorem* [94, 95]. Consequently, physical particles associated with the ghost fields cannot exist and they are merely a mathematical tool to cancel unphysical degrees of the gluon [81, 85]. The variable ξ in Eq. (2.10) is formally a Lagrange multiplier and labels the gauge-fixing parameter in this case. It labels a class of gauges known as R_ξ gauges, which are generalizations of the Lorenz gauge. Depending on the gauge one wants to choose, the gauge-fixing parameter ξ takes different values. A very popular and widely used gauge choice for QFT calculations is the *Feynman-'t Hooft gauge* , i.e., $\xi = 1$, as it often simplifies the calculations. Another prominent gauge choice, and the one used in this work, is the *Landau gauge*, which corresponds to $\xi = 0$. This choice, as we will later see, is very suitable for the functional framework as it cancels the longitudinal part of the gluon propagator thereby reducing the complexity of the equations.

Now that we have solved the problem coming from the gluon quantization in Eq. (2.9) through gauge-fixing and arrived at the basic quantity for our work in Eq. (2.10) we are faced with yet another problem which has to be dealt with before we can start doing calculations. This time, it is a general problem of (most) QFTs, i.e., a lot of occurring integrals are of the form

$$\int_0^\infty \mathrm{d}k \, \frac{k^3}{f(k^4)} \,, \tag{2.11}$$

where $f(k^4)$ is some function depending on the loop momentum k to the fourth power, e.g., two propagators in a loop diagram. This integral is divergent as for large momenta k, which is also known as *UV-divergence*. Plainly, this is a disaster as these integrals and thus the infinite quantities are present in the calculation of physical observables. Since these emergent divergences cannot be circumvented, the QFT-way to deal with them is to use the *renormalization procedure*. For this we first need to *regularize* the integral in Eq. (2.11). The most straightforward way to accomplish this is to introduce a hard UV-cutoff Λ which leads to the following replacement in Eq. (2.11):

$$\int_0^\infty \mathrm{d}k \, \frac{k^3}{f(k^4)} \to \int_0^\Lambda \mathrm{d}k \, \frac{k^3}{f(k^4)} \,. \tag{2.12}$$

There are also a lot of other regularization schemes, e.g., dimensional regularization or Pauli-Villars. Lattice regularization is also among the popular regularization schemes and thus Lattice field theory again does not feature this problem, as the discretization of spacetime serves as a natural cutoff.

By introducing the cutoff in Eq. (2.12) we can now calculate the integral, but have to keep in mind, that the Λ formally needs to be taken to infinity at the end of the calculation. Therefore, we have just shifted the occurrence of the infinities to a different step in the calculation, namely to the end. The results are still dependent on the regularization parameter Λ and therefore still contain the infinities. We can then remove the cutoff dependence of the calculated quantities by renormalizing them appropriately. Gauge-

fixed QCD belongs to a class of theories which are *multiplicative renormalizable* [96–100], i.e., the fields and couplings appearing in the Lagrangian Eq. (2.7) are interpreted as 'bare' (unphysical) and they each get rescaled by an associated *renormalization constant* which then carries the cutoff dependence. For QCD, the fields and quantities in the Lagrangian get rescaled like follows

$$\psi_{\mathrm{B}_f} = \left(Z_2^f\right)^{1/2}\psi\,, \quad A^\mu_{\mathrm{B}} = Z_3^{1/2}A^\mu\,, \quad g_{\mathrm{B}} = Z_g g\,, \quad c_{\mathrm{B}} = \tilde{Z}_3^{1/2}c\,, \quad m_{\mathrm{B};f} = Z_{m_f}m_f\,, \tag{2.13}$$

where Z_2^f denotes the (flavour f) quark field, Z_3 the gluon field, $\tilde{Z}_3$ the ghost field, Z_g the coupling and Z_{m_f} the quark-mass (for quark-flavour f) renormalization constant, respectively. The quantities with the subscript B denote the bare quantities from the Lagrangian Eq. (2.7) and the quantities without an additional subscript are the renormalized, i.e., physical, quantities. As a short note, there are two popular renormalization schemes: The momentum subtraction (MOM) scheme, where one imposes conditions on the physical observables to take a certain (measured) value at a renormalization scale μ. This is a generalization of the onshell renormalization scheme. The other one is the minimal subtraction (MS) or modified minimal subtraction ($\overline{\mathrm{MS}}$) scheme and it is very prominent in perturbative calculations, as one can remove the divergent terms order by order. In this thesis we are investigating the non-perturbative regime of QCD and as such choose a MOM scheme in the following as it is more suitable. A detailed overview of the different schemes can be found in [101].

One can find relations among the renormalization constants via the *Slavnov-Taylor identities* (STIs) [102, 103], which can be derived from gauge invariance. Being the non-Abelian generalizations of the *Ward-Takahashi identities* (WTIs) [104, 105], they relate the QCD correlation functions to one another, such that one can derive the following relations [106]

$$Z_{1F}^f = Z_g Z_2^f Z_3^{1/2}\,, \quad Z_1 = Z_g Z_3^{3/2}\,, \quad \tilde{Z}_1 = Z_g \tilde{Z}_3 Z_3^{1/2}\,, \quad Z_4 = Z_g^2 Z_3^2\,. \tag{2.14}$$

These are the renormalization constants for the interaction vertices of the theory, i.e., the quark-gluon vertex $\left(Z_{1F}^f\right)$, the three-gluon vertex (Z_1), the ghost-gluon vertex $\left(\tilde{Z}_1\right)$ and the four-gluon vertex (Z_4).

2.2 Symmetries of QCD

So far we have only explored the local SU(3) gauge symmetry that QCD needs to fulfil by construction. However, local gauge symmetries are not 'true' symmetries of the system, in the sense that they do not lead to conserved charges and quantum numbers. Rather, they reflect a redundancy in the description. According to *Noether's* (*first*) *theorem* [107] each continuous, global, unbroken symmetry of a Lagrangian has a corresponding conserved current density j^μ, i.e., $\partial_\mu j^\mu = 0$. By virtue of the formula $Q = \int \mathrm{d}^3x\, j^0$ this conserved current also leads to conserved charges Q, i.e., $\partial_t Q = 0$.

Quantum Chromodynamics also features some global symmetries, not all of which are

continuous and many of them are actually broken (or hidden) in some way or another. We will shortly discuss these symmetries in the following, but before we do so a short comment on the types of symmetry breaking is in order. There are three ways in which symmetries are broken:

Explicit symmetry breaking. Here, the Lagrangian of the theory is actually not invariant under a specific symmetry transformation, i.e., there exist terms in the Lagrangian which explicitly violate this symmetry. The Noether current in this case is obviously not conserved.

Spontaneous symmetry breaking. In this situation, the classical Lagrangian is invariant under a symmetry transformation, i.e., the current is conserved. However, if the vacuum state of the theory is not invariant under the action of the charge operator $\hat{Q}$ (corresponding to the conserved current), i.e., it does not annihilate the vacuum $\hat{Q}|0\rangle \neq 0$, then the vacuum expectation values of the theory do not vanish, thus implying the formation of condensates. The symmetry is thus lost 'spontaneously' or dynamically due to the inherent dynamics of the theory. Spontaneous symmetry breaking is therefore also often referred to as dynamical symmetry breaking. *Goldstone's theorem* [108, 109] states that each such charge $\hat{Q}$ not annihilating the vacuum implies the existence of a massless particle (mode), the so-called (*Nambu-*)*Goldstone bosons* [110]. For a very broad and pedagogical overview of the subject, see, e.g., [111].

Anomalous symmetry breaking. In this case, while the classical Lagrangian is invariant under a certain symmetry, it fails to be a symmetry of the full quantum theory for any regularization scheme. Here, the classical Noether current is still conserved while the quantized one is not. Put in other words, this symmetry is a symmetry of the action but not of the measure and thus not of the partition function $\mathcal{Z}$.

2.2.1 Discrete symmetries and the Strong *CP* Problem

Let us start with the few discrete symmetries of the QCD Lagrangian before we come to the continuous symmetries. As it is in general not possible to build a Lorentz-invariant QFT with a Hermitian Hamiltonian that violates *CPT* invariance [112], the QCD Lagrangian in Eq. (2.10) trivially conserves *charge conjugation* (C), *parity transformation* (P) and *time reversal* (T). However, we could in principle add another term to the QCD Lagrangian in Equation (2.10), which is Lorentz invariant, renormalizable, has mass dimension 4 and respects the SU(3) gauge transformations:

$$\mathcal{L}_\theta = \bar{\theta} \cdot \frac{g^2 N_f}{16\pi^2} F^a_{\mu\nu} \tilde{F}^{\mu\nu}_a , \qquad \text{with} \qquad \tilde{F}^{\mu\nu}_a = \frac{1}{2} \cdot \varepsilon^{\mu\nu}{}_{\rho\sigma} F^{\rho\sigma}_a , \tag{2.15}$$

with $\tilde{F}^{\mu\nu}_a$ denoting the dual field strength tensor, ε is the 4-dimensional Levi-Civita symbol and $\bar{\theta}$ can be viewed as a strength parameter of the term. The Lagrangian in Eq. (2.15) is known as the θ-term which conserves charge conjugation, but violates time reversal and

parity and thus, by consequence, also violates *CP* invariance. This is the infamous *Strong CP Problem*. Since $\mathcal{L}_\theta$ can be written as a total divergence of the *Chern-Simons current* [113] it only contributes a surface term to the action and does not change the perturbative physics. In the non-perturbative regime of QCD the θ-term gives rise to an electric dipole moment of the neutron $d_N = (5.2 \cdot 10^{-16} e \cdot \text{cm}) \cdot \bar{\theta}$ [84], where the experimental measurements enforce an upper bound $\bar{\theta} \leq 10^{-10}$ [114]. Thus, due to the smallness of this upper bound it seems reasonable to neglect this term and assume that QCD conserves parity.

2.2.2 Global continuous symmetries

For a continuous global symmetry transformation, in contrast to a local symmetry, the transformation parameter of the symmetry does not depend on the spacetime point x. Such transformations include, e.g., rotating the whole system by an angle ϕ (rotation invariance) or shifting the whole system by a distance a (translation invariance).

Considering QCD, one can make the local gauge transformation in Eq. (2.1) global by setting $\alpha(x) = \alpha$, i.e., removing the spacetime dependence. It is straightforward to check, that the QCD Lagrangian is also trivially invariant under the global SU(3) symmetry. In the following we will shortly introduce the continuous symmetries of QCD.

BRST invariance

In Section 2.1 we saw that the QCD Lagrangian
in Eq. (2.7) gets the addition of a gauge-breaking term and its associated Faddeev-Popov ghosts c and $\bar{c}$ through the DeWitt-Faddeev-Popov procedure, ultimately yielding the gauge-fixed Lagrangian given in Eq. (2.10). The mentioned gauge-breaking term $\frac{1}{2\xi}(\partial_\mu A^\mu)^2$ breaks the gauge symmetry down to a residual symmetry of the entire Lagrangian. This symmetry was first described by Carlo Becchi, Alain Rouet and Raymond Stora [115, 116] and independently by Igor Tyutin [117], hence the common name BRST symmetry. Note now, that since the equations of motion for the gauge parameter $\alpha_a(x)$ and the ghost and antighost fields are the same, i.e., $\Box \alpha_a(x) = \Box c_a(x) = \Box \bar{c}_a(x) = 0$, one can equally use a scaled ghost field to gauge transform by replacing $\alpha_a(x) \to \lambda c_a(x)$, where the parameter λ is Grassmann-valued. We can introduce a BRST operator $\hat{\delta}_\lambda$ which yields the following infinitesimal transformations of the fields (omitting the spacetime argument here):

$$\hat{\delta}_\lambda \psi_i = \lambda \cdot i c_a t^a_{ij} \psi^j \,, \quad \hat{\delta}_\lambda c^a = -\lambda \cdot \frac{1}{2} \cdot f^{abd} c_b c_d \,, \tag{2.16}$$

$$\hat{\delta}_\lambda A^a_\mu = \lambda \cdot D^{ab}_\mu c_b \,, \quad \hat{\delta}_\lambda \bar{c}^a = -\lambda \cdot \xi^{-1} \partial^\mu A^a_\mu \,. \tag{2.17}$$

With these transformations one can show that the gauge-fixed Lagrangian is invariant under BRST transformation. It can therefore be viewed as a generalization of gauge invariance as it holds despite the gauge-breaking term in the Lagrangian. Furthermore, because the parameter λ and the ghost are determined globally, the transformations of different spacetime points are not independent and thus BRST symmetry is a global symmetry. A pedagogical overview of BRST invariance can be found in [84] and a very rigorous

discussion in [81].

The global symmetries mentioned above have associated Noether currents and charges. The BRST 'charge' can perturbatively be used to separate physical from unphysical states. Non-perturbatively, the status of BRST symmetry is still unclear and still subject of current research. A very prominent example of an attempted formulation beyond perturbation theory is the Kugo-Ojima construction, which is also related to the *Kugo-Ojima confinement scenario* [118].

Flavour symmetries

From the QCD Lagrangian in Eq. (2.7) one immediately notices that only the quark fields carry a flavour index f and are hence relevant for the discussion of flavour symmetries. For the following discussion, we will assume the flavour index to take values $f = 1, \dots, N_f$, with N_f denoting an arbitrary number of flavours (to the best of our knowledge $N_f = 6$ in nature). Furthermore, we will introduce the N_f-dimensional generalized spinor $\Psi = (\psi_f)$ to encapsulate each individual flavour. Since the gluons and their interactions with quarks cannot change the flavour of the quarks, all quarks are in principle treated equally within QCD. Correspondingly, the classical Lagrangian would have an additional $\mathrm{U}(N_f)$ flavour symmetry, which is, however, only present if all quark flavours have equal masses. In nature, this is not realized as can be seen by checking the current-quark masses in the PDG [20]. Because these masses originate from the Higgs sector and are external parameters as far as pure QCD is concerned, this symmetry is explicitly broken.

In the following, we will shortly outline how the mass term causes the explicit symmetry breaking and investigate if there is more to the $\mathrm{U}(N_f)$ symmetry than meets the eye. We remember from our QFT lecture, that a Dirac spinor can be decomposed into the direct sum of a left- and a right-handed spinor $\Psi_{\mathrm{L/R}}$, the so-called *Weyl-spinors*. To project out either the individual left- or right-handed part of the spinor, one can utilize the properties of the γ_5 Dirac matrix defined in Eq. (A.21) and define two corresponding projection operators

$$P_{\mathrm{R/L}} = \frac{(\mathbb{I}_{\mathrm{D}} \pm \gamma_5)}{2}\,, \quad \text{with} \quad P_{\mathrm{R/L}}^2 = P_{\mathrm{R/L}}\,,\, P_{\mathrm{L}} P_{\mathrm{R}} = P_{\mathrm{R}} P_{\mathrm{L}} = 0\,,\, P_{\mathrm{L}} + P_{\mathrm{R}} = \mathbb{I}_D\,, \quad (2.18)$$

where $\mathbb{I}_{\mathrm{D}}$ denotes the unit matrix in Dirac space. The left- and right-handed spinors are then obtained via $\Psi_{\mathrm{R/L}} = P_{\mathrm{R/L}}\Psi$. It is now easy to see, that if we split the QCD Lagrangian in Eq. (2.7) into left- and right-handed spinors, which transform independently under

$$\Psi_{\mathrm{L}} \to U_{\mathrm{L}}\Psi_{\mathrm{L}}\,,\, \Psi_{\mathrm{R}} \to U_{\mathrm{R}}\Psi_{\mathrm{R}}\,, \quad \text{with} \quad U_{\mathrm{L}} \in \mathrm{U}_{\mathrm{L}}(N_f)\,,\, U_{\mathrm{R}} \in \mathrm{U}_{\mathrm{R}}(N_f)\,, \quad (2.19)$$

then the only part that is not invariant is the (N_f-dimensional) mass term $M = (m_f)$, which mixes the two spinors $M\Psi_{\mathrm{R}}\Psi_{\mathrm{L}}$. Thus, in the limit of massless quarks (or *chiral limit*) the QCD Lagrangian has an exact $\mathrm{U}_{\mathrm{L}}(N_f) \otimes \mathrm{U}_{\mathrm{R}}(N_f)$ symmetry. Since the group $\mathrm{U}(N)$ is isomorphic to $\mathrm{U}(1) \otimes \mathrm{SU}(N)/\mathbb{Z}_N$ [2] the transformations in Eq. (2.19) can be separated into

[2] $\mathbb{Z}_N$ denotes the cyclic group of N elements, which is also the centre of the group $\mathrm{SU}(N)$. Since it is not of relevance to the present work, we will neglect the subtlety with the centre group and just take $\mathrm{SU}(N_f)$ as the

an $\mathrm{SU}(N_f)$ part times a complex phase:

$$U_{\mathrm{L/R}} = \exp\left(i\alpha_{\mathrm{L/R}}\mathbb{I}_f P_{\mathrm{R/L}}\right) \cdot \exp\left(i\beta^a_{\mathrm{L/R}} t_a P_{\mathrm{R/L}}\right), \tag{2.20}$$

where the $\alpha_{\mathrm{L/R}}$ and $\beta^a_{\mathrm{L/R}}$ are some transformation parameters, $\mathbb{I}_f$ is the unit matrix in N_f flavour space and t_a are the $\mathrm{SU}(N_f)$ generators. Furthermore, instead of using $\{P_{\mathrm{L}}, P_{\mathrm{R}}\}$ as a basis for the transformation one can equally use the components of the projectors, i.e., $\{\mathbb{I}_{\mathrm{D}}, \gamma_5\}$. Shifting the basis in this way has the advantage, that the $\mathrm{U}(1)$ and $\mathrm{SU}(N_f)$ transformations will induce corresponding vector (V) and axialvector (A) currents. With this in mind, the flavour transformations can be written in the following way:

$$\mathrm{U}_{\mathrm{L}}(N_f) \otimes \mathrm{U}_{\mathrm{R}}(N_f) = \mathrm{U}_V(1) \otimes \mathrm{SU}_V(N_f) \otimes \mathrm{SU}_A(N_f) \otimes \mathrm{U}_A(1)\,. \tag{2.21}$$

As is evident from Eq. (2.21), there are actually four distinct global transformations which can be written explicitly as

$$\begin{aligned} \exp\left(i\alpha_V \mathbb{I}_f \mathbb{I}_{\mathrm{D}}\right) &\in \mathrm{U}_V(1)\,, \qquad \exp\left(i\beta^a_V t_a \mathbb{I}_{\mathrm{D}}\right) \in \mathrm{SU}_V(N_f)\,, \\ \exp\left(i\alpha_A \mathbb{I}_f \gamma_5\right) &\in \mathrm{U}_A(1)\,, \qquad \exp\left(i\beta^a_A t_a \gamma_5\right) \in \mathrm{SU}_A(N_f)\,. \end{aligned} \tag{2.22}$$

The corresponding current densities are then given by the following quark bilinears

$$j^\mu = \bar{\Psi}\gamma^\mu \mathbb{I}_{\mathrm{D}} \mathbb{I}_f \Psi\,, \quad j^\mu_a = \bar{\Psi}\gamma^\mu \mathbb{I}_{\mathrm{D}} t_a \Psi\,, \quad j^\mu_{5;a} = \bar{\Psi}\gamma^\mu \gamma_5 t_a \Psi\,, \quad j^\mu_5 = \bar{\Psi}\gamma^\mu\gamma_5 \mathbb{I}_f \Psi\,. \tag{2.23}$$

We know that for a current to be conserved, the four-divergence of the current density has to vanish. The four-divergence of the current densities in Eq. (2.23) can be obtained to be

$$\partial_\mu j^\mu = 0\,, \quad \partial_\mu j^\mu_a = i\bar{\Psi}\mathbb{I}_{\mathrm{D}}[M, t_a]\Psi\,, \quad \partial_\mu j^\mu_{5;a} = i\bar{\Psi}\gamma_5\{M, t_a\}\Psi\,, \quad \partial_\mu j^\mu_5 = 2i\bar{\Psi}\gamma_5 M\Psi\,. \tag{2.24}$$

In the following we will shortly go over each of the four transformations and discuss the phenomenological implications of the current conversations in Eq. (2.24).

$\mathrm{U}_V(1)$ symmetry. Since the Lagrangian is invariant under a global rotation of the quark fields by a phase α_V, this current is actually conserved, as can be seen from the first term in Eq. (2.24). The corresponding charge Q_V corresponds to fermion number conservation, but can be redefined such that it yields *baryon number conservation* in QCD. The associated quantum number is the *baryon number B*.

$\mathrm{SU}_V(N_f)$ symmetry. This symmetry is explicitly broken by the mass matrix M. However, if all quarks were to have the same mass ($m_f = m$) then the Lagrangian would still be invariant and the second term in Eq. (2.24) would become $\partial_\mu j^\mu_a = 0$, i.e., all $(N_f^2 - 1)$

relevant group. An overview about the differences between $\mathrm{SU}(N)$ and $\mathrm{SU}(N)/\mathbb{Z}_N$ and their implications can be found in [119].

currents would be conserved. Even though this is not the case in nature, for QCD one can define two currents which are nevertheless conserved. These are the *isospin* and *hypercharge* currents

$$j_3^\mu = \bar{\Psi}\gamma^\mu t_3 \Psi\,, \quad j_8^\mu = \bar{\Psi}\gamma^\mu t_8 \Psi\,, \tag{2.25}$$

corresponding to the diagonal generators, which commute with each other and also with the mass matrix M. The associated charges are the third component of the isospin I_3 and the hypercharge Y, which then allows an arrangement of hadrons into $\{I_3, Y\}$-multiplets.

Furthermore, the masses of the three lightest quarks, i.e., *up, down and strange*, with $m_u \lesssim m_d \ll m_s$, are very much lighter that the typical scale of the strong interaction Λ_{QCD}. This momentum scale is characterized by the location of the 'Landau pole' [3] of QCD and is around $\Lambda_{\mathrm{QCD}} \approx 200$–$300$ MeV. Thus, QCD retains a very approximate $\mathrm{SU}_V(3) = \mathrm{SU}_f(3)$ flavour symmetry. Because the up and down quark masses are very similar $\Delta m_{ud} = m_d - m_u \approx 2.5$ MeV and the strange quark mass is much heavier by comparison, this approximate $\mathrm{SU}_V(3)$ can be further reduced to an almost exact $\mathrm{SU}_V(2)$ *isospin symmetry*.

$\mathrm{SU}_A(N_f)$ symmetry. This symmetry is explicitly broken by the quark masses not being equal to zero, i.e., $m_f \neq 0\,,\ \forall f$. Even if all quarks had the same mass ($m_f = m$), there remains a non-zero contribution to the four-divergence which is proportional to the quark mass

$$\partial_\mu j^\mu_{5;a} = 2im\bar{\Psi}\gamma_5 t_a \Psi\,, \tag{2.26}$$

which is known as the *partially conserved axialvector current* (*PCAC*) *relation*.

In the limit of massless quarks, this current is of course conserved. As in this limit also the $\mathrm{SU}_V(N_f)$ current is trivially conserved, one has an enlarged flavour symmetry, namely *chiral symmetry*: $\mathrm{SU}_V(N_f) \otimes \mathrm{SU}_A(N_f) \simeq \mathrm{SU}_\mathrm{L}(N_f) \otimes \mathrm{SU}_\mathrm{R}(N_f)$. This symmetry of the massless QCD Lagrangian implies the existence of *chiral partner states*, i.e., states with the same quark content but different parity, e.g., π and σ for the light mesons. However, if the massterm for the quarks is added, the mass splitting of the parity partners in nature is found to be very large, namely $m_\pi \approx 140$ MeV and $m_\sigma \approx 450$ MeV [20]. Thus, one concludes that additionally to being explicitly broken by the quark mass term, something else must be at play here leading to this large mass splitting. This additional effect is the spontaneous or dynamical breaking of the $\mathrm{SU}_A(N_f)$ symmetry by the interaction between quarks and gluons, which is the phenomenon usually implied when talking about *dynamical chiral symmetry breaking* (DCSB). This breaking in the context of QCD yields the above-mentioned residual approximate symmetry by the following breaking pattern $\mathrm{SU}_V(3) \otimes \mathrm{SU}_A(3) \to \mathrm{SU}_V(3)$. As by Goldstone's theorem the dynamical breaking of this symmetry would imply $N_f^2 - 1 = 8$ massless Nambu-Goldstone bosons, i.e., $\pi^\pm\,, \pi^0\,, K^\pm\,, K^0\,, \bar{K}^0\,, \eta_8$. In nature, none of these particles (or any other hadron) is in fact massless due to the current-quark

[3] We use 'Landau pole' in quotation marks, as QCD does not feature a classical Landau pole as for example is present in QED.

masses. The fact that the pions are far lighter than any hadron and even much lighter than the mass of their constituent-quarks (see below) is the reason why they are viewed as the pseudo-Nambu-Goldstone bosons [120] of QCD. Another effect of the DCSB is the emergence of the large *constituent-quark masses*, which is the mass of the effective valence quarks appearing in the conventional classification picture of hadrons. This constituent-quark mass for the up and down quarks is about 300 MeV and magnitudes larger than the respective current-quark mass. Related to this fact, one can show that most of the hadron mass M_H is actually due to gluonic effects because it is connected to the trace of the energy-momentum tensor: $M_H \sim \langle H|T^{\mu}{}_{\mu}|H\rangle$ [121]. While QCD as a classical theory is scale invariant in the chiral limit, i.e., the trace of the energy-momentum tensor vanishes, the quantized theory for sure is not. Quantum effects lead to this trace being proportional to the QCD β-function and non-zero even in the chiral limit. This is known as the *trace anomaly of QCD* [122, 123]. Another important quantity to mention in that regard is the scalar quark condensate $\langle\bar{\Psi}\Psi\rangle$, which, like the mass term in the Lagrangian, mixes left- and right handed spinors and is therefore non-zero except for the chiral limit. It therefore serves as an order parameter for chiral symmetry breaking.The physical value of the condensate and therefore the effect of DCSB can be determined from the *Gell-Mann-Oakes-Renner* (GOMR) relation [124]. We will see the effect of this relation later on in this work.

$\mathbf{U}_A(1)$ symmetry. The corresponding axialvector current in 2.24 is conserved classically for massless quarks $M = 0$. Quantizing the theory, however, does not preserve this symmetry as the current density j_5^{μ} picks up an anomalous contribution. The existence of this anomaly was discovered in the decay of the neutral pion $\pi^0 \to \gamma\gamma$, which had a much higher decay rate than expected. A theoretical description of this anomaly is given in form of the *Adler-Bell-Jackiw anomaly*, as it was first provided by Stephen Adler [125], John Bell and Roman Jackiw [126]. They discovered, that this anomaly is related to the fact that the corresponding Feynman diagrams cannot be regularized to preserve the axial anomaly. An intuitive way to think about how this anomaly comes about in the path-integral formulation of QED was introduced by Kazuo Fujikawa, who found that the anomaly arises when the action is invariant under the symmetry transformation but the functional measure is not [127]. For QCD, the anomalous term picked up by the current corresponds to the topological charge density with which the four-divergence of the current reads

$$\partial_\mu j_5^{\mu} = 2i\bar{\Psi}\gamma_5 M\Psi + N_f \cdot \frac{g^2}{(4\pi)^2} \cdot F^a_{\mu\nu}\tilde{F}^{\mu\nu}_a \,. \tag{2.27}$$

From this one can easily see, that this does not vanish in the chiral limit and thus always violates the symmetry. A phenomenological consequence of this anomaly is the large mass splitting of the η ($m_\eta = 547.8$ MeV) and η' ($m_{\eta'} = 957.7$ MeV) mesons.

2.3 Phenomenological aspects of QCD

In the previous section about symmetries, we have already discussed some mechanisms which influence the phenomenology of QCD. However, we are still missing arguably the two most prominent phenomenological features of QCD: *asymptotic freedom* and (*colour*) *confinement*. Both of these aspects show up most prominently when considering hadron physics and as the topic of this thesis is situated in precisely this field, they need to be introduced.

2.3.1 Asymptotic freedom

To start off, recall that the job of a coupling constant α is to 'measure' or set the strength of the force acting between the constituents of a theory depending on their respective distance. Thus, the coupling constant will vary (unless the theory is conformal) with changing distance between the constituents. Going to momentum rather than position space, this also implies that the coupling depends on a momentum scale Q, i.e., $\alpha(Q)$. This feature is known as the *running* of a coupling. E.g., considering the case of QED, we know that the coupling strength decreases with distance, i.e., the farther we pull an e^-e^+-pair apart, the weaker their attraction will become. Conversely, in momentum space the coupling constant increases with momentum scale until it diverges at the Landau pole, which for standalone QED is approximately at $Q \approx 10^{286}$ eV.[4] In QCD, this behaviour is exactly opposite. Furthermore, in contrast to the QED case, QCD only features a formal Landau pole, meaning that the coupling never actually diverges. From the fact that hadrons in general have a very small spatial extent, typically around 1 fm, and quarks are glued together by the gluon as the force carrier to form them, one can infer that the strong force is very strong at large distances or low momenta/energies. Interestingly, despite often being called the strong force, at high energies, i.e., the *ultraviolet* (UV) momentum regime, the force and hence the strong coupling constant $\alpha_s := \frac{g^2}{4\pi}$ is actually quite small (g denotes the coupling constant from the QCD Lagrangian). The most precise measurement to date gave a value of [128]

$$\alpha_s(M_Z) = 0.1183(9)\,, \tag{2.28}$$

with the mass of the Z boson, i.e., $M_Z = 91.1876(21)$ GeV [20], being the typical energy scale.

Theoretically, this running of the coupling with respect to the momentum scale is encapsulated in the *beta function* (β)

$$\beta(g) = \frac{\partial g}{\partial \ln(Q^2)}\,, \tag{2.29}$$

which can be obtained from the framework of the renormalization group. From Eq. (2.29)

[4] Note, that QED and the theory of weak interactions unify to the electroweak theory long before this energy scale. Furthermore, this is orders of magnitude above the Planck scale. Thus, this Landau pole of QED as a standalone theory is only theoretical and not of practical value.

it immediately follows, that the coupling increases when $\beta > 0$, decreases when $\beta < 0$ and does not change, i.e., is scale invariant, when $\beta = 0$. For QCD to lowest order, the β function can be determined as follows [84]

$$\beta(g) = -\frac{g^3}{(4\pi)^2} \cdot \left(\frac{11}{3} \cdot C_A - \frac{4}{3} \cdot N_f T_F \right), \tag{2.30}$$

where C_A is the quadratic Casimir in the adjoint representation, T_F is the Dynkin index in the fundamental representation and N_f is the number of quark flavours. Using the respective values in Eqs. (A.35) and (A.37) for QCD with $N_c = 3$ yields

$$\beta(g) = -\frac{g^3}{(4\pi)^2} \cdot \left(11 - \frac{2}{3} \cdot N_f \right). \tag{2.31}$$

Thus, the β function for QCD is negative as long as the number of quark flavours fulfils the condition $N_f \leq 16$. As it seems, there are only $N_f = 6$ quark flavours in nature. With this, the condition is always true and the β function is decreasing with increasing energy: a property called asymptotic freedom. Solving for the strong coupling constant to lowest order one obtains

$$\alpha_s(Q) = \frac{2\pi}{\beta_0} \frac{1}{\ln\left(\frac{Q}{\Lambda_{\mathrm{QCD}}}\right)}, \tag{2.32}$$

with $\beta_0 = 11 - \frac{2}{3} \cdot N_f$ corresponding to the first coefficient in the beta function expansion and Λ_{QCD} comes into play as an integration constant and marks the position of the 'Landau pole' of QCD. The value for Λ_{QCD} is determined by considering higher order expansion parameters of the β function in Eq. (2.31). Going to third order in the β function, using the experimentally obtained α_s from Eq. (2.28) and taking the number of relevant quark flavours $N_f = 5$, as the mass of the Z boson sets the energy cutoff such that $m_b \ll m_Z < m_t$, one obtains $\Lambda_{\mathrm{QCD}} \approx 210 - 250$ MeV.

Note, that the formula in Eq. (2.32) is only valid for energies $Q \gg \Lambda_{\mathrm{QCD}}$. At these high energies, one can use the strong coupling constant α_s as an expansion parameter for perturbation theory. However, below the QCD Landau pole perturbation theory fails completely as the coupling is too strong and non-perturbative effects dominate. Thus, Λ_{QCD} serves as a rough estimate for the boundary between the perturbative and non-perturbative regime.

2.3.2 Confinement

A fundamental property of QCD is that free quarks and gluons, both of which carry a colour charge, are not directly observable in experiments, but are rather bound in various combinations to form colourless hadrons. In other words, it is the absence of colour charged asymptotic particle states from the physical spectrum that, from a phenomenological point of view, inspires the notion of *colour confinement* of quarks and gluons. A different way, though related, is to introduce the notion of a *linear rising potential* between two static

quarks. In this picture there exist a flux tube between the quark-antiquark pair representing the potential energy stored in this system. When pulling a quark-antiquark pair apart, the potential energy between them rises linearly (a bit like a rubber band) until it reaches a point where it is energetically favourable to form new hadrons. This phenomenon is called *string breaking*. Note, that in general it is not that trivial to find a precise definition of "confinement" [129], however, for our purposes colour confinement is a sufficient definition. That this linear rising potential between two static quarks exists can be shown by calculating the *Wilson loop* [130] in Lattice QCD [61].

As seen in the last section, at high energies quarks and gluons are asymptotically free and only below the Λ_{QCD} scale they experience confinement. This change from a confined to an asymptotic free state, resembles a phase transition, which often involve (spontaneous) symmetry breaking processes. Local gauge symmetries, like in the present case for $\mathrm{SU}(3)$ colour, cannot break spontaneously due to *Elitzur's theorem* [131]. Certain gauge choices break this gauge symmetry down to a global residual symmetry, which we have seen in Section 2.2.2 to be the BRST invariance for QCD. Elitzur's theorem does not apply to such remnant gauge symmetries, which consequently can break spontaneously. Thus, it may be possible to determine whether a theory is confining or not by investigating if the remnant gauge symmetry is spontaneously broken or not. One such approach is the Kugo-Ojima confinement scenario [118], where the authors argue that both the BRST symmetry and additionally the global gauge symmetry must be conserved for the state space of QCD to feature only colourless states [132]. For this to be true, they find a criterion which implies that the non-perturbative ghost propagator must be more singular, and the fully dressed gluon propagator must be less singular than a simple pole at momentum $p^2 = 0$ [133]. For more information we refer the interested reader to [129, 134]. Another approach to confinement is known as the *Gribov-Zwanziger scenario* [135–137]. This scenario confinement is linked to the Coulomb potential and its relation to the *Gribov horizon*. The Landau gauge *Zwanziger horizon conditions* [136, 138] yield a similar infrared behaviour as the Kugo-Ojima confinement criterion and can actually be related to each other [139].

Chapter 3

Dyson-Schwinger Equations

3.1 Green functions

Green functions or *correlation function* are the heart and soul of all quantum field theories, as all physical properties can be extracted from them. To make it clear which objects we mean by correlation functions, two-point functions for example are (inverse) particle propagators while n-point functions[1] represent interaction vertices of n particles. In general, correlation functions are defined as the time-ordered vacuum expectation values of products of fields. A theory is considered solved once all Green functions are determined. In the path-integral formulation introduced in the last chapter, a Green function G, depending on the product of n fields, can be written as

$$G(x_1, \dots, x_n) := \langle 0|\mathrm{T}\left\{\hat{\Psi}(x_1) \dots \hat{\Psi}(x_n)\right\}|0\rangle = \frac{\int \mathcal{D}[\Psi]\, \mathrm{e}^{-S_{\mathrm{QCD}}}\, \Psi(x_1) \dots \Psi(x_n)}{\int \mathcal{D}[\Psi]\, \mathrm{e}^{-S_{\mathrm{QCD}}}}\,, \tag{3.1}$$

where we have introduced a *generalized quantum field* $\Psi = (\Psi_I)$, with $\Psi_I \in \{\psi_f, \bar{\psi}_f, A^a_\mu, c^a, \bar{c}^a\}$. The index convention is the same as in Chapter 2: f denotes the quark flavour, μ is a Lorentz index and a denotes the adjoint colour index. Furthermore, we have introduced the index I which here and in the following labels fields chosen from the generalized quantum field Ψ. The $\hat{\Psi}(x)$ denotes operators acting on state space, whereas the $\Psi(x)$ in the integral are functions. Correlation functions can also be denoted as follows

$$G[\Psi] = G(x_1, \dots, x_n) := \langle \Psi(x_1) \dots \Psi(x_n) \rangle\,, \tag{3.2}$$

as it reflects the statistical nature of the path-integral as a quantum expectation value and avoids potential confusion whether the Ψ's are functions or operators. We have introduced a shorthand notation $G[\Psi]$ to indicate the dependence on the considered functionals.

To obtain the desired Green functions in a systematic way, one can use the *generating functional* of the theory. This is done by taking the action corresponding to the Lagrangian in Eq. (2.10) and explicitly introduce the *source terms* of the fields in the Lagrangian. With this the Euclidean generating functional, written in a shorthand notation, reads

$$\mathcal{Z}[\mathcal{J}] = \int \mathcal{D}[\Psi]\, \exp\Big(-S_{\mathrm{QCD}}[\Psi] + \langle \Psi, \mathcal{J} \rangle\Big)\,, \tag{3.3}$$

[1] Green functions, n-point functions and correlation functions are used interchangeably.

where we have introduced a generalized (external) source field $\mathcal{J} = (\mathcal{J}_I)$, with $\mathcal{J}_I \in \{\bar{\eta}_f, \eta_f, j_a^\mu, \sigma_a, \bar{\sigma}_a\}$, corresponding to the generalized quantum field from above. The scalar product $\langle \Psi, \mathcal{J} \rangle$ is understood as a four-dimensional integration over all continuous and summation over all discrete indices. At $\mathcal{J} = 0$, the generating functional in Eq. (3.3) reduces to the QCD partition function without the sources given in Eq. (2.9).

By taking functional derivatives of Eq. (3.3) with respect to the sources $\mathcal{J}$, we can now obtain n-point Green functions in the presence of these sources as:

$$G[\Psi]_{\mathcal{J}} = \frac{1}{\mathcal{Z}[\mathcal{J}]} \frac{\delta^n \mathcal{Z}[\mathcal{J}]}{\delta \mathcal{J}(x_1) \dots \delta \mathcal{J}(x_n)} \,. \tag{3.4}$$

Note, that we have kept the $\mathcal{J}$-dependence for now, as it will prove useful in the following. However, to obtain the physical quantities one needs to remember to set the sources to their physical value, i.e., take the limit $\mathcal{J} \to 0$ at the end of a calculation. We will indicate quantities which are still depending on the sources with a subscript $\mathcal{J}$.

Connected Green functions are one of the prime quantities of theoretical interest since they enter in the S-matrix elements and are thus relevant for physical scattering processes. The generating functional for the connected Green functions is obtained from the generating functional $\mathcal{Z}[\mathcal{J}]$ in Eq. (3.3) via $W[\mathcal{J}] := \ln\left(\mathcal{Z}[\mathcal{J}]\right)$. Taking functional derivatives of $W[\mathcal{J}]$ with respect to the sources yields the connected n-point functions.

$$G[\Psi]^{\text{conn.}}_{\mathcal{J}} = \frac{\delta^n W[\mathcal{J}]}{\delta \mathcal{J}(x_1) \dots \delta \mathcal{J}(x_n)} \,. \tag{3.5}$$

For later purposes, it is useful to define a (semi-)classical or mean field $\tilde{\Psi}(x)$ as

$$\tilde{\Psi}(x) := \langle \Psi(x) \rangle_{\mathcal{J}} = \frac{\delta W[\mathcal{J}]}{\delta \mathcal{J}(x)} \,. \tag{3.6}$$

An equally important class of often used correlation functions are those, where the external propagators are amputated and which do not fall apart when cutting one internal propagator line in the Feynman diagrams. These are called *one-particle-irreducible* (*1PI*) correlation functions and describe the irreducible content of interaction vertices. They also have an associated generating functional which is termed (*quantum*) *effective action* Γ. It is obtained as a Legendre transform of $W[\mathcal{J}]$ with respect to the sources:

$$\Gamma[\tilde{\Psi}] := -W[\mathcal{J}] + \left\langle \frac{\delta W[\mathcal{J}]}{\delta \mathcal{J}}, \mathcal{J} \right\rangle = -W[\mathcal{J}] + \langle \tilde{\Psi}, \mathcal{J} \rangle \,. \tag{3.7}$$

This effective action can be viewed as a generalization of the classical action to the quantum level, as one obtains the classical action in the limit $\lim_{\hbar \to 0} \Gamma[\tilde{\Psi}] = S[\tilde{\Psi}]$. The n-point correlation functions can be obtained from the effective action via functional differentiation

with respect to the mean fields:

$$G[\Psi]^{1\mathrm{PI}}_{\mathcal{J}} := \frac{\delta^n \Gamma[\tilde{\Psi}]}{\delta\tilde{\Psi}(x_1)\ldots\delta\tilde{\Psi}(x_n)}\,. \tag{3.8}$$

For example, (source-dependent) three-point functions $G(x,y,z)_{\mathcal{J}}$ and propagators of particles $D(x,y)_{\mathcal{J}}$, which are the inverse of two-point functions, can be obtained as

$$G(x,y,z)_{\mathcal{J}} := \frac{\delta^3 \Gamma[\tilde{\Psi}]}{\delta\tilde{\Psi}(x)\delta\tilde{\Psi}(y)\delta\tilde{\Psi}(z)}\,, \tag{3.9}$$

$$D(x,y)_{\mathcal{J}} := \frac{\delta^2 W[\mathcal{J}]}{\delta\mathcal{J}(x)\delta\mathcal{J}(y)} = \left(\frac{\delta^2\Gamma[\tilde{\Psi}]}{\delta\tilde{\Psi}(x)\delta\tilde{\Psi}(y)}\right)^{-1}\,, \tag{3.10}$$

where in Eq. (3.10) we have used the relation

$$\mathcal{J}(x) = \frac{\delta\Gamma[\tilde{\Psi}]}{\delta\tilde{\Psi}(x)}\,, \tag{3.11}$$

to express the connected correlation function in terms of Γ, which will be useful in the context of Dyson-Schwinger equations (DSEs). As an interesting side note, because Γ reduces to the classical action in the limit $\hbar \to 0$, the 1PI two-point function being the inverse of the connected two-point function explains why the classical action contains the 1PI correlation functions at tree level, i.e., the inverse tree level propagators and the tree level vertices (see graphical Lagrangian in Section 3.2). The main point of the discussion above is that all three generating functionals $\mathcal{Z}[\Psi]$, $W[\Psi]$ and $\Gamma[\tilde{\Psi}]$ completely determine a QFT, as all correlation functions can be derived from them. We refrain from going into more detail here, as the topic of correlation functions is covered extensively in many standard quantum field theory book, e.g., [84, 85, 140, 141].

With this brief introduction to generating functionals and correlation functions we are now ready to tackle the topic of Dyson-Schwinger equations. The basic idea behind them is that instead of extracting the Green functions directly from the path-integral, one derives relations between them. These can be viewed as the *quantum equations of motion* as they describe the propagation of particles from one point in spacetime to another, encapsulating all possible interactions happening along the way. Since the general workings and properties of DSEs are readily available in standard textbooks [82, 140] and in the reviews [106, 142] and are furthermore not the main topic of this thesis, we will in the following only shortly introduce the basic concepts and consider the quark DSE in more detail, as it is the most important one for this work.

Conceptionally, the derivation of Dyson-Schwinger equations is built upon the fact that the integral over a total derivative vanishes if the integrand vanishes at the integration bounds. With quantum fields, this condition is fulfilled as they are expected to vanish at

infinity. Hence, one can apply this idea to Eq. (3.3), which yields

$$0 = \int \mathcal{D}[\Psi] \frac{\delta}{\delta \Psi_I} \mathrm{e}^{-S[\Psi]+\langle \Psi, \mathcal{J} \rangle} = \int \mathcal{D}[\Psi] \left(-\frac{\delta S[\Psi]}{\delta \Psi_I} + \mathcal{J}_I \right) \cdot \mathrm{e}^{-S[\Psi]+\langle \Psi, \mathcal{J} \rangle} \tag{3.12}$$

Replacing all contributing fields Ψ_K in the argument of the action by derivatives with respect to the sources, i.e., $S[\delta/\delta \mathcal{J}_K] = S[\Psi]|_{\Psi_K \to \delta/\delta \mathcal{J}_K}$, we are able to pull this term and the sources $\mathcal{J}_I$ out of the integral and arrive at a more convenient and familiar form of the term in Eq. (3.12), namely a *master DSE*. The following equation shows the master DSE for the *connected and disconnected* (or full) correlation functions

$$\left(\frac{\delta S}{\delta \Psi_I} \left[\frac{\delta}{\delta \mathcal{J}_K} \right] - \mathcal{J}_I \right) \mathcal{Z}[\mathcal{J}] = 0 \,, \tag{3.13}$$

as it is derived from the generating functional $\mathcal{Z}$. The name master DSE is very fitting, as all n-point DSEs can be obtained from this equation. As a short interlude, it is useful to shortly explain the procedure happening in Eq. (3.13). One first takes a functional derivative of the action with respect to a chosen field Ψ_I and after that, according to the shorthand notation introduced in the text above, replaces the remaining fields with the derivatives with respect to their sources, i.e., the term in the square brackets, and lets them act on the generating functional $\mathcal{Z}[\mathcal{J}]$. To derive a desired DSEs from Eq. (3.13), one first chooses a "base" field Ψ_I, e.g., quark, antiquark, gluon, ghost in the case of QCD, and then carries out the procedure described above. After that, one then takes further functional derivatives of this result with respect to the appropriate source terms. Once this is done, one then needs to collect the higher than desired correlation functions into vertices and finally sets the source terms to their physical value, i.e., $\mathcal{J} \to 0$. For example, to obtain the quark DSE for a chosen flavour f containing all – connected and disconnected – correlation functions, one first chooses the external source of the antiquark-field $\bar{\psi}_f$, i.e., η_f as a "base" source and then carries out a further functional derivative with respect to the source of the quark field ψ_f of the same flavour, i.e., $\bar{\eta}_f$. This procedure of deriving DSEs clearly follows a given scheme and is therefore of algorithmic nature. Because of this, there also exist programs which automate the derivation numerically and algebraically [143, 144].

Deriving DSEs for connected *and* disconnected diagrams is interesting, but since disconnected diagrams do not contribute to physical processes, these are not the type of DSEs we are after. Changing from the generating functional $\mathcal{Z}[\mathcal{J}]$ to the generating functional for the connected correlation functions $W[\mathcal{J}]$, we obtain the master DSE for the connected Green functions as

$$\frac{\delta S}{\delta \Psi_I} \left[\frac{\delta W[\mathcal{J}]}{\delta \mathcal{J}_K} + \frac{\delta}{\delta \mathcal{J}_K} \right] - \mathcal{J}_I = 0 \,. \tag{3.14}$$

Furthermore, for the one-particle irreducible (1PI) Green functions, there also exist a master DSE which reads

$$\frac{\delta S}{\delta \Psi_I}\left[\tilde{\Psi}_K + \left\langle \left(\frac{\delta^2 \Gamma[\tilde{\Psi}]}{\delta \tilde{\Psi}_K \delta \tilde{\Psi}_J}\right)^{-1}, \frac{\delta}{\delta \tilde{\Psi}_J}\right\rangle\right] - \frac{\delta \Gamma[\tilde{\Psi}]}{\delta \tilde{\Psi}_I} = 0\,. \tag{3.15}$$

With the identity

$$\frac{\delta}{\delta \mathcal{J}_I(x)} = \int_y \left(\frac{\delta^2 W[\mathcal{J}]}{\delta \mathcal{J}_I(x) \delta \mathcal{J}_J(y)}\right) \frac{\delta}{\delta \Psi_J(y)} \Leftrightarrow \frac{\delta}{\delta \tilde{\Psi}_I(x)} = \int_y \left(\frac{\delta^2 \Gamma[\tilde{\Psi}]}{\delta \tilde{\Psi}_I(x) \delta \tilde{\Psi}_J(y)}\right)^{-1} \frac{\delta}{\delta \mathcal{J}_J(y)} \tag{3.16}$$

which allows for a transformation between the derivative with respect to the sources and the one with respect to the (average) fields and the relation in Eq. (3.6) one can rewrite the argument in the brackets, i.e., the field replacement rule, in Eq. (3.15) as

$$\frac{\delta S}{\delta \Psi_I}\left[\frac{\delta W[\mathcal{J}]}{\delta \mathcal{J}_K(x)} + \frac{\delta}{\delta \mathcal{J}_K(x)}\right] - \frac{\delta \Gamma[\tilde{\Psi}]}{\delta \tilde{\Psi}_I} = 0\,. \tag{3.17}$$

We will later use the 1PI master equation to derive the DSE for the quark propagator. Because the effective action Γ depends on the fields $\tilde{\Psi}$ rather than the sources, one has to send the fields $\tilde{\Psi}_I$ to their physical value (which is zero in most cases) at the end of the derivation as opposed to setting the sources $\mathcal{J}_I$ to zero like it was the case for the master DSEs in Eqs. (3.13) and (3.14).

In some cases it is useful to consider a generalization of the 1PI Green functions, namely the *n-particle irreducible* (nPI) correlation functions. The idea towards this generalization was first introduced by John M. Cornwall, Roman W. Jackiw and E. Terry Tomboulis [145]. Like in the 1PI case, nPI correlation functions are Feynman diagrams where cutting up to n internal lines still does not render them disconnected. The generating functional for these type of correlation functions is the nPI effective action, which is obtained by introducing additional sources for higher vertices and performing a Legendre transformation with respect to these sources. Using the nPI correlation functions can be advantageous when constructing truncation schemes or investigating some analytic relations since the derived Dyson-Schwinger equations form a closed system in this case. This is due to the fact that there are no higher n-point functions than the ones already present in the action. For a review and more information on the nPI framework, see [69, 146–148] and references therein.

Before we take a closer look at the derivation of the quark DSE, it is useful to shortly introduce some common nomenclature. During the derivation of DSEs both perturbative and non-perturbative quantities show up. The non-perturbative quantities contain all the quantum fluctuations and are hence commonly referred to as *full* or *dressed* (or sometimes even as *fully dressed*). The perturbative quantities on the other hand are termed as *free* or *bare*.

3.2 Quark Dyson-Schwinger equation

3.2.1 Derivation

In hadron physics, (anti)quarks are considered the central objects making up bound states and resonances. As all information about quarks is stored in the quark propagator, the quark DSE is therefore an essential and much needed building block for the work at hand. Therefore, it is useful to shortly sketch its derivation and discuss the systematics and truncations. For this we will use a combination of the mathematical formulation and a graphical language to better illustrate the steps happening in the derivation. We therefore introduce the QCD action schematically in the graphical language as

$S_{\mathrm{QCD}}[\bar{\psi},\psi,A]$ =

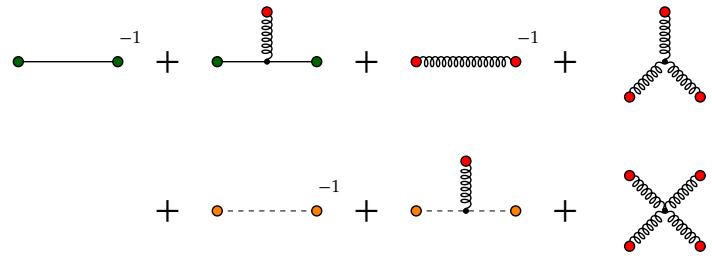

where the dark green dots denote the (anti)quark fields $\bar{\psi}(x)\,,\psi(x)$, the red dots are a representation for the gluon field $A^a_\mu(x)$ and the orange dots represent the ghost fields $\bar{c}$, c. The small black dot is the bare interaction vertex.

With this set, the starting point of the derivation is the 1PI master DSE in Eq. (3.15). For the generalized quantum field Ψ_I we choose the antiquark field $\bar{\psi}_{i,f}(x)$ of flavour f and with fundamental colour index i. We then carry out the functional derivative of the action and the replacements as described in the section above and arrive at:

$$\frac{\delta\Gamma[\psi,\bar{\psi},A]}{\delta\bar{\psi}_{i,f}(x)} = (\partial\!\!\!/ + m_f)\psi_{i,f}(x) + igt_a\gamma^\mu\left[A^a_\mu(x)\psi_{i,f}(x) + \left(\frac{\delta^2 W[\mathcal{J}]}{\delta j^\mu_a(x)\delta\bar{\eta}_{i,f}(x)}\right)\right]. \tag{3.18}$$

In the graphical language, the derivative with respect to the antiquark field corresponds to removing the left green dot in the diagrams containing quark fields. Therefore, in the graphical representation the term in Eq. (3.18) becomes:

$\dfrac{\delta\Gamma[\bar{\psi},\psi,A]}{\delta\bar{\psi}_{i,f}(x)}$ =

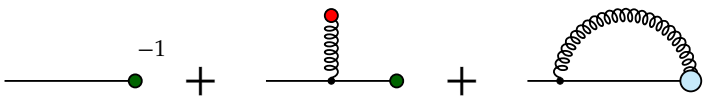

The cyan blob in the last term represents the connected quark-gluon vertex. Taking a further derivative of Eq. (3.18) with respect to the quark field $\psi_{j,f}(y)$ of the same flavour,

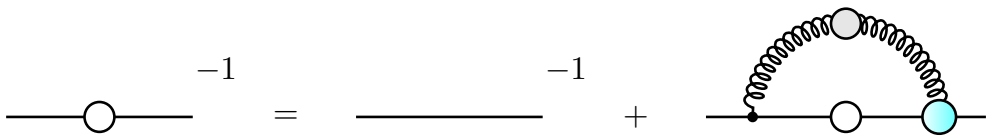

Figure 3.1: Graphical representation of the quark Dyson-Schwinger equation. The white and grey blobs denote the fully dressed quark and gluon propagators respectively and the cyan filled circle represents the fully dressed quark-gluon vertex.

one obtains

$$\begin{aligned}\frac{\delta^2\Gamma[\psi,\bar{\psi},A]}{\delta\bar{\psi}_{i,f}(x)\delta\psi_{j,f}(y)} = (\not{\partial}+m_f)\delta^{(4)}(x-y)\delta_{ij} + igt_a\gamma^\mu A^a_\mu(x)\delta^{(4)}(x-y)\delta_{ij} \\ + igt_a\gamma^\mu\left(\frac{\delta^2 W[\mathcal{J}]}{\delta j^\mu_a(x)\delta\bar{\eta}_{i,f}(x)}\right)\frac{\overleftarrow{\delta}}{\delta\psi_{j,f}(y)}\,,\end{aligned} \tag{3.19}$$

where we have used the relation $\frac{\delta\psi_i(x)}{\delta\psi_j(y)} = \delta^{(4)}(x-y)\delta_{ij}$ in the process. The arrow over the derivative in the last term indicates its acting direction. Using the relations in Eq. (3.16) and quite a bit of algebra, the detailed steps of which can be found, e.g., in Appendix B.4 in [93], one can then rewrite the last term such that Eq. (3.19) reads

$$\begin{aligned}\left.\frac{\delta^2\Gamma[\psi,\bar{\psi},A]}{\delta\bar{\psi}_{i,f}(x)\delta\psi_{j,f}(y)}\right|_{\bar{\psi}=\psi=A_\mu=0} =&(\not{\partial}+m_f)\delta^{(4)}(x-y)\delta_{ij} + igt_a\gamma^\mu A^a_\mu(x)\delta^{(4)}(x-y)\delta_{ij} \\ &- igt_a\gamma^\mu\int_{u,v} D^{ab}_{\mu\nu}(x-u)\cdot\Gamma^{\nu,l}_{b,i}(u,y,v)\cdot S_{lj;f}(v-x)\,.\end{aligned} \tag{3.20}$$

During this rewriting certain fully dressed quantities emerge, i.e., the full gluon propagator $D^{ab}_{\mu\nu}$, the full quark-gluon vertex $\Gamma^{\nu,l}_{b,i}$ and the full quark propagator $S_{lj,f}$ of flavour f. Using the definition in Eq. (3.10), the last thing to finalize the derivation is to set all explicit fields in Eq. (3.20) to zero. This concludes our derivation and the final form of the quark Dyson-Schwinger equation reads

$$S^{-1}_{ij;f}(x-y) = S^{-1}_{0,ij;f}(x-y) + g^2 t_a\gamma^\mu\int_{u,v} D^{ab}_{\mu\nu}(x-u)\cdot\Gamma^{\nu,l}_{b,i}(u,y,v)\cdot S_{lj;f}(v-x)\,, \tag{3.21}$$

with the quantity $S_{0,ij}(x-y)$ denoting the bare inverse quark propagator. The second term is commonly known as the quark self-energy. Note, that we pulled out a factor of ig from the full quark-gluon vertex $\Gamma^{\nu,l}_{b,i}$ such that the self-energy terms gets a positive sign. Eq. (3.21) **is** the exact quantum equation of motion of the (inverse) quark propagator. The graphical depiction of the quark DSE is shown in Fig. 3.1, where the blobs denote the fully dressed quantities.

As mentioned above and can be seen from Eq. (3.21), to solve the quark DSE one needs

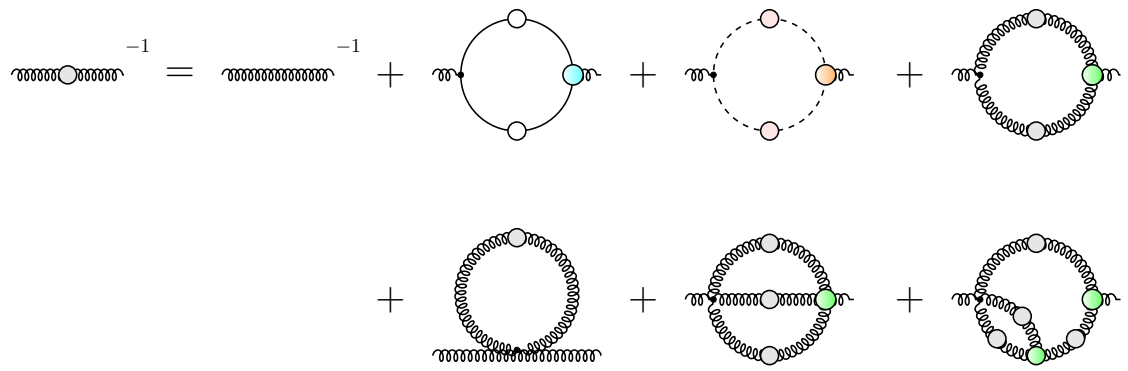

Figure 3.2: Graphical representation of the Dyson-Schwinger equation for the full gluon propagator. The white, orange and grey blobs on the propagators denote the full quark, ghost and gluon propagators, respectively. For the vertices, the cyan blob is the full quark-gluon, the orange is the full ghost-gluon and the green blob corresponds to the fully dressed three-gluon vertex.

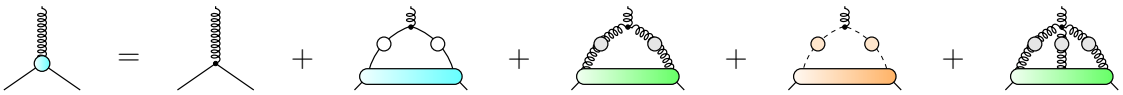

Figure 3.3: Depiction of the Dyson-Schwinger equation for the dressed quark-gluon vertex. The white, orange and grey blobs on the propagators denote the full quark, ghost and gluon propagators, respectively. The filled bars represent higher fully dressed 1PI Green functions.

to know the full gluon and the full quark-gluon vertex. These quantities fulfil their own DSEs, which can be derived in a similar fashion from the 1PI master DSE in Eq. (3.15):

$$\left(D^{ab}_{\mu\nu}\right)^{-1}(x-y) = \frac{\delta^2\Gamma[\bar{\psi},\psi,A_\mu]}{\delta A^\mu_a(x)A^\nu_b(y)}\,, \qquad \Gamma^{\mu,j}_{a,i}(x,y,z) = \frac{\delta^3\Gamma[\bar{\psi},\psi,A_\mu]}{\delta\bar{\psi}_i(x)\delta A^\mu_a(y)\delta\psi_j(z)}\,. \tag{3.22}$$

We will refrain from deriving them here for the sake of brevity and because their full form will prove to not be of essential value for this thesis. The graphical representations of the corresponding DSEs are shown in Figs. 3.2 and 3.3. These DSEs then include even higher full n-point vertices, each fulfilling their own DSEs [149]. This yields a self-consistent, infinite tower of coupled integral equations, which in this form is an exact description of QCD.

3.2.2 General solution of the quark DSE

Since we are generally interested in physics at particular energy scales, it is more convenient for us to consider the momentum space representation of the quark DSE. Fourier transforming the position space representation in Eq. (3.21) and renormalizing the fields (cf. Section 2.1) we get

$$S_f^{-1}(p,\mu) = S_{0;f}^{-1}(p,\mu) + \Sigma_f(p,\mu)\,, \tag{3.23}$$

where p is the external quark momentum and μ denotes a chosen renormalization point. Unless explicitly needed, the Dirac indices will be suppressed for better readability. The quantity $S_{0;f}$ is the renormalized, bare quark propagator of flavour f

$$S_{0;f}^{-1}(p,\mu) = Z_2^f(\mu^2,\Lambda^2)(i\not{p} + Z_{m_f}(\mu^2,\Lambda^2)m_f(\mu^2))\,, \tag{3.24}$$

with $m_f(\mu^2)$ denoting the renormalized quark mass. The quark self-energy Σ is given as

$$\Sigma_f(p,\mu) = g^2(\mu)\, Z_{1F}^f(\mu^2,\Lambda^2)\cdot(\gamma^\mu t_a)\int_b^\Lambda D_{\mu\nu}^{ab}(k,\mu)\cdot\Gamma_b^\nu(b,k,\mu)\cdot S_f(b,\mu)\,, \tag{3.25}$$

with internal quark momentum b, the UV momentum-cutoff Λ, the strong coupling constant g, the renormalization constant of the quark-gluon vertex Z_{1F}^f (cf. STIs Eq. (2.14)) and $k = b - p$ denoting the gluon momentum. It is clear from the bare propagator in Eq. (3.24), that the quark propagator can be expressed via two Dirac structures, i.e., $\not{p}$ and the unit matrix in Dirac space $\mathbb{I}_\mathrm{D}$. To capture the full momentum-dependent behaviour of the quark propagator, one introduces two dressing functions $A(p^2,\mu^2)$ and $B(p^2,\mu^2)$ and attaches them to the Dirac tensors to form the general solution for the full inverse quark propagator as follows [2]:

$$S_f^{-1}(p,\mu) = i\not{p}\cdot A_f(p^2,\mu^2) + B_f(p^2,\mu^2) = Z_f^{-1}(p^2,\mu^2)\cdot(i\not{p} + M_f(p^2))\,. \tag{3.26}$$

Here we have introduced the quark wavefunction $Z_f = A_f^{-1}$ and the renormalization point independent quark mass function

$$M_f(p^2) = \frac{B_f(p^2,\mu^2)}{A_f(p^2,\mu^2)}\,. \tag{3.27}$$

With this, the full quark propagator can be written as

$$S_f(p,\mu) = \frac{-i\not{p}\cdot A_f(p^2,\mu^2) + B_f(p^2,\mu^2)}{p^2\cdot A_f^2(p^2,\mu^2) + B_f^2(p^2,\mu^2)} := -i\not{p}\cdot\sigma_V(p^2,\mu^2) + \sigma_S(p^2,\mu^2)\,, \tag{3.28}$$

where we have introduced two dressing functions corresponding to the vector (γ^μ) and to the scalar $(\mathbb{I}_\mathrm{D})$ Dirac structure, i.e., σ_V and σ_S, respectively. Because the dressing functions depend on the momentum of the quark, we can investigate the transition of the quark mass function $M(p^2)$ and the behaviour of the quark propagator from the UV to the infrared energy region.

It is also useful to consider the charge conjugation of the quark propagator, as it will be important later on in the context of diquarks. Charge conjugation of a quark replaces it

[2] This is only true in vacuum. In medium the spatial and temporal part need to be treated separately due to $O(4)$ symmetry breaking. This yields an additional dressing function in the general solution of the quark propagator [150].

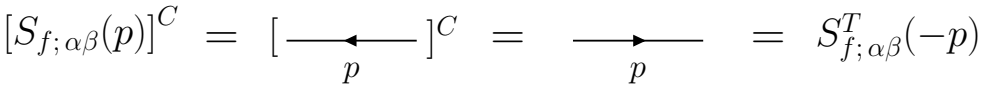

Figure 3.4: Feynman diagram representation of the charge conjugation of the quark propagator. The arrow on the propagator line indicates the spin and momentum flow of the quark propagator. The momentum flow of the quark propagator is inverted and regarding the Dirac structure, the charge conjugation corresponds to transposing the quark propagator.

with the associated antiquark. The charge conjugated quark propagator is obtained via

$$\left[S_{f;\alpha\beta}(p)\right]^C \sim C^T_{\alpha\eta}(-i\not{p})_{\eta\zeta}C_{\zeta\beta} + C^T_{\alpha\eta}\delta_{\eta\zeta}C_{\zeta\beta} = -i\left(-\not{p}^T_{\alpha\beta}\right) + \delta^T_{\alpha\beta} = S^T_{f;\alpha\beta}(-p)\,, \quad (3.29)$$

where we have made use of the relations given in Eq. (A.24). The superscript T denotes transposed quantities. Note, that upon charge conjugation the momentum flow of the quark propagator is flipped. The whole process effectively corresponds to transposing the quark propagator. A visualization of the charge conjugation is shown in Fig. 3.4.

An important fact to note is, that the quark DSE in Eq. (3.23) only depends on the renormalization scale μ^2, while the UV cutoff Λ^2 dependence is fully absorbed in the renormalization constants. As explained in Section 2.1, employing a MOM renormalization scheme imposes conditions for the physical observables to take certain values at the renormalization scale μ^2. The commonly used renormalization condition for the quark DSE reads

$$S_f^{-1}(p,\mu)|_{p^2=\mu^2} = i\not{p} + m_f(\mu^2)|_{p^2=\mu^2}\,, \quad (3.30)$$

imposing the conditions $A(p^2,\mu^2)|_{p^2=\mu^2} = 1$ and $B(p^2,\mu^2)|_{p^2=\mu^2} = m_f(\mu^2)$ on the dressing functions. The renormalization scale for the "physical" observables is consistently set to $\mu = 19$ GeV in this work, which is sufficiently far in the UV for our purposes. One now only needs to solve for the two dressing functions to obtain the full, momentum-dependent information of the quark propagator.

Numerically, the quark DSE in Eq. (3.23) is solved via an iterative process, as the full (inverse) quark propagator appears on both sides of the equation. Furthermore, one needs the full gluon propagator and full quark-gluon vertex as an input, which we will discuss in the next section. These are given as the general solution to their respective DSEs in Figs. 3.2 and 3.3 as:

$$D^{ab}_{\mu\nu}(k) = \left(\delta_{\mu\nu} - \frac{k_\mu k_\nu}{k^2}\right)\cdot\frac{Z(k^2,\mu^2)}{k^2}\cdot\delta^{ab} := T_{\mu\nu}(k)\cdot\frac{Z(k^2,\mu^2)}{k^2}\cdot\delta^{ab}\,, \quad (3.31)$$

$$\Gamma^\mu_a(b,k,\mu) = t_a\cdot\sum_{l=1}^{12} f_l(b^2,k^2,b\cdot k,\mu^2)\cdot\tau^\mu_l(b,k)\,. \quad (3.32)$$

The $T_{\mu\nu}(k)$ denote the transversal projector. In Landau gauge ($\xi \to 0$), the longitudinal part of the gluon propagator vanishes. Thus, we only need one dressing function $Z(k^2)$.

The f_l denote the twelve dressing functions of the full quark-gluon vertex.

3.2.3 Truncations

Because the tower of DSEs is infinite, it does not constitute a closed system and a solution without truncations and/or modelling is not feasible in finite time and with limited computing power. Some early models employed to study the quark DSE include the Munczek-Nemirovsky [151, 152] and the Nambu-Jona-Lasinio model [153, 154]. These models, although able to capture qualitative phenomenological features, have obvious shortcomings due to lack of dynamics, localization of the gluon propagator or neglection of the dynamics contained in the (dressed) quark-gluon vertex.

To tackle the quark DSE numerically, we use one of the most prominent and successful truncations of the DSE tower that is available in the literature, i.e., the *Rainbow-Ladder truncation* (*RL*). The idea behind this truncation is to reduce the complicated object that is the full quark-gluon vertex given in Eq. (3.32) – initially consisting of twelve tensor structures and accompanying dressing functions – to its leading Dirac tensor structure and make a model ansatz for the corresponding vertex dressing, i.e.,

$$\Gamma^{\mu}_{a}(b,k,\mu) = \gamma^{\mu} t_a \cdot \Gamma(k^2,\mu^2)\,. \tag{3.33}$$

Neglecting the dependence on the (internal) quark momentum b^2, the (model) dressing function only depends on the gluon momentum k^2. This reduces the complexity of the equation drastically, as the quark-gluon vertex DSE decouples from the system. The caveat of course is, that the model needs to be chosen carefully not to omit possible important dynamics stored in the full quark-gluon vertex.

We can now reinsert the ansatz in Eq. (3.33) into Eq. (3.25) and combine the model dressing function $\Gamma(k^2)$ together with the gluon dressing $Z(k^2)$ and the coupling strength $g(k^2)$ into an *effective running coupling* (or effective interacting strength)

$$\alpha(k^2) = \frac{g^2(\mu^2)}{4\pi} \cdot \frac{1}{\tilde{Z}_3 Z_2} \cdot Z(k^2,\mu^2)\Gamma(k^2,\mu^2)\,. \tag{3.34}$$

In this work we choose not to solve the corresponding gluon DSE to obtain the gluon dressing function $Z(k^2)$, but we will use an appropriate parameterization for the effective running coupling instead. As this corresponds to absorbing the structure of the quark-gluon vertex into the gluon and modelling the dynamics of both quantities plus the coupling, the quark DSE completely decouples from the tower of DSEs and forms a closed system. Employing the effective running coupling in the quark DSE in Fig. 3.1 corresponds to the replacement shown in Fig. 3.5 in the self-energy term.

With this, the self-energy term expands into a sum of diagrams which contain ever more gluon exchanges. This structure graphically resembles a rainbow, hence the name **Rainbow**-Ladder truncation. We will see in the next section where the Ladder part of the name comes from. To model the most important dynamics as good as possible, the explicit form of the effective coupling $\alpha(k^2)$ is motivated by physics. In the UV momentum region, the momentum dependence of $\alpha(k^2)$ should resemble the behaviour known from

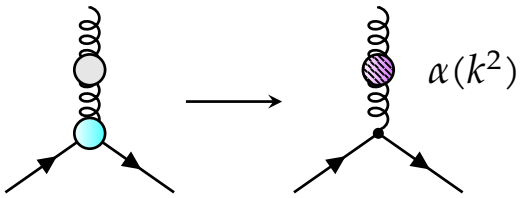

Figure 3.5: Graphical depiction in terms of Feynman diagrams of combining the dynamics of the full gluon propagator (*grey blob*) and the full quark-gluon vertex (*cyan blob*) into an *effective gluon* (*hatched, purple*) with a bare quark-gluon vertex.

(resummed) perturbative QCD, which preserves the important property of asymptotic freedom. When going to the IR momentum region, the interaction needs to be sufficiently strong to enable dynamical chiral symmetry breaking – which would come automatically when solving the coupled DSE system.

In the past, several models have been employed for $\alpha(k^2)$, using the UV limit together with an ansatz for the IR behaviour [155–158]. In this work, we will use a very frequently chosen and very successful parameterization first introduced by Pieter Maris and Peter C. Tandy in [159, 160]. We will therefore in the following simply refer to it as the "Maris-Tandy (MT) model" or "Maris-Tandy interaction". The parameterization of the effective running coupling in the MT model reads [3]

$$\alpha(k^2) = \pi \cdot \eta_{\mathrm{MT}}^7 \left(\frac{k^2}{\Lambda_{\mathrm{MT}}^2}\right)^2 \exp\left(-\eta_{\mathrm{MT}}^2 \cdot \frac{k^2}{\Lambda_{\mathrm{MT}}^2}\right) + \pi \cdot \frac{2\gamma_m \left(1 - \exp\left(-\frac{k^2}{\Lambda_t^2}\right)\right)}{\ln\left(\mathrm{e}^2 - 1 + \left(1 + \frac{k^2}{\Lambda_{\mathrm{QCD}}^2}\right)^2\right)}, \tag{3.35}$$

where the first term characterizes the IR properties and the second term accounts for the UV behaviour of the interaction. The latter is constrained by perturbative QCD, as it approaches the asymptotic behaviour of the QCD running coupling in the limit $k^2 \to \infty$, cf. Eq. (2.32). The QCD scale here is given as $\Lambda_{\mathrm{QCD}}^{N_f=4} = 0.234\,\mathrm{GeV}$, while the anomalous dimension of the quark mass function is obtained as $\gamma_m = {}^{12}/_{(11 \cdot N_c - 2 \cdot N_f)}$. N_c is the number of colours, which is $N_c = 3$ for conventional QCD. The number of flavours chosen for the interaction in this work is $N_f = 4$, which does not necessarily coincide with the number of flavours used, but rather serves as a model parameter to determine Λ_{QCD} for the MT interaction [69, 159, 160]. The interaction in Eq. (3.35) also features three model parameters – a UV parameter $\Lambda_t = 1\,\mathrm{GeV}$, a dimensionless parameter η_{MT} and an IR scale Λ_{MT}. Since this work is focussed on hadron physics, we are more interested in the infrared properties and thus the latter two parameters are the important ones as they govern the IR behaviour of our model interaction. The values for these parameters are fixed to $\eta_{\mathrm{MT}} = 1.8$ and $\Lambda_{\mathrm{MT}} = 0.72\,\mathrm{GeV}$ in this work, such that certain properties of the pion, i.e., its mass and

[3] In the literature, Eq. (3.35) is sometimes expressed with a different set of parameters, i.e., $\{D, \omega\}$. These are related to the $\{\eta, \Lambda\}$ parameters used here via: $\omega = {}^{\Lambda}/_{\eta}$ and $D = \eta\Lambda^2$.

its leptonic decay constant, are reproduced. As a last step, we note that the ghost-gluon vertex in Landau gauge is actually not UV divergent [161, 162], thus we can choose $\tilde{Z}_1 = Z_g \tilde{Z}_3 Z_3^{1/2} = 1$. With this, the renormalization constant for the quark-gluon vertex simplifies to: $Z_{1F}^f = Z_2^f / \tilde{Z}_3$. Finally, we can make the following replacement in the quark DSE Eq. (3.23) (omitting all the arguments of the renormalization constants and dressing functions for simplicity):

$$Z_{1F}^f \cdot g^2 Z\Gamma \sim Z_{1F}^f \cdot Z_g^{-2} \cdot Z_3^{-1} \cdot Z_{1F}^f = \left(Z_2^f\right)^2 \cdot \Big(\underbrace{Z_g^2 \cdot \tilde{Z}_3^2 \cdot Z_3}_{=\tilde{Z}_1^2=1} \Big)^{-1} = \left(Z_2^f\right)^2 . \tag{3.36}$$

Putting everything together, the quark Dyson-Schwinger equation in its closed and final form reads

$$S_f^{-1}(p,\mu) = S_{0;f}^{-1}(p,\mu) + \left(Z_2^f(p^2,\mu^2)\right)^2 \cdot C_F \int_b^\Lambda \frac{\alpha(k^2)}{k^2} \, T_{\mu\nu}(k) \, \gamma^\mu \cdot S_f(b,\mu) \cdot \gamma^\nu \,, \tag{3.37}$$

where we have used Eq. (A.30) to get the quadratic Casimir operator C_F defined in Eq. (A.35). Since the full quark propagator will serve as an input for the main considerations of this work, we will discuss the solution of Eq. (3.37) in the next section.

Before we do so, just note that there is an alternative way to systematically approach and truncate the tower of equations. For this, one chooses a certain nPI effective action and derives the coupled system of DSEs from the respective master equation. Furthermore, one truncates above a certain order in the loop expansion. This yields a closed system of equations as in this case, the DSEs do not contain higher n-point functions than present in the (effective) action, see [69, 163] and references therein for a more detailed description and its application to the meson sector and [68] for a successful application of this method to study the glueball spectrum. For reasons of saving computing power and that this systematic approach is not yet readily available for the systems studied in this work, we resort to the Maris-Tandy interaction described above.

3.2.4 Numerical solutions

To obtain the solution for the full quark propagator of a chosen flavour f numerically, we need to solve Eq. (3.37) for the two dressing functions $A_f(p^2)$ and $B_f(p^2)$. To do so, we project out the dressing functions individually and then solve the two resulting coupled equations simultaneously. Since the parameters of the MT model are fixed in our case (cf. last section), the only external input needed is the renormalized quark mass at the renormalization point for the chosen quark flavour, i.e., $m_f(\mu^2)$. In this work, we go to the isospin symmetric limit, i.e., $m_u = m_d$, and from here on denote the up and down quark with a common letter: $u/d = n$. This is a good approximation, as SU(2) isospin symmetry is an almost exact symmetry (cf. Section 2.2.2) and the MT interaction is anyhow flavour blind. A sketched description of the solution process is given in Appendix B.1 in [164].

The solution for the up/down-quark propagator is displayed in the *left* panel of Fig. 3.6. Here, we show the obtained dressing functions A_f and B_f and the resulting quark mass

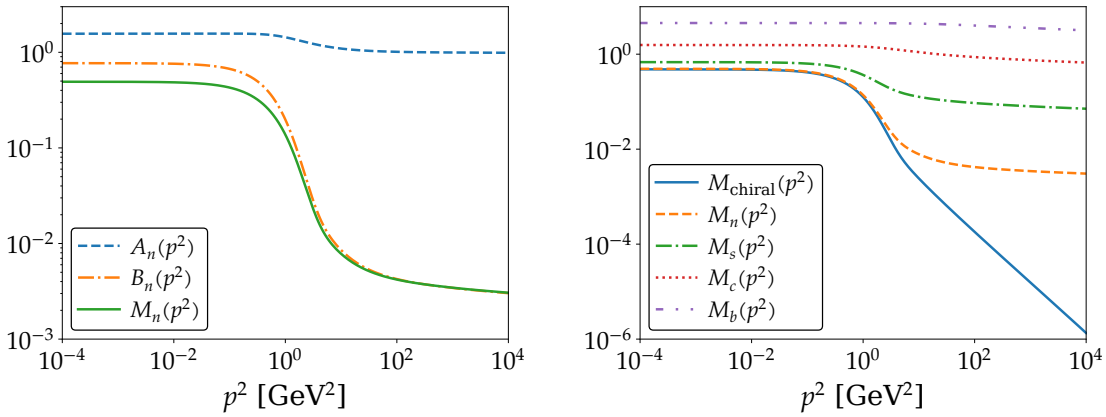

Figure 3.6: *Left panel*: Quark dressing functions $A(p^2)$ (*blue, dashed*), $B(p^2)$ (*orange, dash-dotted*) and $M(p^2)$ (*green, solid*) for current-quark mass $m_n(\mu^2) = 3.7$ MeV. *Right panel*: Quark mass functions for the chiral limit (*blue, solid*), up/down (*orange, dashed*), strange (*green, dash-dotted*), charm (*red, dotted*) and bottom (*violet, dash-doubledotted*) quarks. The respective current-quark masses used as an input will be discussed in Chapter 4.

function M_f, defined in Eq. (3.27), as functions of $p^2 \in \mathbb{R}^+$ in a log-log plot. We choose $m_n(\mu^2) = 3.7$ MeV as a realistic u/d current-quark mass. We see, that all dressing functions approach asymptotic values in the IR and the UV and the greatest change happens around $p^2 = 1\,\text{GeV}^2$. The important physics in this plot is given in the quark mass function $M_n(p^2)$. It shows the evolution of the quark mass from the current-quark mass in the ultraviolet ($m_n = 3.7\,\text{MeV}$), enforced by to our renormalization condition in Eq. (3.30), to the much heavier constituent-quark mass in the infrared momentum region $M(p^2 \lesssim 1\,\text{GeV}^2) \approx 492\,\text{MeV}$. This behaviour is commonly referred to as dynamical mass generation and is a direct effect of the dynamical chiral symmetry breaking of QCD, which we discussed in the **SU**$_A(N_f)$ **symmetry** subsection in Section 2.2.2. Solving the quark DSE for the other quark flavours of interest for this work, that is the *strange* (s), *charm* (c) and *bottom* (b) quarks, we obtain the respective quark mass functions, which are shown in the *right* panel of Fig. 3.6. From this graph we see, that compared to the current-quark mass of the respective quark flavour, the effect of the dynamical mass generation gets less and less pronounced for the heavier quark flavours.

Now we are prepared to take a closer look at the structure of the full quark propagator in Eq. (3.28), in particular at the denominator

$$\text{den}(S_f(p^2)) = \frac{1}{p^2 \cdot A_f^2(p^2) + B_f^2(p^2)}\,. \tag{3.38}$$

We see that the propagator will have poles for certain values of $p^2 \in \mathbb{C}$, which is not surprising, as this is a generic property of propagators. As we will discuss in more detail in the following chapter, whenever a particle propagator has a pole for timelike p^2, i.e., with negative real part, one obtains the mass plus the decay width of that particle, depending on whether the pole is located on the negative real axis or in the complex plane. However, the

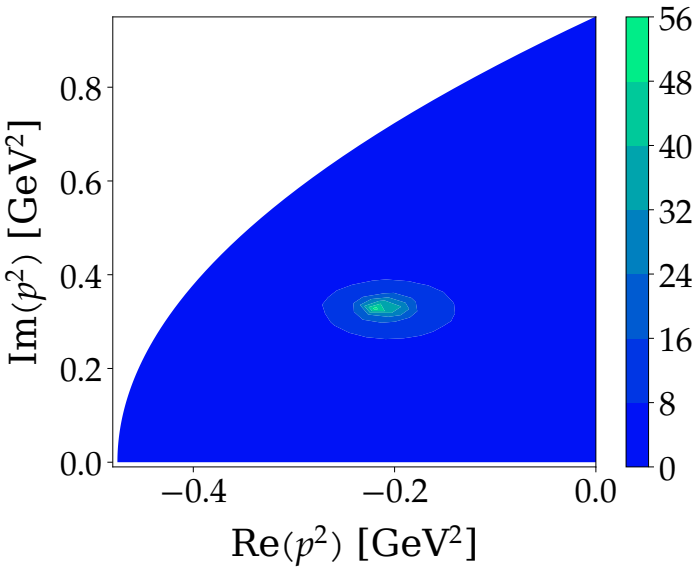

Figure 3.7: The structure of the vector dressing function σ_V of the up/down-quark propagator in the complex plane, shown as a contour plot. The x- and y-axes represent the real and imaginary part of p^2. The same current-quark mass was used as in the left panel in Fig. 3.6. The singularities occur roughly at $p^2 \approx (-0.2 \pm 0.3i)\,\mathrm{GeV}^2$.

quark is not an observable particle and therefore the poles in Eq. (3.38) will have a different interpretation. We will nevertheless investigate the structure of the quark propagator in the complex p^2 plane, as it will be necessary for the later considerations in this work. The first observation we make is, that the dressing functions satisfy certain (anti)symmetries under complex conjugation (denoted by the asterisk):

$$A_f((p^2)^*) = A_f^*(p^2)\,, \qquad B_f((p^2)^*) = B_f^*(p^2)\,, \tag{3.39}$$

We conclude, that while the real part of A_f and B_f is symmetric under complex conjugation, the imaginary part is antisymmetric. Therefore, any pole structures of the full quark propagator show up with a complex conjugate partner. This behaviour of complex conjugate poles is known to occur in rainbow-ladder truncations [165]. To visualize the structure of the full quark propagator, we solve the up/down-quark DSE in Eq. (3.37) for complex p^2 and show the resulting σ_V dressing function as a two-dimensional contour plot in Fig. 3.7. Showing only the upper half-plane of $\mathrm{Im}(p^2)$ is sufficient, as the poles occur as complex conjugate pairs. One can clearly see, that the up/down-quark propagator has a singularity at $p^2 \approx (-0.2 \pm 0.3i)\,\mathrm{GeV}^2$. For a detailed analysis of the pole structures of the quark propagator using DSEs with the Maris-Tandy model see [166].

A short note is in order here. Solving the quark DSE by simply choosing p^2 to be complex leads to the gluon momentum $k^2 = b^2 + p^2 \pm 2\sqrt{p^2}\sqrt{b^2}$ in the integration of Eq. (3.37) to be complex, constituting the interior of a parabola. Making the argument for the effective coupling in Eq. (3.34) complex, the logarithmic tail of $\alpha(k^2)$ develops branch cuts during

the integration. For small current-quark masses the effect of blindly integrating over the branch cut is negligible and the position of the poles is not affected. We will call this *naive integration*. However, going to heavier quark flavours requires going further and further into the complex p^2-plane. Here the effect of the branch cut is too severe, which leads to numerical artefacts obstructing the calculation. To avoid this one can follow two strategies:

- One can resort to path deformation techniques and choose an integration path for the internal quark momentum b^2 such that the branch cut is not hit, see, e.g., [167]. As a caveat, one needs to trust that there are no further emerging branch cuts or poles – which are very hard to catch – disturbing the path deformation.
- Alternatively, one can shift the integration variable from the internal quark momentum b to the gluon momentum k [4]. This in turn renders the gluon momentum real and the internal quark momentum becomes complex. For the internal quark momentum b^2 one then sets up parabolas in the complex plane with increasing apex and opening and solves the quark DSE on these parabolas. Because these parabolas fill the complex plane one after the other like shells, this method is termed *shell-method* [168]. A very pedagogical introduction can be found in Appendix B.2 of [164]. Note as a caveat, that choosing a parabola too close to the complex conjugate poles will lead to longer computation times or even non-convergence of the quark DSE.

The up/down-quark propagator in Fig. 3.7 was obtained via the naive integration as it allows to visualize also p^2 beyond the complex conjugate poles. Choosing the naive integration here is possible, because as explained above, the up/down current-quark mass is light enough such that the branch cut effect is negligible. In the following calculations of this work, we employ the shell-method to calculate the quark propagator in the complex plane, as we are then not restricted to only the light quark flavours.

With this, we have now introduced and discussed the most important quantities needed as an input for the subsequent investigations of this work, i.e., the rainbow-ladder truncation together with the Maris-Tandy model and the full quark propagator as a solution to the quark DSE in said truncation. This then concludes our considerations about Dyson-Schwinger equations and we are now ready to move on and tackle the main topic of this work, namely hadrons and hadronic bound state equations.

[4] This is straightforward, since the integral is formally translation invariant.

Chapter 4

Bethe-Salpeter Equations

Up to now, we have learned what types of fields and possible interactions between them are present in the context of QCD and how the particles associated to the fields propagate from one spacetime point to another via the concept of correlation functions and their equations of motion, i.e., the Dyson-Schwinger equations. While these subjects are fascinating in their own right, the main topic of this thesis is the extraction and investigation of hadron properties. To obtain the properties of hadrons in ordinary, non-relativistic quantum mechanics, we would compute a potential and solve the Schrödinger equation. However, since we are dealing with the relativistic framework of QFTs in this work, we need to address how to calculate hadron properties like masses etc. in this context. Put into one question: Is there an analogue of the Schrödinger equation in the context of QFTs?

The answer to this question is of course 'yes'. These analogues are called *Bethe-Salpeter equations* (*BSEs*), introduced by Hans Bethe and Edwin E. Salpeter in 1951 [169], and are the central object of this thesis. The following chapter aims at providing a short overview over the derivation and solution of these equations in general. In this context, we will discuss the properties of mesons and diquarks, i.e., solutions to the two-body BSE, with total spin $J = 0, 1$, as they will be important for the internal structure of four-quark states.

4.1 Derivation

As already mentioned in Section 3.1, correlation functions are the central objects containing all information of quantum field theories. It should therefore come as no surprise, that also the properties of hadrons are contained in Green functions. In particular, scattering amplitudes and cross-sections are the important quantities in this context. The question now is: How do we extract hadron properties from correlation functions?

The answer to this question is related to an important quantity when dealing with correlation functions, which is also related to experiment: the *spectral representation*. As its definition and derivation are given in any standard QFT book, e.g., [81, 83–85], we refrain from discussing it in detail here and only highlight some aspects. Usually the spectral representation is derived in the context of two-point functions and as a start one considers the eigenstates $|\xi\rangle$ of the Hamiltonian of the theory. Each state is characterized by a momentum $\vec{P}$ and an associated energy $E_{\vec{P}} = (\vec{P}^2 + M_\xi^2)^{1/2}$, where M_ξ labels the mass of the state. Possible mutiparticle states in this formulation are characterized by the centre-of-mass momentum $\vec{P}$ plus relative momenta between the particles and their energy spectrum forms a continuum. The complete set of eigenstates of course constitutes the

whole state space of the theory and as a consequence one can formulate a completeness relation

$$\mathbb{I} = \sum_{\tilde{\xi}} \frac{1}{(2\pi)^3} \int \frac{\mathrm{d}^3 P}{2E_{\vec{P}}} |\xi\rangle \langle\xi| \,, \tag{4.1}$$

where the sum over ξ is formal, including also integrals over relative momenta for possible multiparticle states, and the denominator in the integral measure is the Lorentz-invariant energy of the states, forcing them to be on-shell. Inserting Eq. (4.1) into the two-point correlation function then yields the spectral representation, which tells us, that on-shell particles in Eq. (4.1) produce poles in the respective propagators whenever the momentum $\vec{P}^2$ equals the physical mass of the particle $M^2_{\tilde{\xi}}$. For more information and useful proofs, see [170].

For the QCD Hamiltonian, the whole state space is enormous, including not only the colour-singlet hadrons like mesons, baryons, glueballs and multiquark states, but also (unphysical) coloured states like diquarks. One can therefore also formulate a completeness relation of the form in Eq. (4.1) for QCD. Since the two-point correlation functions in QCD, i.e., quark and gluon propagators, cannot produce physical hadron poles upon insertion of the completeness relation, a generalization of the spectral representation to n-point functions is needed.

Fortunately, this is possible and we will do so in the following considering a generic n-quark meson bound state, consisting of $n/2$ quarks and $n/2$ antiquarks of arbitrary flavour. This choice was made as all investigated hadrons in this thesis will be mesons. The Green function for our n-quark meson state will contain $2n$ fields (n quark and n antiquark fields) and read

$$G^{(2n)}_{\mathcal{A}_1 \dots \mathcal{A}_n; \mathcal{B}_1 \dots \mathcal{B}_n}(x_1, \dots, x_n; y_1, \dots y_n) = \langle 0|\mathrm{T}\{\psi_{\mathcal{A}_1}(x_1)\bar{\psi}_{\mathcal{A}_2}(y_1) \dots \psi_{\mathcal{B}_{(n-1)}}(x_n)\bar{\psi}_{\mathcal{B}_n}(y_n)\}|0\rangle \,, \tag{4.2}$$

with the $\mathcal{A}_i$, $\mathcal{B}_i$ denoting the combination of Dirac, flavour and colour indices for the quark and antiquark fields, respectively, to avoid clutter. Inserting the completeness relation Eq. (4.1) for QCD into Eq. (4.2) and using a subsequent Fourier transformation to go to momentum space, one can see that each on-shell hadron with momentum $P^2 = -M^2_{\tilde{\xi}}$ produces a pole in the correlation function and the spectral representation of the correlation function $G^{(2n)}$ thus reads

$$G^{(2n)}_{\mathcal{A}_1 \dots \mathcal{A}_n; \mathcal{B}_1 \dots \mathcal{B}_n}(\{p_i\}, \{q_i\}, P) = \sum_{\tilde{\xi}} \frac{\Psi^{(n)}_{\tilde{\xi}; \mathcal{A}_1 \dots \mathcal{A}_n}(\{p_i\}, P) \bar{\Psi}^{(n)}_{\tilde{\xi}; \mathcal{B}_1 \dots \mathcal{B}_n}(\{q_i\}, P)}{P^2 + M^2_{\tilde{\xi}}} + \text{regular terms} \,, \tag{4.3}$$

where the sum contains all the possible hadrons with the given quark content and quantum numbers $I\left(J^{P(C)}\right)$, the sets $\{p_i\}$ and $\{q_i\}$ denote the $n-1$ relative momenta (because of momentum conservation at the 'vertex' Ψ) between the (anti)quarks and P labels the total momentum of the hadron. In Eq. (4.3) we have introduced the *Bethe-Salpeter wave function*

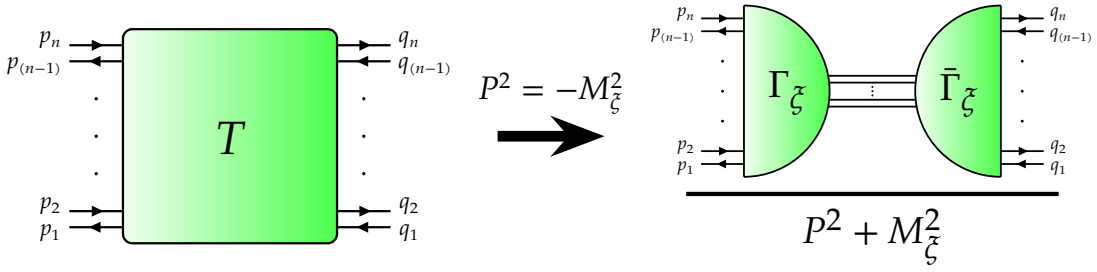

Figure 4.1: Graphical illustration of the approximate form for the $2n$-(anti)quark T matrix at the pole of a hadron $|\xi\rangle$ given in Eq. (4.9). The n-quark T-matrix is represented by the green box, while the n-quark Bethe-Salpeter amplitudes are depicted as the green half-circles. The (anti)quark propagators are represented by lines with an arrow indicating the spin and momentum flow. Arrows pointing from right-to-left denote quarks and from left-to-right denote antiquarks. The associated quark momenta are shown as given in the main text.

(*BSWF*) [171]

$$\Psi^{(n)}_{\xi;\,A_1\ldots A_n} = \langle 0|\psi_{A_1}\bar{\psi}_{A_2}\ldots\psi_{A_{(n-1)}}\bar{\psi}_{A_n}|\xi\rangle \tag{4.4}$$

as the transition element between vacuum and the on-shell hadron state. Caution: even though the name BS *wave function* would suggest otherwise, we cannot directly obtain probability information from these objects as would be the case for the usual wave functions in quantum mechanics [170]. At the pole location of a hadron $|\xi\rangle$, the sum in Eq. (4.3) gets dominated by this term and the correlation function approximately reads

$$G^{(2n)}(\{p_i\},\{q_i\},P) \overset{P^2=-M_\xi^2}{\approx} \frac{\Psi^{(n)}_\xi(\{p_i\},P)\,\bar{\Psi}^{(n)}_\xi(\{q_i\},P)}{P^2+M_\xi^2}\,. \tag{4.5}$$

The $\bar{\Psi}$ here denotes the charge conjugated BSWF. To make the equations more readable, we choose to suppress most of the momentum dependencies and all indices except for the state label ξ for now.

The correlation function in Eq. (4.2) also satisfies an equation of motion, which in this context is called *Dyson equation* (suppressing all indices and arguments here):

$$G^{(2n)} = G_0^{(n)} + G_0^{(n)} K^{(n)} \cdot G^{(2n)}\,. \tag{4.6}$$

The $G_0^{(n)}$ denotes the product of n non-interacting (free) full quark propagators and $K^{(n)}$ is an nPI scattering kernel (as we have n (anti)quarks) with respect to the quark propagators. Each multiplication implies an integration over all loop momenta. The full correlation function $G^{(2n)}$ can be related to the $(2n)$-quark T-matrix, i.e., the non-trivial part of the scattering matrix S, via $G^{(2n)} = G_0^{(n)} + G_0^{(n)}\,T^{(2n)}\,G_0^{(n)}$, which in turn also fulfils its own Dyson equation

$$T^{(2n)} = K^{(n)} + K^{(n)} G_0^{(n)} \cdot T^{(2n)}\,. \tag{4.7}$$

This relation between G and T also implies the following relation between the BSWF Ψ and the *Bethe-Salpeter amplitude* (*BSA*) Γ, which is the amputated wave function:

$$\Psi^{(n)}_{\xi} = G^{(n)}_0 \cdot \Gamma^{(n)}_{\xi} \,. \tag{4.8}$$

Thus, by inserting this into Eq. (4.3) and amputating the quark legs, one obtains a similar spectral representation for $T^{(2n)}$, which at the pole of a given hadron reduces to

$$T^{(2n)}(\{p_i\},\{q_i\},P) \overset{P^2=-M^2_{\xi}}{\approx} \frac{\Gamma^{(n)}_{\xi}(\{p_i\},P)\,\bar{\Gamma}^{(n)}_{\xi}(\{q_i\},P)}{P^2+M^2_{\xi}} \,. \tag{4.9}$$

This expression in terms of Feynman diagrams is given in Fig. 4.1. We stress, that the object in the numerator of Eq. (4.9), also often termed the *residue* R_{ξ} at the hadron pole

$$R_{\xi}(\{p_i\},\{q_i\},P) = \Gamma^{(n)}_{\xi}(\{p_i\},P)\,\bar{\Gamma}^{(n)}_{\xi}(\{q_i\},P) \,, \tag{4.10}$$

contains all the non-trivial information about T in the vicinity of the particle pole and therefore all the information about the state itself. While this also holds for the BSWF Ψ, we will use the BSA Γ throughout this work.

To extract the information about a hadron, we first need to calculate the corresponding BSA Γ at the physical pole. To do this, let's say we are at the pole of the hadron we want to investigate. We can then insert Eq. (4.9) for the T-matrix in its Dyson equation Eq. (4.7):

$$\frac{\Gamma^{(n)}_{\xi}\,\bar{\Gamma}^{(n)}_{\xi}}{P^2+M^2_{\xi}} = K^{(n)} + K^{(n)} G^{(n)}_0 \cdot \frac{\Gamma^{(n)}_{\xi}\,\bar{\Gamma}^{(n)}_{\xi}}{P^2+M^2_{\xi}} \,. \tag{4.11}$$

By comparing the residues on both sides, this equation reduces to

$$\frac{\Gamma^{(n)}_{\xi}\,\bar{\Gamma}^{(n)}_{\xi}}{P^2+M^2_{\xi}} = K^{(n)}\, G^{(n)}_0 \cdot \frac{\Gamma^{(n)}_{\xi}\,\bar{\Gamma}^{(n)}_{\xi}}{P^2+M^2_{\xi}} \,, \tag{4.12}$$

from which we can now cancel the denominator and the charge conjugated BSA $\bar{\Gamma}$ to find the homogeneous Bethe-Salpeter equation:

$$\Gamma^{(n)}_{\xi} = K^{(n)}\, G^{(n)}_0 \cdot \Gamma^{(n)}_{\xi} \,, \tag{4.13}$$

which will be the main equation of interest in this thesis. A pictographic sketch of this derivation in shown in Fig. 4.2. From this it is easy to see, that, by applying the usual Feynman rules, the homogeneous BSE is an integral equation featuring $n-1$ integrals over the respective relative momenta.

A short note regarding the naming is in order here. Since the original formulation of the BSE was in the context of two-body systems, the name 'Bethe-Salpeter equation' is often reserved for such systems, e.g., mesons and diquarks. However, this formulation was first extended to three-body systems like baryons by Ludvig D. Faddeev [172, 173]

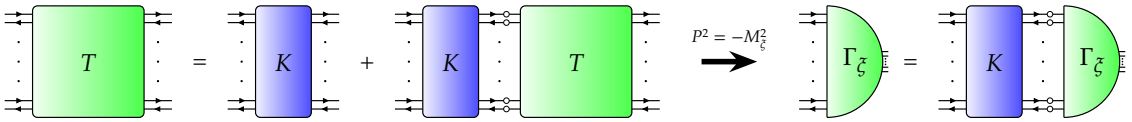

Figure 4.2: Graphical representation showing the derivation of the homogeneous n-quark Bethe-Salpeter equation from the Dyson equation of the n-quark T-matrix. The T-matrix is again shown as the green box, the blue box depicts the interaction kernel $K^{(n)}$, the blobs on the line represent fully dressed quark propagators and the green half-circles are the n-quark Bethe-Salpeter amplitudes.

and then finally generalized to n-particle systems by O. Yakubovsky [174]. Hence, the generalizations of the BSEs are generally known as *Faddeev-Yakubovsky equations* (*FYEs*). Throughout this thesis, we will use these two terms interchangeably.

The homogeneous BSE in Eq. (4.13) can be viewed as an eigenvalue equation for the matrix $K^{(n)}G_0^{(n)}$ with the eigenvalue being equal to **one**. The BSAs Γ_ξ take the role of an eigenvector in this picture. A more general formulation of Eq. (4.13) would be to introduce an eigenvalue $\lambda_\xi(P^2)$ depending on the squared total hadron momentum P^2 and write

$$\lambda_\xi(P^2)\,\Gamma_\xi^{(n)} = K^{(n)}\,G_0^{(n)}\cdot\Gamma_\xi^{(n)}\,. \tag{4.14}$$

There is of course a similar equation for the BSWF. With this more general formulation, we normally do not solve the BSE directly at the pole of the hadron, but instead vary P^2 and calculate the associated eigenvalues $\lambda_\xi(P^2)$. The resulting *eigenvalue curve* (*EVC*) satisfies the condition $\lambda_\xi(P^2 = -M_\xi^2) = 1$ at the pole of the considered hadron, which reduces Eq. (4.14) to Eq. (4.13) rendering the BSE solved. The state label ξ now differentiates whether we have obtained the ground state of a hadron with the considered (anti)quark content and quantum numbers $I\left(J^{P(C)}\right)$, i.e., the largest eigenvalue with $\xi = 0$, or a radially excited state, which are labelled with the next lower eigenvalues with $\xi = 1, 2, \ldots$.

This more general procedure is useful for various reasons. Firstly, when we consider states which are experimentally measured, we know the position of the pole and can try to solve the BSE at or in the region of the experimentally given mass. However, if we want to investigate particles which have not yet been measured and predict their masses, we do not have this information. By considering a range of P^2 and investigating the behaviour of the EVC, we can see where the condition $\lambda = 1$ is met and thus make predictions about the masses. Secondly, in a perfect world with enough time and computing power, we would be able to know and include all the important interactions in the kernel $K^{(n)}$ and calculate the masses to arbitrary precision. However, in practice, most of the time, we need to truncate the system or model some part of the interactions to make the computations feasible. Depending on the employed model, the mass spectrum of hadrons can vary greatly. Investigating the EVC can give important insights on the reliability of the used model.

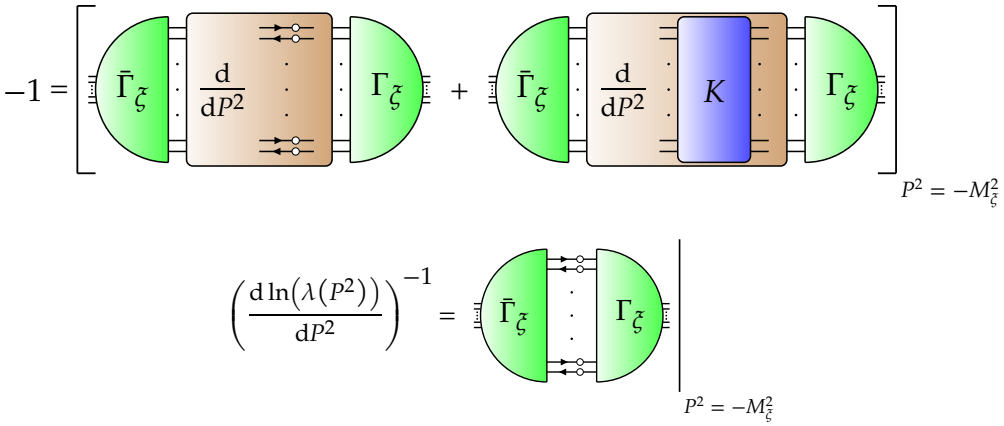

Figure 4.3: Graphical representation of the Cutkosky-Leon (*top*) and the Nakanishi (*bottom*) normalization condition for the Bethe-Salpeter amplitude Γ_ξ in the language of Feynman diagrams.

4.1.1 Normalization and general structure of the BSAs

Reintroducing the omitted momentum dependencies, the obtained BSA $\Gamma_\xi(\{p_i\}, P)$ contains the non-trivial, momentum-dependent information about the on-shell hadron $|\xi\rangle$. They can thus be used to calculate further properties of the associated hadron, e.g., leptonic decay constants, form factors for hadronic decays just to name a few. Similarly to the wave function in quantum mechanics, Γ_ξ (or Ψ_ξ) needs to be properly normalized in order to be used in further calculations. This normalization constant can be determined by using either of the two following criteria.

The Cutkosky-Leon criterion was first formulated by Richard E. Cutkosky and M. Leon in [175] and starts by considering the derivative of the correlation function G with respect to P^2. Since for this work we are more interested in the BSA than the BSWF, we will reformulate the derivation in terms of T rather than the originally considered G. The obtained results can be converted into each other with a bit of algebra. Considering the derivative of T with respect to P^2 now yields the following relation[1]:

$$\frac{\mathrm{d}T^{(2n)}}{\mathrm{d}P^2} = -T^{(2n)} \frac{\mathrm{d}\left(T^{(2n)}\right)^{-1}}{\mathrm{d}P^2} T^{(2n)} . \tag{4.15}$$

Inserting Eq. (4.9) straightforwardly yields the normalization condition

$$1 = \left[\bar{\Gamma}_\xi^{(n)} \frac{\mathrm{d}\left(T^{(2n)}\right)^{-1}}{\mathrm{d}P^2} \Gamma_\xi^{(n)} \right]_{P^2=-M_\xi^2} . \tag{4.16}$$

Reformulating Eq. (4.7) as $T = (\mathbb{I} - KG_0)^{-1}K$ and inverting this yield the inverse of the

[1] Since T and its inverse T^{-1} fulfil $T\,T^{-1} = \mathbb{I}$, differentiating this product yields $(T\,T^{-1})' = 0$, where $'$ denotes a generic derivative. By applying the chain rule, we get: $T'\,T^{-1} + T\,(T^{-1})' = 0$ and consequently obtain $T' = -T\,(T^{-1})'\,T$.

T-matrix as

$$\left(T^{(2n)}\right)^{-1} = \left(K^{(n)}\right)^{-1} - G_0^{(n)} \,. \tag{4.17}$$

Inserting this into Eq. (4.16) and fixing $P^2 = -M_\xi^2$ from here on gives

$$1 = \left[\bar{\Gamma}_\xi^{(n)} \frac{\mathrm{d}\left(K^{(n)}\right)^{-1}}{\mathrm{d}P^2} \Gamma_\xi^{(n)} - \bar{\Gamma}_\xi^{(n)} \frac{\mathrm{d}G_0^{(n)}}{\mathrm{d}P^2} \Gamma_\xi^{(n)} \right]_{P^2=-M_\xi^2} \tag{4.18}$$

$$= \left[\bar{\Gamma}_\xi^{(n)} \left(K^{(n)}\right)^{-1} \frac{\mathrm{d}K^{(n)}}{\mathrm{d}P^2} \left(K^{(n)}\right)^{-1} \Gamma_\xi^{(n)} - \bar{\Gamma}_\xi^{(n)} \frac{\mathrm{d}G_0^{(n)}}{\mathrm{d}P^2} \Gamma_\xi^{(n)} \right]_{P^2=-M_\xi^2} . \tag{4.19}$$

As a last step, we can now use $(K)^{-1} \cdot \Gamma_\xi = G_0 \cdot \Gamma_\xi$ from Eq. (4.13) and write

$$-1 = \left[\bar{\Gamma}_\xi^{(n)} \left(\frac{\mathrm{d}G_0^{(n)}}{\mathrm{d}P^2} + G_0^{(n)} \frac{\mathrm{d}K^{(n)}}{\mathrm{d}P^2} G_0^{(n)} \right) \Gamma_\xi^{(n)} \right]_{P^2=-M_\xi^2} . \tag{4.20}$$

A graphical representation of this final form of the Cutkosky-Leon normalization condition in terms of Feynman diagrams can be found in the top panel of Fig. 4.3.

Alternatively, there is the Nakanishi criterion which was formulated by Noboru Nakanishi [176] and reads

$$\left(\frac{\mathrm{d}\ln\left(\lambda(P^2)\right)}{\mathrm{d}P^2} \right)^{-1} \Bigg|_{P^2=-M_\xi^2} = \bar{\Gamma}_\xi^{(n)} G_0^{(n)} \Gamma_\xi^{(n)} \,. \tag{4.21}$$

Here one takes the derivative of the (logarithm of the) eigenvalue $\lambda(P^2)$ with respect to P^2 and connects it to a closed loop involving the BSAs and the product of dressed quark propagators $G_0^{(n)}$. The Nakanishi criterion in Eq. (4.21) is depicted in the bottom panel of Fig. 4.3 in terms of Feynman diagrams.

For this work, we choose to work with the Nakanishi normalization criterion, for the few cases that we need to apply it explicitly, as it is the less complex one not involving a two-loop diagram. In the context of the four-body equation later on in this work, only the right-hand side of Eq. (4.21) will be of importance, but we will elaborate on this further once we get there.

It is now time to take a closer look at the mathematical formulation of the Bethe-Salpeter amplitude $\Gamma_\xi(\{p_i\}, P)$. As is the case for the wave function in quantum mechanics, the BSWF Ψ and therefore its amplitude Γ can be split into different parts, each describing an individual aspect of the hadron. These aspects are of course the total spin J (given in terms of Dirac matrices), the colour and the flavour structure of the hadron with given quantum numbers $I(J^{PC})$. Therefore, we can consider our BSA to live in a product space consisting of the 4×4 dimensional Dirac-, the $N_c \times N_c$ dimensional colour- and the $N_f \times N_f$

dimensional flavour-space. Explicitly written, the BSA then reads

$$\Gamma^{(\mu\nu\ldots);A_1\ldots A_n;a_1\ldots a_n}_{\xi;\alpha_1\ldots\alpha_n}(\{p_i\},P) = \Gamma^{(\mu\nu\ldots)}_{\mathrm{D(irac)};\alpha_1\ldots\alpha_n}(\{p_i\},P) \otimes \Gamma^{A_1\ldots A_n}_{\mathrm{C(olour)}} \otimes \Gamma^{a_1\ldots a_n}_{\mathrm{F(lavour)}}\,, \tag{4.22}$$

with Lorentz indices $\mu\nu\ldots$ denoting states of higher spin, i.e., $J = 1, 2, \ldots$. Each (anti)quark carries a Dirac, colour and flavour index, which for the general case considered here will amount to n Dirac, colour and flavour indices, represented by lower case greek letters $\alpha_1, \ldots, \alpha_n$, capital latin letters $A_1, \ldots, A_n$ and lower case latin letters $a_1, \ldots, a_n$, respectively.

We start by first considering the explicit form of the Dirac part of the amplitude Γ_{D}. In general, it can be expanded in a suitable tensor basis as

$$\Gamma^{(\mu\nu\ldots)}_{\mathrm{D};\alpha_1\ldots\alpha_n}(\{p_i\},P) = \sum_{j=1}^{N_{\mathrm{D}}} f_{j;\xi}(\Omega;P^2)\,\tau^{(\mu\nu\ldots)}_{j;\alpha_1\ldots\alpha_n}(\{p_i\},P)\,, \tag{4.23}$$

with the basis elements τ_j inheriting the Dirac and Lorentz- structure of Γ_ξ. Each basis element comes with a Lorentz-invariant *dressing function* $f_{j;\xi}$ containing the information about the (on-shell) hadron in question. Thus, they are the quantities we ultimately want to obtain from a BSE calculation, as will become apparent in the next sections. The argument of the dressing functions Ω denote all Lorentz-invariant combinations that can be formed by combining the $n-1$ relative momenta between the (anti)quarks $\{p_i\}$ with each other and with P. The number of elements in Ω can be calculated via $N_E = \sum_{k=0}^{n-1} \binom{n+1-k}{1}$. N_{D} labels the number of Dirac basis elements needed, which is not only dependent on the spin of the state but also on the relative momenta between the quarks and therefore on the number of quarks of the hadron.

The colour structure of the amplitude is usually pretty straightforward to construct. One needs to consider the constituents of the hadron and combine the respective colour representations, i.e., fundamental ($\mathbf{N}_c$) or antifundamental ($\overline{\mathbf{N}}_\mathbf{c}$) for a quark or antiquark, respectively, in a direct product to form the desired overall colour structure. In the case of observable hadrons, we need to obtain an overall colour singlet $\mathbf{1}_c$, but for the case of diquarks or unphysical mesons in a coloured representation, the resulting object still carries a colour charge. We will delve deeper into this topic at a later stage of this work. Lastly, the flavour part of the amplitude can be directly constructed by considering the isospin of the hadron of interest and the Pauli antisymmetry of the quarks.

4.2 Two-quark BSE

With the introduction of the structure of a generic n-body FYE in the last section, we will now concretize this and consider the case $n = 2$, which is the first of two interesting cases for the work at hand. The two-body BSE allows to investigate conventional mesons, i.e., a colour singlet quark-antiquark ($q\bar{q}$) state and diquarks, which would be a coloured quark-quark (qq) object. The reasons for considering this system are twofold. First, using this 'simple' system, we will be able to explore the construction of the different parts of the BSA for given quantum numbers, consider the explicit form of the two-body interaction kernel

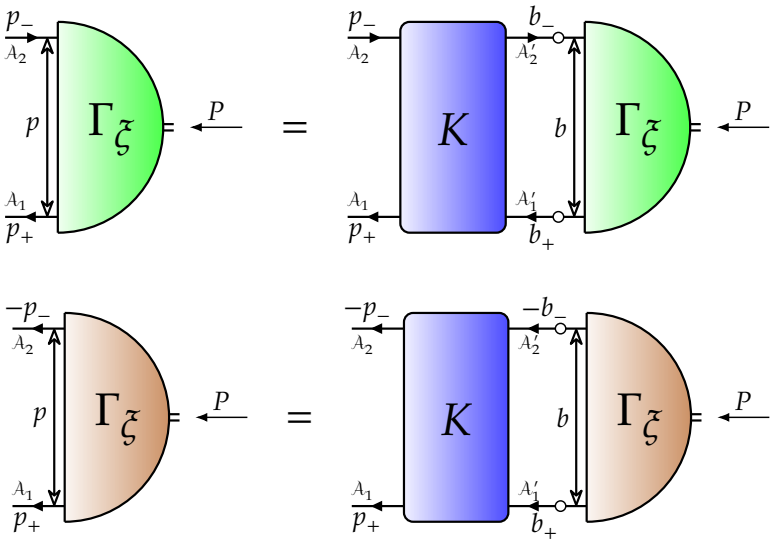

Figure 4.4: Feynman diagram representation of the $q\bar{q}$ meson BSE (*top*) and for the qq diquark BSE (*bottom*). The green and copper half-circles represent the meson and diquark BSA, respectively. The $\mathcal{A}_1^{(\prime)}$, $\mathcal{A}_2^{(\prime)}$ represent a combination of Dirac, colour and flavour indices and the p/b denote the relative momenta between the external/internal quarks which carry the individual momenta $p_\pm/b_\pm$ as defined in the text. The P denotes the total hadron momentum and K here is the two quark interaction kernel.

and how the homogeneous BSE is then solved in practice. Second, and more importantly, the masses obtained as a result of solving the two-body equation will be an important ingredient for the four-quark state calculations later on in this work.

We introduced the general n-quark homogeneous BSE in terms of Feynman diagrams on the right in Fig. 4.2. Setting $n = 2$, we get the diagrams shown in Fig. 4.4. The BSE in the top panel is the BSE for a meson and the one shown in the bottom is the BSE for a diquark, with the green and copper coloured half-circles denoting the respective BSAs. Furthermore, as discussed in Section 4.1, we will have $n - 1$ relative momenta between the n (anti)quarks, that is *one* relative momentum for the present case, which we will call p or b, depending on whether the external quarks or the quarks within the loops are considered. Also the number of Dirac, colour and flavour indices needed are now only two and the n-body BSA in Eq. (4.22) for the two-body case reads

$$\Gamma^{(\mu);A_1A_2;a_1a_2}_{\xi;\alpha_1\alpha_2}(p,P) = \Gamma^{(\mu)}_{\mathrm{D};\alpha_1\alpha_2}(p,P) \otimes \Gamma_{\mathrm{C}}^{A_1A_2} \otimes \Gamma_{\mathrm{F}}^{a_1a_2}\,. \tag{4.24}$$

We kept only one 'optional' Lorentz index μ, as the highest total spin we will consider is $J = 1$. As a BSA acts like a vertex between the quarks and the hadron, it has to fulfil the usual Feynman rules of momentum conservation at every vertex. Therefore, the individual momenta $p_\pm$ for the quark and the antiquark given in Fig. 4.4 can be defined as follows

$$p_+ = p + \eta P\,, \qquad p_- = p - (1-\eta)\,P\,, \tag{4.25}$$

and similarly for the internal relative momentum b. The $\eta \in [0,1]$ here is a *partitioning parameter*, which determines how the hadron momentum P is distributed among the two quarks. Because the results has to be independent of this parameter, we can in principle choose an arbitrary value for this parameter. From a technical standpoint, however, it will be beneficial to determine an optimal value based on the masses of the two constituents. For this, we need to determine the maximal apex M_A on the negative real momentum axis such that the parabolic momentum domain of the quark propagator shown in Fig. 3.7 excludes the poles. This maximal apex is different for each current-quark mass and is compiled in Table 4.1. Using the maximal apices, one can determine the optimal value for the partitioning parameter as

$$\eta = \frac{M_{A_1}}{M_{A_1} + M_{A_2}}\,, \tag{4.26}$$

where M_{A_1} and M_{A_2} are the maximal apices of the quark with momentum p_+ and the (anti)quark with momentum p_- respectively. For example, if the quarks have the same mass, it is reasonable to choose $\eta = 0.5$. However, if the masses are different, which is the case for heavy-light mesons and diquarks, attributing more of the hadron momentum P to the heavier of the two quarks will prove favourable.

The quark-(anti)quark interaction kernel in the two-body case depends on three momenta, the external/internal quark momenta p/b and the total hadron momentum P, i.e., $K(p,b,P)$. As the homogeneous BSE is an integral equation by nature, the meson BSE (*top* in Fig. 4.4) explicitly reads

$$\Gamma^{(\mu)}_{\xi;\,\mathcal{A}_1\mathcal{A}_2}(p,P) = \int_b \left(K^{(2)}\right)^{\mathcal{A}_1'\mathcal{A}_2'}_{\mathcal{A}_1\mathcal{A}_2}(p,b,P)\left\{S_1(b_+)\Gamma^{(\mu)}_{\xi}(b,P)S_2(b_-)\right\}_{\mathcal{A}_1'\mathcal{A}_2'}, \tag{4.27}$$

where the combination of dressed quark propagators and the BSA given in the curly brackets in the integral is formed by contracting the Dirac, colour and flavour indices of the respective objects starting from the quark line in the bottom and going against the spin line. We labelled the two quark propagators with a subscript to indicate that they do not necessarily need to be the same. The explicit form of the diquark BSE (*bottom* in Fig. 4.4) is obtained by charge conjugating the antiquark propagator S_2 to make it a quark propagator:

$$\Gamma^{(\mu)}_{\xi;\,\mathcal{A}_1\mathcal{A}_2}(p,P) = \int_b \left(K^{(2)}\right)^{\mathcal{A}_1'\mathcal{A}_2'}_{\mathcal{A}_1\mathcal{A}_2}(p,b,P)\left\{S_1(b_+)\Gamma^{(\mu)}_{\xi}(b,P)S_2^T(-b_-)\right\}_{\mathcal{A}_1'\mathcal{A}_2'}. \tag{4.28}$$

As shown in Eq. (3.29), charge conjugation corresponds to transposing the quark propagator and flipping the momentum argument of it, which then allows for it to be traced against its spin line. Because the sign of the quark with the momentum p_-/b_- is flipped by the charge conjugation, the momentum conservation at the BSA still holds with the definitions in Eq. (4.25).

Before we come to the construction of the BSA itself, we need to discuss the form of the

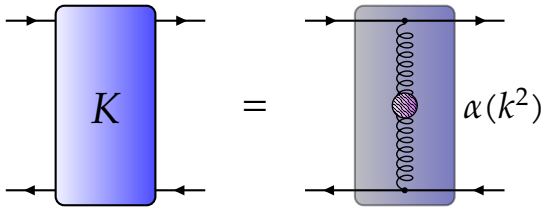

Figure 4.5: Graphical depiction of the two-body kernel given in Eq. (4.30). As explained in the main text, one uses the same effective gluon exchange of the MT model as in the quark DSE here, cf. Eq. (3.35).

BSE kernel $K^{(2)}$, which has so far been kept quite general. In Section 3.2 we discussed the explicit form of the self-energy diagram in the quark DSE and the need for truncation. This self-energy kernel Σ of the quark DSE can be related to the scattering kernel K in the two-body BSE via the axial-vector Ward-Takahashi identity (axWTI) [64]

$$\left(\gamma_5\Sigma_{f_2}(p_-) + \Sigma_{f_1}(p_+)\gamma_5\right)_{\alpha_1\alpha_2} = -\int_b \left(K^{(2)}\right)^{\alpha_1'\alpha_2'}_{\alpha_1\alpha_2} \left(\gamma_5 S_{f_2}(b_-) + S_{f_1}(b_+)\gamma_5\right)_{\alpha_1'\alpha_2'}, \quad (4.29)$$

which ensures the correct implementation of chiral symmetry and the dynamical breaking of it. This relation also forces our two-body scattering kernel to have the same form as the self-energy kernel in Eq. (3.25), consisting of a bare vertex, a full gluon propagator and a full quark-gluon vertex. We are now faced with the same problem we had in the quark DSE: We need the fully dressed quantities as an input. However, not only the form of the self-energy kernel, but also the truncation scheme and the applied model translates to the two-body kernel K via Eq. (4.29). We therefore apply the Rainbow-Ladder truncation also to the BSE in Eq. (4.27). In doing so, the kernel becomes a sum of ever more gluon exchanges, a structure which graphically looks like a ladder, hence the second part of the name of the truncation. Furthermore, we also apply the MT model for the gluon exchanges between the quarks, with which the two-body scattering kernel written explicitly reads

$$\left(K^{(2)}\right)^{A_1A_2;A_1'A_2'}_{\alpha_1\alpha_2;\alpha_1'\alpha_2'}(p,b,P) = -Z_2^{f_1}Z_2^{f_2}\,\frac{4\pi\alpha(k^2)}{k^2}\,T_{\rho\sigma}(k)(\gamma^\rho)_{\alpha_1\alpha_1'}(\gamma^\sigma)_{\alpha_2'\alpha_2}\,(t_a)^{A_1A_1'}(t^a)^{A_2'A_2}, \quad (4.30)$$

with $k = b - p$ the gluon momentum. As the quarks in the BSE do not necessarily need to be the same, we get two quark field renormalization constants Z_2, one for each flavour. Because this flavour dependence is fairly weak, the value does not change much for the different flavours and the two explicit Z_2^f's are usually combined to a Z_2^2.

Putting this kernel into the meson BSE Eq. (4.27) we get

$$\begin{aligned}\Gamma^{(\mu);A_1A_2,a_1a_2}_{\xi;\alpha_1\alpha_2}(p,P) = &-Z_2^{f_1}Z_2^{f_2}\cdot\left\{t_a\Gamma_{\mathrm{C}}t^a\right\}^{A_1A_2}\cdot\Gamma_{\mathrm{F}}^{a_1a_2}\\ &\cdot\int_b \frac{4\pi\alpha(k^2)}{k^2}\,T_{\rho\sigma}(k)\left\{\gamma^\rho S_1(b_+)\Gamma_{\mathrm{D}}^{(\mu)}(b,P)S_2(b_-)\gamma^\sigma\right\}_{\alpha_1\alpha_2},\end{aligned} \quad (4.31)$$

where we have split up the BSA in the integral to show the different contractions happening, which are again indicated by the curly brackets. Since the colour and flavour parts of the amplitude do not have momentum arguments, we have pulled them out of the integral. Furthermore, as the employed MT interaction is flavour blind, the flavour part of the BSE is not contracted with anything and therefore not changed. One arrives at a similar equation for the diquarks when inserting the MT interaction into Eq. (4.28). The two-body BSE in Eq. (4.31) is then the final form of the $q\bar{q}$ meson BSE which we will solve in the following.

4.2.1 Construction of the BSA

Having obtained the general form of the equation we want to solve, we now need to consider the form of the BSA for the quantum numbers $I(J^{P(C)})$ we want to investigate. Of particular interest for the present work are (pseudo)scalar and (axial)vector mesons and diquarks, i.e., hadrons with total spin $J = 0, 1$.

In the following, we will first cover the Dirac part of the BSA, where we will distinguish between the cases of $J = 0$ and $J = 1$. After that, we will move on and discuss the colour and flavour parts for the mesons and diquarks.

Dirac basis for $J = 0$

For the case of hadrons with $J = 0$, i.e., (pseudo)scalar mesons and diquarks, the BSA and therefore Γ_D is a Lorentz scalar. As established in Eq. (4.23), we can write the Dirac part of the BSA as sum of Dirac tensors and their dressing functions, which for the this case reads

$$\Gamma_{\mathrm{D};\alpha_1\alpha_2}(p,P) = \sum_{j=1}^{N_\mathrm{D}} f_j(p^2, z; P^2)\, \tau_{j;\alpha_1\alpha_2}(p,P)\,, \tag{4.32}$$

with the angular variable $z := \hat{p}\cdot\hat{P}$ and the hatted quantities denoting normalized momenta in this context. We have written out the Lorentz-invariant quantities of the dressing functions explicitly here. The number of Dirac basis elements needed for $J = 0$ is $N_\mathrm{D} = 4$, with the most popular choice in the BSE framework being [177]:

$$\begin{aligned} \tau_1(p,P) &= \mathbb{I}_\mathrm{D}\,, & \tau_3(p,P) &= -i\not{p}\,, \\ \tau_2(p,P) &= -i\not{P}\,, & \tau_4(p,P) &= [\not{P},\not{p}]\,. \end{aligned} \tag{4.33}$$

To make the accompanying dressing functions in Eq. (4.32) real and positive in all components, one can introduce the factors of i and negative signs as done in Eq. (4.33) and also some scalar factors which are mentioned a little further down. Not doing so will not alter the BSA, as the scalar prefactors can get absorbed into the dressing functions. Using a partial-wave decomposition as described in detail in [69] for the meson case, one can identify the first two basis elements τ_1 and τ_2 as the s-wave basis elements, because they involve only the unit matrix in Dirac space and the total momentum of the hadron P and therefore no angular momentum. The other two have an angular momentum of unit one

as they include the relative momentum between the quark p and are therefore p-waves. Both of these components are needed to describe a meson as a relativistic bound state.

The choice of Dirac basis elements in Eq. (4.33) now specifies a generic state with $J = 0$, but it does not distinguish between a scalar or pseudoscalar state. To do that, we note that these two states transform differently under parity and thus acting with the parity transformation operator $\mathcal{P}$ on a scalar or pseudoscalar BSA Γ yields a different eigenvalue $P = \pm 1$. The parity transformation of a BSA is given in Eq. (C.3), which for the present case of $J = 0$ reads

$$\mathcal{P}\big(\Gamma(p,P)\big) = \gamma^4\,\Gamma(\Pi p, \Pi P)\,\gamma^4\,, \tag{4.34}$$

where $\Pi = \mathrm{diag}(-1,-1,-1,1)$. For mesons, we need to multiply the elements by $\mathbb{I}_\mathrm{D}$ for scalar mesons, which have positive parity ($P = +$), and by γ_5 for pseudoscalar mesons, which have negative parity ($P = -$).

To get the Dirac basis elements for the diquarks with spin $J = 0$, we need to multiply the basis elements given in Eq. (4.33) with a charge conjugation matrix C from the right

$$\begin{aligned} \tau_1(p,P) &= \mathbb{I}_\mathrm{D}\,C\,, & \tau_3(p,P) &= -i\not{p}\,C\,,\\ \tau_2(p,P) &= -i\not{P}\,C\,, & \tau_4(p,P) &= [\not{P},\not{p}]\,C\,. \end{aligned} \tag{4.35}$$

In doing so, we also change the transformation properties under the parity transformation Eq. (4.34) with $\mathbb{I}_\mathrm{D}$ corresponds to pseudoscalar ($P = -$) diquarks and multiplying the basis elements by γ_5 yields scalar ($P = +$) diquarks[2].

We already discussed the addition of factors to render the dressing functions real and positive below Eq. (4.33). In this context, it is also customary to pull out a scalar factor of $(p\cdot P)$ from certain dressing functions and include it in the Dirac basis elements. Depending on whether the basis elements have been multiplied by γ_5 or by $\mathbb{I}_\mathrm{D}$ this factor is included in either τ_3 or τ_2, respectively.

Dirac basis for $J = 1$

For the (axial)vector mesons and diquarks, the BSA is a Lorentz vector and thus carries a Lorentz index. As the Dirac part of the BSA inherits the Lorentz structure, we can write it explicitly as

$$\Gamma^\mu_{\mathrm{D};\alpha_1\alpha_2}(p,P) = \sum_{j=1}^{N_\mathrm{D}} f_j(p^2,z;P^2)\;\tau^\mu_{j;\alpha_1\alpha_2}(p,P)\,, \tag{4.36}$$

again with $z := \hat{p}\cdot\hat{P}$. The basis elements needed in the case of $J = 1$ are in principle the same as given in Eq. (4.33), but they need to be contracted with the vectors from the set $\{\gamma^\mu_\perp, p^\mu_\perp\}$ to from a Lorentz vector. This then yields $N_\mathrm{D} = 8$ Dirac basis elements for which

[2] The charge conjugation matrix can be pulled out, so we can write ΓC for the diquark BSA. The parity transformation in Eq. (4.34) then yields $\mathcal{P}(\Gamma C) = \gamma^4\,(\Gamma\gamma^4\gamma^2)\,\gamma^4 = -\gamma^4\,\Gamma\,\gamma^4\,C = -\mathcal{P}(\Gamma)C$

a popular choice in the BSA framework is [177]:

$$\begin{aligned}
\tau_1^\mu(p,P) &= i\gamma_\perp^\mu\,, & \tau_5^\mu(p,P) &= p_\perp^\mu\,\mathbb{I}_\mathrm{D}\\
\tau_2^\mu(p,P) &= \gamma_\perp^\mu\,\not{P}\,, & \tau_6^\mu(p,P) &= ip_\perp^\mu\,\not{P}\\
\tau_3^\mu(p,P) &= -\gamma_\perp^\mu\,\not{p} + p_\perp^\mu\,\mathbb{I}_\mathrm{D}\,, & \tau_7^\mu(p,P) &= -ip_\perp^\mu\,\not{p}\\
\tau_4^\mu(p,P) &= i\gamma_\perp^\mu\,[\not{P},\not{p}] + 2ip_T^\mu\,\not{P}\,, & \tau_8^\mu(p,P) &= p_\perp^\mu\,[\not{P},\not{p}]
\end{aligned} \tag{4.37}$$

where the subscript $\perp$ indicates transversality with respect to the total hadron momentum P. Factors of i and negative signs are chosen in this way to again render most of the dressing functions real and positive. Additionally, one can again pull out scalar factors $(p\cdot P)$ to render all dressing functions real and positive. However, the basis element to which this factor is then added will here not only depend on the parity but also on the charge conjugation parity quantum number.

As was the case for the $J=0$ states, we can distinguish between the vector and axialvector states by looking how the corresponding BSA transforms under parity transformation. In the (axial)vector case, the generic parity transformation in Eq. (C.3) reads

$$\mathcal{P}\Big(\Gamma^\mu(p,P)\Big) = -\Pi^{\mu\sigma}\,\gamma^4\Gamma_\sigma(\Pi p,\Pi P)\,\gamma^4\,. \tag{4.38}$$

Multiplying the basis elements in Eq. (4.37) by $\mathbb{I}_\mathrm{D}$ gives $P=-1$, so a vector meson, and a multiplication by γ_5 yields a parity eigenvalue $P=+1$, which is an axialvector meson.

For the diquarks, the procedure is analogous to the $J=0$ case. To get the basis elements, we multiply the Dirac basis elements by the charge conjugation matrix from the right, i.e., $\tau_j^\mu \to \tau_j^\mu\,C$, which again negates the parity transformations for the different basis elements. Therefore, the $\gamma_5\tau_j^\mu\,C$ basis elements correspond to a vector $(P=-)$ diquark and the $\tau_j^\mu\,C$ Dirac elements to an axialvector $(P=+1)$ diquark.

In the discussion below Eq. (4.37), we mentioned that the additional scalar $(p\cdot P)$ factors can get assigned to different basis elements depending on the parity of the state. For the different quantum numbers 1^{PC} a collection which basis element gets this factor can be found in Table 2 of [177]. One interesting thing to note from this table is, that the scalar factor for the two axialvector states $1^{+\pm}$ is assigned completely opposite for the different C-parity states. This is expected, as the two BSAs should transform with opposite sign under a C-parity transformation given in Eq. (C.1).

As a final note on the Dirac part of the BSA, one can of course only consider a subset of the basis elements above and truncate the sums in Eq. (4.32) and Eq. (4.36) accordingly. A nice graphical overview showing the effect this has on the masses of the π and ρ meson can be found in Figure 3.8 in [164]. For the computed two-body hadron masses in this thesis, we always work with the full set of basis elements.

4.2.2 Colour part of the BSA

The following section on the colour part of the BSA will be discussed in terms of a general $\mathrm{SU}(N_c)$ group and its representations. We have already established in Section 2.1

that quarks are spinor fields carrying a colour charge, which live in the fundamental n-dimensional multiplet representation of the colour group $\mathrm{SU}(N_c)$, which is commonly denoted as $\mathbf{N_c}$. Consequently, the antiquarks carry an anticolour and live in the associated n-dimensional anti-multiplet representation $\overline{\mathbf{N}}_\mathbf{c}$. For the case of mesons, we combine the quark and antiquark, or rather their respective representations together via a tensor product

$$\mathbf{N_c} \otimes \overline{\mathbf{N}}_\mathbf{c} = \left(\mathbf{N_c^2 - 1}\right) \oplus \mathbf{1}_c \,, \tag{4.39}$$

and obtain the direct sum of a colour singlet $\mathbf{1}_c$ and a part which has the dimension of the adjoint representation. The observable mesons are colour singlets, so for the colour amplitude we only keep this part, which is represented by a Kronecker delta

$$\Gamma_\mathrm{C}^{\mathrm{ms};A_1A_2} = \delta^{A_1A_2} \,, \tag{4.40}$$

with the colour indices A_1, $A_2 = 1, 2, \ldots, N_c$. In terms of colour forces, the colour singlet corresponds to an attractive force between the quark and the antiquark, binding them together. The $\left(\mathbf{N_c^2 - 1}\right)$ part would correspond to a repulsive force and the resulting mesons will not be bound.[3]

To form a diquark, we need to combine the representations of two quarks via a tensor product

$$\mathbf{N_c} \otimes \mathbf{N_c} = \frac{\mathbf{N_c(N_c + 1)}}{\mathbf{2}} \oplus \overline{\frac{\mathbf{N_c(N_c - 1)}}{\mathbf{2}}} \,. \tag{4.41}$$

to get a direct sum of a $N_c(N_c + 1)/2$-dimensional multiplet representation and a $N_c(N_c - 1)/2$-dimensional anti-multiplet representation. In the case of $N_c = 3$, this would be $\mathbf{6_c}$ and $\bar{\mathbf{3}}_\mathbf{c}$ respectively. As none of the representations in the direct sum is a colour singlet, this further underlines the fact that diquarks carry a colour charge and are therefore non-observable objects. They are nevertheless interesting, as they can be used as building blocks to form multiquark states, see, e.g., [17] for an extensive review. The attractive colour force in this case, which binds the quarks together, is the one in the $\overline{\mathbf{N_c(N_c-1)/2}}$ representation, with the other denoting the repulsive colour force. Similar to the meson case, we will only consider the attractive colour force here. Mathematically, combining the two colour indices from the quarks and getting one out for the diquarks is achieved by a Levi-Civita symbol

$$\Gamma_\mathrm{C}^{\mathrm{dq};A_1A_2} = \varepsilon^{A_1A_2B} \,, \tag{4.42}$$

again with the colour indices A_1, A_2, $B = 1, 2, \ldots, N_c$, where B is the colour index for the diquark.

[3] The eigenvalue curve in this case will be negative, i.e., the condition $\lambda = 1$ cannot be met.

4.2.3 Flavour part of the BSA

The flavour part of the Bethe-Salpeter amplitude is constructed by considering the isospin of the state as well as the flavour charges strangeness, charm and bottomness. The only two quarks carrying isospin, are the up and down quarks with $I = 1/2$, because they can be considered to obey the almost exact $\mathrm{SU}_V(2)$ symmetry. Like is the case for the spin, one can choose to consider the isospin projection along a particular axis, in most cases one considers the third component I_3 (z-axis). The up quark gets assigned a value of $I_3 = +1/2$ and the down quark correspondingly gets $I_3 = -1/2$. For the respective antiquarks the sign of the I_3 is flipped, i.e., $I_3^{\bar{u}} = -1/2$ and $I_3^{\bar{d}} = +1/2$. All the other quark flavours have isospin $I = 0$ by default, but carry a respective flavour charge.

First, we consider the case of the flavour BSA for mesons. A meson made up of two light quarks, i.e., up and down quark, can have either isospin $I = 0$ (isospin singlet) or $I = 1$ (isospin triplet). The corresponding flavour BSAs look like the following:

$$I = 0: \quad \Gamma_{\mathrm{F}} = \frac{1}{\sqrt{2}}\left(u\bar{u} + d\bar{d}\right), \qquad I = 1: \quad \Gamma_{\mathrm{F}} = \begin{cases} u\bar{d} & , I_3 = +1 \\ \frac{1}{\sqrt{2}}\left(u\bar{u} - d\bar{d}\right) & , I_3 = 0 \\ d\bar{u} & , I_3 = -1 \end{cases}, \tag{4.43}$$

When we only consider states with up and down quarks, we can represent the quarks using vectors transforming under $\mathrm{SU}(2)$, i.e., $u = (1,0)^T$ and $d = (0,1)^T$ and the corresponding transposed vectors for the antiquarks. Using this vector notation for the quarks, one can represent the isospin-triplet flavour wave functions using the Pauli matrices σ_i:

$$\Gamma_{\mathrm{F}}^{+} = \frac{1}{2}(\sigma_1 + i\sigma_2), \qquad \Gamma_{\mathrm{F}}^{-} = \frac{1}{2}(\sigma_1 - i\sigma_2), \qquad \Gamma_{\mathrm{F}}^{0} = \frac{1}{\sqrt{2}}\sigma_3, \tag{4.44}$$

which would correspond for example to the triplet states $\pi^{\pm}$, π^0 or $\rho^{\pm}$, ρ^0.

In the case of states including more flavours, one can consider a general $\mathrm{SU}(N_f)$, where N_f is the number of flavours needed and then represent the quarks as unit vectors with N_f entries. For example, for heavy-light mesons like D-mesons, we can choose $N_f = 4$ and consequently represent the quarks as $u = (1,0,0,0)^T$, $d = (0,1,0,0)^T$, $s = (0,0,1,0)^T$ and $c = (0,0,0,1)^T$ where the vectors representing the antiquarks are again transposed. To then form the flavour BSA for the D-mesons in a matrix representation we combine the quarks and antiquarks accordingly:

$$D^+ = c\bar{d} = \begin{pmatrix} 0 & 0 & 0 & 0 \\ 0 & 0 & 0 & 1 \\ 0 & 0 & 0 & 0 \\ 0 & 0 & 0 & 0 \end{pmatrix}, \quad D^0 = c\bar{u} = \begin{pmatrix} 0 & 0 & 0 & 1 \\ 0 & 0 & 0 & 0 \\ 0 & 0 & 0 & 0 \\ 0 & 0 & 0 & 0 \end{pmatrix}, \tag{4.45}$$

$$D^- = d\bar{c} = \begin{pmatrix} 0 & 0 & 0 & 0 \\ 0 & 0 & 0 & 0 \\ 0 & 0 & 0 & 0 \\ 0 & 1 & 0 & 0 \end{pmatrix}, \quad \bar{D}^0 = u\bar{c} = \begin{pmatrix} 0 & 0 & 0 & 0 \\ 0 & 0 & 0 & 0 \\ 0 & 0 & 0 & 0 \\ 1 & 0 & 0 & 0 \end{pmatrix}. \tag{4.46}$$

This procedure works for any flavour combination.

When considering the flavour BSA for the case of diquarks, we need to keep in mind, that states with equal quark content underlie Pauli antisymmetry. Therefore, the flavour wavefunction for diquarks depends on the isospin, but additionally also on the spin of the state. Let us first look at the case for diquarks with up and down quarks again. For diquarks with $J = 0$, we have, that the spins need to be antiparallel in order to form an antisymmetric flavour wavefunction. For the case $J = 1$, the spins can be aligned parallel and the flavour wavefunction is symmetric in this case. The flavour BSAs here read

$$I = 0: \quad \Gamma_{\mathrm{F}} = \frac{1}{\sqrt{2}}[ud], \qquad I = 1: \quad \Gamma_{\mathrm{F}} = \begin{cases} uu \\ \frac{1}{\sqrt{2}}\{ud\} \\ dd \end{cases}, \tag{4.47}$$

with $[ud] = ud - du$ and $\{ud\} = ud + du$ denoting antisymmetrization and symmetrization respectively. Analogously to the meson case, using the vector representation for the quarks, one can again represent the flavour BSA in form of a matrix.
In the case of heavy-light diquarks Qq, with q and Q representing the light and heavy quark respectively, the isospin is fixed to $I = 0$ and the flavour BSA can be chosen symmetric or antisymmetric, i.e.,

$$\Gamma_{\mathrm{F}}^{\mathrm{sym.}} = \{Qq\}, \qquad \Gamma_{\mathrm{F}}^{\mathrm{asym.}} = [Qq], \tag{4.48}$$

such that the overall wavefunction is antisymmetric.

4.3 Solution of the two-body BSE

Since we have now constructed and discussed the different parts of the BSA for the quantum numbers of interest for this work, we need to insert it into the two-body BSE in Eq. (4.31) and solve the eigenvalue equation. The solution we want to obtain in the end is the mass of the hadron, i.e., where the eigenvalue satisfies $\lambda(P^2) = 1$, and the dressing functions at that point, as they contain the information about the hadron on its mass shell. However, upon inserting our BSA in Eq. (4.31) we note, that the Dirac, colour and flavour contractions are not yet closed and cannot be traced. That is, because in order to solve for an individual dressing function, we first need to project it out from the BSA on the left-hand side of Eq. (4.31). To do this, one constructs a suitable projector containing a Dirac, colour and flavour part, which then in turn closes the contractions on the right-hand side of the BSE.

As the full Bethe-Salpeter amplitude consists of a Dirac, a colour and a flavour part, also

the full projector $\mathbb{P}$ needs components living in all three of these spaces. Additionally, we need as many projectors as we have elements in the respective parts of the BSA, i.e., N_{D} for the Dirac, usually one for the colour and three for the all light flavour case (usually only one for the heavy-light case). We will denote the individual projectors in the different spaces by $\mathbb{P}^{\mathrm{D}}_i$, $\mathbb{P}^{\mathrm{C}}_i$ and $\mathbb{P}^{\mathrm{F}}_i$. In principle, the choice of the projectors in the different spaces is arbitrary as long as they fulfil the requirement

$$\mathrm{tr}\Big\{\mathbb{P}^{\mathrm{X}}_i\,\mathbb{B}^{\mathrm{X}}_j\Big\} = \delta^{\mathrm{X}}_{ij}\,, \tag{4.49}$$

with $\mathrm{X} \in \{\mathrm{D},\mathrm{C},\mathrm{F}\}$ and $\mathbb{B}^{\mathrm{X}}_j$ denoting basis elements in a respective space X. Starting with the Dirac space, since the basis elements in Eq. (4.33) and Eq. (4.37) each form a closed set and are therefore orthogonal, we can transpose and normalize them via Eq. (4.49) and use them as projectors for the Dirac part, i.e., $\mathbb{P}^{\mathrm{D};i}_{(\mu)} = \left(\tau^i_{(\mu)}\right)^T$. The same holds true for the colour and flavour parts. By virtue of Eq. (4.49) the colour BSA gets a normalization factor:

$$\Gamma^{\mathrm{ms};A_1A_2}_{\mathrm{C}} = \frac{\delta^{A_1A_2}}{\sqrt{N_c}}\,, \qquad \Gamma^{\mathrm{dq};A_1A_2}_{\mathrm{C}} = \frac{\varepsilon^{A_1A_2B}}{\sqrt{2}}\,, \tag{4.50}$$

for the meson (ms) and diquark (dq) colour BSA, respectively, and the colour projector is identified as $\mathbb{P}^{\mathrm{C}} = \Gamma^T_{\mathrm{C}}$. For the flavour BSA, the all light flavour BSAs ($N_f = 2$) in Eq. (4.44) for example get a normalization constant and read

$$\Gamma^{+}_{\mathrm{F}} = \frac{1}{2}(\sigma_1 + i\sigma_2)\,, \qquad \Gamma^{-}_{\mathrm{F}} = \frac{1}{2}(\sigma_1 - i\sigma_2)\,, \qquad \Gamma^{0}_{\mathrm{F}} = \frac{1}{\sqrt{2}}\sigma_3\,, \tag{4.51}$$

with the projector chosen as $\mathbb{P}^{\mathrm{F}} = \Gamma^T_{\mathrm{F}}$.

Once we have obtained a suitable full projector $\mathbb{P}$, we can let it act on the meson BSE in Eq. (4.31) to project out an individual dressing function f_j as

$$\begin{aligned} f_j(p^2,z;P^2) = &- Z_2^{f_1}Z_2^{f_2}\cdot\mathrm{tr}\Big\{\Gamma^T_{\mathrm{C}}t_a\Gamma_{\mathrm{C}}t^a\Big\}\cdot\mathrm{tr}\Big\{\Gamma^T_{\mathrm{F}}\Gamma_{\mathrm{F}}\Big\} \\ &\cdot\int_b \frac{4\pi\,\alpha(k^2)}{k^2}\,T_{\rho\sigma}(k)\,\mathrm{tr}\Big\{\mathbb{P}^{\mathrm{D};j}_{(\mu)}\gamma^\rho S_1(b_+)\Gamma^{(\mu)}_{\mathrm{D}}(b,P)S_2(b_-)\gamma^\sigma\Big\}\,, \end{aligned} \tag{4.52}$$

As discussed around Eq. (4.31), the flavour part of the BSA does not get changed by the MT interaction and the trace of the flavour elements just evaluates to one. The trace of the colour part evaluates to C_F in the meson BSE and to $-C_F/2$ in the diquark BSE[4].

Doing this projection for every dressing function, one can write the resulting system of equations as

$$\lambda\big(P^2\big)F(p^2,z;P^2) = \int_b \mathcal{K}(p,b,P)\cdot F(b^2,z';P^2)\,, \tag{4.53}$$

[4] $\mathrm{tr}\Big\{\big(\Gamma^{\mathrm{dq}}_{\mathrm{C}}\big)^T t_a\Gamma^{\mathrm{dq}}_{\mathrm{C}}\,(t^a)^T\Big\} = -\frac{1}{2}\mathrm{tr}\Big\{t_at^a\Big\} = -\frac{1}{2}\cdot C_F$.

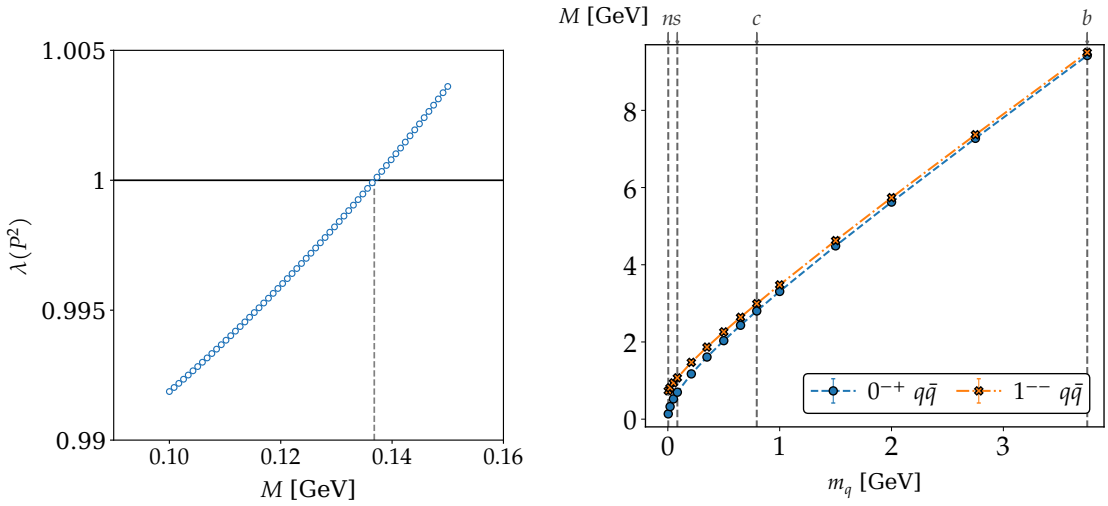

Figure 4.6: *Left*: Eigenvalue curve for the π meson. We show the obtained eigenvalues for different values of the hadron mass M. $M > 0$ corresponds to $P^2 \in \mathbb{R}^-$. As a reference we plotted the $\lambda = 1$ as a horizontal line. The grey dashed line indicates the position of the bound state. *Right*: Quark mass evolution curve (QMEC) of a pseudoscalar (*blue*) and vector (*orange*) $q\bar{q}$ mesons. The hadron masses for the different current-quark masses were obtained from their respective EVCs. The dashed and dash-dotted lines are fits to the data with a fit function given in the text. The grey dashed vertical lines indicate the current-quark masses of the u/d, s, c and b quarks.

with $z' := \hat{b} \cdot \hat{P}$, $F = (f_1, f_2, \ldots, f_{N_D})^T$ the vector collecting the dressing functions and $\mathcal{K}$ a matrix combining the Dirac part of the MT interaction together with the quark propagators, The elements of $\mathcal{K}$ in the case of the meson BSE are given as

$$\mathcal{K}_{ji} = \frac{4\pi\,\alpha(k^2)}{k^2}\, T_{\rho\sigma}(k)\, \mathrm{tr}\Big\{ \mathbb{P}^{\mathrm{D};j}_{(\mu)}\, \gamma^\rho S_1(b_+)\, \tau_i^{(\mu)}(b,P) S_2(b_-) \gamma^\sigma \Big\}\,. \tag{4.54}$$

In the case of the diquark BSE, $\mathcal{K}$ gets an overall negative sign. Comparing now the BSE for the meson and for the diquark, we note that they differ only by a factor of $\frac{1}{2}$ coming from the colour trace in the case of the diquark.

4.3.1 Mass spectrum

The equation in Eq. (4.53) together with the matrix kernel $\mathcal{K}$ in Eq. (4.54) is now the eigenvalue equation we put onto the computer to obtain the masses of the mesons and diquarks. To obtain the location of the mass of the hadrons, we apply the procedure outlined below Eq. (4.14) and scan a range of P^2 until we find the position where $\lambda(P^2 = -M^2) = 1$. As an example of how the obtained eigenvalue curve looks like, we show the EVC for the $q\bar{q}$ meson BSE with a current-quark mass of $m_q = 3.7$ MeV, i.e., the π meson, in the *left* panel of Fig. 4.6. As can be clearly seen, we get a crossing of $\lambda = 1$ around $M = 137$ MeV and have therefore obtained a bound state in the correct mass region of the pion.

It is also interesting to investigate how the mass of hadrons behaves upon variation of

q	n	n_h	s_l	s	s_h	s_{eh}	c_{el}
m_q	3.7	20	50	85	210	350	500
M_A^2	230	300	380	420	850	1320	1900
q	c_l	c	c_h	c_{eh}	b_{el}	b_l	b
m_q	650	795	1000	1500	2000	2750	3750
M_A^2	2450	3100	3800	6200	9200	15000	25000

Table 4.1: Current quark masses m_q (in MeV) and their maximal apices M_A^2 (in MeV^2) for the parabolic squared quark momentum domain (see discussion in Section 3.2.4 and around Eq. (4.26)) for the quark propagators used in the meson and diquark BSE. The subscripts l and h indicate a 'lighter' and 'heavier' version of that quark flavour with the additional e meaning 'extra'. The reason for the additional quark masses is explained in the main text.

the mass of the quarks. In this work, we want to consider mesons and diquarks containing light, strange, charm all the way up to bottom quarks. We therefore fix the values for the current-quark masses for the light, strange, charm and bottom quarks and then choose two or four quark masses in between the respective values to better investigate the behaviour. The quark masses chosen throughout this work are given in Table 4.1. As a short interlude, we have to quickly mention how we fix the current-quark masses for the different quark flavours. The pion is sort of the general benchmark particle of the DSE/BSE framework. One first chooses the two model parameters of the MT interaction in Eq. (3.35) to reproduce the value for the pion leptonic decay constant $\mathbf{f}_\pi = 92$ MeV, which is mostly quark mass independent. After that, one fixes the input quark mass for the light up/down quark specifically fixed to reproduce the pion mass, i.e., we choose a value of $m_n = 3.7$ MeV. There have been investigations in the past if and how the MT parameters need to be modified for heavier quarks [178], but we choose to fix the parameters as discussed below Eq. (3.35) for all current-quark masses. The input quark masses for the charm quark is fixed such that the sum of the pesudoscalar and vector $c\bar{n}$ meson, i.e., D and D^*, matches the sum of the experimental values [20]. The current quark mass of the strange is fixed to reproduce the K meson masses and such that the sum of the strange partners of D and D^*, that is D_s and D_s^*, matches the sum of the experimentally measured values. The same is applied to the current-quark mass of the bottom quark with the addition, that also the $b\bar{b}$ mesons should match the experimental values [20].

With this out of the way, we can now investigate the behaviour of the meson and diquark masses when varying the current-quark mass. To do so, we calculate the masses for a $q\bar{q}$ meson or qq diquark for all the input quark masses in Table 4.1. The masses for the hadrons are again obtained from the respective eigenvalue curves. The resulting masses can be plotted against the current-quark masses to obtain what we call a quark mass evolution curve (QMEC). We show the QMEC for the pseudoscalar and as a comparison also for the vector $q\bar{q}$ mesons with equal quarks in the right panel of Fig. 4.6. One can clearly see, that the curve is almost linear for quark masses above m_c and starts to bend downwards when going to $m_q \to m_n$. While the mass for the pseudoscalar mesons approaches $M_{\text{ps}} \to 0$ for

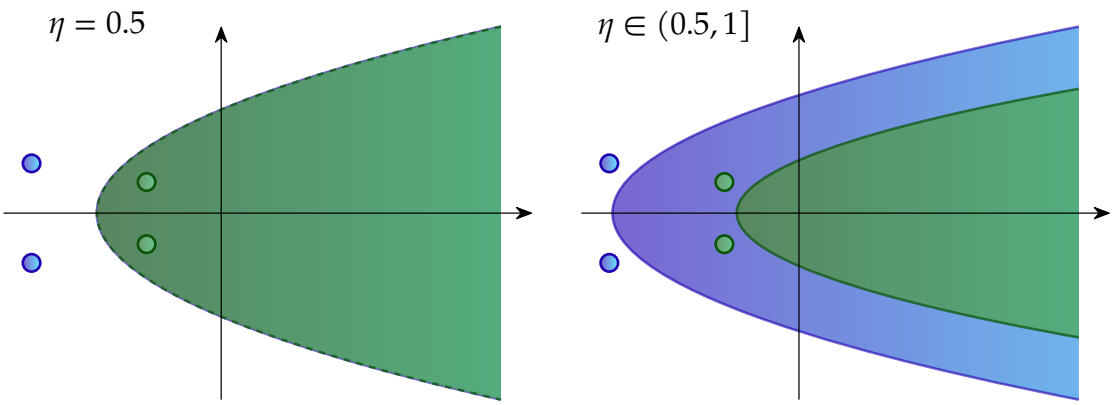

Figure 4.7: Visualization of the parabolic momentum region the quark propagator needs to be sampled for in the BSE for a heavy-light hadron, the green curve and poles correspond to the lighter and the blue region and poles to the heavier quark. *Left*: Choosing the momentum partitioning parameter $\eta = 0.5$ is not ideal, as the poles of the lighter quark lie within its integration domain. *Right*: Sending more momentum through the heavier quark, i.e., choosing an asymmetric momentum routing, remedies this situation.

$m_q \to 0$, the mass for the vector mesons goes to some value $M_{\text{vc}} \neq 0$. This of course is a direct observation of chiral symmetry breaking discussed in Section 2.2, with the pions as the associated Nambu-Goldstone bosons becoming massless in the chiral limit. As introduced in Section 2.2, in this context the Gell-Mann-Oakes-Renner relation (GMOR) [124]

$$\mathbf{f}_{\text{ps}}^2 M_{\text{ps}}^2 = -2m_q \frac{\langle \bar{q}q \rangle}{N_f}, \tag{4.55}$$

is of importance. It not only relates the pseudoscalar meson mass to the current-quark mass, but also the leptonic decay constant $\mathbf{f}_{\text{ps}}$ to the quark condensate. From this relation, we can determine the value for the quark condensate (typically $\langle \bar{q}q \rangle \approx -(280\,\text{MeV})^3$ for u/d quarks), which is one of the order parameters for DCSB, and furthermore establish how the meson mass should behave when varying the quark mass. The GMOR relation in Eq. (4.55) tells us that the pseudoscalar mass goes with $M_{\text{ps}} \propto \sqrt{m_q}$. Based on this, we employ a fit function to the QMEC in Fig. 4.6, shown as the dashed and dash-dotted curves, of the form

$$M(m_q) = \sqrt{\sum_{i=0}^{n} a_i m_q^i}, \tag{4.56}$$

where the number of elements in the polynomial needed for the QMEC curves shown in Fig. 4.6 is usually $n = 1$.

For this work, we will however not only need mesons and diquarks with equal quark content, but also heavy-light mesons $(Q\bar{q})$ and diquarks (Qq), with $Q \in \{c, b\}$ and $q \in \{n, s, c, b\}$, will play a crucial role later on. The masses for these hadrons are in principle

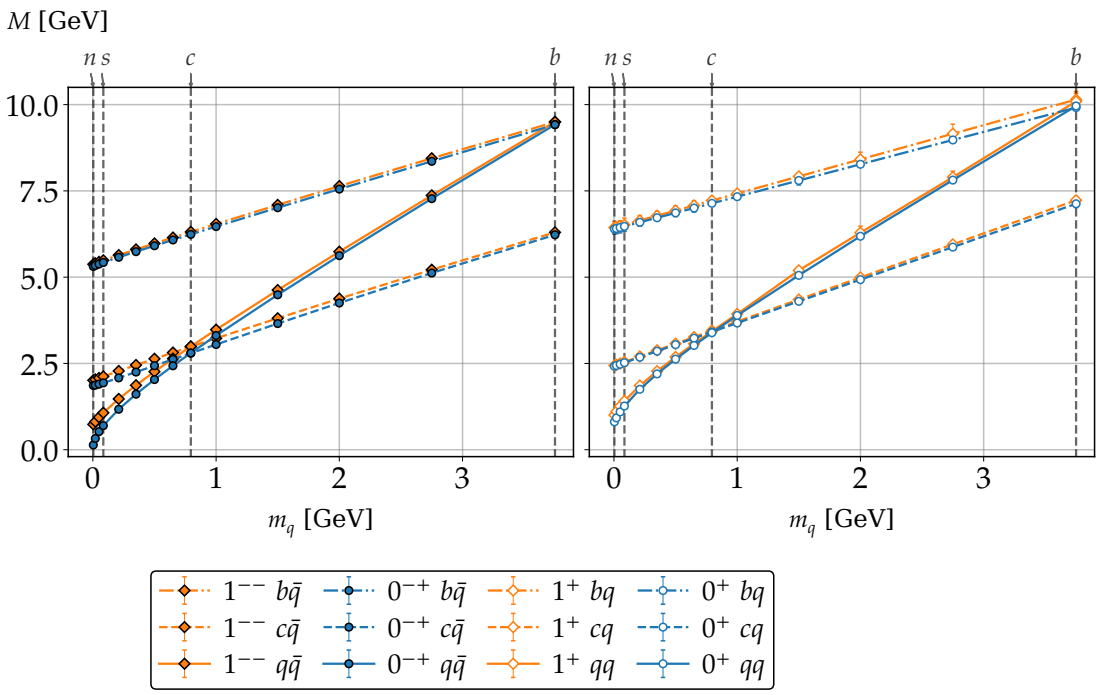

Figure 4.8: Quark mass evolution curves for pseudoscalar (0^{-+}) mesons and scalar (0^{+}) diquarks (*blue circles*) as well as vector (1^{--}) mesons and axialvector (1^{+}) diquarks (*orange diamonds*) with hidden- and open-flavour. The solid, dashed and dash-dotted lines represent the fits applied to the QMECs of the $q\bar{q}/qq$, $c\bar{q}/cq$ and $b\bar{q}/bq$ mesons/diquarks.

also obtained from their eigenvalue curves. However, due to the unequal quark masses, the quark pole can be hit in the integration in Eq. (4.53). To somewhat remedy this, one can use the partitioning parameter η we introduced in Eq. (4.25) and find an optimal value for it such that no quark poles are hit. Graphically, one can visualize this problem as shown in Fig. 4.7. As we can see in the *left* panel, the optimal choice for equal quarks, i.e., $\eta = 0.5$, fails for the heavy-light quarks, as the poles for the light quarks (shown in green) are then inside its integration domain (also shown in green). The optimal value is calculated via Eq. (4.26) and in the heavy-light case for $Q\bar{q}/Qq$ is usually $\eta \in (0.5, 1]$. This remedies the situation, as can be seen in the *right* panel of Fig. 4.7. Now the integration domains for the respective quarks exclude the respective poles and one can ideally determine the hadron mass directly from the eigenvalue curve as discussed above.

In some cases, mostly for the diquarks and if the mass difference between the quarks is too big, even the asymmetric routing cannot remove the poles from the integration domain. In these cases, to obtain an estimate result for the mass, we use a combination of extrapolations of the EVCs and extrapolation/fitting of the resulting QMECs, which will be explained in the following. As we have mentioned above, to get the QMECs, one needs to obtain the hadron masses from the respective EVCs. In the mentioned cases, where the quark poles in the integration domain obstruct the direct computation of the mass, we calculate the EVC to a certain threshold given by $M_{\text{thresh}} = {}^{M_{A_1}}/_{\eta}$ and then

use a method involving the Schlessinger point method (SPM) [179] to extrapolate the EVC to the point where $\lambda = 1$. The method is described in detail in Appendix C.5. It yields a mass value plus an estimate for the extrapolation error, the latter of which will be neglected for the two-body states as it is not relevant for the work at hand. We note, that for consistency reasons, we also apply the extrapolation method in Appendix C.5 to states where the value could be determined directly from the EVC. After having done this, we look at the behaviour of the resulting QMECs and apply the fit function in Eq. (4.56) to an appropriate degree in the polynomial to obtain the final estimate of the hadron masses which cannot be calculated directly, i.e., for heavy-light mesons $Q\bar{q}$ when $m_q \to m_n$. The obtained QMECs for the pseudoscalar and vector mesons with equal and non-equal quark pairs are shown left in Fig. 4.8, as blue circles and orange diamonds, respectively, together with the applied fits. As is evident from Fig. 4.8, the masses for the heavy-light 0^{-+} and 1^{--} mesons are very close together across the whole range of quark masses m_q. For the $Q\bar{n}$ states the mass difference $\Delta M_{Q\bar{q}} = M_{\mathrm{vc};\,Q\bar{q}} - M_{\mathrm{ps};\,Q\bar{q}}$ decreases when increasing the mass of the heavy quark m_Q. This is an expected behaviour, as according to *heavy-quark spin symmetry* (*HQSS*) [180] for $m_Q \to \infty$ these two states should be (approximately) mass degenerate, i.e., $\Delta M_{Q\bar{q}} \to 0$. For the equal quark QMECs, the masses approach each other ever closer above the charm quark mass.

We have applied the same procedure to calculate the QMECs for the scalar and axialvector diquarks which are shown right in Fig. 4.8. Again, we calculated the diquark masses directly if possible and used extrapolation otherwise. The applied fits then yield the diquark masses especially for the heavy-light diquarks Qq with $m_q \to m_n$. One can see, that the QMECs for the heavy-light diquarks are very close together, as was the case for the heavy-light mesons. The axialvector bq QMEC diverts a little from the scalar bq one towards $m_Q \to m_b$. This is because here the extrapolation of the mass was more inaccurate due to the steep slope of the EVC.

The masses for the pseudoscalar and vector mesons and the scalar and axialvector diquarks obtained from the QMECS in Fig. 4.8 are compiled in Table 4.2. We have arranged them according to their quark model classification with the quarks getting heavier in each row from top to bottom. Whenever possible, we also calculated the relative error of our obtained masses in the rainbow-ladder MT model to the experimental values from the PDG [20] as

$$\Delta m^{\mathrm{rel.}} = \frac{|m_{\mathrm{PDG}} - m_{\mathrm{RL}}|}{m_{\mathrm{PDG}}}\,, \tag{4.57}$$

which provides a nice overview of the qualitative reliability of the used MT interaction. Collecting values in a table is very useful, but it always helps to visualize relations to get a better feel for them. For the meson spectra, we show our calculated masses in comparison to the respective experimental values from the PDG in Fig. 4.9. We see, that the mass spectra qualitatively agree very nicely, apart from the $c\bar{c}$ states, which are a little too low in mass. Because the bases to calculate the EVCs for scalar and axialvector diquarks are just the bases for the pseudoscalar and vector mesons respectively times the charge conjugation matrix C, we conclude that also the masses for these diquarks should be qualitatively good.

	0^{-+}			1^{--}			0^+	1^+
	PDG	m_{RL}	$\Delta m^{\mathrm{rel.}}$	PDG	m_{RL}	$\Delta m^{\mathrm{rel.}}$	m_{0^+}	m_{1^+}
$n\bar{n}$	$\pi/\eta^\dagger$	137	0.0%	ρ/ω	736	5.2%	809	1006
$s\bar{n}$	K	501	1.1%	K^*	913	0.1%	1072	1259
$s\bar{s}$	–	698	–	ϕ	1070	5.0%	1266	1412
$c\bar{n}$	D	1860	0.4%	D^*	2011	0.1%	2421	2439
$c\bar{s}$	D_s	1937	1.6%	D_s^*	2124	0.5%	2523	2543
$c\bar{c}$	η_c	2803	6.1%	J/ψ	2992	3.4%	3415	3433
$b\bar{n}$	B	5310	0.6%	B^*	5375	0.9%	6396	6403
$b\bar{s}$	B_s	5425	1.1%	B_s^*	5487	1.3%	6473	6492
$b\bar{c}$	B_c	6232	0.7%	–	6302	–	7139	7269
$b\bar{b}$	η_b	9421	0.2%	Υ	9500	0.4%	9915	10394

Table 4.2: Mesons composed of a quark-antiquark pair ($Q\bar{q}$) with quantum numbers $J^{PC} = 0^{-+}, 1^{--}$ are categorized according to their classification in the quark model. We present the experimental candidates as reported in [20], along with the masses (m_{RL}) calculated using our rainbow-ladder approach. The relative error between these calculated masses and those listed in the PDG is also provided where applicable. The last two columns display the calculated rainbow-ladder masses for the corresponding Qq diquarks with quantum numbers $J^P = 0^+, 1^+$. All values are reported in MeV. † : In this work, the masses of the π and η mesons are considered degenerate, as we neglect the strange quark component in the η and the indirect effects of the topological mass through octet-singlet mixing.

The masses for scalar (0^{++}) and axialvector (1^{++}) mesons in the light, charm and bottom region were also obtained analogously. However, the mass spectrum is known to be less reliable if not outright inaccurate in the rainbow-ladder truncation with the MT interaction. We show the obtained masses in Table C.1.

4.3.2 Dressing functions

The last thing we shortly need to discuss are the obtained dressing functions. First up, a big disclaimer is in order here. While the obtained masses are measurable quantities and therefore have to be *gauge invariant*, the dressing functions for the associated hadrons are in principle *gauge dependent* objects! As is so often the case in QFT, this only means that one needs to be careful when extracting information directly from these quantities. Regardless of this, by looking at the magnitudes of the dressing functions, one can infer the importance of the accompanying Dirac basis elements for the investigated state. In Fig. 4.10 we show the individual dressing functions f_j for the pseudoscalar ($j = 1, 2, 3, 4$) and the vector ($j = 1, \ldots, 8$) mesons. We do not show the values for the magnitudes on the y-axis, as it is not important for the present case and the universal normalization constant just scales

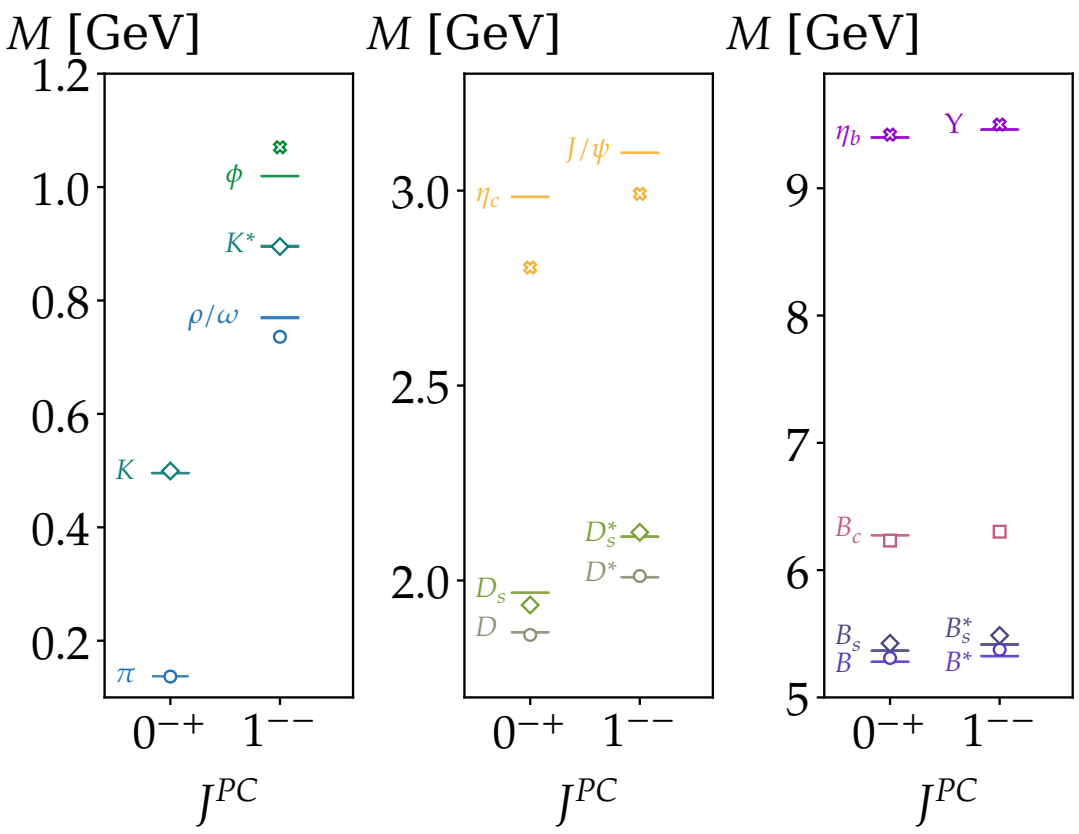

Figure 4.9: Meson mass spectra in the light (*left*), charm (*middle*) and bottom (*right*) region. We show the experimental PDG values as the boxes with the height of the box indicating the respective error. The two-body BSE results in the rainbow-ladder truncation are plotted as the data points in the same colour as the boxes.

the value but cannot change the ordering [5]. Furthermore, the shown dressing functions are intended to serve as illustration of the above argument and to show their behaviour for different relative momenta p^2. Because the dependence of the dressing functions on the angular variable z is not overly strong for these two states, we choose to show f_j's for $z = 0$. Note however, that this negligible dependence on the angular variable is not a universal behaviour. For the π meson, i.e., *left* in Fig. 4.10, the contribution hierarchy for the different Dirac tensors is the following: $\tau_1 > \tau_3 > \tau_2 > \tau_4$. Meaning, that including only τ_1 and solving the BSE in Eq. (4.53) already gives a reasonable result for the mass of $M_{\tau_1} \approx 120$ MeV. Including more Dirac elements then only leads to better and better results for the mass until we reach the experimental value. For the ρ meson (*right* in Fig. 4.10) we find, that having obtained a "base mass" using only τ_1 ($M_{\tau_1} \approx 888$ MeV), the contribution coming from τ_5 and τ_3 has the biggest influence in pushing the observable quantities, e.g., the mass of the state, towards the correct region. How much the inclusion of different Dirac basis elements in the Dirac part of the BSA affects the values for the mass and the

[5] For the interested reader, properly normalized dressing functions can be found in Figure 3.6 in Ref. [164].

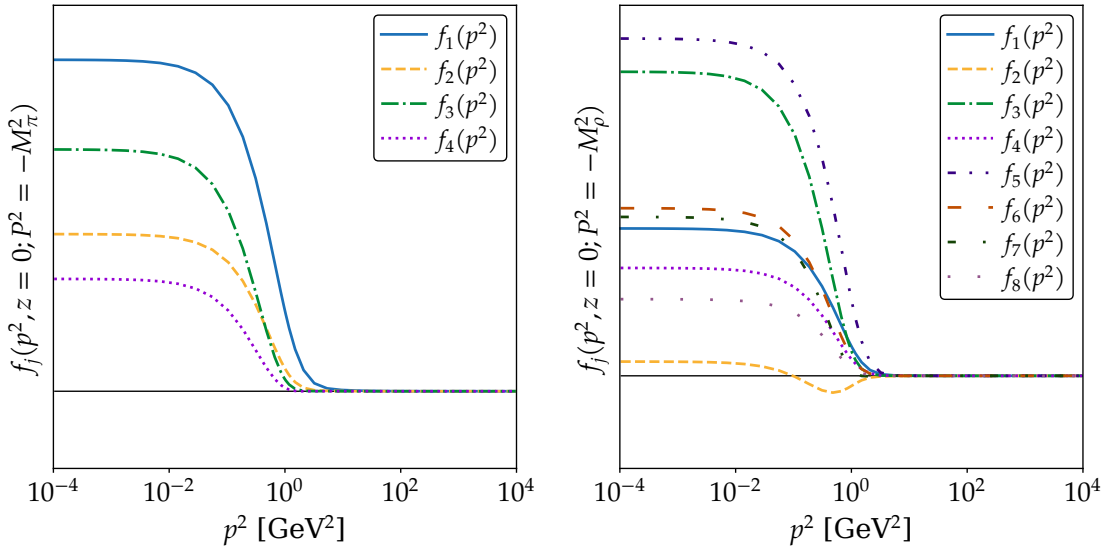

Figure 4.10: On-shell dressing functions f_j for the π (*left*) and ρ (*right*) mesons plotted against the relative momentum p^2 (log scale). Since the dependence of the f_j on the angular variable z is not overly strong for these states, it is sufficient to choose the point $z = 0$. The thinner black line indicates the zero.

leptonic decay constant of the π and the ρ meson is depicted very nicely in Figure 3.8 of [164].

Summary

With this, we close the discussion about the two-body BSE with a short recap. After an overview on the construction of the individual parts of the BSA, we discussed how the BSE is actually solved in practice and what are potential intricacies, i.e., the quark propagator poles. We then introduced the EVC as the result of the BSE and the QMECs as a way to investigate the behaviour of a hadron mass with changing current-quark mass. Furthermore, we compared our obtained mass spectrum for pseudoscalar and vector mesons with the current experimental values from the PDG and discussed the dressing functions and what one can learn from them. With this, we are now ready to move on to the main topic of this thesis, that is investigating the properties of four-quark states.

Chapter 5

Four-quark Faddeev-Yakubovsky equation

We now have all the ingredients we need to finally address the main topic of this work, namely the solution of the four-body Faddeev-Yakubovsky equation. Considering the case $n = 4$ of the generic n-body FYE introduced in Section 4.1, we get the four-body FYE as

$$\Gamma^{(4)} = K^{(4)} G_0^{(4)} \cdot \Gamma^{(4)} . \tag{5.1}$$

This is the second and more important of the two interesting special cases considered in this work. The four-body FYE allows to investigate the properties of four-quark states, which are exotic mesons consisting of two quarks and two antiquarks. In particular, we want to consider four-quark states containing at least two (anti)quarks of heavy flavour, i.e., charm and bottom.

This chapter is structured as follows. First, we will introduce the four-quark FYE and discuss the interactions between the four quarks. After that, we will introduce the general Dirac, colour and flavour Bethe-Salpeter amplitudes (BSA) and discuss their symmetries under charge conjugation and Pauli symmetry. We will then move on to discuss the phase space and the emergence of internal two-body pole structures. Based on this observation, we will introduce the concept of the physically motivated BSA and how to utilize it. Finally, we will close the chapter with considerations on the thresholds and limitations regarding the numerical solution of the four-body FYE.

5.1 The Four-Body Equation

We start by considering a generic four-quark state containing two quarks Q_1, Q_2 and two antiquarks $\bar{Q}_3$, $\bar{Q}_4$. The explicit flavour of the four quarks is not of immediate importance here and will be discussed later when we distinguish between hidden- and open-flavour four-quark states. Before we discuss the structure of the four-quark BSA, we need to take a closer look at the interactions between the four (anti)quarks. As one can imagine, the four constituents of the hadron can interact mutually in three different ways: there can be correlations involving only two, three and also all four of the constituents. The corresponding interaction kernel $K^{(4)}$ in Eq. (5.1) therefore features irreducible two-, three-

and four-body interactions and can be written as

$$K^{(4)} = \tilde{K}^{(2)} + \tilde{K}^{(3)} + \tilde{K}^{(4)}\,, \tag{5.2}$$

with the $\tilde{K}$ denoting the irreducible kernels. The corresponding four-body Faddeev-Yakubovsky equation with the full kernel given in Eq. (5.2) is shown in terms of Feynman diagrams in Fig. 5.1, which is just the special case $n = 4$ of the generic n-body FYE shown in Fig. 4.2. The two- and three-body interactions shown here only showcase one of the possible interactions for brevity, with the others indicated by the *cyclic perm.* text. The third term in the two-body interactions is necessary to avoid the overcounting of diagrams coming from the iteration of the first two terms, see [171, 181–183] for more details. Looking closer at the two-body interactions in Fig. 5.1, one can identify three different interactions pairs: $(Q_1Q_2)(\bar{Q}_3\bar{Q}_4)$ which resembles an internal diquark-antidiquark pair and $(Q_1\bar{Q}_3)(Q_2\bar{Q}_4)$ and $(Q_1\bar{Q}_4)(Q_2\bar{Q}_3)$ which both resemble meson-meson pairings within the four-quark states. We will from here on also refer to these internal clusterings as meson-meson ($\mathcal{M}_1$ for $(13)(24)$ and $\mathcal{M}_2$ for $(14)(23)$) or diquark-antidiquark ($\mathcal{D}$ for $(12)(34)$) *interaction topologies*.

For the thesis at hand, we choose to neglect the three- and four-body forces, as has been done in all previous works on this topic using the DSE/BSE framework, see [70] for a recent review and references therein. This reduces the equation shown in Fig. 5.1 to just the highlighted part. There are a few reasons for justifying doing so. Firstly, we have already established earlier in this work that most hadrons are resonances and therefore unstable with respect to strong decays, i.e., hadron to hadrons. The decay of a four-quark state with given quark content into two mesons with the quarks and antiquarks distributed accordingly is therefore a pretty straightforward picture, see, e.g., the σ meson as a $\pi - \pi$ resonance [184]. This together with the closeness of some four-quark states to the respective two-meson threshold, as is the case for the $\chi_{c1}(3872)$ and the $T_{cc}^{+}(3875)$, provides the first hints that the two-body forces might be dominating. By neglecting the three- and four-body forces as an approximation and calculating the masses of the four-quark states using only the two-body correlations, one can a-posteriori argue whether this approximation is justified based on the accuracy of the obtained results. A further reason is, that the calculation of three- and four-body forces is computationally very expensive and if the notion of the two-body forces being dominant proves to be a proper description of the states in question, the effort is not really worth it. It is worth mentioning, that looking at the large N_c limit of QCD considering only gluon exchanges, the leading order three- and four-body interactions actually become subleading in this limit, see Appendix B.1.1.

Retaining only the two-body forces, the four-quark interaction kernel $K^{(4)}$ then reads

$$K^{(4)} = \sum_{aa'} \tilde{K}_a^{(2)} \cdot \left(G_0^{(2)}\right)^{-1}_{a'} + \tilde{K}_{a'}^{(2)} \cdot \left(G_0^{(2)}\right)^{-1}_{a} - \tilde{K}_a^{(2)} \cdot \tilde{K}_{a'}^{(2)}\,. \tag{5.3}$$

If we combine this kernel with the propagator matrix $G_0^{(4)}$, certain full propagators cancel out and the matrix we want to calculate the eigenvalues for in the four-body BSE then

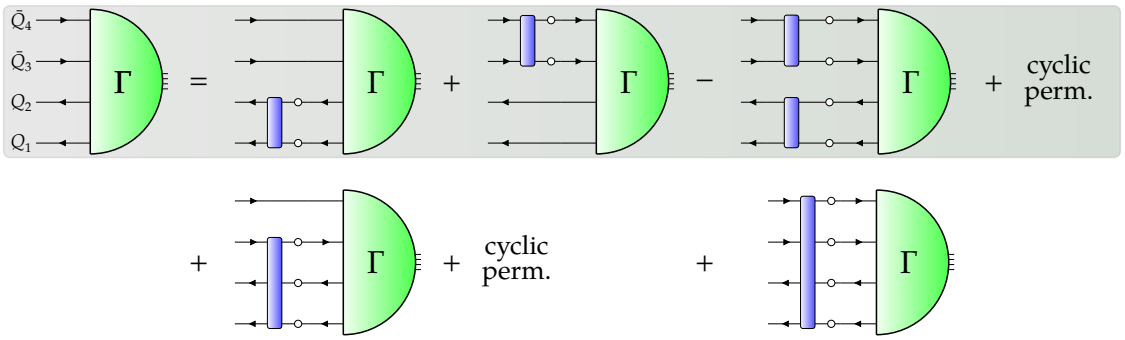

Figure 5.1: Four-body FYE for a $Q_1Q_2\bar{Q}_3\bar{Q}_4$-state given in terms of Feynman diagrams. The first three diagrams show the two-body interactions between (Q_1Q_2) and $(\bar{Q}_3\bar{Q}_4)$ with the permutations $(Q_1\bar{Q}_3)(Q_2\bar{Q}_4)$ and $(Q_1\bar{Q}_4)(Q_2\bar{Q}_3)$ not shown for brevity. The first term in the second row shows the $(Q_1Q_2\bar{Q}_3)$ interaction of the irreducible three-body interactions with additional three permutations also suppressed for brevity. The last term then shows the four-body interaction. The free quark propagators are again denoted by lines with an arrow indicating the spin flow and the corresponding fully dressed quantities are shown with a blob. The highlighted section is the equation actually used in this work, as the three- and four-body interactions will be neglected, see main text.

reads

$$K^{(4)}G_0^{(4)} = \sum_{aa'} K_a^{(2)} + K_{a'}^{(2)} - K_a^{(2)} \cdot K_{a'}^{(2)} \,, \tag{5.4}$$

which is the form of the kernel shown in the first line of Fig. 5.1, with $K_{a,a'}^{(2)} = \tilde{K}_{a,a'}^{(2)} \cdot (G_0^{(2)})_{a,a'}$. The a and a' denote interaction between the (anti)quark pairs and aa' represents one of three combinations $(12)(34)$, $(13)(24)$ and $(14)(23)$. The numbers given in the interaction combinations here correspond to the indices of the quarks of the $Q_1Q_2\bar{Q}_3\bar{Q}_4$ four-quark state. For the irreducible two-body kernels $\tilde{K}^{(2)}$ we again use the Rainbow-Ladder truncation together with the Maris-Tandy (MT) interaction as given in Eq. (4.30) and shown in Fig. 4.5.

5.1.1 Dirac part of the four-quark BSA

Having established the interactions we will use, it is now time to construct the four-quark BSA. We will again start with the Dirac part of the BSA. Being the special case $n = 4$ of the n-quark BSA given in Eq. (4.22), we will have *three* relative momenta k, q and p for our four-quark state. The Dirac part of the BSA again reads

$$\Gamma^{(\mu)}_{\alpha_1\alpha_2\alpha_3\alpha_4}(k,q,p,P) = \sum_{j=1}^{N_\mathrm{D}} f_j(\Omega; P^2)\, \tau^{(\mu)}_{j;\alpha_1\alpha_2\alpha_3\alpha_4}(k,q,p,P) \,, \tag{5.5}$$

with $\Omega = \{k^2, q^2, p^2, k\cdot q, k\cdot p, q\cdot p, k\cdot P, q\cdot P, p\cdot P\}$ containing 9 Lorentz invariant momentum variables. As we have seen in Section 4.2, the number of Dirac basis elements N_D will

be different depending on the total spin of the particle J. For this work, we will consider four-quark states with total spin $J = 0$ and $J = 1$ (hence only one Lorentz index μ in Eq. (5.5)), which need a total of $N_{\mathrm{D}} = 256$ and $N_{\mathrm{D}} = 768$ Dirac basis elements respectively. How these elements are determined is written in detail in the supplemental material of [67]. Since we later only want to construct a small subset of these, it is not necessary to go into further detail here.

Once the full basis of hundreds of Dirac basis elements is constructed, we use that the total spin J is described by the Pauli-Lubanski pseudovector [185, 186]

$$W^{\mu} := \frac{1}{2} \cdot \varepsilon^{\mu\nu\rho\sigma} \hat{P}_{\nu} J_{\rho\sigma} = S^{\mu} + L^{\mu} \,, \tag{5.6}$$

first constructed by Józef Lubański [187, 188]. The operator W^2 applied to the individual basis elements yields eigenvalues $j(j+1)$, which in turn allows us to make a partial wave decomposition and classify the tensors according to s-, p-, d- and f-waves. In this thesis, we will make the assumption that the s-wave Dirac tensors are dominant and restrict ourselves to consider only those. This assumption is reasonable, as the majority of the observed hadronic decays for the states we want to investigate in the present work are s-wave according to the PDG [20]. The $N^s_{\mathrm{D}} = 16$ for $J = 0$ and $N^s_{\mathrm{D}} = 48$ for $J = 1$ s-wave Dirac basis elements both constitute Fierz complete sets [67, 184]. Depending on the accuracy of the obtained masses for the investigated four-quark states, we can a posteriori make arguments in favour or against the assumption of considering only s-wave elements. It will prove useful in the following to orthogonalize the three relative momenta k, q and p together with the total momentum P to obtain four orthonormal momenta n_i^{μ} $(i = 1, \ldots 4)$. Now using Ω_{ω}, $\Omega_{\omega'} \in \{\mathbb{I}_{\mathrm{D}}, \varepsilon\gamma_5\}$, with $\epsilon \in \{-1, 1\}$, and the positive/negative-energy projector $\Lambda_{\pm} = (\mathbb{I} \pm \not{n}_4)/2$, where $n_4^{\mu} = \hat{P}^{\mu}$, we can cast the Dirac basis elements in Eq. (5.5) for $J = 0$ in a very compact form:

$$\tau_j^{(\mu)}(k, q, p, P) = \Gamma_k^{(\mu)} \Lambda_{\lambda} \Omega_{\omega} \gamma_5 (C) \otimes \left(C^T\right) \gamma_5 \Omega_{\omega'} \Lambda_{\lambda'} \Gamma_l^{(\mu)} \,, \tag{5.7}$$

where the charge conjugation matrix in the brackets is only relevant when considering the basis in the diquark-antidiquark topology. With $\Gamma_k, \Gamma_l \in \{\mathbb{I}_{\mathrm{D}}, \not{n}_1, \not{n}_2, \not{n}_3\}$ this compact form contains in principle all 256 basis elements of the $J = 0$ four-quark state. To get the respective basis for the $J = 1$ four-quark state, one attaches an additional ϵn_i^{μ} with $i = 1, 2, 3$ to the basis elements in Eq. (5.7). Taking the 256 basis elements times three then yields the 768 linearly independent basis elements for the $J = 1$ state. Focussing on the s-wave tensors, we identify the following combinations for $\Gamma_k \otimes \Gamma_l$:

$$J = 0: \quad \Gamma_k^{(\mu)} \otimes \Gamma_l^{(\mu)} = \{\mathbb{I}_{\mathrm{D}} \otimes \mathbb{I}_{\mathrm{D}}, \sqrt{1/3}\, \gamma_{\perp}^{\mu} \otimes \gamma_{\mu}^{\perp}\} \tag{5.8}$$

$$J = 1: \quad \Gamma_k^{(\mu)} \otimes \Gamma_l^{(\mu)} = \{\gamma_{\perp}^{\mu} \otimes \mathbb{I}_{\mathrm{D}}, \mathbb{I}_{\mathrm{D}} \otimes \gamma_{\perp}^{\mu}, \epsilon\varepsilon^{\mu\nu\rho\sigma} n_{\nu}^4 \gamma_{\rho} \otimes \gamma_{\sigma}\} \,, \tag{5.9}$$

with $\gamma_{\perp}^{\mu} = T^{\mu\nu}(P)\gamma_{\nu}$ the transversalized gamma matrices with respect to the total momentum.

The s-wave basis elements obtained for $J = 0$, 1 when combining Eq. (5.8) and Eq. (5.7)

both correspond to four-quark states with positive parity, i.e., $J^P = 0^+, 1^+$. The negative parity basis elements are obtained by contracting either side of the direct product by γ^5. As we mentioned before, we have three different interaction topologies for which the basis elements $\tau_j^{(\mu)}$ in Eq. (5.7) explicitly written read:

$$\mathcal{D}: \quad \left(\Gamma_k^{(\mu)}\Lambda_\lambda\Omega_\omega\gamma_5 C\right)_{\alpha_1\alpha_2} \otimes \left(C^T\gamma_5\Omega_{\omega'}\Lambda_{\lambda'}\Gamma_l^{(\mu)}\right)_{\alpha_3\alpha_4}, \tag{5.10}$$

$$\mathcal{M}_1: \quad \left(\Gamma_k^{(\mu)}\Lambda_\lambda\Omega_\omega\gamma_5\right)_{\alpha_1\alpha_3} \otimes \left(\gamma_5\Omega_{\omega'}\Lambda_{\lambda'}\Gamma_l^{(\mu)}\right)_{\alpha_2\alpha_4}, \tag{5.11}$$

$$\mathcal{M}_2: \quad \left(\Gamma_k^{(\mu)}\Lambda_\lambda\Omega_\omega\gamma_5\right)_{\alpha_1\alpha_4} \otimes \left(\gamma_5\Omega_{\omega'}\Lambda_{\lambda'}\Gamma_l^{(\mu)}\right)_{\alpha_2\alpha_3}. \tag{5.12}$$

In total we get $N_{\mathrm{D}}^s = 16$, for $J = 0$, and $N_{\mathrm{D}}^s = 48$, for $J = 1$, s-wave basis elements. When using the complete set of s-wave basis elements, it does not matter in which topology the basis elements are chosen as they each form a Fierz complete set, i.e., can be transformed into each other via Fierz transformations.

5.1.2 Colour part of the four-quark BSA

To construct the colour part of the four-quark BSA, we need to combine the colour group representations of the two quarks and two antiquarks via tensor products as discussed in Section 4.2.2. Taking the corresponding multiplet representations $\mathbf{N}_c$ and $\overline{\mathbf{N}}_\mathbf{c}$ of the general colour group $\mathrm{SU}(N_c)$ this direct product reads

$$\mathbf{N}_c \otimes \mathbf{N}_c \otimes \overline{\mathbf{N}}_\mathbf{c} \otimes \overline{\mathbf{N}}_\mathbf{c}. \tag{5.13}$$

How to evaluate this tensor product is described in great detail in Appendix B.1 and the resulting irreducible representations are collected in Table B.1. We can see, that we get two colour singlets $\mathbf{1}_c$ and many other representations, which are however all coloured and thus of no real interest for the investigations of this thesis. We will explore the two colour singlets in more detail below.

Since we have established the notion of the dominant two-body interactions in the last section, we can also group the tensor products in Eq. (5.13) according to the different meson-meson and diquark-antidiquark interaction topologies:

$$\mathcal{D}: \quad \left(\mathbf{N}_\mathbf{c} \otimes \mathbf{N}_\mathbf{c}\right) \otimes \left(\overline{\mathbf{N}}_\mathbf{c} \otimes \overline{\mathbf{N}}_\mathbf{c}\right), \tag{5.14}$$

$$\mathcal{M}_{1/2}: \quad \left(\mathbf{N}_\mathbf{c} \otimes \overline{\mathbf{N}}_\mathbf{c}\right) \otimes \left(\mathbf{N}_\mathbf{c} \otimes \overline{\mathbf{N}}_\mathbf{c}\right). \tag{5.15}$$

We can evaluate the sub-tensor products in the brackets using the relations we found in the case of the two-body BSA, i.e., Eq. (4.39) and Eq. (4.41). For the following explicit calculation we set $N_c = 3$, as it provides a clearer overview and because it is the natural value. The case for arbitrary N_c can be found at the end of Appendix B.1. The resulting colour representations in the direct sum look very much like the ones corresponding to a (anti)diquark or a meson, depending on the interaction topologies. Hence, we will refer to the respective colour representations as diquarks and mesons here. Evaluating the

remaining tensor product we get the following direct sums:

$$\mathcal{D}: \quad \left(\mathbf{6} \oplus \bar{\mathbf{3}}\right) \otimes \left(\bar{\mathbf{6}} \oplus \mathbf{3}\right) = \mathbf{1}_{\mathbf{6}\otimes\bar{\mathbf{6}}} \oplus \mathbf{1}_{\bar{\mathbf{3}}\otimes\mathbf{3}} \oplus \dots , \tag{5.16}$$

$$\mathcal{M}_{1/2}: \quad \left(\mathbf{8} \oplus \mathbf{1}\right) \otimes \left(\mathbf{8} \oplus \mathbf{1}\right) = \mathbf{1}_{\mathbf{8}\otimes\mathbf{8}} \oplus \mathbf{1}_{\mathbf{1}\otimes\mathbf{1}} \oplus \dots . \tag{5.17}$$

Thus, depending on the interaction topology, we can obtain an overall colour singlet four-quark state by combining either a diquark and an antidiquark in a antitriplet-triplet ($\bar{\mathbf{3}}_\mathbf{c} \otimes \mathbf{3}_\mathbf{c}$) or sextet-antisextet ($\mathbf{6}_\mathbf{c} \otimes \bar{\mathbf{6}}_\mathbf{c}$) representation or by combining two mesons either in a singlet-singlet ($\mathbf{1}_\mathbf{c} \otimes \mathbf{1}_\mathbf{c}$) or octet-octet ($\mathbf{8}_\mathbf{c} \otimes \mathbf{8}_\mathbf{c}$) representation. As mentioned above, all other obtained representations correspond to overall coloured objects and are suppressed here. These four combinations to form a colour singlet for the four-quark state can be further grouped according to the exerted colour force between the two internal two-body particles.[1]

In the following, we will construct the mathematical formulation for the colour part of our four-quark BSA. For this, we will again keep N_c general and only concretize if necessary. We start by considering the attractive combination of two colour singlets forming the overall four-quark colour singlet structure. As shown in Eq. (4.40), the colour singlet structure for a $q\bar{q}$ meson is realized by a Kronecker delta combining the respective colour indices. Since we have effectively two meson colour singlets in our four-quark state for the present case, we use two Kronecker deltas with the respective colour indices to form the four-quark colour BSA:

$$C_{\mathbf{11}} = \frac{\delta^{A_1A_3}\,\delta^{A_2A_4}}{N_c}\,, \qquad C'_{\mathbf{11}} = \frac{\delta^{A_1A_4}\,\delta^{A_2A_3}}{N_c}\,, \tag{5.18}$$

where $C_{\mathbf{11}}$ and $C'_{\mathbf{11}}$ correspond to the $\mathcal{M}_1$ and $\mathcal{M}_2$ meson-meson interaction topology respectively. The N_c in the denominator is a conventional normalization for the terms. Similar to the meson-meson case above, for the attractive diquark-antidiquark topology in the antitriplet-triplet representation one can combine two times the colour structure of the two-body diquarks in Eq. (4.42) as $\varepsilon^{A_1A_2B}\varepsilon^{A_3A_4}{}_B$. By virtue of the contraction of equal indices of Levi-Civita symbols, this combination can be written in terms of Kronecker deltas and thus as a linear combination of the meson-meson colour BSAs given in Eq. (5.18). Also the repulsive combinations can be expressed in terms of linear combinations of the attractive meson-meson colour BSAs. Explicitly, these colour BSAs then read:

$$C_{\bar{\mathbf{3}}\mathbf{3}} = -\frac{\left(C_{\mathbf{11}} - C'_{\mathbf{11}}\right)}{\sqrt{2 - \frac{2}{N_c}}}\,, \qquad C_{\mathbf{6}\bar{\mathbf{6}}} = \frac{\left(C_{\mathbf{11}} + C'_{\mathbf{11}}\right)}{\sqrt{2 + \frac{2}{N_c}}}\,, \tag{5.19}$$

[1] Recall from Section 4.2.2, that the colour singlet and the colour (antitriplet) correspond to attractive forces between the (anti)quarks, while the octet and sextet representations correspond to repulsive colour forces. Combining two internal clusters living in an attractive representation also yields a force acting attractively between them. On the contrary, the combination formed by combining two internal clusters living in the repulsive representations results in a net repulsive force between them.

$$C_{\mathbf{88}} = \frac{\left(C_{\mathbf{11}} - N_c\, C'_{\mathbf{11}}\right)}{\sqrt{N_c^2 - 1}}\,, \qquad C'_{\mathbf{88}} = \frac{\left(C'_{\mathbf{11}} - N_c\, C_{\mathbf{11}}\right)}{\sqrt{N_c^2 - 1}}\,. \tag{5.20}$$

As it will be important later on, we note that the tensors

$$\left\{C_{\mathbf{11}}, C_{\mathbf{88}}\right\}\,, \quad \left\{C'_{\mathbf{11}}, C'_{\mathbf{88}}\right\} \quad \text{and} \quad \left\{C_{\bar{\mathbf{3}}\mathbf{3}}, C_{\mathbf{6}\bar{\mathbf{6}}}\right\}\,, \tag{5.21}$$

are mutually orthogonal.

5.1.3 Flavour four-quark BSA and symmetries

For the construction of the Dirac and colour basis elements of the four-quark BSA above, we had to know which of the constituents are quarks and which are antiquarks, but we did not need to consider the individual flavours of the quarks. To construct the flavour part of the four-quark BSA, we need to take a closer look at the overall flavour combination of our $Q_1Q_2\bar{Q}_3\bar{Q}_4$ state. In general, four-quark states can be classified into two different categories based on the flavour BSA: *hidden- and open-flavour*. To make the classification, one needs to determine the overall flavour charges, i.e., strangeness $\mathcal{S}$, charm $\mathcal{C}$ and bottom $\mathcal{B}$, of the four-quark state by summing up the individual flavour charges of each quark. For a four-quark state to be classified as hidden-flavour, all overall flavour charges must be zero. Furthermore, hidden-flavour four-quark states have a definite charge conjugation quantum number. Correspondingly, if one or more of the flavour charges are non-zero, the four-quark state falls into the open-flavour category. The main focus of this work is to investigate the properties of heavy-flavour four-quark states, i.e., states featuring hidden- or open-charm or bottom flavour charges. To this end, the flavour BSA for the hidden-flavour four-quark states will from here on be written as $Q_1Q_2\bar{Q}_3\bar{Q}_4 = Qq\bar{q}\bar{Q}$, while the open-flavour four-quark states will be written as $Q_1Q_2\bar{Q}_3\bar{Q}_4 = QQ'\bar{q}\bar{q}'$, with Q, $Q' \in \{b, c\}$ and q, $q' \in \{b, c, s, d, u\}$ denoting the heavy and 'light' quarks respectively. For the open-flavour BSA, the two heavy quarks as well as the two light quarks are allowed to take different flavours, which is forbidden for the hidden-flavour states.

Since we are using the same RL truncation and flavour-blind MT interaction as in the two-body BSE case, the flavour trace will evaluate to one when contracting the flavour part with its projector (see discussion around Eq. (4.52)) and thus is of no importance there. However, it plays a vital part in the construction of the full four-quark BSA. For a four-quark state with given quantum numbers $I(J^{P(C)})$, the flavour BSA actually imposes conditions on the explicit form of the combined Dirac-colour BSAs such that the overall symmetries of the hidden- or open-flavour four-quark states are fulfilled respectively. This will become clearer down below.

Let us start by considering the flavour BSA for the hidden-flavour four-quark states. As stated above, the flavour structure there reads $Qq\bar{q}\bar{Q}$. This state effectively only contains two different quark flavours, one for Q and one for q, and the respective antiflavours. As established earlier, the quark and antiquark are related via charge conjugation. Thus, the hidden-flavour four-quark state with quark content $Qq\bar{q}\bar{Q}$ is subject to charge conjugation symmetry under the exchange and charge conjugation of the quarks $(14)(23)$. Regardless

of the isospin, the flavour BSA has positive C-parity in $(14)(23)$. This charge conjugation symmetry in the indices $(14)(23)$ also has to be fulfilled by the colour and the Dirac part accordingly, such that the overall BSA has the charge conjugation quantum number C of the investigated state. Since the colour BSAs in Eqs. (5.18) and (5.19) consist of linear combinations of Kronecker deltas, they all have positive C-parity. Thus, it comes down to the Dirac elements to fulfil the correct transformation properties under charge conjugation. The corresponding transformation here reads (see also [74])

$$C_{\alpha_1\alpha_1'}\, C_{\alpha_2\alpha_2'}\, C_{\alpha_3\alpha_3'}\, C_{\alpha_4\alpha_4'}\, \Gamma^{(\mu)}_{\alpha_4'\alpha_3'\alpha_2'\alpha_1'}(-p_4,-p_3,-p_2,-p_1) = \pm\, \Gamma^{(\mu)}_{\alpha_1\alpha_2\alpha_3\alpha_4}(p_1,p_2,p_3,p_4)\,, \tag{5.22}$$

with $C_{\alpha_i\alpha_i'}$ denoting the charge conjugation matrices defined in Eq. (A.23) with explicit Dirac indices. Note, that we could have equally chosen $Q_1Q_2\bar{Q}_3\bar{Q}_4 = Qq\bar{Q}\bar{q}$ as the hidden-flavour flavour BSA, which would imply that this state needs to have C-parity under the exchange and charge conjugation of the quarks $(13)(24)$.

The situation is a little more involved, when considering the open-flavour four-quark states. As a reminder, the flavour structure here reads $QQ'\bar{q}\bar{q}'$. The two heavy quarks and the two 'light' antiquarks are not related by charge conjugation in this case and need not necessarily be of the same flavour either. However, as (anti)quarks are fermions, the total four-quark BSA has to obey Pauli antisymmetry under the quark exchanges (12) or (34). The corresponding transformations are given as

$$\begin{aligned} (12):&\quad \Gamma^{(\mu)}_{A_2A_1A_3A_4}(p_2,p_1,p_3,p_4) = -\Gamma^{(\mu)}_{A_1A_2A_3A_4}(p_1,p_2,p_3,p_4)\,,\\ (34):&\quad \Gamma^{(\mu)}_{A_1A_2A_4A_3}(p_1,p_2,p_4,p_3) = -\Gamma^{(\mu)}_{A_1A_2A_3A_4}(p_1,p_2,p_3,p_4)\,, \end{aligned} \tag{5.23}$$

with the A_i collecting the Dirac, colour and flavour indices. In order to construct the BSA for an open-flavour four-quark state with quantum numbers $I(J^P)$ which fulfils the corresponding transformation(s) given in Eq. (5.23), we need to look how the Dirac, colour and flavour part individually transform under the transformation(s). First, we consider the flavour BSA. Here, the flavour sub-clusters QQ' and $\bar{q}\bar{q}'$ relevant for Eq. (5.23) are of (anti)diquark nature. As we will see in the following, whether the flavour combination in a sub-cluster transforms symmetric or antisymmetric under (12) or (34) is determined by the isospin and the flavours of the quarks. Note that, since isospin is an additive quantum number, the total given isospin of the four-quark state is determined from the individual isospins of the sub-clusters. Take the $I = 0$ and $I = 1$ flavour BSAs for light-light diquarks in Eq. (4.47). The $I = 0$ flavour combination is antisymmetric under exchange of the quarks, i.e., $[ud] \to [du] = -[ud]$, while the corresponding $I = 1$ flavour BSAs are symmetric. For the combinations QQ' and $\bar{q}\bar{q}'$ with $Q \neq Q'$ and $\bar{q} \neq \bar{q}'$ (with $\bar{q}' \neq \bar{u}/\bar{d}$) the isospin is either $I = 0$ or $I = \frac{1}{2}$ and the flavour BSA can be symmetric or antisymmetric as shown in Eq. (4.48). Lastly, the flavour combinations QQ' and $\bar{q}\bar{q}'$ with $Q = Q'$ and $\bar{q} = \bar{q}' \neq \bar{u}/\bar{d}$ are automatically symmetric under quark exchange. The symmetry of the flavour part dictates the symmetry the combined Dirac-colour tensors need to fulfil, see Appendix B.2.2.

The transformation of the colour BSAs in Eqs. (5.18) and (5.19) under Eq. (5.23) is fairly

Flavour $(QQ'\bar{q}\bar{q}')$				Colour		Dirac	
$Q \neq Q'$	$Q = Q'$	$\bar{q} \neq \bar{q}'$	$\bar{q} = \bar{q}'$	$C_{\bar{3}3}$	$C_{6\bar{6}}$	S	A
$\pm$	$+$	$\pm$	$+$	$-$	$+$	$-$	$+$

Table 5.1: Overview of how the individual flavour, colour and Dirac parts of the open-flavour four-quark BSA transform under quark exchanges (12) or (34). One can combine the three parts of the BSA according to the individual transformation properties to form an overall BSA which satisfies Eq. (5.23).

straightforward. The two colour singlets $C_{\mathbf{11}}$ and $C'_{\mathbf{11}}$ transform into each other under (12) and (34), i.e., $C_{\mathbf{11}} \leftrightarrow C'_{\mathbf{11}}$. And since the other colour BSAs are linear combinations of these two, we get the following transformation properties:

$$C_{\bar{\mathbf{3}}\mathbf{3}} \leftrightarrow -C_{\bar{\mathbf{3}}\mathbf{3}}\,, \qquad C_{\mathbf{6}\bar{\mathbf{6}}} \leftrightarrow C_{\mathbf{6}\bar{\mathbf{6}}}\,, \qquad C_{\mathbf{88}} \leftrightarrow C'_{\mathbf{88}}\,. \tag{5.24}$$

The two colour singlet structures coming from the diquark-antidiquark combinations transform with a different sign, which will have important consequences later on.

To consider the transformation of the Dirac BSA, we take the s-wave tensors in the diquark basis given in Eq. (5.10). The basis elements in the sub-spaces contain either $S = \gamma_5 C$ or $A = \gamma^\mu C$, denoting scalar (S) and axialvector (A) diquark basis elements respectively. Since the quark exchange in (12) or (34) correspond to transposing the basis elements when using the diquark basis, we can use the relations of Dirac matrices in Eq. (A.24) to determine the transformation properties as

$$S \to \left(\gamma_5 C\right)^T = \left(C^T \gamma_5^T\right) = \Big(\underbrace{C^T C^T}_{=-\mathbb{I}_\mathrm{D}}\gamma_5 C\Big) = -\gamma_5 C = -S\,, \tag{5.25}$$

$$A \to \left(\gamma^\mu C\right)^T = \left(C^T \left(\gamma^\mu\right)^T\right) = \Big(\underbrace{C^T C^T}_{=-\mathbb{I}_\mathrm{D}}\left(-\gamma^\mu\right) C\Big) = \gamma^\mu C = +A\,. \tag{5.26}$$

We have summarized the symmetry transformations discussed above in a condensed form in Table 5.1, while a more detailed depiction of the tensors with definite Pauli symmetry can be found in Tables B.5 and B.6.

5.2 Phase space and physical BSA

After having discussed the colour, flavour and Dirac BSAs and their symmetries for hidden- and open-flavour four-quark states, it is now time to investigate the momentum structure of the BSA a little closer. The momentum dependence of the four-quark BSA can be expressed in terms of the four quark momenta p_1, p_2, p_3, p_4, as shown for the general case in Eq. (4.22). As already shown in Eq. (5.5), it is more convenient for us to work with the

three relative momenta k, q, p and the total hadron momentum P, which are defined as

$$\begin{aligned} k^\mu &= \frac{\left(p_{12}^+\right)^\mu - \left(p_{34}^+\right)^\mu}{2} + \left(\frac{1-2\sigma_{12}^+}{2}\right) P^\mu\,, \qquad p^\mu = \frac{\left(p_{23}^+\right)^\mu - \left(p_{14}^+\right)^\mu}{2} + \left(\frac{1-2\sigma_{23}^+}{2}\right) P^\mu\,, \\ q^\mu &= \frac{\left(p_{13}^+\right)^\mu - \left(p_{24}^+\right)^\mu}{2} + \left(\frac{1-2\sigma_{13}^+}{2}\right) P^\mu\,, \qquad P^\mu = \sum_{i=1}^{4} p_i^\mu\,. \end{aligned} \tag{5.27}$$

To avoid lengthy terms also in the future, we introduce the shorthand notation $x_{ij}^{\pm} = x_i \pm x_j$, with x denoting an arbitrary quantity. As can be seen from the quark momenta involved in the definition, each of the relative momenta can be associated with a specific sub-cluster, i.e., the momentum k^μ is the relative momentum for the diquark-antidiquark cluster ($\mathcal{D}$), the q^μ for the meson-meson $\mathcal{M}_1$ cluster and the p^μ for the $\mathcal{M}_2$ topology. If we ever need to switch from the relative momenta to the quark momenta, we can use

$$\begin{aligned} p_1^\mu &= \frac{k^\mu + q^\mu - p^\mu}{2} + \sigma_1 P^\mu\,, & p_2^\mu &= \frac{k^\mu - q^\mu + p^\mu}{2} + \sigma_2 P^\mu\,, \\ p_3^\mu &= \frac{-k^\mu + q^\mu + p^\mu}{2} + \sigma_3 P^\mu\,, & p_4^\mu &= -\frac{k^\mu + q^\mu + p^\mu}{2} + \sigma_4 P^\mu\,. \end{aligned}$$

We introduced *quark momentum partitioning parameters* σ_1, σ_2, σ_3, σ_4, for the same reason as in the case for the two-body BSE in Section 4.2, to optimally distribute the total hadron momentum amongst the four quarks according to their respective masses. The sum of the σ_i's evaluates to one, i.e., $\sum_{i=1}^{4} \sigma_i = 1$.

We choose the following four-vectors for the three relative momenta and the total hadron momentum

$$k^\mu = \sqrt{k^2}\begin{pmatrix} 0 \\ 0 \\ \bar{z}_k \\ z_k \end{pmatrix}, \quad q^\mu = \sqrt{q^2}\begin{pmatrix} \sin(\alpha)\bar{y}_q\bar{z}_q \\ \cos(\alpha)\bar{y}_q\bar{z}_q \\ y_q\bar{z}_q \\ z_q \end{pmatrix}, \quad p^\mu = \sqrt{p^2}\begin{pmatrix} 0 \\ \bar{y}_p\bar{z}_p \\ y_p\bar{z}_p \\ z_p \end{pmatrix}, \quad P^\mu = \sqrt{P^2}\begin{pmatrix} 0 \\ 0 \\ 0 \\ 1 \end{pmatrix}, \tag{5.28}$$

with z_x, $y_x \in [-1,1]$ ($x = k,q,p$ here)[2] and $\alpha \in [0,2\pi]$ denoting various angular variables between the relative momenta and the total momentum. As all angular variables are called either z or y, the subscript denotes the associated relative momentum. It is a convenient choice to consider the hadron in its rest frame and hence the total hadron momentum P^μ does not feature spatial components.

With the above definitions out of the way and P^2 setting the mass scale of the hadron, we can take a closer look at the nine Lorentz invariants of the dressing functions, contained in the set Ω in Eq. (5.5). They can generally be grouped into three different sub-categories: relative momenta squared k^2, q^2, p^2, which can also be identified as Mandelstam variables,

[2] With the angular variables: z_x, $y_x = \cos(...)$, $\bar{z}_x$, $\bar{y}_x = \sin(...)$, where the dots represent some angle specific to the chosen relative momentum x.

angular variables purely amongst the relative momenta $\omega_1 = k \cdot q$, $\omega_2 = k \cdot p$, $\omega_3 = q \cdot p$ and angular variables between the relative momenta and the total momentum $\eta_1 = p \cdot P$, $\eta_2 = q \cdot P$, $\eta_3 = k \cdot P$[3]. One can make use of the permutation group S_4 via a machinery developed and described in detail in [184] and [77], to cast these variables into a singlet S_0, a doublet D and two triplets T_0, T_1:

$$S_0 := \frac{k^2 + q^2 + p^2}{4}, \tag{5.29}$$

$$D := S_0 \begin{pmatrix} a \\ s \end{pmatrix}, \tag{5.30}$$

$$T_0 := S_0 \begin{pmatrix} u \\ v \\ w \end{pmatrix}, \qquad T_1 := \sqrt{S_0 P^2} \begin{pmatrix} u' \\ v' \\ w' \end{pmatrix}. \tag{5.31}$$

The singlet S_0 determines the momentum scale of the dressing functions and will be the only dimensionful quantity in the following. We have pulled factors of S_0 and $\sqrt{S_0 P^2}$ out of the doublet and triplets to render the quantities a, s, u, v, w, u', v', w' dimensionless. The variables a and s in the doublet D are therefore defined as

$$a := \sqrt{3} \cdot \frac{q^2 - p^2}{4 S_0}, \qquad s := \frac{p^2 + q^2 - 2 \cdot k^2}{4 S_0}. \tag{5.32}$$

The a and s can serve as axis to span a plane which is effectively a Mandelstam plane. The variables in the triplets are related to the quantities from Ω via

$$u = -\frac{\omega_1 + \omega_2 + \omega_3}{4 S_0}, \quad v = -\sqrt{2} \cdot \frac{\omega_1 + \omega_2 - 2 \cdot \omega_3}{4 S_0}, \quad w = \sqrt{6} \cdot \frac{\omega_1 - \omega_2}{4 S_0}, \tag{5.33}$$

for the triplet T_0 and

$$u' = -\frac{\eta_1 + \eta_2 + \eta_3}{\sqrt{12\, S_0 P^2}}, \quad v' = -\frac{\eta_1 + \eta_2 - 2 \cdot \eta_3}{\sqrt{24\, S_0 P^2}}, \quad w' = \frac{\eta_1 - \eta_2}{\sqrt{8\, S_0 P^2}}, \tag{5.34}$$

for the triplet T_1. Note, that the triplets contain only angular variables and none of the Mandelstam variables.

With the definitions in Eqs. (5.29) to (5.31), we can express the momentum dependencies of the dressing functions in Eq. (5.5) in terms of the S_4 multiplet variables

$$f_j\big(\Omega;\, P^2\big) \to f_j\big(S_0,\, D,\, T_0,\, T_1;\, P^2\big). \tag{5.35}$$

This grouping into elements of the S_4 permutation group firstly renders the momentum dependence of the dressing functions more overseeable and secondly provides us with

[3] The variable names for the angular quantities are chosen to match the definitions in [77].

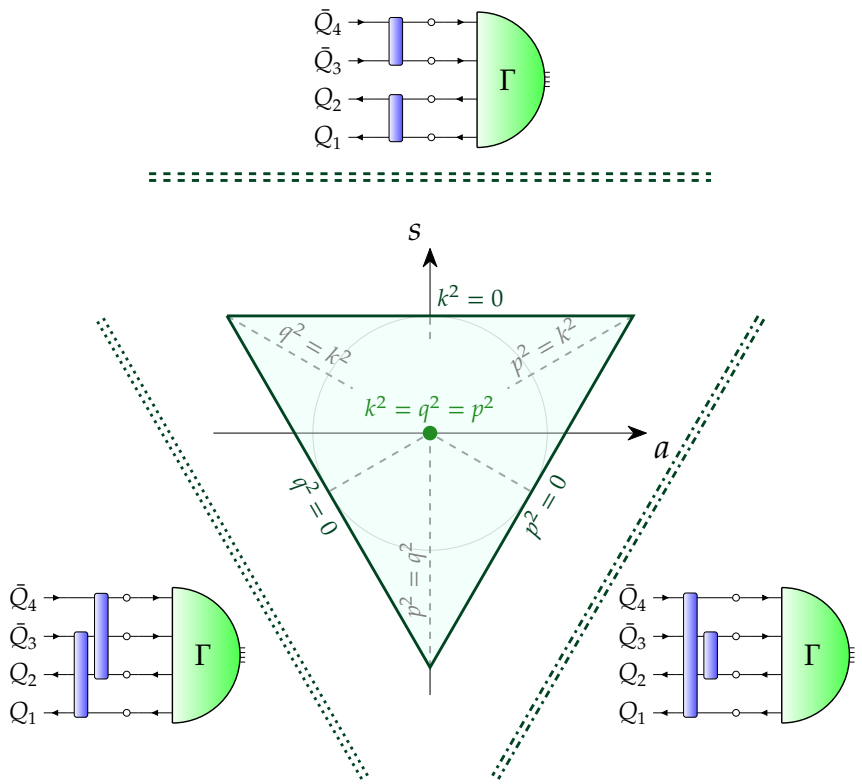

Figure 5.2: Graphical depiction of the doublet phase space with the two-body pole structures depicted as two lines parallel to the border of the triangle. The interior of the triangle is the spacelike domain of the Mandelstam variables while the exterior denotes the timelike domain. The point in the middle of the triangle is called the central limit. The dotted, dash-dotted and dashed lines represent the singularity structures coming from the $\mathcal{M}_1$, $\mathcal{M}_2$ and $\mathcal{D}$ interaction topology respectively. We also depict the respective Feynman diagrams alongside the corresponding pole structure.

a systematic way to determine how much the inclusion of certain groups of variables – now given in terms of the doublet and the triplets – affects the result of the four-quark FYE, i.e., the mass. The dressing functions always need to depend on the singlet S_0, as it carries the momentum scale dependence. The doublet and triplets on the other hand, can be individually 'switched off' during the solution of the BSE. Comparing the solutions for the mass of the all-light four-quark state ($f_0(500)$), it was found that while the inclusion of the doublet significantly alters the resulting mass, the effect of including the two triplets is comparably tiny [66, 77]. Neglecting the triplet variables in the momentum dependencies of the dressing functions is therefore a good approximation for the $f_0(500)$, and we therefore assume that this holds also everywhere else. Why this assumption is reasonable will be discussed in the following.

Since the mass of the four-quark state is significantly altered by including the doublet variable, it seems that the doublet phase space carries the relevant momentum dependence. To reuse the case of the all-light four-quark state investigated in [66]: solving the

four-quark BSE with only the S_0 dependence of the dressing functions yields a mass of around $M \approx 1.5\,\text{GeV}$, effectively four times the constituent quark mass for u/d quarks. Including also the doublet variable, this mass reduces to about $M \approx 400\,\text{MeV}$, which is in the correct ballpark for the σ meson. Evidently, something important happens in the doublet phase space during the solution process, i.e., the iteration, of the four-quark BSE. What happens is the following: without knowing anything about mesons and diquarks beforehand, the four-quark BSE in Fig. 5.1 (neglecting the three- and four-body diagrams in the second line) upon iteration dynamically generates two-body $Q_i\bar{Q}_j$ ($i = 1, 2$, $j = 3, 4$) and $Q_1Q_2/\bar{Q}_3\bar{Q}_4$ scattering matrices, which each feature a respective meson or (anti)diquark singularity structure. These two-body poles appear in the timelike region of the Mandelstam variables k^2, q^2 and p^2. To illustrate this, we can visualize the doublet phase space, i.e., the Mandelstam plane spanned by a and s, as the interior of an upside-down triangle which is bounded by lines where $k^2 = 0$, $q^2 = 0$ and $p^2 = 0$, see Fig. 5.2. At the corners of the triangle as well as along the grey dashed lines the Mandelstam variables have to fulfil the conditions $k^2 = q^2$, $k^2 = p^2$ or $q^2 = p^2$. In the centre of the triangle, all three relative momenta are equal. This point is called the *central limit* (CL) and will become important later on. The interior of the triangle is the spacelike domain of the Mandelstam variables and the exterior represents the timelike domain. The emergent two-body pole structures in the timelike domain of the Mandelstam variables are depicted as the dotted, dash-dotted and dashed lines parallel to the edges of the triangle. Alongside them we show the respective interaction topology responsible for the emergence of this particular two-body singularity. The dotted lines parallel to the $q^2 = 0$ border represent the meson-meson pole coming from the $\mathcal{M}_1$ interaction topology, the dash-dotted lines parallel to the $p^2 = 0$ border are the meson-meson pole emerging from the $\mathcal{M}_2$ topology and the dashed lines parallel to the $k^2 = 0$ border are the diquark-antidiquark singularity in the $\mathcal{D}$ interaction topology. In [66] it was further argued, that the closer these pole structures are to the boundary of the Mandelstam triangle, the more they affect the result of the equation. E.g., in the case of the σ meson, the $\pi - \pi$ poles in the two meson-meson topologies are very close to the boundary compared to the light-light scalar diquark-antidiquark poles. Hence, the σ can be described solely as a $\pi - \pi$ resonance with subleading effects coming from the diquark-antidiquark components [66, 77]. The pole structures can also enter the interior of the triangle, i.e., the integration domain. In this case, the four-quark becomes a resonance as the two-body poles introduce a physical (decay) threshold into the system.

This dynamic generation of the internal two-body singularities is numerically a very expensive endeavour. To reduce the computational effort, one can pull out the dependence on the doublet D from the dressing functions and put in the emerging pole structures by hand, since they will anyway be generated during the solution process, see [66, 67, 189]. Thus, the dressing function only depends on the singlet S_0

$$f_j\big(S_0, D\big) \to f_j\big(S_0\big) \cdot P_a^j \cdot P_{a'}^j \,. \tag{5.36}$$

The two two-body pole structures put in by hand are given as

$$P_a^j \cdot P_{a'}^j = \frac{1}{\left(p_a^+\right)^2 + m_a^2} \cdot \frac{1}{\left(p_{a'}^+\right)^2 + m_{a'}^2}, \tag{5.37}$$

with $a = (13), (14), (12)$ and the corresponding $a' = (24), (23), (34)$ denoting the pairs of indices associated with the respective topology. The mass terms m_a and $m_{a'}$ denote the respective on-shell two-body masses. As an approximation, we assume that the pole structure in Eq. (5.37) captures the relevant momentum dependence of the dressing functions on the doublet phase space and furthermore considers the four-body FYE in the central limit. The central limit is defined in [184] as the point where all three Mandelstam variables have the same absolute value and are orthogonal to each other. Hence, the momenta in Eq. (5.28) can be written as

$$\{q^\mu, p^\mu, k^\mu\} = \frac{2 \cdot S_0}{\sqrt{3}} \{e_1^\mu, e_2^\mu, e_3^\mu\}, \qquad P^\mu = iM \cdot e_4^\mu, \tag{5.38}$$

where e_i^μ denote the standard $\mathbb{R}^4$ unit vectors. Because they are all orthogonal to each other and also orthogonal to P^μ from Eq. (5.28), all scalar products vanish except for the Mandelstam variables which take the values $k^2 = q^2 = p^2 = \frac{4S_0}{3}$. This will significantly reduce computation time.

Physical BSA

In principle, we are now ready to solve the four-quark FYE for given quantum numbers $I(J^{P(C)})$ and quark content $Q_1Q_2\bar{Q}_3\bar{Q}_4$. One takes the 16 or 48 s-wave tensors, depending on whether $J = 0$ or $J = 1$, in one of the interaction topologies given in Eqs. (5.10) to (5.12) – preferably the one best suited for the given quantum numbers – makes the pole ansatz for the dressing functions in Eq. (5.36) to form the Dirac part and combines that with the respective colour and flavour tensors such that the resulting BSA either fulfils charge conjugation of Pauli symmetry. When solving the four-quark BSE in this way, one obtains 16 or 48 dressing functions for the chosen interaction topology and since the tensors form a Fierz complete set, the dressing functions in the other topologies can be obtained by Fierz transformations. For more details, see appendix of [78].

However, for this work we choose to use an ansatz for the BSA which is inspired by the actual decay channels measured in experiment or the supposed decay channels for states which have not been measured yet. We call this ansatz the *'physical' BSA*, which was first introduced in [67, 78]. The idea behind it is the following: First, we choose the state we want to investigate and look at the quantum numbers and the supposed quark content of the state. Based on this, we determine all possible internal meson-meson or diquark-antidiqurk pairs, for which the combination of the respective quantum numbers results in the quantum numbers of the four-quark state. As an example, take the $\chi_{c1}(3872)$ $(cn\bar{n}\bar{c})$ with quantum numbers $0(1^{++})$. The quantum numbers of this four-quark state can be build by combining

d	$J^P = 0^+$	$J^P = 1^+$
$\mathcal{M}_1$	$\phi_1 = \gamma^5_{\alpha_1\alpha_3}\gamma^5_{\alpha_2\alpha_4}$	$\psi_1^\pm = \left(\gamma^5_{\alpha_1\alpha_3}(\gamma_\perp^\mu)_{\alpha_2\alpha_4} \pm (\gamma_\perp^\mu)_{\alpha_1\alpha_3}\gamma^5_{\alpha_2\alpha_4}\right)$
$\mathcal{M}_2$	$\phi_2 = \gamma^5_{\alpha_1\alpha_4}\gamma^5_{\alpha_2\alpha_3}$	$\psi_2^\pm = \left(\gamma^5_{\alpha_1\alpha_4}(\gamma_\perp^\mu)_{\alpha_2\alpha_3} \pm (\gamma_\perp^\mu)_{\alpha_1\alpha_4}\gamma^5_{\alpha_2\alpha_3}\right)$
$\mathcal{M}_1$	$\phi_3 = (\gamma_\perp^\mu)_{\alpha_1\alpha_3}(\gamma_\mu^\perp)_{\alpha_2\alpha_4}$	$\psi_3 = \varepsilon^{\mu\nu\rho\sigma}\hat{P}_\nu(\gamma_\rho)_{\alpha_1\alpha_3}(\gamma_\sigma)_{\alpha_2\alpha_4}$
$\mathcal{M}_2$	$\phi_4 = (\gamma_\perp^\mu)_{\alpha_1\alpha_4}(\gamma_\mu^\perp)_{\alpha_2\alpha_3}$	$\psi_4 = \varepsilon^{\mu\nu\rho\sigma}\hat{P}_\nu(\gamma_\rho)_{\alpha_1\alpha_4}(\gamma_\sigma)_{\alpha_2\alpha_3}$
$\mathcal{D}$	$\phi_5 = (\gamma^5 C)_{\alpha_1\alpha_2}(C^T\gamma^5)_{\alpha_3\alpha_4}$	$\psi_5 = (\gamma^5 C)_{\alpha_1\alpha_2}(C^T\gamma_\perp^\mu)_{\alpha_3\alpha_4}$
$\mathcal{D}$	$\phi_6 = (\gamma_\perp^\mu C)_{\alpha_1\alpha_2}(C^T\gamma_\mu^\perp)_{\alpha_3\alpha_4}$	$\psi_6 = (\gamma_\perp^\mu C)_{\alpha_1\alpha_2}(C^T\gamma^5)_{\alpha_3\alpha_4}$
$\mathcal{D}$	–	$\psi_7 = \varepsilon^{\mu\nu\rho\sigma}\hat{P}_\nu(\gamma_\rho^\perp C)_{\alpha_1\alpha_2}(C^T\gamma_\sigma^\perp)_{\alpha_3\alpha_4}$

Table 5.2: Collection of the relevant Dirac basis elements for quantum numbers $J^P = 0^+, 1^+$. The associated interaction topology of indicated in the column d. With the transversalized gamma matrices $\gamma_\perp^\mu = T^{\mu\nu}(P)\gamma_\nu$ and $\hat{P}$ denoting the normalized total hadron momentum.

- a D meson $(c\bar{n})$ with $\frac{1}{2}(0^-)$ and a $\bar{D}^*$ meson $(n\bar{c})$ with $\frac{1}{2}(1^-)$,
- a J/ψ meson $(c\bar{c})$ and an ω meson[4] $(n\bar{n})$, both of which have $0(1^{--})$,
- a scalar diquark S_{cn} with 0^+ and an axialvector antidiquark $A_{\bar{n}\bar{c}}$ with 1^+, which also results in the overall quantum numbers of the four-quark state.

The first combination $(D\bar{D}^*)$ is the pole structure in the $\mathcal{M}_1$ topology, the $J/\psi\omega$ combination corresponds to the pole structure in the $\mathcal{M}_2$ topology and the $S_{cn}A_{\bar{n}\bar{c}}$ combination is the pole structure in the $\mathcal{D}$ topology. After constructing all possible internal meson-meson or diquark-antidiquark combinations. The PDG [20] states dominant s-wave decay channels, based on which we decide which of the internal structures we take into account. For states which have not been measured, we have to assume that the s-wave combination of two-body particles which are lowest in mass is the dominant 'decay' channel – unless certain combinations can be ruled out due to physical reasons. Note, that with our choice to consider only the s-wave Dirac basis elements we restrict ourselves to the s-wave decays. Considering the present case of the $\chi_{c1}(3872)$, the two meson-meson decays given above are the dominant ones in the PDG and we can therefore take them into account for the physical BSA. A list of the possible internal two-body pairings for a lot of the heavy-light four-quark states also considered in this thesis is given in the Appendix of [74] and in Section 5.2.

To construct the physical BSA, we form a linear combination of all the dominant and allowed pole structures in the different topologies, i.e., we write the BSA as

$$\Gamma^{(\mu)}_{\text{physical}} = \Gamma^{(\mu)}_{\mathcal{M}_1} + \Gamma^{(\mu)}_{\mathcal{M}_2} + \Gamma^{(\mu)}_{\mathcal{D}}\,, \tag{5.39}$$

where we have omitted the momenta for brevity. For the Dirac part of the sub-BSAs $\Gamma^{(\mu)}_d$, with $d \in \{\mathcal{M}_1, \mathcal{M}_2, \mathcal{D}\}$, we then only consider a sub-set of the original s-wave Dirac

[4] In lack of a measured light 0^{--} meson

elements for four-quark states with $J^P = 0^+$ and $J^P = 1^+$, which are collected in Table 5.2. We have chosen to display the basis elements with their explicit Dirac indices rather than as a direct product to better illustrate which quark combinations are involved for the different interaction topologies.[5] The individual tensors making up ϕ_j and ψ_j correspond to the leading tensor structure for pseudoscalar and vector mesons, see Eqs. (4.33) and (4.37). To keep the main text sort of concise, we have relegated the explicit considerations regarding the transformation properties of the tensors in Table 5.2 under charge conjugation and Pauli (anti)symmetry to Appendices C.1.2 and C.1.3. The respective transformation properties are summarized in Tables B.2 and B.6 and the appendix of [74].[6] Here, we also want to investigate hidden-flavour four-quark states with quantum numbers $J^{PC} = 0^{-+}$ and 1^{--}. For this, we need to construct the leading order tensor structures for $J^P = 0^-$ and $J^P = 1^-$, which has been done in Appendix B.2 with the resulting tensors compiled in Table B.3. The transformations under charge conjugation and Pauli (anti)symmetry of these tensors are also given in Appendices C.1.2 and C.1.3 and a compiled overview can be found in Tables B.4 and B.6.

We can write the physical BSA as

$$\Gamma^{(\mu)}_{\text{phys.}}(k,q,p,P) \approx \sum_{d\in\{\mathcal{M}_1,\mathcal{M}_2,\mathcal{D}\}} f_d(S_0)\cdot P^d_a \cdot P^d_{a'} \cdot \tau^{(\mu)}_{\text{D};d}(k,q,p,P)\otimes \tau^{\text{C}}_d \otimes \tau^{\text{F}}_d\,, \tag{5.40}$$

with $a = (13), (14), (12)$ and $a' = (24), (23), (34)$ as before. The $\tau^{(\mu)}_{\text{D};d}$ denotes the Dirac part of the BSA for a given topology d. As is evident from Tables B.2, B.4 and B.6, not all Dirac tensors in Tables 5.2 and B.3 have a definite charge conjugation or Pauli (anti)symmetry. This means, they do not necessarily transform into themselves upon the symmetry transformations in question. Therefore, the $\tau^{(\mu)}_{\text{D};d}$ represent either tensors or linear combinations of the tensors in Tables 5.2 and B.3 which have a definite symmetry under either C-parity or Pauli (anti)symmetry, depending on whether the state is hidden- or open-flavour. The $\tau^{(\mu)}_{\text{D};d}$ are explicitly given in Section 5.2. Because our physical BSA is a linear combination of the three interaction topologies, we can pair each Dirac tensor with the attractive and repulsive colour tensor τ^{C}_d in the respective topology , i.e., the colour singlet structures given in Eqs. (5.18) and (5.19). The flavour part τ^{F}_d is effectively only there to impose a condition on how the combined Dirac-colour tensor needs to transform under charge conjugation or Pauli symmetry such that the full BSA has the correct transformation properties. Once the full physical BSA is constructed the τ^{F}_d can be pulled out of the sum, as it traces out in the calculation.

For the physical BSAs used in this work, we chose *one internal two-body cluster per interaction topology* $\mathcal{M}_1$, $\mathcal{M}_2$ and $\mathcal{D}$ and separately pair it with the corresponding attractive and repulsive colour singlet structures to investigate the effect coming from the individual contributions. As an aside, for hidden-flavour four-quark states the different topologies will be referred to as (heavy-light) meson-meson for the $\mathcal{M}_1$, hadro-quarkonium for the $\mathcal{M}_2$ and (heavy-light) diquark-antidiquark for the $\mathcal{D}$ topology. The quarkonium part in the

[5] In the direct product notation, the tensors are of the form: $\phi_1 = \gamma^5\otimes\gamma^5$, $\psi^\pm_1 = \left(\gamma^5\otimes\gamma^\mu_\perp \pm \gamma^\mu_\perp\otimes\gamma^5\right)$ etc.

[6] Note, that in [74] they use a combination of Dirac-colour tensors while in Tables B.2 and B.6 we consider only the Dirac tensors.

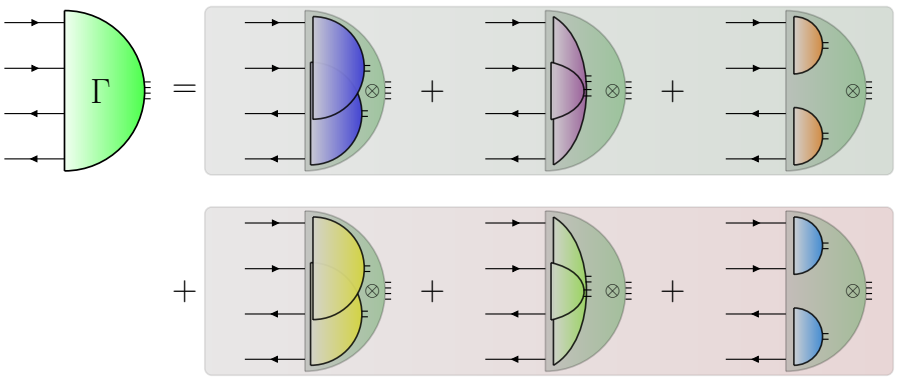

Figure 5.3: Graphical depiction of the physical BSA in terms of Feynman diagrams. The green half-circle represents the physical BSA and the internal half-circles are the different physical components. The dark blue/yellow, violet/green and orange/light blue sub-clusters represent the $\mathcal{M}_1$ $((13)(24))$, $\mathcal{M}_2$ $((14)(23))$ and $\mathcal{D}$ $((12)(34))$ configurations. The diagrams with the green background represent the configurations with attractive colour singlets and the ones with the red background the corresponding repulsive colour forces.

hadro-quarkonium will change to charmonium or bottomonium, depending on whether $Q\bar{Q} = c\bar{c}$ or $Q\bar{Q} = b\bar{b}$. For the open-flavour four-quark states, we have two (heavy-light) meson-meson topologies $\mathcal{M}_1$ and $\mathcal{M}_2$ and a (heavy-heavy)(light-light) diquark-antidiquark topology $\mathcal{D}$.

In total, the physical BSA we use contains six elements, i.e.,

$$\Gamma^{(\mu)}_{\text{phys.}}(k,q,p,P) = \sum_{j=0}^{5} f_j(S_0) \cdot P^j_a \cdot P^j_{a'} \cdot \tau^{(\mu)}_{\text{D};j}(k,q,p,P) \otimes \tau^{\text{C}}_j \otimes \tau^{\text{F}}_j \,, \tag{5.41}$$

with a, a' same as above. The dressing functions f_j are associated with the different physical components taken into account for the four-quark state in question. We have compiled the list of the chosen physical components used for the hidden- and open-flavour four-quark states investigated in this work in Tables 5.3 and 5.4. How these components are chosen and how the explicit Dirac basis elements are constructed is relegated to Appendix B.2; see also the supplemental material of [74] and Appendix A of [189] and [190]. The consideration of the attractive as well as the repulsive colour forces for heavy-flavour four-quark states is an extension of previous work where only the attractive colour singlets were taken into account, see [67, 74, 79]. Graphically, the physical BSA used in this work can generically be represented as shown in Fig. 5.3. On the left-hand side, we have the physical BSA, represented as the green half-circle. On the right-hand side we show the different internal clustering of the quarks. The half-circles connecting quarks $(13)(24)$ (dark blue and yellow) represent the physical components in the $\mathcal{M}_1$ topology, the ones connecting $(14)(23)$ (violet and green) represent the $\mathcal{M}_2$ sub-clusters and the ones connecting $(12)(34)$ (orange and light blue) are the $\mathcal{D}$ components. As stated above, each of the combinations appears twice in Fig. 5.3: the diagrams highlighted in green come with the attractive colour singlets $\tau^{\text{C}}_0 = C_{\mathbf{11}}$ (dark blue), $\tau^{\text{C}}_1 = C'_{\mathbf{11}}$ (violet), $\tau^{\text{C}}_2 = C_{\bar{\mathbf{3}}\mathbf{3}}$ (orange) and the diagrams

highlighted in red feature the corresponding repulsive colour singlets $\tau_3^{\mathrm{C}} = C_{\mathbf{88}}$ (yellow), $\tau_4^{\mathrm{C}} = C'_{\mathbf{88}}$ (green), $\tau_5^{\mathrm{C}} = C_{\mathbf{6\bar{6}}}$ (light blue). The graphical representation in Fig. 5.3 is not to be confused with the two-body interactions in the two-body approach to four-quark states described in [75, 79, 164]. In our case, the internal half-circles represent quark pairings and not full two-body BSAs, as is the case in the aforementioned works.

Numerical Solution

The physical BSA given in Eq. (5.41) is the final form we use in the work. We therefore insert $\Gamma^{(\mu)}_{\mathrm{phys.}}$ into the four-body FYE in Eq. (5.1) to get

$$\Gamma^{(\mu)}_{\mathrm{phys.}} = K^{(4)} G_0^{(4)} \Gamma^{(\mu)}_{\mathrm{phys.}}\,, \tag{5.42}$$

with the kernel $K^{(4)}G_0^{(4)}$ given in Eq. (5.3). As was the case for the two-body BSE, the quantities we want to obtain are the dressing functions at the physical point, as they contain all the non-trivial information about the hadron in question. Therefore, they need to be projected out of the sum in Eq. (5.41) by constructing appropriate projectors in the Dirac, colour and flavour space such that the condition given in Eq. (4.49) holds.

The most straightforward to construct is the flavour projector, which is just the flavour BSA transposed, i.e., $\mathbb{P}^{\mathrm{F}} = \Gamma^T_{\mathrm{F}}$. Similarly to the two-body case, the flavour part traces to one on the right-hand side of Eq. (5.42), as the MT is flavour blind. The colour projectors are also straightforward to obtain. For a colour tensor τ_j^{C} associated with a dressing function f_j, the projector is just that colour tensor transposed $\mathbb{P}_j^{\mathrm{C}} = \left(\tau_j^{\mathrm{C}}\right)^T$. On the right-hand side of Eq. (5.42) we will have traces of the form $\mathrm{tr}\left\{\mathbb{P}_j^{\mathrm{C}} t_a t^a \Gamma_{\mathrm{C}}\right\}$, with t_a denoting the generator of $\mathrm{SU}(N_c)$. The explicit form of the traces in the different topologies is discussed in Appendix B.1.1. Last but not least, we need to consider the Dirac part. Because our chosen Dirac tensors do not constitute a full Fierz complete basis, our projectors $\mathbb{P}^{\mathrm{D};i}_{(\mu)}$, corresponding to a dressing function f_i, will be of the form

$$\mathbb{P}^{\mathrm{D};i}_{(\mu)} = \sum_{j=0}^{N_\Xi - 1} \kappa_{ij} \cdot \left(\chi^{\mathrm{D};j}_{(\mu)}\right)^T, \tag{5.43}$$

where $\chi^{\mathrm{D};j}_{(\mu)}$ are the N_Ξ individual Dirac tensors appearing in the sets $\Xi_{\mathrm{D};I\left(J^{P(\mathrm{C})}\right)}$ in Appendix B.2 for a given four-quark state. The scalar coefficients κ_{ij} are determined via

$$\kappa^{-1}_{ij} = \mathrm{tr}\left\{\left(\chi^{\mathrm{D};i}_{(\mu)}\right)^T \cdot \chi^{(\mu)}_{\mathrm{D};j}\right\}. \tag{5.44}$$

This then yields a set $\mathrm{P}_{N_\Xi} = \left\{\mathbb{P}^{\mathrm{D};i}_{(\mu)}\right\}_{i=0}^{N_\Xi - 1}$ of N_Ξ projectors fulfilling

$$\left\{\mathbb{P}^{\mathrm{D};i}_{(\mu)} \cdot \chi^{(\mu)}_{\mathrm{D};j}\right\} = \delta^{ij}. \tag{5.45}$$

We then only need to choose the projectors projecting out the desired Dirac basis elements

for a given four-quark state. Consider, for example, the $\Xi_{\mathrm{D};0(1^{++})}$ basis. The Dirac basis tensors appearing here are ψ_1^-, ψ_4, $\psi_5 - \psi_6$. Note, that tensors featuring a linear combination of tensors, i.e., $\psi_1^- = \psi_{1_1} - \psi_{1_2}$ and $\psi_5 - \psi_6$, have a certain symmetry to them which means that it is sufficient to project out only one of the individual elements from the linear combination. Therefore, we have $N_\Xi = 5$ Dirac elements $\chi^{\mathrm{D};j}_{(\mu)}$ from the set $\mathrm{X}_5 = \{\psi_{1_1}, \psi_{1_2}, \psi_4, \psi_5, \psi_6\}$. As a result, we get the set of P_5 projectors, projecting onto each element in the set X_5. From the set P_5, we then choose the projectors $\mathbb{P}^{\mathrm{D};0}_{(\mu)}$, $\mathbb{P}^{\mathrm{D};2}_{(\mu)}$ and $\mathbb{P}^{\mathrm{D};3}_{(\mu)}$, projecting on ψ_{1_1}, ψ_4 and ψ_5 respectively, as our Dirac projectors for the $I(J^{PC}) = 0(1^{++})$ channel. Finally, since we only want the dressing function without the associated poles, one can attach the inverse poles to the Dirac projector. To then get the full projector for a dressing function f_j, we combine the chosen Dirac projectors with the inverse poles and the colour projectors associated with the desired dressing function. For the present case, we get the projectors:

$$\mathbb{P}^0_{(\mu)} = \mathbb{P}^{\mathrm{D};0}_{(\mu)} \cdot \left(P^0_{(13)} \cdot P^0_{(24)}\right)^{-1} \cdot C_{\mathbf{11}}\,, \qquad \mathbb{P}^3_{(\mu)} = \mathbb{P}^{\mathrm{D};0}_{(\mu)} \cdot \left(P^0_{(13)} \cdot P^0_{(24)}\right)^{-1} \cdot C_{\mathbf{88}}\,, \tag{5.46}$$

$$\mathbb{P}^1_{(\mu)} = \mathbb{P}^{\mathrm{D};1}_{(\mu)} \cdot \left(P^1_{(14)} \cdot P^1_{(23)}\right)^{-1} \cdot C'_{\mathbf{11}}\,, \qquad \mathbb{P}^4_{(\mu)} = \mathbb{P}^{\mathrm{D};1}_{(\mu)} \cdot \left(P^1_{(14)} \cdot P^1_{(23)}\right)^{-1} \cdot C'_{\mathbf{88}}\,, \tag{5.47}$$

$$\mathbb{P}^2_{(\mu)} = \mathbb{P}^{\mathrm{D};2}_{(\mu)} \cdot \left(P^2_{(12)} \cdot P^2_{(34)}\right)^{-1} \cdot C_{\bar{\mathbf{3}}\mathbf{3}}\,, \qquad \mathbb{P}^5_{(\mu)} = \mathbb{P}^{\mathrm{D};2}_{(\mu)} \cdot \left(P^2_{(12)} \cdot P^2_{(34)}\right)^{-1} \cdot C_{\mathbf{6}\bar{\mathbf{6}}}\,. \tag{5.48}$$

From the tables Tables 5.3 and 5.4 it is clear, that the Dirac basis elements for the attractive and repulsive internal physical components are mostly the same, especially for the meson-meson components. While the Dirac projectors are constructed such that they project out only a specific sub-cluster, they would project out both the attractive and repulsive component. This is where the mutual orthogonality in Eq. (5.21) comes in, which cancels either the attractive or the repulsive component, depending on which dressing function is projected out.

Thresholds

At the end of the discussion about the phase space of the four-body equation, we mentioned that the two-body poles in the different topologies introduce physical thresholds into the system. In the context of the two-body equations in Section 4.3, we have already encountered singularity structures which introduce thresholds into the system in the form of the quark poles. To remedy this, we used a quark momentum partitioning parameter to optimally distribute the total hadron momentum P^μ amongst the two quarks, such that the quark poles are just outside the respective integration domain, cf. Fig. 4.7. For the same reason, we also use four quark partitioning parameters $\sigma_{1,2,3,4}$ in the momenta of the four-body FYE in Eq. (5.27). Recall from Section 4.2 that the result cannot depend on the choice of the partitioning parameter. This argument is also valid here, i.e., our results are independent of the choices for the σ_i's. Without considering the two-body poles, the σ_i's can be calculated in a similar fashion as done in the two-body case, i.e., Eq. (4.26) for

the four-body equation becomes

$$\sigma_i = \frac{M_{A_i}}{\sum_{j=1}^{4} M_{A_j}} \,. \tag{5.49}$$

The M_{A_i} are the maximal apices of the parabola of the quark momenta in the complex plane, which are compiled in Table 4.1. With this, the maximal mass $P_{\max} = iM_{\max}$ that can be calculated without the quark poles affecting the equation is $M_{\max} = \sum_{j=1}^{4} M_{A_j}$.

For the four-body FYE, we additionally have the singularity structures coming from the internal two-body poles in Eq. (5.37) to worry about, which we will do in the following. As stated above, these poles obstruct the direct calculation (without using path deformation), when they enter the integration domain. To see when this is the case, we write out the denominators explicitly as

$$\begin{aligned} \mathrm{den}\left(P_a^j\right) &= x^2 \pm \sigma_a^+ \, x \cdot P + (\sigma_a^+)^2 P^2 + m_a^2 \,, \\ \mathrm{den}\left(P_{a'}^j\right) &= x^2 \mp \sigma_{a'}^+ \, x \cdot P + (\sigma_{a'}^+)^2 P^2 + m_{a'}^2 \,, \end{aligned} \tag{5.50}$$

with x denoting one of the relative momenta. As long as the conditions

$$(\sigma_a^+)^2 P^2 + m_a^2 > 0 \,, \qquad (\sigma_{a'}^+)^2 P^2 + m_{a'}^2 > 0 \,, \tag{5.51}$$

are fulfilled, the poles are outside the triangle and thus outside the integration domain. From this, one can formulate conditions for σ_a^+ and $\sigma_{a'}^+$ to maximize the range of P^μ for which the equation can be solved without hitting pole structures. Because of $\sum_{i=1}^{4} \sigma_i = 1$, it is sufficient to formulate a condition for either σ_a^+ or $\sigma_{a'}^+$ as the other one follows straightforwardly. The maximal mass $P_{\max} = iM_{\max}$ which can be reached for a specific interaction topology, is the sum of the two-body masses $M_{\max} = m_a + m_{a'}$. Thus, the conditions for σ_a^+ or $\sigma_{a'}^+$, which maximize the range of P^μ for a given topology, read

$$\sigma_a^+ = \frac{m_a}{m_a + m_{a'}} \,, \qquad \sigma_{a'}^+ = \frac{m_{a'}}{m_a + m_{a'}} \,. \tag{5.52}$$

These are the *two-body momentum partitioning parameters* (*TBMPP*), which distribute the total momentum P^μ amongst the two constituents in the internal two-body clusters according to the masses of the two-body particles. Each of the interaction topologies has one TBMPP associated with it, which we call η for the $\mathcal{M}_1$, ζ for the $\mathcal{M}_2$ and χ for the $\mathcal{D}$ topology. Using the definition in Eq. (5.52), these parameters are defined as

$$\eta = \frac{m_{13}}{m_{13} + m_{24}} \,, \qquad \zeta = \frac{m_{14}}{m_{14} + m_{23}} \,, \qquad \chi = \frac{m_{12}}{m_{12} + m_{34}} \,. \tag{5.53}$$

For the case of the $\chi_{c1}(3872)$ we considered earlier, the two-body masses for the subclusters are $m_{13} = m_D$, $m_{24} = m_{\bar{D}^*}$ for $\mathcal{M}_1$; $m_{14} = m_{J/\psi}$, $m_{23} = m_\omega$ for $\mathcal{M}_2$; $m_{12} = m_{S_{cn}}$, $m_{34} = m_{A_{n\bar{c}}}$ for $\mathcal{D}$.

One can now compare the maximal masses $M_{\max}$, the ones coming from the quark sin-

gularities and the ones from the two two-body poles, and check which of these singularity structures affects the equation first. In almost all cases, one of the two-body pole structures will enter the integration domain way before any of the quark singularities do. Considering the case of the $\chi_{c1}(3872)$ again, the $M_{\max}$ coming from the quark and two-body poles are:

$$\begin{aligned} M_{\max}^{\text{quark}} &= \sum_{i=1}^{4} M_{A_i} = 4.48\,\text{GeV}\,, \qquad M_{\max}^{\mathcal{M}_1} = m_D + m_{\bar{D}^*} = 3.87\,\text{GeV}\,, \\ M_{\max}^{\mathcal{M}_2} &= m_{J/\psi} + m_{\omega} = 3.73\,\text{GeV}\,, \quad M_{\max}^{\mathcal{D}} = m_{S_{cn}} + m_{A_{\bar{n}\bar{c}}} = 4.86\,\text{GeV}\,, \end{aligned} \tag{5.54}$$

where we have used our calculated two-body masses in Table 4.2. Clearly, the $J/\psi\omega$ pole structure is the first to enter the integration domain, followed by the $D\bar{D}^*$ pole and only then the quark poles start to affect the equation. For this reason, it makes sense to first determine the two-body momentum partitioning parameters η, ζ and χ as shown in Eq. (5.53), to optimally split the hadron momentum P^μ amongst the constituents of the two-body clusters. After that, one uses the following relations

$$\begin{aligned} \sigma_1 &= \frac{\eta + \zeta + \chi - 1}{2}\,, \qquad \sigma_2 = \frac{-\eta - \zeta + \chi + 1}{2}\,, \\ \sigma_3 &= \frac{\eta - \zeta - \chi + 1}{2}\,, \qquad \sigma_4 = \frac{-\eta + \zeta - \chi + 1}{2}\,, \end{aligned} \tag{5.55}$$

relating the σ_i's to the two-body momentum partitioning parameters to optimally distribute the fractions of the hadron momentum P^μ amongst the quarks of the two-body particles. Determining the parameters in this order maximizes the range of P^μ, for which we can solve the four-body FYE, without any singularity structures interfering with the calculation.

$I(J^{PC})$	$Q_1Q_2\bar{Q}_3\bar{Q}_4$	Physical components					
		$\mathbf{1}\otimes\mathbf{1}$		$\mathbf{1}\otimes\mathbf{1}$	$\mathbf{8}\otimes\mathbf{8}$		$\mathbf{8}\otimes\mathbf{8}$
		f_0	f_1	f_2	f_3	f_4	f_5
$0(0^{-+})$	$bn\bar{n}\bar{b}$	$\bar{B}^*B_1$	$\chi_{b0}\eta$	$\eta_b\tilde{f}_0$	$\bar{B}^*B_1$	$\chi_{b0}\eta$	$\eta_b\tilde{f}_0$
	$cn\bar{n}\bar{c}$	$D^*\bar{D}_1$	$\chi_{c0}\eta$	$\eta_c\tilde{f}_0$	$D^*\bar{D}_1$	$\chi_{c0}\eta$	$\eta_c\tilde{f}_0$
$0(1^{--})$	$bn\bar{n}\bar{b}$	$\bar{B}B_1$	$\chi_{b0}\omega$	$\Upsilon\tilde{f}_0$	$\bar{B}B_1$	$\chi_{b0}\omega$	$\Upsilon\tilde{f}_0$
	$cn\bar{n}\bar{c}$	$D\bar{D}_1$	$\chi_{c0}\omega$	$J/\psi\tilde{f}_0$	$D\bar{D}_1$	$\chi_{c0}\omega$	$J/\psi\tilde{f}_0$
		$\mathbf{1}\otimes\mathbf{1}$		$\bar{\mathbf{3}}\otimes\mathbf{3}$	$\mathbf{8}\otimes\mathbf{8}$		$\mathbf{6}\otimes\bar{\mathbf{6}}$
$0(0^{++})$	$bn\bar{n}\bar{b}$	$\bar{B}B$	$\Upsilon\omega$	$S_{bn}S_{\bar{n}\bar{b}}$	$\bar{B}B$	$\Upsilon\omega$	$S_{bn}S_{\bar{n}\bar{b}}$
	$cn\bar{n}\bar{c}$	$D\bar{D}$	$J/\psi\omega$	$S_{cn}S_{\bar{n}\bar{c}}$	$D\bar{D}$	$J/\psi\omega$	$S_{cn}S_{\bar{n}\bar{c}}$
$0(1^{++})$	$bn\bar{n}\bar{b}$	$\bar{B}B^*$	$\Upsilon\omega$	$S_{bn}A_{\bar{n}\bar{b}}$	$\bar{B}B^*$	$\Upsilon\omega$	$S_{bn}A_{\bar{n}\bar{b}}$
	$cn\bar{n}\bar{c}$	$D\bar{D}^*$	$J/\psi\omega$	$S_{cn}A_{\bar{n}\bar{c}}$	$D\bar{D}^*$	$J/\psi\omega$	$S_{cn}A_{\bar{n}\bar{c}}$
$1(1^{+-})$	$bn\bar{n}\bar{b}$	$\bar{B}B^*$	$\Upsilon\pi$	$S_{bn}A_{\bar{n}\bar{b}}$	$\bar{B}B^*$	$\Upsilon\pi$	$S_{bn}A_{\bar{n}\bar{b}}$
	$cn\bar{n}\bar{c}$	$D\bar{D}^*$	$J/\psi\pi$	$S_{cn}A_{\bar{n}\bar{c}}$	$D\bar{D}^*$	$J/\psi\pi$	$S_{cn}A_{\bar{n}\bar{c}}$

Table 5.3: Physical content of the hidden-flavour BS amplitude for quark and colour configurations investigated in this work, with $n \in \{u, d\}$. We only explicitly show the quark configurations involving the light $n\bar{n}$ quark pair. The $\tilde{f}_0$ here denotes the $f_0(1370)$. Scalar and axialvector diquarks are denoted by S and A respectively, with the subscript denoting the (anti)quark content of the diquark. We grouped the physical components according to their attractive and repulsive colour structure; f_0,f_1,f_2,f_3,f_4,f_5 correspond to the dressing functions for that particular component and colour channel. For reasons explained in Appendix B.2.2, we chose to neglect the diquark component for 0^{-+} and 1^{--} channels and instead considered a second $\mathcal{M}_2$ channel as f_2 and f_5. How these physical content is chosen is given in great detail in Appendix B.2 and [189].

$I(J^P)$	$Q_1Q_2\bar{Q}_3\bar{Q}_4$	Physical components					
		$\mathbf{1}\otimes\mathbf{1}$		$\bar{\mathbf{3}}\otimes\mathbf{3}$	$\mathbf{8}\otimes\mathbf{8}$		$\mathbf{6}\otimes\bar{\mathbf{6}}$
		f_0	f_1	f_2	f_3	f_4	f_5
$0(1^+)$	$bb\bar{n}\bar{n}$	$\bar{B}\bar{B}^*$	$\bar{B}^*\bar{B}^*$	$A_{bb}S_{\bar{n}\bar{n}}$	$\bar{B}\bar{B}^*$	$\bar{B}^*\bar{B}^*$	$S_{bb}A_{\bar{n}\bar{n}}$
	$bc\bar{n}\bar{n}$	$\bar{B}D^*$	$\bar{B}^*D$	$A_{bc}S_{\bar{n}\bar{n}}$	$\bar{B}D^*$	$\bar{B}^*D$	$S_{bc}A_{\bar{n}\bar{n}}$
	$cc\bar{n}\bar{n}$	DD^*	D^*D^*	$A_{cc}S_{\bar{n}\bar{n}}$	DD^*	D^*D^*	$S_{cc}A_{\bar{n}\bar{n}}$
	$bb\bar{s}\bar{s}$	$\bar{B}_s\bar{B}_s^*$	–	$A_{bb}A_{ss}$	$\bar{B}_s\bar{B}_s^*$	–	–
	$bc\bar{s}\bar{s}$	$\bar{B}_sD_s^*$	$\bar{B}_s^*D_s$	$S_{bc}A_{ss}$	$\bar{B}_sD_s^*$	$\bar{B}_s^*D_s^*$	$A_{bc}S_{ss}$
	$cc\bar{s}\bar{s}$	$D_sD_s^*$	–	$A_{cc}A_{ss}$	$D_sD_s^*$	–	–
$\frac{1}{2}(1^+)$	$bb\bar{n}\bar{s}$	$\bar{B}\bar{B}_s^*$	$\bar{B}_s\bar{B}^*$	$A_{bb}S_{\bar{n}\bar{s}}$	$\bar{B}\bar{B}_s^*$	$\bar{B}_s^*\bar{B}^*$	$S_{bb}A_{\bar{n}\bar{s}}$
$1(1^+)$	$bb\bar{q}\bar{q}$	$\bar{B}\bar{B}^*$	–	$A_{bb}A_{\bar{n}\bar{n}}$	$\bar{B}\bar{B}^*$	–	–
	$bc\bar{q}\bar{q}$	$\bar{B}D^*$	$\bar{B}^*D$	$S_{bc}A_{\bar{n}\bar{n}}$	$\bar{B}D^*$	$\bar{B}^*D^*$	$A_{bc}S_{\bar{n}\bar{n}}$
	$cc\bar{q}\bar{q}$	DD^*	–	$A_{cc}A_{\bar{n}\bar{n}}$	DD^*	–	–
$0(0^+)$	$bb\bar{s}\bar{s}$	$\bar{B}_s\bar{B}_s$	$\bar{B}_s^*\bar{B}_s^*$	$A_{bb}A_{\bar{s}\bar{s}}$	$\bar{B}_s\bar{B}_s$	$\bar{B}_s^*\bar{B}_s^*$	$S_{bb}S_{\bar{s}\bar{s}}$
	$bc\bar{s}\bar{s}$	$\bar{B}_sD_s$	$\bar{B}_s^*D_s^*$	$A_{bc}A_{ss}$	$\bar{B}_sD_s$	$\bar{B}_s^*D_s^*$	$S_{bc}S_{ss}$
	$cc\bar{s}\bar{s}$	D_sD_s	$D_s^*D_s^*$	$A_{cc}A_{\bar{s}\bar{s}}$	D_sD_s	$D_s^*D_s^*$	$S_{cc}S_{\bar{s}\bar{s}}$
$1(0^+)$	$bb\bar{n}\bar{n}$	$\bar{B}\bar{B}$	$\bar{B}^*\bar{B}^*$	$A_{bb}A_{\bar{n}\bar{n}}$	$\bar{B}\bar{B}$	$\bar{B}^*\bar{B}^*$	$S_{bb}S_{\bar{n}\bar{n}}$
	$bc\bar{n}\bar{n}$	$\bar{B}D$	$\bar{B}^*D^*$	$A_{bc}A_{\bar{n}\bar{n}}$	$\bar{B}D$	$\bar{B}^*D^*$	$S_{bc}S_{\bar{n}\bar{n}}$
	$cc\bar{n}\bar{n}$	DD	D^*D^*	$A_{cc}A_{\bar{n}\bar{n}}$	DD	D^*D^*	$S_{cc}S_{\bar{n}\bar{n}}$

Table 5.4: The physical content of the open-flavour Bethe-Salpeter amplitude for the quark and colour configurations examined in this work, with $n \in \{u, d\}$. States containing $\bar{c}\bar{c}$ are analogous to those with $\bar{s}\bar{s}$ and are thus not shown explicitly. Scalar and axial-vector diquarks are represented by S and A, respectively, with the subscript indicating the quark content of the diquark. The physical components are grouped based on their attractive and repulsive colour structure. The dressing functions f_0,f_1,f_2,f_3,f_4,f_5 correspond to specific components and colour channels. Empty slots in the meson-meson channels remain unoccupied due to physical constraints, while those in diquark channels are forbidden by symmetry considerations. For more detail, see Appendix B.2.1 .

Rest of this page intentionally left blank.

Chapter 6

Results

6.1 Mass spectra

In this section, we display and discuss our obtained mass spectra for the hidden- and open-flavour four-quark states with total spin $J = 0$ and $J = 1$. In this context, we investigate the importance of the repulsive colour forces for the different four-quark states considered in this thesis. We do this, by comparing the mass spectrum of a four-quark state with quantum numbers $I(J^{P(C)})$ obtained by using solely the attractive colour forces with the mass spectrum we get when we additionally include also the repulsive colour forces. This provides a good overview of how much the repulsive colour forces affect the different channels. Furthermore, using the obtained masses for the different investigated channels, we also calculate the binding energy with respect to the lowest lying meson-meson threshold for a given channel. We also compare our mass spectra and binding energies to the experimental values in [20] (if available for the investigated channel) and to predictions from other theoretical approaches.

The masses of the four-quark states shown in the following are obtained in a similar fashion as described in Section 4.3.1. We determine the quark mass evolution curve (QMEC) from the masses obtained by the corresponding eigenvalue curves (EVC). The QMECs are then fitted by polynomials of the form Eq. (4.56) to obtain the final predictions for the four-quark masses plus an error estimate, which is the extrapolation error from the EVC (cf. Appendix C.5) plus an error coming from the fit (cf. Appendix C.6).

Comparing the "attractive colour forces only" spectra to the spectra with attractive and repulsive colour forces, e.g., left and right panel in Figs. 6.1 and 6.2, we see that in some cases, the error bars for the spectra including the attractive and repulsive colour forces are larger compared to the spectra with only attractive colour components. This is explained in more detail in Appendix C.6, but can be shortly summarized as follows. Solving the four-quark FYE in Eq. (5.42) with only the repulsive colour components in Tables 5.3 and 5.4 yields negative eigenvalues, i.e., the state is never bound. Thus, the inclusion of the repulsive colour forces in general lowers the calculated eigenvalues, leading to an increase in mass. This increase in mass, however, leads to the two-body thresholds coming into effect earlier in the QMECs in Appendix C.6. Thus, the range of quark masses which need to be extrapolated with the polynomial increases, leading to potential larger error bars for the final masses. This larger fit range is also the reason, why the excited states may have larger error bars than the ground states. The two-body thresholds are the same for ground and excited states, but the excited states are heavier, thus the threshold effects occur earlier

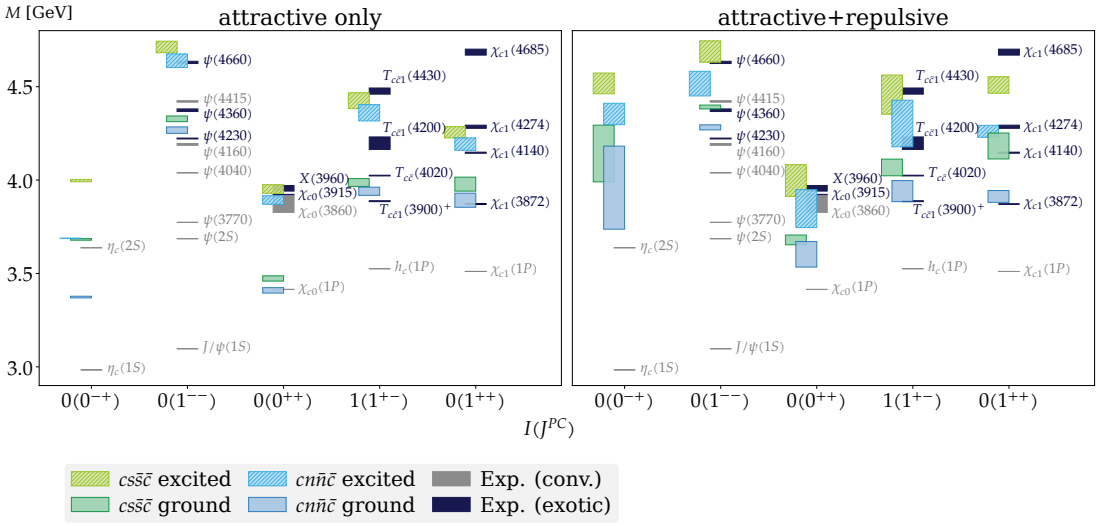

Figure 6.1: Hidden-charm four-quark mass spectrum for the ground and first radial excited states compared to experiment [20]. *Left*: Spectrum obtained by using only the attractive colour forces. *Right*: The mass spectrum with attractive and repulsive colour channels included. The height of the box is the error estimate for the extracted masses. The grey and black boxes represent the real parts of the pole positions from the PDG for the conventional and exotic hadrons respectively. Pale grey states are not yet well established. Spectrum in the left panel is taken from [189].

in the QMEC.

6.1.1 Hidden-flavour mass spectrum

We commence with the spectra of the hidden-flavour four-quark states investigated in this work. The attractive and repulsive physical components taken into account for the hidden-charm and hidden-bottom states are given in Table 5.3. As a reminder, the physical components correspond to (heavy-light) meson-meson, hadro-quarkonium and (heavy-light) diquark-antidiquark components for the $\mathcal{M}_1$, the $\mathcal{M}_2$ and $\mathcal{D}$ topologies respectively. The quark mass evolution curves used to extract the spectrum are shown in Appendix C.6.1.

The obtained mass spectra for the ground and first radial excited states of the investigated hidden-flavour quantum numbers in the charm and bottom sector compared to the masses, i.e., the real part of the pole, from the PDG [20] are shown in Fig. 6.1 and Fig. 6.2 respectively. In the left panel we show the spectrum obtained by using only the attractive colour channels, i.e., the first three columns in Table 5.3, while in the right panel we display the spectrum obtained by using the attractive and repulsive colour forces. The associated numerical values for the masses are compiled in Tables C.2 and C.3. The white rows show the values for the attractive only basis and the green highlighted rows show the ones for the attractive plus repulsive basis. Additionally, we show the binding energies $E_B = M - M_{\text{th}}$ with respect to the lightest heavy-light meson-meson thresholds M_{th} in a given channel. The threshold M_{th} is obtained by using our calculated masses from the two-body BSE in Tables 4.2 and C.1.

Hidden-charm mass spectrum

As stated above, in Fig. 6.1 we show the obtained masses plus (extrapolation) error for the ground and first radial excited states for hidden-charm four-quark states. We will now go through the different channels one by one from right to left and compare the obtained spectra for the attractive only and the attractive plus repulsive colour forces. The following section follows the arguments given in [189].

$0(1^{++})$. Starting with the $0(1^{++})$ channel, we see that the $cn\bar{n}\bar{c}$ ground state agrees very well with the experimental $\chi_{c1}(3872)$ in both cases. Moving on to the $cs\bar{s}\bar{c}$ ground state, we see that for the attractive only basis (left panel in Fig. 6.1), we get a state very close to the corresponding $cn\bar{n}\bar{c}$ ground state. The reason for this is the slight plateau like behaviour of the corresponding QMEC in the left panel of Fig. C.5. Comparing this to the $cs\bar{s}\bar{c}$ ground state with attractive and repulsive colour forces, we see that its mass gets shifted up to match the experimental $\chi_{c1}(4140)$. This identification fits quite well, as the observed hadronic decay for this state is $\chi_{c1}(4140) \to J/\psi\phi$, i.e., $((c\bar{c})(s\bar{s}))$, which is our physical hadro-charmonium component for this state. The excited $cn\bar{n}\bar{c}$ state for attractive only is found in the region of the $cs\bar{s}\bar{c}$ ground state using attractive and repulsive forces. Adding the repulsive colour channel, this state moves up a bit to the $\chi_{c1}(4274)$. However, checking the PDG [20], the observed decay for the $\chi_{c1}(4274)$ is also $J/\psi\phi$, which does not match with the internal clusters we take into account here. Therefore, we conclude that this state either has undiscovered decay modes or the radial excitation of the $\chi_{c1}(3872)$ is still missing from the spectrum. Regarding the excited $cs\bar{s}\bar{c}$ state, we find that its mass moves up considerably when we include the repulsive channels in the right panel. This state is now closer to the $\chi_{c1}(4685)$ than to the $\chi_{c1}(4274)$, albeit being too low in mass. To shortly summarize, we see that while considering only the attractive colour components produces the $cn\bar{n}\bar{c}$ ground state correctly, the rest of the spectrum is a little off. Including the repulsive colour forces in this channel remedies this, which can especially be seen in the spectrum for the $cs\bar{s}\bar{c}$ states. For the excited $cn\bar{n}\bar{c}$ state, it is presently not clear whether the spectrum is missing a state or if the $\chi_{c1}(4274)$ has additional hadronic decay modes making it a suitable candidate.

$1(1^{+-})$. Considering now the second axialvector channel, i.e., $1(1^{+-})$, the mass of the $cn\bar{n}\bar{c}$ ground state stays the same when comparing the left and right panel in Fig. 6.1. The attractive plus repulsive mass matches the $T_{c\bar{c}1}(3900)^+$ within the error. For the corresponding excited $cn\bar{n}\bar{c}$ state the "attractive only" and the attractive plus repulsive results agree within the error bars. The latter can be identified with the $T_{c\bar{c}1}(4200)^+$, which according to the observed decay ($T_{c\bar{c}1}(4200)^+ \to J/\psi\pi^+$) could be the radial excitation of the $T_{c\bar{c}1}(3900)^+$. Looking at the seen hadronic decays of the remaining exotic candidates, i.e., $T_{c\bar{c}}(4020) \to h_c(1P)\pi; D^*\bar{D}^*$ and $T_{c\bar{c}1}(4430)^+ \to J/\psi\pi^+; \psi(2S)\pi^+$, we see that none of those is expected to have quark content $cs\bar{s}\bar{c}$. More likely, the $T_{c\bar{c}1}(4430)^+$ is a further radial excitation of the $T_{c\bar{c}1}(3900)^+$, while the $T_{c\bar{c}}(4020)$ does not have established quantum numbers as of the time of writing. Therefore, our $cs\bar{s}\bar{c}$ ground and excited states serve

as estimates where states with this quark content could be located in this channel. Summarizing, we find that our $cn\bar{n}\bar{c}$ ground and excited states match with the corresponding experimental candidates if we include the repulsive as well as the attractive colour forces. Meanwhile, the $cs\bar{s}\bar{c}$ states do not have any appropriate experimental candidates and serve as predictions. Overall, the effect of the repulsive forces is observed to be rather small in this channel.

$0(0^{++})$. In the scalar $0(0^{++})$ channel, we find a $cn\bar{n}\bar{c}$ ground state which using only the attractive colour forces is consistent with the experimental $\chi_{c0}(1P)$. This, however, is considered a conventional $c\bar{c}$ state according to the PDG [20]. Also the $cs\bar{s}\bar{c}$ ground state is found very close to the $cn\bar{n}\bar{c}$ ground state, which again is due to the behaviour of the corresponding QMEC in Fig. C.7. These states are definitely too low to be identified with the exotic candidates in this channel. Including the repulsive colour forces, the situation improves slightly as the masses of both $cn\bar{n}\bar{c}$ and $cs\bar{s}\bar{c}$ ground states increases by about 200 MeV, see Table C.2. They are still too low to match the exotic candidates. However, regardless if we only include the attractive or attractive plus repulsive colour forces, we find the excited $cn\bar{n}\bar{c}$ state to be consistent with the $\chi_{c0}(3915)$. The hadronic decay modes $\chi_{c0}(3915) \to J/\psi\omega$ and $\chi_{c0}(3915) \to D^+D^-$ match up with our chosen physical components in Table 5.3. The excited $cs\bar{s}\bar{c}$ state is in the correct mass range to be identified with the $X(3960)$ [191], which because of its hadronic decay to $D_s^+D_s^-$ is believed to have $cs\bar{s}\bar{c}$. To the best of our knowledge, there is no evidence in the literature that would point to either $\chi_{c0}(3915)$ or $X(3960)$ being radial excitations. We therefore tentatively conclude, that the matching of our excited state with the experimental candidates is accidental and we cannot access the real ground state with our current theoretical setup. It might be, that the inclusion of further components in our physical BSA will lead to an increase in mass. Or maybe the mixing of four-quark states with conventional $c\bar{c}$ mesons has a significant effect in this channel. Exploring these important possibilities is relegated to future work. Overall, we observe that including the repulsive forces has a rather small effect on the masses in this channel.

$0(1^{--})$. In the vector $0(1^{--})$ channel, the lowest exotic candidate is the $\psi(4230)$. Regardless whether we use the attractive only or the attractive plus repulsive physical basis, we find our $cn\bar{n}\bar{c}$ ground state in close vicinity of the $\psi(4230)$. Based on our chosen physical components in Table 5.3, this is also the first state that should be picked up by our analysis, as the conventional states below all feature different decay patterns, cf. [20]. Note, that from Table C.2 we see that this state is far above the $D\bar{D}_1$ threshold, while in nature it is measured very close to said threshold. This is because our calculated D_1 meson is much lower than the PDG one, cf. Table C.1, decreasing the threshold significantly.[1] The $cs\bar{s}\bar{c}$ ground state moves up in mass to match the experimental $\psi(4360)$ very well when we include the repulsive colour components. However, an identification of our $cs\bar{s}\bar{c}$ ground state with the $\psi(4360)$ is questionable, as the observed decays do not point towards a $s\bar{s}$

[1] Note: using the PDG mass for the $D_1(2420)$ meson increases the mass of our 1^{--} $cn\bar{n}\bar{c}$ ground state by about $50 - 100$ MeV.

component. Theoretical studies using *effective field theory* (*EFT*) more point towards a D^*D_1 molecular interpretation [192, 193], which would render the $\psi(4360)$ the spin partner of the $\psi(4230)$. Because of this and as the other state in the vicinity, i.e., the $\psi(4415)$ is considered a conventional meson, we conclude that the $cs\bar{s}\bar{c}$ ground state is still missing from the experimental spectrum. Our obtained mass may serve as an estimate of the mass range where it could be found. Including the repulsive colour components, the masses for both $cn\bar{n}\bar{c}$ and $cs\bar{s}\bar{c}$ excited states move downward. Our $cs\bar{s}\bar{c}$ excited state can now clearly identified with the $\psi(4660)$, as it is now within our error bars. According to the seen hadronic decays, i.e., $\psi(4660) \to D_s^+ D_{s1}(2536)^-$, $\psi(4660) \to D_s^+ D_{s2}(2573)^-$ and $\psi(4660) \to \psi(2S)\pi^+\pi^-$ (probably from $\psi(4660) \to \psi(2S)f_0(980)$), the $\psi(4660)$ is in line with a $cs\bar{s}\bar{c}$ quark content. The excited $cn\bar{n}\bar{c}$ state does not match with any experimental candidate and therefore may serve as prediction for such a radial excitation of the $\psi(4230)$. To sum up, we find that our $cn\bar{n}\bar{c}$ ground state is in good agreement with the $\psi(4230)$, while the corresponding $cn\bar{n}\bar{c}$ excited state and $cs\bar{s}\bar{c}$ ground state serve as predictions for possible experimental candidates. The excited $cs\bar{s}\bar{c}$ state is then again in line with the experimental $\psi(4660)$. Including also the repulsive colour components in this channel seems to affect the results the least out of all the investigated channels.

$0(0^{-+})$. Finally, we consider the pseudoscalar $0(0^{-+})$ channel. This channel does not feature any experimental exotic candidates at the time of writing. Therefore, our obtained results may serve as a prediction for the ground and first excited four-quark states in this channel. Starting with the $cn\bar{n}\bar{c}$ ground state using only the attractive colour channels, we find it in the same mass region as its scalar partner and close to our $\chi_{c0}\eta$ threshold (keep in mind that the η only features an $n\bar{n}$ component and is thus are mass degenerate with the π). Including also the repulsive colour channels increases the mass by about 600 MeV moving it closer to our $D^*\bar{D}_1$ threshold. From an EFT standpoint, the lowest pseudoscalar four-quark state in the charmonium region should be heavier than the $\psi(4230)$ and around the $D^*\bar{D}_1$ threshold [194]. The $cs\bar{s}\bar{c}$ ground and $cn\bar{n}\bar{c}$ excited state are almost degenerate when we use only the attractive colour channels and in the vicinity of the conventional $\eta_c(2S)$. Including the repulsive colour channels, both of these masses increase by around 400 and 600 MeV respectively. Also the mass for the excited $cs\bar{s}\bar{c}$ state increases by over 500 MeV when we use the full physical basis. The error bars get significantly larger when going from the attractive only to the attractive plus repulsive basis. This is to be expected, as the corresponding QMEC for the latter case gets affected earlier by the internal two-body thresholds. The masses in this channel are affected the most by the inclusion of the repulsive forces.

Hidden-bottom mass spectrum

In Fig. 6.2 we show the calculated masses and error for the ground and first radial excited four-quark states in the bottom region together with the experimentally measured states. We again show the masses obtained by using only the attractive colour forces in the left panel and the one with attractive plus repulsive colour channels in the right panel. The

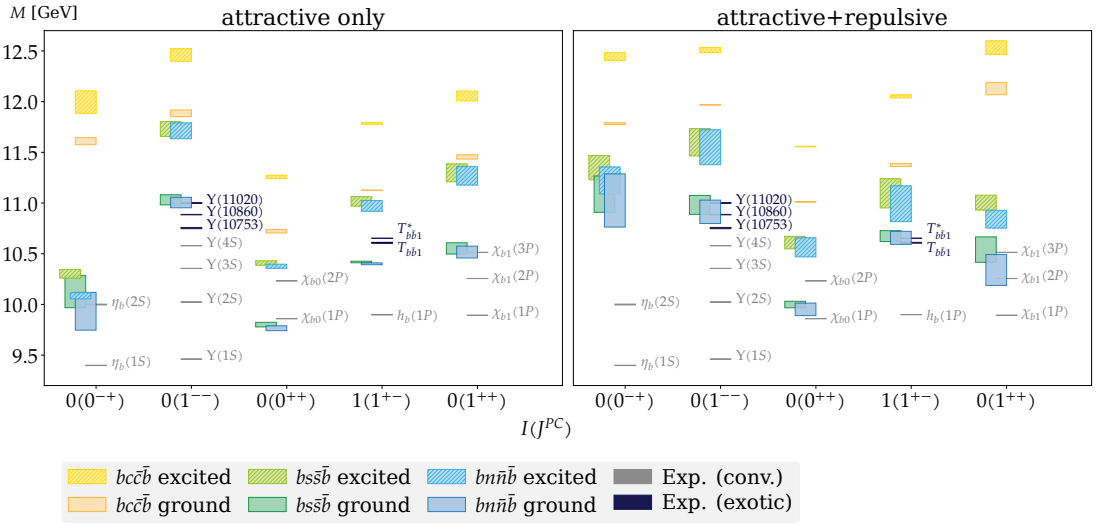

Figure 6.2: Same as Fig. 6.1 but for the hidden-bottom four-quark ground and first excited states. The $T_{b\bar{b}1}$ and $T^*_{b\bar{b}1}$ denote the $T_{b\bar{b}1}(10610)$ and $T_{b\bar{b}1}(10650)^+$ respectively.

associated numerical values are given in Tables C.2 and C.3. Similar as for the hidden-charm case, we will go through the channels from right to left, discuss the different spectra obtained with attractive only versus attractive plus repulsive colour channels and compare the spectra to the experimental situation. It is quite clear when we compare the experimental situation in the charmonium region in Fig. 6.1 to the bottomonium region, the latter presently features much less experimentally measured states. There are theoretical predictions for the $bn\bar{n}\bar{b}$ ground states in the 0^{++}, 1^{++} and 2^{++} channels coming from EFT [195], which are referred to as W_{bJ} states.

$0(1^{++})$. Starting again in the $0(1^{++})$ channel, we see that there are currently no exotic candidates in this channel to which we could compare our findings. Therefore, all the following masses can be understood as predictions. We find the $bn\bar{n}\bar{b}$ ground state for the attractive only colour channels (left panel in Fig. 6.2) mass degenerate with the $\chi_{b1}(3P)$. This is however the second radial excitation of the $\chi_{b1}(1P)$ and therefore considered a conventional state. Including the repulsive colour component, the mass moves down by 170 MeV but is still consistent with the attractive only result within our error. The W_{b1} is predicted to be a resonance several MeV above threshold [195], which does not match our result. The mass of the $bs\bar{s}\bar{b}$ ground state does not get modified by the inclusion of the repulsive channels. The $bc\bar{c}\bar{b}$ ground state however moves up significantly by about 680 MeV. For the excited states, we find that the $bn\bar{n}\bar{b}$ and $bs\bar{s}\bar{b}$ states move down in mass upon inclusion of the repulsive colour channels. This might be attributed to the threshold effects in the corresponding QMEC in Appendix C.6. The $bc\bar{c}\bar{b}$ excited state increases by about 500 MeV to match its lowest meson-meson two-body threshold, i.e., $\eta_b\Upsilon$.

$1(1^{+-})$. Moving to the $1(1^{+-})$ channel, we have the $T_{b\bar{b}1}(10610)$ and $T_{b\bar{b}1}(10650)^+$ as experimental candidates (denoted as $T_{b\bar{b}1}$ and $T^*_{b\bar{b}1}$ in Fig. 6.2). Based on the observed hadronic decays of these two states, see [20], they are expected to have quark content $bn\bar{n}\bar{b}$. The physical components chosen for this channel suggest, that our $bn\bar{n}\bar{b}$ ground state should correspond to the $T_{b\bar{b}1}(10610)$ rather than the $T_{b\bar{b}1}(10650)^+$, for which the dominant hadronic decay channel is $T_{b\bar{b}1}(10650)^+ \to B^{*+}\bar{B}^{*0}$. The $bs\bar{s}\bar{b}$ and $bc\bar{c}\bar{b}$ ground states currently do not have associated experimental candidates. When including the attractive and repulsive colour forces, the masses of the ground states move up by 250 MeV, which yields a $bn\bar{n}\bar{b}$ ground state in accordance with the experimental $T_{b\bar{b}1}(10610)$ state. The $bs\bar{s}\bar{b}$ ground state is found almost mass degenerate again. The masses for the $bn\bar{n}\bar{b}$ and $bs\bar{s}\bar{b}$ excited states increase slightly and the error gets larger as the two-body threshold effects occur earlier in this QMEC than for the case where we only use the attractive colour channels. The excited $bc\bar{c}\bar{b}$ state does not have this problem, as it is still significantly below the threshold. Its mass increases by about 250 MeV.

$0(0^{++})$. The scalar $0(0^{++})$ channel also does not feature any exotic experimental candidates at the time of writing. The situation we find is similar to the case in the charm region. The $bn\bar{n}\bar{b}$ and $bs\bar{s}\bar{b}$ ground states are found very low when using only the attractive only colour channels. Including also the repulsive ones, the masses move up by about 200 MeV. The W_{b0} state is found by EFT [195] to be slightly above the $\bar{B}B$ threshold, which is again in the range where we find our $bn\bar{n}\bar{b}$ excited state using the attractive and repulsive forces.

$0(1^{--})$. The vector $0(1^{--})$ channel again features many experimental states and also a few which can be considered exotic candidates. The nature of the $\Upsilon(10860)$ and the $\Upsilon(11020)$ is not quite clear, as they are also candidates for the $\Upsilon(5S)$ and $\Upsilon(6S)$, which would indicate that they are radial excitations of the $\Upsilon(1S)$. This would render the $\Upsilon(10753)$ the only exotic candidate in this channel. As was the case in the charm region for the vector channel, we do not observe a drastic change of the masses when including the repulsive forces. The ground state $bn\bar{n}\bar{b}$ mass decreases slightly, with our ground state close to the $\Upsilon(10753)$, justifying a possible identification. For our $bs\bar{s}\bar{b}$ ground state, the mass also decreases slightly when we include the repulsive colour channels. However, we cannot make a clear identification with an experimental exotic candidate, as they are probably either conventional excited states or complicated superpositions of $bn\bar{n}\bar{b}$, $bs\bar{s}\bar{b}$ and conventional $b\bar{b}$ states, as suggested in [196]. The excited $bn\bar{n}\bar{b}$ and $bs\bar{s}\bar{b}$ states also move downward in mass, when we include the repulsive colour channels, which can be explained by the difference in shape of the corresponding QMECs in Appendix C.6. The $bc\bar{c}\bar{b}$ ground and first excited states do not change upon inclusion of the repulsive channels, but rather can be determined more accurately.

$0(0^{-+})$. Lastly, we look at the pseudoscalar $0(0^{-+})$ channel. This channel is also completely devoid of experimental exotic candidates. Therefore, our results can be understood as predictions for the mass range of a possible experimental candidate. The situation is very similar as it was in the charm region. Using the attractive only basis, i.e., the first three

components in Table 5.3, we find a $bn\bar{n}\bar{b}$ ground state which is in the same mass region as the scalar ground state with the same quark content. Also, the corresponding excited state and the $bs\bar{s}\bar{b}$ ground and excited states are found very close together. Including also the repulsive colour channels leads to an increase in mass of about 1 GeV for the $bn\bar{n}\bar{b}$ and $bs\bar{s}\bar{b}$ ground and excited states, which are again found in the vicinity of the ground states. The $bc\bar{c}\bar{b}$ ground state stays roughly in the same mass region and its error is slightly smaller. Its excited state increases in mass by about 400 MeV.

In all channels we observe that for increasing $q\bar{q}$ mass, the states get more deeply bound. This behaviour was also observed in earlier work [67, 74, 75]. Predictions for the mass of the $bc\bar{c}\bar{b}$ state coming from QCD sum rules [197], diquark-antidiquark models [198] and lattice-QCD inspired quark models [199] mostly yield a state close to the respective threshold or unbound, which would be at odds with our observation. Whether this trend of increasing binding is correct or not remains to be seen.

6.1.2 Open-flavour mass spectra

We now move on to discuss the mass spectra for the open-flavour four-quark states. The attractive and repulsive physical components we took into account for the different quantum numbers J^P are compiled in Table 5.4. As a brief reminder, the physical components given in the aforementioned table correspond to two heavy-light meson-meson components for the $\mathcal{M}_1$ and $\mathcal{M}_2$ topologies and a (heavy-heavy)(light-light) diquark-antidiquark component for the $\mathcal{D}$ interaction topology. The quark mass evolution curves to obtain the spectra are shown and discussed in Appendix C.6.2. We compare the spectra obtained by using only the attractive colour channels, i.e., the first three rows in Table 5.4, with the one obtained by additionally including the repulsive colour channels. We will first discuss our results in the $J^P = 1^+$ channel and then for the $J^P = 0^+$ channel. This section partially follows [190].

$J^P = 1^+$

In Fig. 6.3 we show our obtained mass spectra for the open-bottom, open-bottom-charm and open-charm four-quark states with $J^P = 1^+$ using only the attractive (*left*) and the attractive plus repulsive colour channels (*right*). In Fig. 6.4 we show the masses for the open-bottom-strange ($bb\bar{n}\bar{s}$) ground and excited states. The corresponding numerical values are compiled in Tables C.4 to C.6. At the time of writing, this channel features only one experimentally measured open-flavour four-quark state containing a pair of heavy quarks (bottom or charm), i.e., the $T_{cc}^+(3875)$ in the $0(1^+)$ channel with suggested quark content $cc\bar{n}\bar{n}$ [30, 31]. This is shown as the black box in the $cc\bar{q}\bar{q}$ spectra. There are, however, numerous studies using lattice QCD (e.g., [32, 34, 36, 37, 200–205] or see [63] for an extensive overview) and phenomenological models (e.g., [33, 35, 206–219]) investigating the binding energies of the T_{cc}^+ and its heavier partners, which are termed T_{bb}^- ($bb\bar{n}\bar{n}$), $T_{bb\bar{s}}^-$ ($bb\bar{n}\bar{s}$) and T_{bc} ($bc\bar{n}\bar{n}$). We compiled the obtained binding energies from the aforementioned literature in Fig. 6.5. As a reference to compare our results to, we averaged the binding energies in Fig. 6.5 for the T_{bc}, T_{bb}^- and $T_{bb\bar{s}}^-$ and subtracted it from *our calculated* lowest

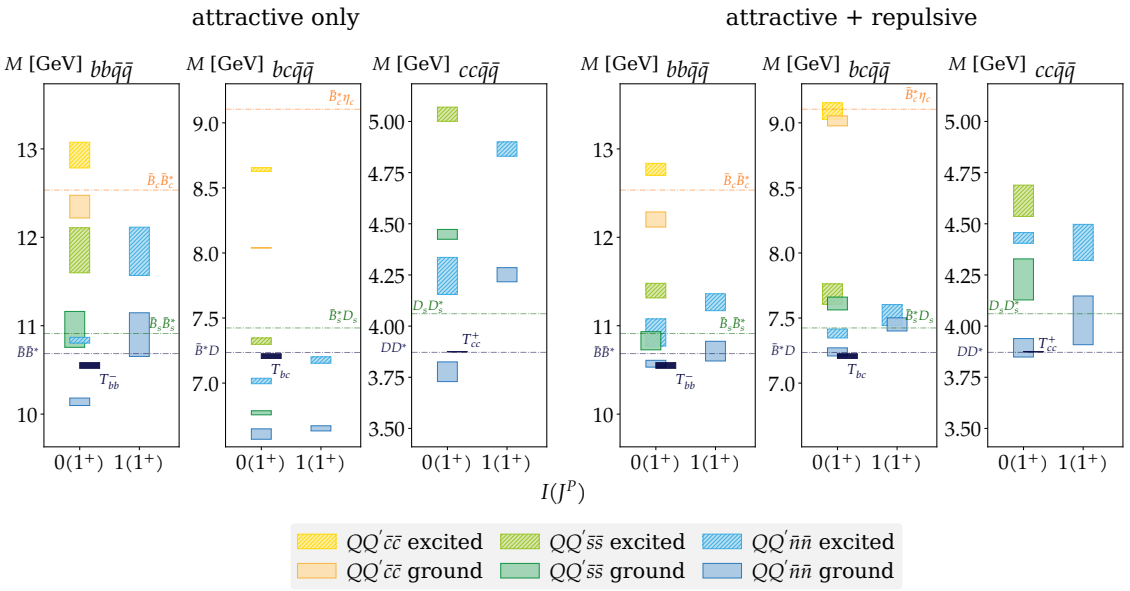

Figure 6.3: Spectra for open-flavour $J^P = 1^+$ states. *Left:* Spectra obtained by using only attractive colour channels. *Right:* Spectra obtained including also the repulsive colour channels. In both cases we display the spectra for open-bottom ($bb\bar{q}\bar{q}$), open-bottom-charm ($bc\bar{q}\bar{q}$), and open-charm ($cc\bar{q}\bar{q}$) systems from left to right. The heights of the boxes represent the uncertainties in the extracted masses. For reference, the lowest relevant thresholds for the respective four-quark systems are included (colour-coded to match the box colours, see Table 5.4). The black box corresponds to the experimentally observed T_{cc}^+ state, while the boxes for T_{bb}^- and T_{bc} represent averaged theoretical predictions. Figure adapted from [190] .

meson-meson threshold. The results are shown as black boxes in Figs. 6.3 and 6.4. To provide a further reference, especially for the states with $\bar{q}\bar{q} \neq \bar{n}\bar{n}$, we plot the corresponding lowest meson-meson thresholds.

From Fig. 6.3 we observe, that using only the attractive colour forces, we find our $bb\bar{n}\bar{n}$, $cc\bar{n}\bar{n}$ ground states for isospin $I = 0$ and in fact the whole $bc\bar{q}\bar{q}$ spectrum very strongly bound. Only by including also the repulsive colour channels, we find our states in the correct mass regions. Thus, the interplay of attractive and repulsive forces seems to be of crucial importance for the open-flavour states with spin $J = 1$. In the open-bottom spectrum, our $I = 0$ $bb\bar{n}\bar{n}$ ground state moves up by about 400 MeV to match the theoretical prediction of the T_{bb}^-. Our calculated binding energy is right in the middle of the predictions from the literature (top left in Fig. 6.5). The corresponding excited state also moves up a little in mass. The masses of the ground and excited states of the isospin $I = 1$ partner states move down somewhat and can be determined much more accurately when we use the attractive plus repulsive colour channels. Same goes for the $bb\bar{q}\bar{q}$ states with $\bar{q} \neq \bar{n}$. The binding energy of the isospin $I = 1$ $bb\bar{n}\bar{n}$ state is in the region expected from other theoretical approaches (bottom left panel in Fig. 6.5), with the threshold still within our error bar. The $bb\bar{s}\bar{s}$ is found shallowly bound but the $\bar{B}_s\bar{B}_s^*$ threshold is still within the error bar.

For the isospin $I = 1/2$ channel, we see from Fig. 6.4 that using only the attractive colour

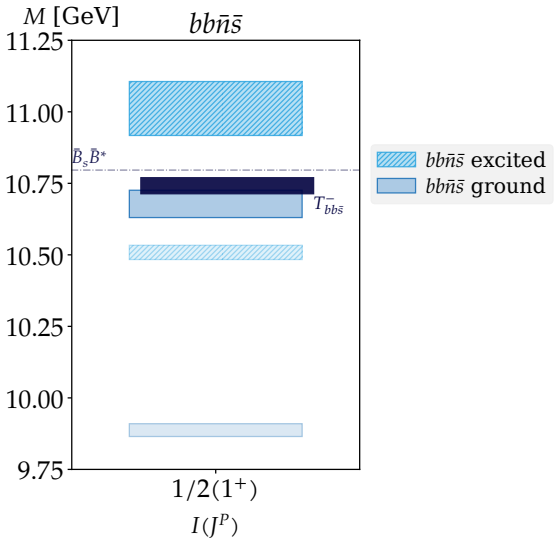

Figure 6.4: Ground and first radial excited state for the $bb\bar{n}\bar{s}$ state using only the attractive colour channels (shown as transparent) and using the attractive plus repulsive colour channels (shown as full boxes). The black box represents the averaged theoretical predictions for the $T^-_{bb\bar{s}}$.

channels, the $bb\bar{n}\bar{s}$ ground and excited states are very deeply bound (opaque states). Only by including the repulsive colour channels, the mass of the ground state moves up into the region of the theoretical predictions. We see from Fig. 6.5, that our obtained binding energy is in accordance with the theoretical predictions within the error, albeit still a little too low. In [63] it is stated, that the binding energy for the $T^-_{bb\bar{s}}$ is expected from the lattice to be between $E_B^{\text{lat.}} = -(30 - 100)$ MeV. Using the attractive plus repulsive colour channels, the first excited state is found to be a resonance above the threshold. While we do not show the $bb\bar{q}\bar{s}$ states for $\bar{q} \neq \bar{n}$ in Fig. 6.4, we give their masses and binding energies in Table C.5.

In the open-bottom-charm spectrum, our $I = 0$ $bc\bar{n}\bar{n}$ ground state increases by about 600 MeV right up to the $\bar{B}^*D$ threshold. At the time of writing, there is no common consensus whether this state is bound or not, as can be seen from the corresponding plot in Fig. 6.5. Our obtained binding energy is slightly above threshold and in line with recent lattice results [37, 204], which claim a very shallow bound state. The excited $bc\bar{n}\bar{n}$ state is found far above threshold, as are the ground and excited isospin $I = 1$ partner states. The $bc\bar{s}\bar{s}$ ground and excited states are also both above the $\bar{B}_s^*D_s$ threshold. Coming to the open-charm spectrum, our $I = 0$ $cc\bar{n}\bar{n}$ ground state increases by about 100 MeV upon inclusion of the repulsive colour channels, yielding a binding energy of $E_B = 20 \pm 50$ MeV, which is in good agreement with the experimental value, i.e., $\delta m_{\text{BW}} = -273(61)$ keV [30, 31], and the theoretical predictions (top right in Fig. 6.5). All other states are found far above the respective thresholds. The binding energy of the isospin $I = 1$ ground state is, albeit a little low, consistent with the expected values from phenomenology within our error bar (bottom right in Fig. 6.5).

Comparing the binding energies of our (heavy-heavy)(light-light) ground states in the case of attractive plus repulsive colour channels, we observe a clear hierarchy with

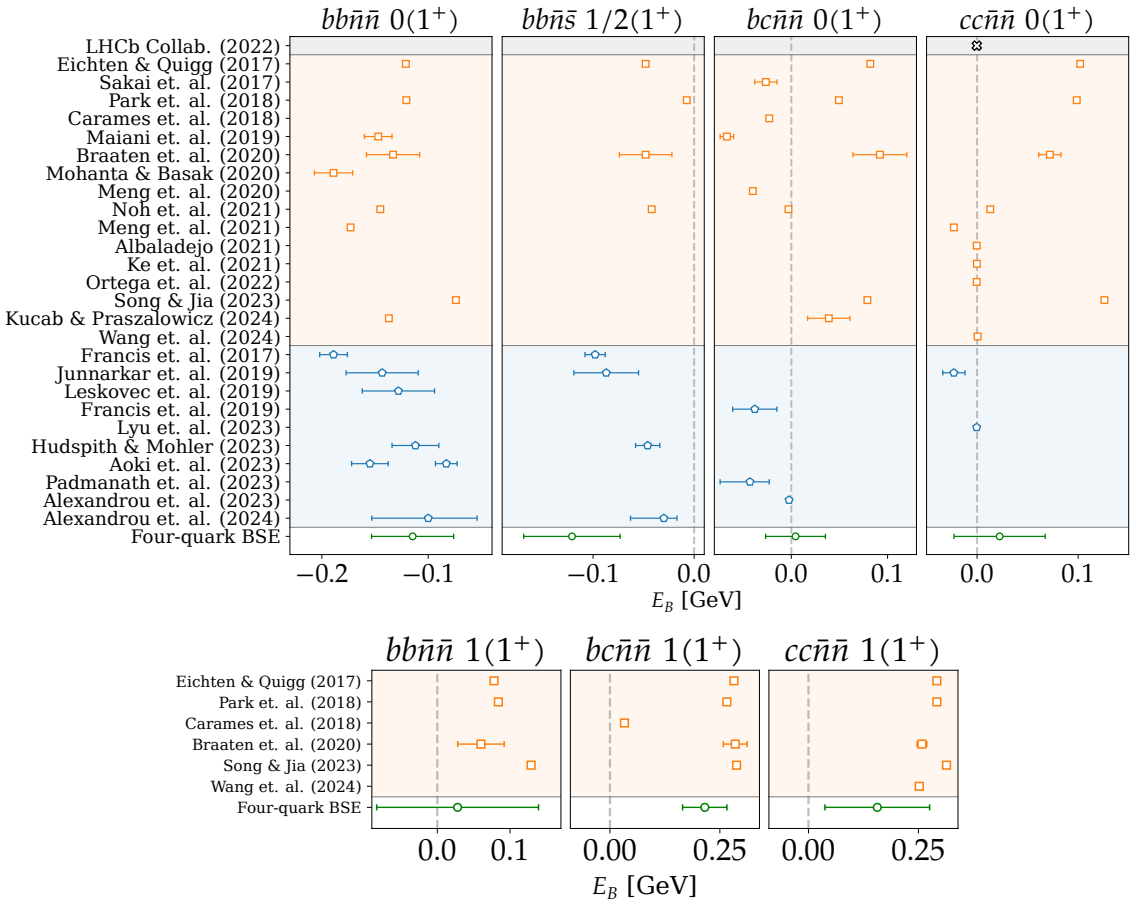

Figure 6.5: Comparison of the binding energy E_B of the $J^P = 1^+$ ground states obtained from theoretical models and (if available) experimental results (*black cross*). The results in green are from this work. The blue points are results from the lattice [32, 34, 36, 37, 200–205] and the orange squares are from phenomenological models [33, 35, 206–219]. The grey dashed lines are the lowest meson-meson thresholds for the respective channel.

the $bb\bar{n}\bar{n}$ being deeply bound, the $bc\bar{n}\bar{n}$ at best shallowly bound and the $cc\bar{n}\bar{n}$ right at the DD^* threshold. This matches the predicted behaviour of decreasing binding energy with decreasing heavy quark mass [34, 37, 200, 202, 220–224]. The binding energy of the $bb\bar{n}\bar{s}$ ground state shows a little less binding energy than its $bb\bar{n}\bar{n}$ partner, which is also observed on the lattice [63, 205]. The ground states of the isospin partners $1(1^+)$ are all found to be unbound (bottom row in Fig. 6.5). This is a known behaviour, e.g., from lattice QCD [225, 226], as the repulsive forces are stronger for $I = 1$. For the excited $QQ'\bar{n}\bar{n}$ states we find that the $bc\bar{n}\bar{n}$ excited state has the lowest excitation energy, followed by the $bb\bar{n}\bar{n}$ and then the $cc\bar{n}\bar{n}$. The best explanation we currently have for this behaviour is related to the different symmetry structure of the $QQ' = bc$ state compared to the $QQ' = bb$, cc states. We note, that our heaviest ground states with $\bar{q}\bar{q} = \bar{c}\bar{c}$ and $\bar{b}\bar{b}$ are all found to be deeply bound, cf. Table C.4. This matches the observed behaviour also seen for the hidden-flavour four quark states in Table C.2. It remains to be seen, whether this binding

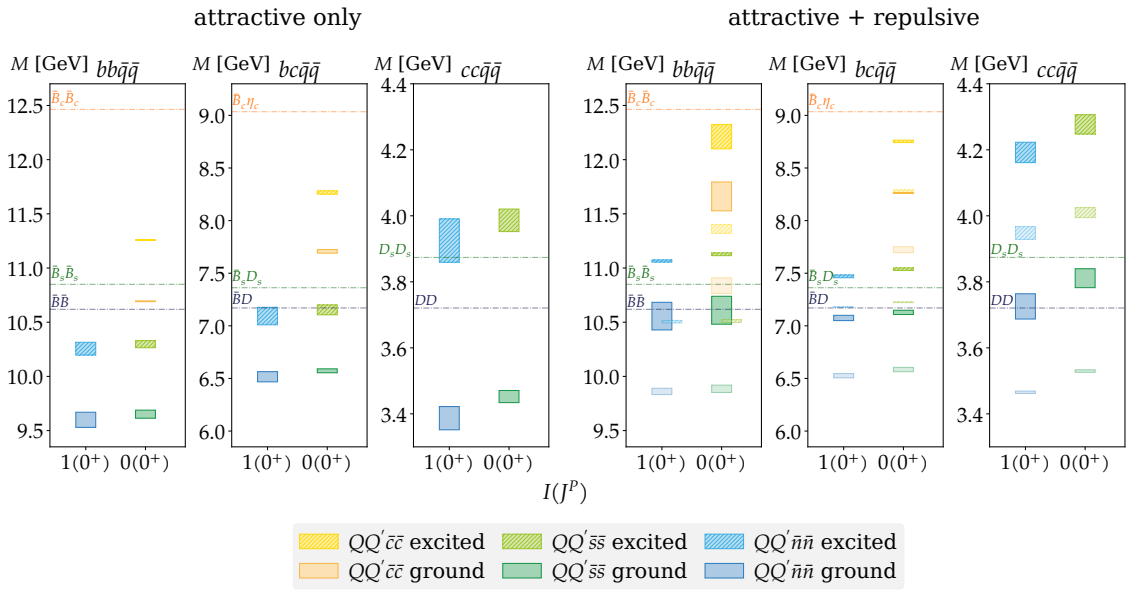

Figure 6.6: Same as in Fig. 6.3, but for the spectra for open-flavour states with $J^P = 0^+$. For spectra with attractive plus repulsive colour channels, we show the masses obtained with the full basis as transparent and the ones obtained by using the 'reduced' basis as usual .

is too strong. Considerations for the $bb\bar{c}\bar{c}$ from lattice QCD using the Born-Oppenheimer (BO) approximation suggest that these states should be unbound [225]. However, one can argue that the BO approximation is not entirely free of doubt in this case, because of the heavy charm quarks involved.

$J^P = 0^+$

Our results for the open-bottom, open-bottom-charm and open-charm spectra for the $J^P = 0^+$ channel are displayed in Fig. 6.6. The corresponding numerical values are given in Tables C.7 and C.8.

We will first discuss the effect of the repulsive colour channels on the mass spectra. For this, we note that the very transparent states in the spectra using the attractive plus repulsive channels (right panel in Fig. 6.6) correspond to taking all physical components given in Table 5.4 into account, while the non-opaque states use a subset of these. This will be explained a little later. Comparing the spectra in the left panel of Fig. 6.6 to the spectra obtained using the full basis in the right panel, we see that the repulsive channels affect the ground states by a few 100 MeV (cf. Table C.7) while the excited states are largely unaffected. Using the full attractive plus repulsive basis, the states can be determined more accurately, as can be seen by the smaller error bars. However, regardless whether we use the attractive only or the full attractive plus repulsive basis, we find all ground states very deeply bound. The corresponding excited states are comparably closer to the respective thresholds and in the same mass region as their $J^P = 1^+$ counterparts. Thus, we find a similar situation as in the hidden-flavour 0^{++} channel. However, in the open-flavour

case, there can be no contributions coming from possible four- and two-quark state mixing.

Interestingly, recent lattice studies on open-flavour scalar four-quark states only consider the $DD/\bar{B}\bar{B}$ meson-meson and $S_{cc/bb}S_{\bar{n}\bar{n}}$ diquark-antidiquark operators for the $bb\bar{n}\bar{n}/cc\bar{n}\bar{n}$ states [34] and $\bar{B}D$ (and $\bar{B}^*D^*$) meson-meson and $S_{bc}S_{\bar{n}\bar{n}}$ diquark-antidiquark operators for the $bc\bar{n}\bar{n}$ state [37, 221]. We know, that including additional operators in the operator basis on the lattice leads to an improved accuracy for the results and is not comparable with us reducing our physical components taken into account. However, we can take the lattice study as inspiration and consider a *'reduced' physical component basis* by excluding the vector-vector meson-meson and the $A_{QQ'}A_{\bar{q}\bar{q}}$ diquark-antidiquark component. Using the reduced basis, we find that our ground states move up considerably. They are now in the mass region where the first radial excited states for the full basis are found, see right panel in Fig. 6.6. We thus conclude, that the attractive $A_{QQ'}A_{\bar{q}\bar{q}}$ and vector-vector meson-meson components lead to an overly strong binding in the $J^P = 0^+$ channel.

Comparison to earlier works using the four-body FYE

In the charm region, the spectra of hidden- and open-flavour four-quark states with only attractive colour channels were already investigated in previous works using the four-body FYE [67, 74]. Our obtained results for the "attractive only" differ slightly from those obtained in the aforementioned works mainly due to two reasons.

The first reason is a slight inconsistency in [67, 74], as the two-body momentum partitioning parameters were all set to $\eta = \zeta = \chi = 0.5$ in the two-body pole terms Eq. (5.37) for all investigated states. Although the result is independent of the choice of these parameters, a non-optimal choice of these parameters leads to the two-body poles affecting the calculation earlier than they would for an optimal choice. As a consequence, the maximum value of P^2 cannot exhaust its full range and the eigenvalue curve needs to be extrapolated over a larger momentum range. This in turn causes larger extrapolation errors. With the method described at the end of Section 5.2 we manage to remedy this.

The second reason is the used extrapolation. In [67, 74] they consistently used quadratic polynomials to extrapolate the EVC, which was standard procedure at that time. However, as mentioned in Appendix C.5, we found that the quadratic extrapolation often overshoots the mass for the investigated states, while a cubic polynomial provides much better extrapolation results. For this reason, some of the results in [67, 74] already agree very well with the findings in the literature, e.g., the agreement of the $T_{cc}(3875)^+$ mass in [74] with the experimental value from the PDG. Reanalysing the states investigated in the mentioned works using the improved extrapolation method given in Appendix C.5, we find that our "attractive only" results are consistently lower in mass. In Section 6.1.2 we see that when we only use the attractive forces for the $T_{cc}(3875)^+$, our obtained mass is 90 MeV below the threshold, while only the inclusion of the repulsive channels renders it in accordance with the DD^* threshold.

Summary

In general, we observe that the inclusion of the repulsive colour forces in the physical Bethe-Salpeter amplitude leads to a significant improvement for the calculated spectra, see the comparison plots in Figs. 6.1 and 6.2 for the hidden- and Figs. 6.3 and 6.6 for the open-flavour four-quark states.

When taking a closer look at the effect of the repulsive forces for the spectra in the different investigated channels, we make the following observations: The biggest effect of the repulsive forces is observed in the $0(0^{-+})$ channel, where the masses of the states increase by several hundred MeV. Also for four-quark states with $J^{P(C)} = 1^{+(+)}$, the inclusion of the repulsive forces significantly affects the calculated spectra. Concerning the hidden-flavour $0(1^{++})$ channel in the charm region, we nicely reproduce the observed experimental spectrum in this channel when the repulsive forces are included. For the open-flavour $J^P = 1^+$ states, the ground state masses increase significantly to match the theoretical predictions from other approaches. The effect of the repulsive forces on the $1(1^{+-})$ and the hidden- and open-flavour scalar spectra is found to be rather small and the $0(1^{--})$ channel seemingly is affected the least, with the spectra almost unchanged.

When comparing our obtained mass spectra to the literature, we find that while the hidden-flavour spectra agree nicely with experiment, the best agreement is observed for the axialvector open-flavour ground states, i.e., $cc\bar{n}\bar{n}$, $bc\bar{n}\bar{n}$, $bb\bar{n}\bar{n}$ and $bb\bar{n}\bar{s}$. These agree exceptionally well with recent lattice results and other predictions from the literature, which is a good benchmark for the approximations used in this work.

The scalar channel, however, is a somewhat special case for both the hidden- and the open-flavour four-quark states, as the ground states are found very deeply bound regardless whether we only include the attractive colour forces, see also [74, 75], or use the full attractive plus repulsive physical components. Interestingly, the first radial excited states agree with the measured or predicted exotic candidates in this channel. At the present moment, we do not have an obvious explanation for this behaviour and further research regarding this is needed.

Regardless of the channel, we see from the QMECs in Appendix C.6 that increasing the mass of the $q\bar{q}$ and $\bar{q}\bar{q}$ (anti)quark-antiquark pair, our states get deeper and deeper bound. This behaviour was also observed by earlier works in the functional framework [67, 74, 75]. Results from lattice QCD using the Born-Oppenheimer approximation for the $bb\bar{c}\bar{c}$ state argue agains this behaviour [225]. Although, the use of the Born-Oppenheimer approximation for these systems is not entirely free of doubt, this deep binding behaviour is definitely worth investigating in future works.

6.2 Norm contributions

A very interesting and highly debated property of four-quark states is their internal structure. Regarding this, one can identify four different possibilities. The first and most obvious is that all four quarks interact strongly with each other, e.g., via three- and four-gluon vertices, such that they are all bunched together tightly in space, forming a *compact* state.

Since we neglect the three- and four-body interaction kernels in this work, we will not discuss this possibility further. For the other three possibilities, one needs to assume dominant two-body forces, as is done in this work. The resulting groupings of (anti)quarks are two meson-meson type clusters and one cluster of diquark-antidiquark nature. Many approaches in the literature then use one of these possibilities to describe the properties of four-quark states. There is the *meson-molecule* picture [16], which considers spatially separated mesons interacting via contact or one π exchange making up the four-quark state. This state then simply falls apart into the two heavy-light mesons at the corresponding threshold. Thus, this picture is especially relevant for four-quark states very close to heavy-light meson-meson thresholds, e.g., the $\chi_{c1}(3872)$ and the $T_{cc}(3875)^+$. Only relevant for the hidden-flavour four-quark states is the *hadro-quarkonium* picture [39], which suggests that the four-quark state has a heavy $Q\bar{Q}$ core with the light $q\bar{q}$ pair revolving around it. This is motivated by the experimental observation of final states involving a charmonium/bottomonium state and a light hadron. Last, there is the *diquark-antidiquark* picture, which considers a diquark and antidiquark pair tightly packed together in space because of the colour force. This is arguably the most widely used picture first developed for the considerations of four-quark states by Robert J. Jaffe [21]. Four-quark states made from a diquark-antidiquark pair are generally referred to as *tetraquarks*.

As is typical for a quantum theory, the above two-body clusters should not be mutually exclusive and a four-quark state is most likely a superposition of all possible internal clusterings. This is indeed captured by our physical BSA in Eq. (5.41). The question is then, how do we determine which of the internal physical components in Tables 5.3 and 5.4 is the most important for the considered four-quark states? In past works [67, 74, 75], the authors calculated the QMEC using the full (attractive) physical basis and then systematically switched off certain physical components to see the effects on the QMEC and therefore on the mass of the four-quark state. Based on how well the QMEC of a certain combination of physical components matches the QMEC of the full physical basis, one can draw conclusions about the dominance of the internal clusters. For example, in the case of the $\chi_{c1}(3872)$, the QMEC for the $D\bar{D}^*$ alone agrees reasonably well with the QMEC of the full result across a wide range of current-quark masses. The contribution from the $J/\psi\omega$ cluster is only marginal and the $S_{cn}A_{\bar{n}\bar{c}}$ cluster is almost negligible (cf. Fig. 2 in [67]).

In this work, we explore a different strategy to extract the information about the internal structure of the investigated four-quark states. In Section 4.3.2 we already discussed that one can use the dressing function to gauge the importance of the accompanying Dirac structure for a given hadron. Based on this, we investigate the dressing functions $f_j(S_0)$ in Eq. (5.41) and in particular their norm contributions similar to [227–229], where the authors investigated and quantified the orbital angular momentum composition and strength of different internal diquark clusters for baryons. To obtain the norm contributions, we use the canonical Nakanishi normalization condition described in Section 4.1.1, in particular we use the right-hand side of Eq. (4.21). That is, we use our physical BSA given in Eq. (5.41), containing six physical components in our case, and contract it with its charge conjugate $\bar{\Gamma}$ with full quark propagators in between, i.e., $\bar{\Gamma}\, G_0\, \Gamma$. From this we get 6×6 diagrams which are displayed in Fig. 6.7. The sum of all 36 matrix elements yields the total norm, shown

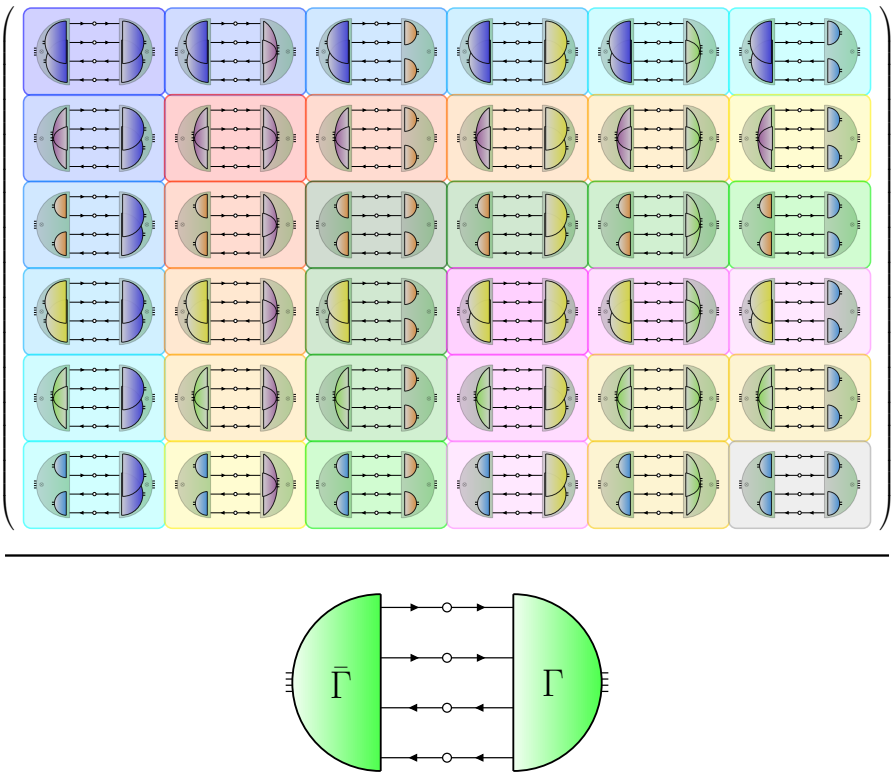

Figure 6.7: Graphical illustration of the norm contribution matrix. The entries in the matrix represent overlap integrals contributing to the total normalization of the four-quark state, which is shown in the denominator. Diagonal entries correspond to norm contributions coming from the physical components in Tables 5.3 and 5.4 and off-diagonal terms correspond to the mixing between them. The colours are chosen to match the calculated norm contributions in Fig. 6.8.

in the denominator. The diagonal entries are the contributions to the norm coming purely from each physical component in Tables 5.3 and 5.4. The off-diagonal elements represent the mixing between the different physical components.

Statements about the internal structure of physical four-quark states are only possible when using the on-shell BSAs for a particular quark configuration. Similar to the masses, this is potentially a problem for heavy-light four-quark states. However, since every eigenvalue in the EVC comes with a set of eigenvectors, i.e., the dressing functions, one can calculate the norm contributions for every mass in the eigenvalue curve. This then yields a norm contribution curve (NCC). From this NCC one can obtain the individual norm contributions in a similar way as the masses are obtained from the EVCs. For four-quark states containing only heavy quarks, the mass can be read off directly from the EVC and also the norm contributions can be read off directly from the NCC. However, for a heavy-light four-quark state, the lighter the 'light' quark gets, the harder it gets to obtain the norm contributions directly. Similar to the EVC case, we resort to extrapolation in these cases, but instead of the SPM, we simply use a polynomial to fit to the data and extrapolate to our physical mass, i.e., the masses compiled in Appendix C.7. In the

style of the QMEC, one obtains the norm contributions for a given four-quark state with quark content $Qq\bar{q}\bar{Q}$, $QQ'\bar{q}\bar{q}'$ across a range of current-quark masses for q. The resulting norm contribution quark mass evolution curve (NCQMEC) is then fitted by a suitable polynomial for the quark masses where the norm contributions are directly obtainable and extrapolated to the physical $m_q = m_n$ quark mass. Thus, we obtain an estimate of the on-shell norm contributions for heavy-light four-quark states. The NCQMECs for the investigated four-quark states in this work are shown in Appendix C.8.

Before we discuss our results, we need to mention a slight caveat. Because the four-quark FYE is formulated in momentum space, we cannot access the spatial structure of the internal clusters directly and therefore cannot make statements about the spatial extent of, e.g., a meson-molecule. We made some efforts in this direction using a three-dimensional Fourier transform to go into position space, see Appendix C.4, but the results are still inconclusive.

In the following, we will discuss first the obtained norm contributions corresponding to the hidden-flavour four-quark states discussed in Section 6.1.1 and then for the investigated open-flavour four-quark states from Section 6.1.2. Note, that the norm contributions are shown without an error estimate, as they anyhow serve as a qualitative study of the internal structure of the investigated four-quark states.

6.2.1 Hidden-flavour norm contributions

Our norm contributions for the hidden-flavour four-quark states with $I(J^{PC}) = 0(0^{-+})$, $0(1^{--})$, $0(0^{++})$, $1(1^{+-})$ and $0(1^{++})$ are shown in Fig. 6.8. The colour coding of the results is according to the correlations shown in the norm contribution matrix in Fig. 6.7. We only display the results for the $cn\bar{n}\bar{c}$, $bn\bar{n}\bar{b}$ and $bc\bar{c}\bar{b}$ ground states for each channel, since they hardly change for the excited states or states with hidden strangeness ($cs\bar{s}\bar{c}$ and $bs\bar{s}\bar{b}$). For each matrix entry, we show the results obtained with only the attractive colour forces as transparent on the left and the results using the attractive plus repulsive colour channels on the right. Like we did for the spectra, we will go through the channels from right to left and discuss the obtained results.

Starting out with the $0(1^{++})$ channel, we see that using only the attractive colour forces, this channel is solely dominated by the $\langle f_0|f_0\rangle$ correlation with about 80%, regardless of the quark configuration. For $cn\bar{n}\bar{c}$ and $bn\bar{n}\bar{b}$, this corresponds to the contribution coming purely from the attractive $D\bar{D}^*$ and $\bar{B}B^*$ physical components respectively. The contributions coming from the other physical clusters and the mixings are all below 10%. If we also include the repulsive colour channels, we find that the contribution from the attractive $D\bar{D}^*$ and $\bar{B}B^*$ physical components is still dominating with about 60%, but there is a very strong contribution of about 35% coming from the $\langle f_0|f_4\rangle$ correlation. For the $cn\bar{n}\bar{c}(bn\bar{n}\bar{b})$ ground states this corresponds to the mixing between the attractive $D\bar{D}^*(\bar{B}B^*)$ and the repulsive $J/\psi\omega(\Upsilon\omega)$ component. For the $bn\bar{n}\bar{b}$ state, there is also a sizeable contribution of about 20% coming from the pure repulsive $\Upsilon\omega$ component. This correlation vanishes when we go to $bc\bar{c}\bar{b}$. This importance of the repulsive forces is also reflected in the QMECs shown in Fig. C.5, where a significant increase of the masses can be seen. Overall, the observed norm contributions nicely confirm the hierarchy found by investigating only the QMECs [67,

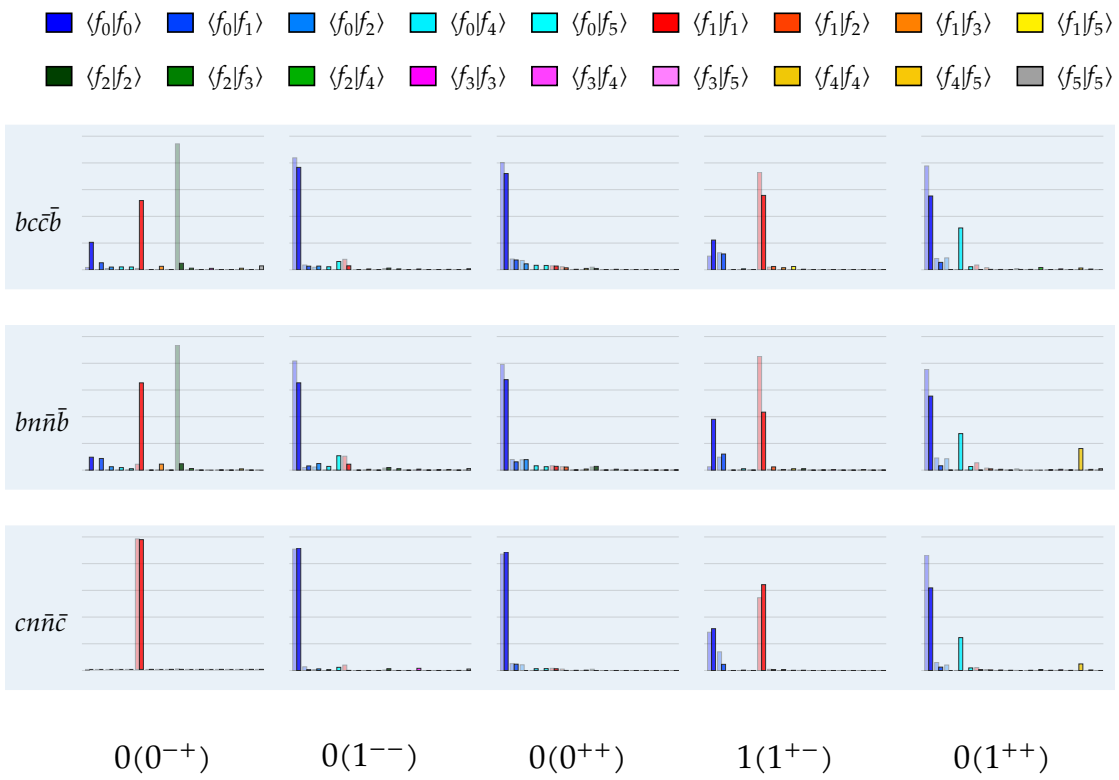

Figure 6.8: Norm contributions for the ground states of the investigated hidden-flavour four-quark states using only the attractive (*opaque, left*) and the attractive plus repulsive colour channels (*full, right*). The results for the exited states look very similar and are therefore not shown. The distance between the horizontal lines in the bar plots is 20%. The colour coding of the bars is according to the matrix entries in Fig. 6.7. The correlations given on top are plotted in this order (reading left to right) from left to right in the bar plots.

75]. For the hidden-charm state $\chi_{c1}(3872)$ it mirrors the observed dominant hadronic decay, which is $D\bar{D}^*$ ($D^0\bar{D}^0\pi^0$ and $D^0\bar{D}^{*0}$ channels combined) with about 86% and $J/\psi\omega$ with about 8% [20]. The strong $D\bar{D}^*$ component is expected in the wavefunction of the $\chi_{c1}(3872)$ as this state is very close to the corresponding two-body threshold, compare Table C.2.

Moving to the $1(1^{+-})$ channel, we find a very interesting picture. Using only the attractive colour forces, we find that the $cn\bar{n}\bar{c}$ state is dominated by the contribution coming from the $\langle f_1|f_1\rangle$ correlation ($\sim 55\%$), which would be the purely attractive $J/\psi\pi$ physical component, followed by the contribution coming purely from the attractive $D\bar{D}^*$ component ($\sim 30\%$) and the mixing between them. For the $bn\bar{n}\bar{b}$ ground state, this dominance of the attractive $\Upsilon\pi$ component gets even stronger ($> 80\%$) and the pure attractive $\bar{B}B^*$ component vanishes. Including the repulsive colour forces, the situation for the hidden-charm state does not really change, both pure attractive contributions get a little stronger, while the mixing between the two components gets a little weaker. For the hidden-bottom region, however, we see a drastic increase from the pure attractive $\bar{B}B^*$

component and a significant reduction of the attractive $\Upsilon\pi$ component. The repulsive colour forces seem not to be of great importance for this channel, which is also reflected in the corresponding QMECs Fig. C.6. The internal structure of the $cn\bar{n}\bar{c}$ state in this channel, i.e., the $T_{c\bar{c}1}(3900)$, is still debated in the literature, as the mass is very close to, but slightly above, the $D\bar{D}^*$ threshold. According to the observed hadronic decays, the $D\bar{D}^*$ channel is preferred over the $J/\psi\pi$ channel by a factor of 6 [230]. The conclusion drawn from this is, that the $J/\psi\pi$ component might be suppressed, which in turn implies that the $T_{c\bar{c}1}(3900)$ might be explained as a $D\bar{D}^*$ molecule. A coupled-channel analysis by the HAL-QCD lattice collaboration [231, 232] studied this state and found a very strong $D\bar{D}^* - J/\psi\pi$ mixing potential, which points towards this state not solely having a meson-meson or hadro-charmonium structure. The conclusion drawn by the authors was that this strong potential leads to the $T_{c\bar{c}1}(3900)$ forming as a threshold cusp. Additionally, a study using EFT [233, 234] to investigate the experimental data suggests that the $D\bar{D}^*$ component is at least equally important as non-molecular structures. For the hidden-bottom state, i.e., the $T_{b\bar{b}1}(10610)$, the common picture in the literature is that of a $\bar{B}B^*$ molecule, because of the closeness to the $\bar{B}B^*$ threshold [56] and the dominant hadronic decay $T_{b\bar{b}1}(10610) \to B^+\bar{B}^{*0} + B^{*+}\bar{B}^0$ of about 86% [20]. The contributions we observe for the $bn\bar{n}\bar{b}$ state are a little at odds with this picture. However, they are consistent with the observed contributions for our $cn\bar{n}\bar{c}$ state.

In the $0(0^{++})$ channel, we observe that regardless whether we take only the attractive or the attractive plus repulsive colour forces into account, the contribution coming from the purely attractive heavy-light meson-meson physical components dominate the states in this channel, over 80% for the hidden-charm and about 70% for the hidden-bottom states. All other contributions are below 10%. This confirms results from previous studies [74, 75], where also a dominant $D\bar{D}$ component was found. For the $cs\bar{s}\bar{c}$ state, the dominant $D_s\bar{D}_s$ component fits the observed decay channel of the $X(3860)$ [235].

Similarly, in the $0(1^{--})$ the states are almost exclusively dominated by the attractive heavy-light meson-meson component. For the $cn\bar{n}\bar{c}$ state, the attractive $D\bar{D}_1$ component is about 93% using either the attractive or the full physical components. This is in good agreement with Refs. [236, 237], where the authors conclude that the description of the $\psi(4230)$ as a $D\bar{D}_1$ molecule agrees with experimental data. Moreover, the closeness of the $\psi(4230)$ to the $D\bar{D}_1$ threshold, which is the lowest relevant s-wave heavy-light meson-meson threshold in this channel [16, 56, 238], also points towards a strong meson-molecule component in the wavefunction. For the $cs\bar{s}\bar{c}$ state, i.e., the $\psi(4660)$, the internal structure is still heavily debated. The observed decays allow for an interpretation as a hadro-charmonium $\psi(2S)f_0(980)$ [239], a $D_s^{(*)}\bar{D}_{s1}(2536)$ meson-molecule [240] or a p-wave tetraquark $(\mathrm{dq} - \overline{\mathrm{dq}})$ [241]. We find it heavily dominated by the attractive $D_s\bar{D}_{s1}$ component with about 80%, with all other contributions being subleading. We find a similar picture for the hidden-bottom states, where the attractive heavy-light meson-meson components make up about 80% of the state. However, when we include the repulsive colour forces, we see that for the $bn\bar{n}\bar{b}$ state there is a contribution of about 12% coming from the $\langle f_0|f_5\rangle$ correlation, which would be the mixing between the attractive $\bar{B}B^*$ and the repulsive $\Upsilon f_0(1370)$ component.

Last but not least, there is the $0(0^{-+})$ channel. Here we find that the $cn\bar{n}\bar{c}$ is exclusively hadro-charmonium dominated with the $\langle f_1|f_1\rangle$ correlation, i.e., the purely attractive $\chi_{c0}\eta$ physical component, making up almost 100%. With the η being mass degenerate with the π in this work, this incidentally is also the lowest threshold of the considered internal clusters. The situation might change, when taking the $s\bar{s}$ component and the singlet-octet mixing of the η into account. This needs to be explored in future work. Interestingly, for the $bn\bar{n}\bar{b}$ state, using only the attractive colour forces we find the state exclusively dominated by the attractive $\eta_b f_0(1370)$ component. When we include also the repulsive colour forces, this contribution almost vanishes and, similar to the $cn\bar{n}\bar{c}$ case, the pure attractive $\chi_{b0}\eta$ is the most prominent with about 60%. There is also a significant contribution coming from the pure attractive $\bar{B}^* B_1$ component and the $\bar{B}^* B_1 - \chi_{b0}\eta$ mixing.

6.2.2 Open-flavour norm contributions

In Fig. 6.9 we show our obtained norm contributions for the ground states of the open-flavour four-quark states with $J^P = 0^+$ and 1^+. For the scalar open-flavour four-quark states, we labelled the column with a general isospin I, as the states with a $\bar{n}\bar{n}$ antiquark pair have $I = 1$ in this channel and the rest has $I = 0$. The colour coding is again according to the correlations shown in the matrix in Fig. 6.7. We display the heavy quark combination cc, bc, and bb together with the light $(\bar{n}\bar{n})$ and a heavy antiquark pair $(\bar{c}\bar{c})$. As the results for the other heavy quark pairs look very similar, we have omitted these for the sake of clarity. Same goes for the norm contributions of the excited states. For each quantum number, we show the results using only the attractive colour channels (shown in opaque) and the results with the attractive plus repulsive colour forces.

Starting with the $I(J^P) = 0(1^+)$ channel, we find that the $cn\bar{n}\bar{c}$ (T_{cc}^+) state has a very strong contribution coming from the pure attractive DD^* component. For the attractive only basis, the contribution is about 70%, with the rest coming from the $DD^* - A_{cc}S_{\bar{n}\bar{n}}$ mixing and the contribution coming purely from $A_{cc}S_{\bar{n}\bar{n}}$. Switching on the repulsive channels, we find that the state is exclusively dominated by the DD^* component. This behaviour is expected as the mass of the T_{cc}^+ is almost at the DD^* threshold, which renders this state a prime candidate for a meson-molecule. As mentioned in the introduction to this section, we cannot access the internal spatial structure at the present moment. When we consider the bottom partner, i.e., the $bb\bar{n}\bar{n}$ (T_{bb}^-), we see that using only the attractive colour channels, the dominance is very similar to the charm case. The pure attractive $\bar{B}\bar{B}^*$ component is the strongest, followed by the pure $A_{bb}S_{\bar{n}\bar{n}}$ component and the mixing between these two. Including also the repulsive colour forces, the situation changes quite drastically. Now, we find that the strongest contribution is actually coming from the attractive $A_{bb}S_{\bar{n}\bar{n}}$, closely followed by the $\bar{B}\bar{B}^* - A_{bb}S_{\bar{n}\bar{n}}$ mixing and the attractive $\bar{B}\bar{B}^*$ component. There are also contributions of about 10% coming from the mixing of the attractive $\bar{B}\bar{B}^*$ and the attractive $A_{bb}S_{\bar{n}\bar{n}}$ with the repulsive $\bar{B}^*\bar{B}^*$ component.

The situation changes again when we look at the $bc\bar{n}\bar{n}$ state. This state is heavily dominated by the purely attractive $\bar{B}^* D$ component ($> 70\%$), regardless whether we include only the attractive or also the repulsive colour channels. For the attractive only colour forces we have small contributions coming from the attractive $\bar{B}D^*$, the attractive $\bar{B}D^* - \bar{B}^* D$

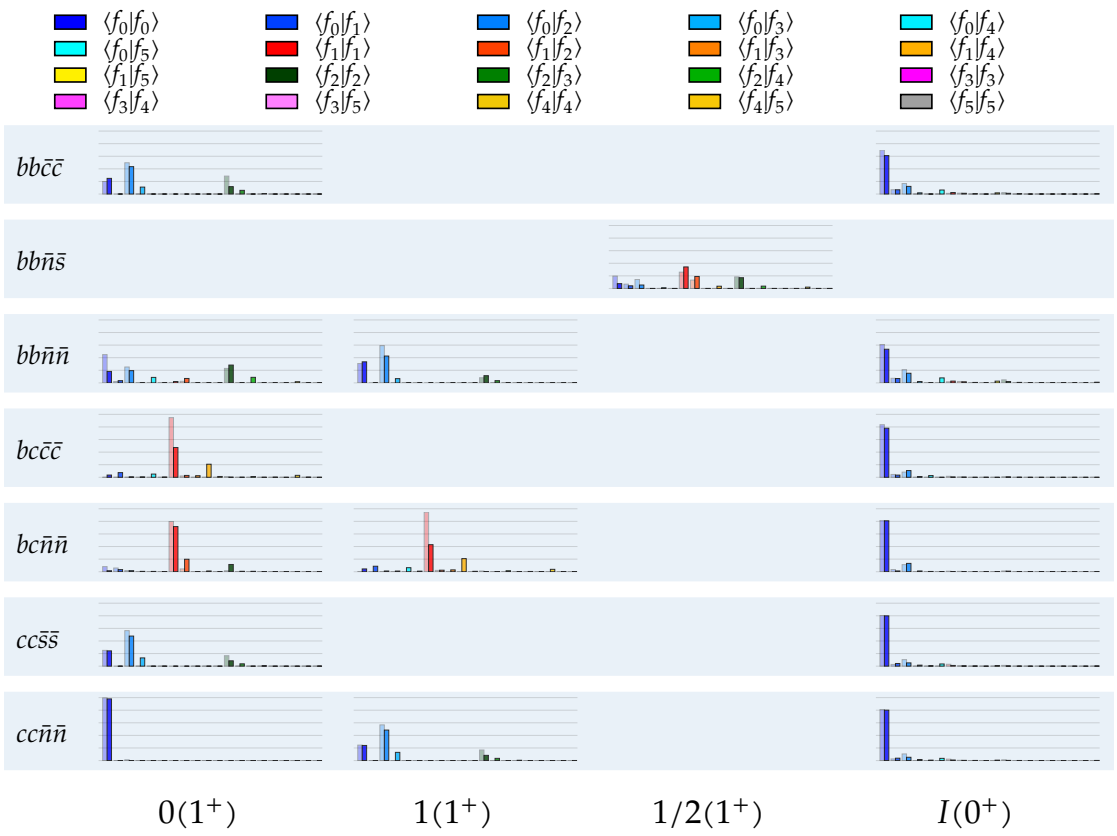

Figure 6.9: Same as in Fig. 6.8 but for the investigated open-flavour four-quark states. The $J^P = 0^+$ is labelled with a general isospin I, see main text for details. We only show the $bc\bar{c}\bar{c}$ and $bb\bar{c}\bar{c}$ as examples for a heavy antiquark pair, as the states with $\bar{s}\bar{s}$ and $\bar{b}\bar{b}$ (the latter antiquark pair is only valid for $bc\bar{q}\bar{q}$) look very similar. Also the norm contributions for the excited states do not differ much and are therefore omitted. Note, that for $I = 1$ the states with $\bar{s}\bar{s}$, $\bar{c}\bar{c}$ or $\bar{b}\bar{b}$ do not exist.

and $\bar{B}^*D - A_{bc}S_{\bar{n}\bar{n}}$ mixing. Including also the repulsive colour forces, the contribution coming from the attractive $\bar{B}^*D - A_{bc}S_{\bar{n}\bar{n}}$ mixing component becomes stronger as does the pure attractive $A_{bc}S_{\bar{n}\bar{n}}$ component. The contributions coming from the $\bar{B}D^*$ cluster decrease in turn. This is very different from the bb and cc case and is probably related to the different symmetries for the bc case [242, 243].

Going to the $I(J^P) = 1(1^+)$ channel, we observe a strikingly different pattern. Here, the $cc\bar{n}\bar{n}$ and $bb\bar{n}\bar{n}$ show a very similar internal dominance, with the mixing component of the attractive heavy-light meson-meson and the attractive diquark-antidiquark cluster contributing the most, closely followed by the attractive meson-meson component. As the $cc\bar{s}\bar{s}$ and $bb\bar{c}\bar{c}$ (for $0(1^+)$) have the same flavour symmetry, they show the same dominance pattern. For the $bc\bar{n}\bar{n}$ state, we find that the pure attractive $\bar{B}^*D$ component gives the biggest contributing with a significant contribution coming from its mixing with the repulsive $\bar{B}^*D^*$ component.

Lastly, we have the $I(J^P) = \frac{1}{2}(1^+)$ channel. Here, we observe a similar pattern of dominant channels for both the attractive only and attractive plus repulsive basis. The

dominant contribution is coming from the purely attractive $\langle f_1|f_1\rangle$ component ($\sim 34\%$), which is the $\bar{B}_s\bar{B}^*$ component (cf. Table 5.4). The attractive $A_{bb}S_{\bar{n}\bar{s}}$ component ($\langle f_2|f_2\rangle$) and its mixing with the attractive $\bar{B}_s\bar{B}^*$ component also contribute about 20%. Interestingly, even though the $\bar{B}_s\bar{B}^*$ and $\bar{B}\bar{B}_s^*$ threshold are very close together ($\sim$ 3 MeV using our two-body masses), the contribution coming from the former is much stronger. Using only the attractive colour forces, we see that the attractive $\bar{B}\bar{B}_s^*$ contributes about 20%, which decreases to sub 10% when including the repulsive colour channels.

In general, we observe that for the $J^P = 1^+$ states the mixing of the attractive components with the repulsive vector-vector meson-meson component seems to be of vital importance to render our results quantitative. Furthermore, the attractive diquark-antidiquark component and its mixings seems to become more important with increasing binding energy of the state.

Going to the $J^P = 0^+$ case, we see that the picture does not change regardless which quark configuration is considered or whether we include only attractive or attractive plus repulsive colour channels. The states in this channel are all mostly dominated by the attractive heavy-light meson-meson component. Going from $QQ' = cc$ over $QQ' = bc$ to $QQ' = bb$, we see that the contribution coming from the pure attractive meson-meson component gets a little smaller, while its mixing with the attractive diquark-antidiquark component increases steadily. For the bb and cc case, there is also some contribution coming from the mixing between the two attractive heavy-light meson-meson components and the attractive meson-meson in the $\mathcal{M}_1$ topology with the repulsive diquark-antidiquark component.

Summary

Inspired by [227–229], we developed and explored a novel method of using the norm contributions to make statements about the internal structure of the four-quark states investigated in this work. This allows to visualize the portion of the different attractive and repulsive physical components and the mixings between them for a given four-quark state. For the hidden-flavour four-quark states (see Fig. 6.8), we find that our results of a dominant heavy-light meson-meson component for the $J^{PC} = 1^{++}$, 0^{++} and 1^{--} agrees with the observed dominant hadronic decay channels. Interestingly, for the 1^{++} we find a significant contribution coming from the mixing of attractive and repulsive colour forces. The situation in the 1^{+-} channels is a little more diverse, as this state seems to be an admixture of the attractive heavy-light meson-meson and the hadro-quarkonium component, with the latter being the dominant part of the wavefunction. Albeit being at odds with the preferred decay channel for this system, there are studies claiming a similar situation [231–234] at least in the charm region. Such studies are at the present missing in the bottom region, where the common picture is that of a $\bar{B}B^*$ meson-molecule for the $T_{b\bar{b}1}(10610)$. Interestingly, the very strong dominance of the $\Upsilon\pi$ component found when only using attractive colour forces reduces drastically when including also the repulsive colour channels, rendering the contribution on par with the one coming from the attractive $\bar{B}B^*$. The 0^{-+} channel is fully dominated by the attractive $\chi_{c0}\eta$ hadro-charmonium component in the charm region. Similarly, the attractive $\chi_{b0}\eta$ component is also the dominant one in the bottom region,

when we consider the attractive plus repulsive forces, with a significant contribution from the attractive $\bar{B}^* B_1$. Comparing this to the attractive only case, there the state was dominated by $\eta_b f_0(1370)$.

For the open-flavour four-quark states (see Fig. 6.9) we find that overall the dominant contributions qualitatively agree when comparing the attractive only with the attractive plus repulsive results. We observe a pure dominance of the attractive heavy-light pseudoscalar-vector meson-meson component in the $J^P = 0^+$ channel, regardless of the internal quark configuration. For the $J^P = 1^+$ states with isospin $I = 0$ (and $I = 1/2$), we see an interesting evolvement of the norm contributions when going from $cc\bar{n}\bar{n}$ over $bc\bar{n}\bar{n}$ to $bb\bar{n}\bar{n}$. For the $cc\bar{n}\bar{n}$ we have a 100% dominance of the attractive DD^* component, probably due to this state being found at the corresponding threshold. The $QQ' = bc$ state, which is very close to the $\bar{B}^* D$ threshold, is dominated by the $\bar{B}^* D$ component, with some contributions coming from other components. For the $QQ' = bb$ states then, which are both deeply bound, we find a very diverse picture of contributions, the strongest coming from the attractive diquark-antidiquark and pseudoscalar-vector meson-meson components and the mixing between them. There are, however, also non-negligible contributions coming from the mixing of these components with repulsive channels. This mixings are probably responsible for rendering our result in quantitative agreement with predictions from the literature, cf. Fig. 6.5. Overall, we observe an increasing importance of the attractive diquark-antidiquark component with increasing binding energy. For the isospin $I = 1$ partner states, we find that for $QQ' = bb$ and cc the states are dominated by the mixing between the attractive meson-meson and diquark-antidiquark components, while the $QQ' = bc$ state is also dominated by the $\bar{B}^* D$ component with a considerable contribution coming from its mixing with the repulsive $\bar{B}^* D^*$ component.

Rest of this page intentionally left blank.

Chapter 7

Conclusions and Outlook

Summary. In this work we used the functional framework of combining Dyson-Schwinger and Bethe-Salpeter/Faddeev-Yakubovsky equations (DSEs and BSEs/FYEs) to investigate the properties of heavy-light four-quark state candidates. Assuming the two-body forces in the four-body FYE to be dominant, one can employ a physically motivated Ansatz for the Bethe-Salpeter amplitude (BSA), which includes all the three possible internal clusterings: two meson-meson and one diquark-antidiquark. Building on [77, 78], which only considered attractive (colour) forces between the internal clusters, we extended this to also include repulsive forces.

With this setup, we focussed on calculating the mass spectra of the ground and first radial excited states for hidden- and open-flavour heavy-light four-quark candidates with total spin $J = 0, 1$ in the charm (~ 4 GeV) and bottom (~ 10 GeV) energy region. To investigate the importance of including also the repulsive forces between the internal clusters, we calculated the mass spectra once with and once without the repulsive forces and compared the two results. Additionally, we compared our results to the obtained experimental values (if available for the considered channel) or predictions coming from other theoretical approaches. Overall, we observe that the inclusion of the repulsive forces leads to an increase in mass and the resulting spectra agree much better with the results from the literature, compared to the spectra using only the attractive forces. Especially, the spectra for states with total spin $J = 1$ are found in very good agreement with literature results. In the hidden-charm and hidden-bottom sector, we quantitatively reproduced the whole experimental spectrum for the $J = 1$ states, while the 0^{++} ground states were consequently found too low. We also predicted a mass region, where the pseudoscalar (0^{-+}) ground and excited states should be looked for. For the open-flavour four-quark candidates, we also find our results for the mass of the T^-_{bb} ($bb\bar{n}\bar{n}$), $T^-_{bb\bar{s}}$ ($bb\bar{n}\bar{s}$), T_{bc} ($bc\bar{n}\bar{n}$) and $T_{cc}(3875)^+$ ($cc\bar{n}\bar{n}$) (with $n = u/d$) states with $J = 1$ in quantitative agreement with results from other theoretical approaches. The corresponding $J = 0$ spectra are again found to be very deeply bound. An approach of neglecting certain internal structures remedies this situation somewhat in this case. This intriguing strong binding of the scalar hidden- and open-flavour four-quark ground states is something that needs to be investigated in future work.

An interesting and highly debated property of four-quark states is their internal composition. Because our physical BSA is a superposition of all three different internal clusterings, our approach does not have an a priori prejudice towards a particular internal configuration. Rather, the underlying dynamics of the equation determine which of the possible

internal clusters is preferred. In this work, we explored a novel method of extracting this information, by considering the norm contributions of the individual internal components of the physical BSA and the mixing between them. This allows us to make more precise statements about the internal composition than was possible in previous works, e.g., [67, 74, 75]. We find that the hidden-flavour four-quark states are largely dominated by the contribution coming from the attractive heavy-light meson-meson component. Only the 0^{-+} and 1^{+-} states have significant contributions coming from the respective hadro-quarkonium components and the mixings with the heavy-light meson-meson component. For the open-flavour four-quark state with $J = 1$, we observe a very diverse picture. While the states very close to heavy-light meson-meson thresholds, i.e., T^{+}_{cc} and T_{bc}, are largely dominated by the respective component, deeply bound states, e.g., T^{-}_{bb} and $T^{-}_{bb\bar{s}}$, get significant contributions also from the diquark-antidiquark components. The $J = 0$ states on the other hand are completely dominated by the lowest heavy-light meson-meson components.

Caveats. While the above results sound overall very exciting, some caveats are in order here. Most of the results for the masses and the norm contributions rely heavily on extrapolation as certain internal singularity structures restrict the range where we can directly solve the four-quark FYE. The corresponding error estimate can nicely be determined via the method described in Appendix C.5.

We cannot, however, currently assess the systematic uncertainties coming from the following sources. First is the systematic uncertainty coming from the Rainbow-Ladder truncation and the employed effective model for the interaction. Furthermore, although the assumption of dominant two-body forces is well-supported by many arguments and a posteriori results, the effect of three- and four-body forces cannot be estimated. We also restricted the Dirac basis elements taken into account to the leading *s*-wave elements, completely neglecting any *p*- *d*- or *f*-wave elements. Although it can be argued, that they might be subleading for states in the vicinity of hadronic *s*-wave decay thresholds, the contributions from these elements may not be negligibly small. Lastly, for this work we restricted the phase space and only considered the central limit, which is quite a rough approximation.

Since we cannot currently provide an error estimation for the above approximations, we wanted to state them here to be kept in mind when looking at the results. Overall, we find that despite all these approximations, our obtained results are very accurate when compared to the literature.

Outlook. The results and developments in this thesis can be taken as basis for further research, as there are quite a few areas where the calculations can be improved. First, at some point it is desirable to replace the effective model for the interaction with a more systematic approach, e.g., system derived from the *n*PI effective action (see, e.g., [244] for an application to the glueball spectrum). In a more complete approach one should include also the three- and four-body forces, at least to estimate how much they contribute in an actual calculation. Moreover, one could systematically relax the approximations mentioned

above and determine a more profound system which is still numerically feasible.

In this work, we only calculated the masses of the four-quark states. Since most of the states in nature are resonances, it would be very interesting to calculate also the decay width of the states. This is possible, by solving the BSE on the first Riemann sheet, using path deformation to go beyond the decay threshold, and searching for the pole structure on the unphysical Riemann sheets via analytic continuation. First results for the light scalar mesons were obtained in the two-body approach in [79]. In the early stages of the thesis project, we also investigated this using the four-body approach. We quickly realized, that the complexity of the phase space and the necessity to find a path deformation dynamic in four variables made this endeavour very complicated. A brief overview of this is provided in Appendix C.3.

Furthermore, since the BSE/FYE is formulated in momentum space, we cannot directly access the spatial structure of the internal components. Applying a three-dimensional Fourier transform, one might be able to calculate quantities like the mean distance $\langle r \rangle$ between the components of the different internal clusters and compare them to predictions from other theoretical approaches. We also started to investigate this, but the obtained results were inconclusive. An introduction can be found in Appendix C.4.

For the $\chi_{c1}(3872)$ and other hidden-flavour four-quark candidates, there is of course the possibility that these states might be a superposition of a conventional $q\bar{q}$ meson and a four-quark meson. To investigate the ratio of conventional to exotic meson for a given state, one can build a coupled system involving the two-body BSE together with the four-body FYE. Using the two-body approach, this has been done in [79]. Although this is also possible with the approach presented in this work, we unfortunately did not manage to do it due to the limited time of the project and relegated it to future work.

For certain quantum numbers, there is also the possibility that the four-quark states can also mix with other exotic mesons, like hybrids or glueballs. In the future, it would also be interesting to couple the different systems and investigate how much each of them contributes for a given hadron.

Lastly, there are many more possible exotic states featuring charm and strange quarks, e.g., the T_{cs} and $T_{c\bar{s}}$ states and all charm states, e.g., $T_{cc\bar{c}\bar{c}}(6900)^0$ and $T_{cc\bar{c}\bar{c}}(6200)$, which can be investigated using the framework presented in this work. Also the possibility of the scalar $D^*_{c0}(2317)^\pm$ and axialvector $D_{s1}(2460)^\pm$ as possible $D_s^+\pi^0$ and $D_s^{*+}\pi^0$ four-quark states would be very interesting to investigate in the future.

Rest of this page intentionally left blank.

Appendix A

Definitions and Conventions

A.1 Units

As is often customary to reduce the notation in Quantum Field Theory, we also use *natural units* throughout this work, i.e.,

$$\hbar = c = 1\,. \tag{A.1}$$

With this we can express every unit, i.e., energy (E), momentum $(\vec{p})$, mass (M), temperature (T), length (L) and time (t) in terms of the typical energy unit of electronvolts (eV) or multiples thereof (keV, MeV, GeV, ...). The following relations hold

$$[E] = [\vec{p}] = [M] = [T] = [L]^{-1} = [t]^{-1}\,. \tag{A.2}$$

Lengths are also frequently given in the unit of femtometres (fm). We can convert between eV and fm via the relation

$$\hbar c = 1 = 0.197\,316\,496\,\text{GeV fm}\,. \tag{A.3}$$

A.2 Euclidean space

Nature can be described very well using a four-dimensional *Minkowski spacetime*. In general, a d-dimensional Minkowski spacetime features a *metric tensor* $\eta^{\mu\nu} = \eta^{\nu\mu} \in \mathbb{R}^{d\times d}$ with one temporal and $d-1$ spatial dimensions given by

$$\eta^{\mu\nu} = \eta_{\mu\nu} = \text{diag}\{1, -1, \dots, -1\}\,, \tag{A.4}$$

with the $\mu, \nu = 0, \dots, d-1$ occurring as Lorentz indices and $\eta_{\mu\nu}$ denoting the inverse metric tensor. A vector x^μ in Minkowski spacetime is denoted with a superscript notation and takes the form $x^\mu := (x^0, \vec{x})$ with $\vec{x} \in \mathbb{R}^{d-1}$. A corresponding *covector* x_μ is denoted by a subscript and is related to the vector x^μ via

$$x_\mu = \eta_{\mu\rho} x^\rho\,. \tag{A.5}$$

A derivative with respect to a vector x^μ produces a covector

$$\partial_\mu := \frac{\partial}{\partial x^\mu} \,. \tag{A.6}$$

Throughout this work we use the *Einstein summation convention*, meaning that if an index μ occurring once as superscript and once as subscript in one single term it is summed over (or *contracted*):

$$x^\mu y_\mu = \sum_\mu x^\mu y_\mu \,. \tag{A.7}$$

Such a contraction can also be written as a dot product

$$x \cdot y := x^\mu y_\mu \,, \tag{A.8}$$

for brevity of if there is risk of confusion.
Furthermore, we make use of the *Feynman slash notation* to indicate a contraction of a vector with a Dirac matrix γ^μ in Eq. (A.20):

$$\not{A} := \gamma^\mu A_\mu \,. \tag{A.9}$$

Written explicitly, the scalar product from Eq. (A.8) in Minkowski spacetime reads

$$x \cdot y = x^\mu y_\mu = x^\mu \eta_{\mu\nu} y^\nu = x^0 y^0 - \sum_{i=1}^{d-1} x^i y^i = x^0 y^0 - \langle \vec{x}, \vec{y} \rangle \,. \tag{A.10}$$

However, due to computational advantages, in this thesis we exclusively consider *Euclidean spacetime* as the convention for the non-perturbative treatment of QCD. The metric tensor in Euclidean spacetime reads

$$\delta^{\mu\nu} = \delta_{\mu\nu} = \mathrm{diag}\{1, 1, \dots, 1\} = \mathbb{I}_d \,, \tag{A.11}$$

where $\mathbb{I}_d$ denotes the d-dimensional unit matrix. To get from Minkowski to Euclidean spacetime it is necessary to perform a *Wick rotation*, i.e, a "rotation" of the temporal component x^0 from the real into the negative imaginary axis while leaving the spatial components unaffected. This corresponds to the following replacement:

$$x^0 \to x_E^d := -i x_M^0 \,, \qquad \vec{x}_E = \vec{x}_M \,. \tag{A.12}$$

Leaving the general case and considering the case realized in nature, i.e., a *four-dimensional spacetime* ($d = 4$) with three spatial and one temporal component, the Euclidean temporal component will furthermore be denoted as x^4. Note, that with the Euclidean spacetime the placement of the index, i.e., super- or subscript formally does not matter because of the metric being the unit matrix. We will, nevertheless, keep using the super- and subscript notation for convenience.

The Minkowski scalar product from Eq. (A.10) turns into

$$x_M \cdot y_M = (-i)^2 x^4 y^4 - \langle \vec{x}, \vec{y} \rangle = -x_E \cdot y_E \,. \tag{A.13}$$

As the Euclidean scalar product differs from the Minkowski one by a minus sign, we get that a four-vector is spacelike, iff

$$x \cdot y > 0 \,. \tag{A.14}$$

It furthermore follows directly that

$$\partial_4 = i\partial_0 \qquad \text{and} \qquad p^4 = ip^0 \,. \tag{A.15}$$

Using the replacement from the Wick rotation in Eq. (A.12) we find that also the integrals get Wick rotated [245]

$$\int_{-\infty(1+i\epsilon)}^{\infty(1+i\epsilon)} \mathrm{d}x^0 \;\to -i \int_{-\infty}^{\infty} \mathrm{d}x^0 \;= \int_{-\infty}^{\infty} \mathrm{d}x^4 \,. \tag{A.16}$$

With that, it is possible to perform the four-dimensional integration

$$\int \frac{\mathrm{d}^4 b}{(2\pi)^4} \tag{A.17}$$

using four-dimensional spherical coordinates (*hyperspherical coordinates*). The integral then reads

$$\int_b := \int \frac{\mathrm{d}^4 b}{(2\pi)^4} = \frac{1}{(2\pi)^4} \int_0^\infty \mathrm{d}b^2 \, \frac{b^2}{2} \int_{-1}^1 \mathrm{d}z \, \sqrt{1-z^2} \int_{-1}^1 \mathrm{d}y \int_0^{2\pi} \mathrm{d}\alpha \,, \tag{A.18}$$

where we have introduced $\int_b$ as a frequently used shorthand.

Fermionic fields in Minkowski or Euclidean spacetime inevitably require the use of the Dirac matrices. Considering a general metric tensor $g^{\mu\nu}$, i.e., $\eta^{\mu\nu}$ and $\delta^{\mu\nu}$ in Minkowski and Euclidean respectively, the Dirac matrices γ^μ have to satisfy the *Clifford algebra*

$$\{\gamma^\mu, \gamma^\nu\} = \gamma^\mu \gamma^\nu + \gamma^\nu \gamma^\mu = 2g^{\mu\nu} \,. \tag{A.19}$$

In principle, we do not need to specify an explicit representation for the Dirac matrices, we only have to demand the following relations to hold

$$\gamma^4 = \gamma^0 \,, \quad \vec{\gamma}_E = i\vec{\gamma}_M \,. \tag{A.20}$$

Assuming the Euclidean Dirac matrices to be Hermitian, we can also define the fifth Dirac

matrix γ_5 as

$$\gamma_5 = -\gamma_1\gamma_2\gamma_3\gamma_4 = -\frac{1}{24}\cdot\varepsilon^{\mu\nu\rho\sigma}\gamma_\mu\gamma_\nu\gamma_\rho\gamma_\sigma\,, \tag{A.21}$$

which has the following properties:

$$(\gamma_5)^\dagger = \gamma_5\,, \quad (\gamma_5)^2 = \mathbb{I}_4\,, \quad \{\gamma_5, \gamma_\mu\} = 0\,. \tag{A.22}$$

A frequently used matrix in this work is the charge conjugation matrix C, which is defined as:

$$C = \gamma^4\gamma^2\,, \quad C^T = C^{-1} = C^\dagger = -C\,, \tag{A.23}$$

with C^T denoting the transpose of the matrix. The Dirac matrices transform under charge conjugation in the following way

$$\begin{aligned} C\gamma_5^T C^T = \gamma_5 \quad &\Leftrightarrow \quad \gamma_5^T = C^T\gamma_5 C\,, \\ C\gamma_\mu^T C^T = -\gamma_\mu \quad &\Leftrightarrow \quad \gamma_\mu^T = C^T(-\gamma_\mu)C\,. \end{aligned} \tag{A.24}$$

A.3 SU(N)

The symmetry group of QCD is the *Lie group* SU(N_c), where $N_c = 3$ is the number of colours realized in nature. It is therefore useful to shortly discuss the structure and properties of the group SU(N) and more importantly its *Lie algebra*.

The group SU(N), which stands for special (S) unitary (U) group, is defined by

$$\mathrm{SU}(N) := \left\{U \in \mathrm{GL}(N,\mathbb{C}) \,|\, U^\dagger U = \mathbb{I}\,, \det(U) = 1\right\}, \tag{A.25}$$

where $\mathrm{GL}(N,\mathbb{C})$ denotes the general linear group over the complex numbers and $U^\dagger = U^{-1}$ is the adjoint matrix $(U^T)^* = (U^*)^T$. The dimension of the group as a real manifold is $N^2 - 1$. Each SU(N) group has an associated Lie algebra denoted by $\mathfrak{su}(N)$ which also has (real) dimension $N^2 - 1$. A Lie algebra is a vector space $\mathfrak{g}$ which is equipped with the *Lie bracket* $[\cdot,\cdot] : \mathfrak{g}\times\mathfrak{g} \to \mathfrak{g}$ as an operation of how elements of the algebra interact with one another. In quantum mechanical context this is also called the commutator. As stated before, this vector space $\mathfrak{g}$ (i.e., the Lie algebra $\mathfrak{su}(N)$) has dimension N^2-1, i.e., it consists of $N^2 - 1$ basis elements t^a, also often called the generators of a Lie group. They have to obey the Lie brackets

$$[t^a, t^b] = if^{ab}{}_c t^c\,, \tag{A.26}$$

where $f^{ab}{}_c$ labels the totally antisymmetric structure constants of the algebra $\mathfrak{su}(N)$ and $a, b, c = 1, \ldots, N^2 - 1$ are the SU(N) indices of the generators. In the context of SU(2) the structure constants f^{abc} are the Levi-Civita symbols ε^{abc}. Given a representation R, a group

element of SU(N) can be written as an exponential map

$$U(\vec{\alpha}) = \exp\left(i \sum_{a=1}^{N^2-1} \alpha_a t^a \right), \tag{A.27}$$

with $\alpha_a \in \mathbb{R}$.

The generators t^a also fulfil an orthogonality relation

$$\mathrm{tr}[t^a t^b] = T(R) \cdot \delta^{ab}, \tag{A.28}$$

where the Dynkin index $T(R)$ depends on the chosen representation. Furthermore, each Lie group has $N-1$ (equal to the rank of the group) Casimir operators $\hat{C}$ that commute with all generators, i.e.,

$$[\hat{C}, t^a] = 0. \tag{A.29}$$

The most-important form of the Casimir operator for our purposes is the quadratic form:

$$(t^a t_a)_{ij} =: C_2(R) \cdot \delta_{ij}, \tag{A.30}$$

with $i, j = 1, \ldots, N$ denoting the colour indices of the fundamental representation and $C_2(R)$ is the quadratic Casimir operator which is also representation dependent.
One can generally distinguish between $N-1$ irreducible representations (R) which are labelled by the Casimir operators. For QCD with $N = N_c = 3$ we therefore have 2 irreducible representations:

Fundamental representation R_F: In the fundamental representation, the generators t^a of a matrix group like SU(N) can be chosen as traceless Hermitian complex $N \times N$ matrices,

$$(t^a)^\dagger = t^a, \qquad \mathrm{tr}[t^a] = 0, \qquad t^a \in \mathbb{C}^{N \times N}. \tag{A.31}$$

For the group SU(2), the generators are proportional to the Pauli matrices. Analogously, for SU(3) they can be given by the *Gell-Mann* matrices $t^a = \lambda^a/2$, with

$$\lambda^1 = \begin{pmatrix} 0 & 1 & 0 \\ 1 & 0 & 0 \\ 0 & 0 & 0 \end{pmatrix}, \qquad \lambda^2 = \begin{pmatrix} 0 & -i & 0 \\ i & 0 & 0 \\ 0 & 0 & 0 \end{pmatrix}, \qquad \lambda^3 = \begin{pmatrix} 1 & 0 & 0 \\ 0 & -1 & 0 \\ 0 & 0 & 0 \end{pmatrix}, \tag{A.32}$$

$$\lambda^4 = \begin{pmatrix} 0 & 0 & 1 \\ 0 & 0 & 0 \\ 1 & 0 & 0 \end{pmatrix}, \qquad \lambda^5 = \begin{pmatrix} 0 & 0 & -i \\ 0 & 0 & 0 \\ i & 0 & 0 \end{pmatrix}, \tag{A.33}$$

$$\lambda^6 = \begin{pmatrix} 0 & 0 & 0 \\ 0 & 0 & 1 \\ 0 & 1 & 0 \end{pmatrix}, \qquad \lambda^7 = \begin{pmatrix} 0 & 0 & 0 \\ 0 & 0 & -i \\ 0 & i & 0 \end{pmatrix}, \qquad \lambda^8 = \frac{1}{\sqrt{3}} \begin{pmatrix} 1 & 0 & 0 \\ 0 & 1 & 0 \\ 0 & 0 & -2 \end{pmatrix}. \tag{A.34}$$

The Dynkin index and the quadratic Casimir operator in the fundamental representation are given by

$$T_F := T(R_F) = \frac{1}{2}, \qquad C_F := C_2(R_F) = \frac{(N^2-1)}{2N}. \tag{A.35}$$

Adjoint representation R_A: In the adjoint representation the generators are represented by $(N^2-1) \times (N^2-1)$ matrices, where the elements are defined by the structure constants

$$(t^a)^{bc} = -if^{abc}. \tag{A.36}$$

The Dynkin index and the quadratic Casimir then read:

$$T_A := T(R_A) = N, \qquad C_A := C_2(R_A) = N. \tag{A.37}$$

Appendix B

Basis construction

B.1 Colour structure of a four-quark state

As stated in Chapter 2, quark and antiquark fields are Dirac spinors which transform under the fundamental representation of SU(N_c). Thus, in colour space the quark and antiquark fields can be represented by the multiplet ($\mathbf{N_c}$) and antimultiplet ($\overline{\mathbf{N}}_\mathbf{c}$) representations respectively. In a four-quark state with two quarks and two antiquarks we combine the respective representations via direct products as

$$\mathbf{N_c} \otimes \mathbf{N_c} \otimes \overline{\mathbf{N}}_\mathbf{c} \otimes \overline{\mathbf{N}}_\mathbf{c}\,, \tag{B.1}$$

to get the overall colour structure of the BSA.

To explicitly calculate the tensor product of the representations, we first introduce Young diagrams (and Young tableaux) [246] as a very convenient way to describe representations. Young diagrams are basically a finite collection of boxes, with each allowed arrangement for a given group uniquely corresponds to an irreducible representation. In the case of SU(N), the fundamental ($\mathbf{N_c}$) and the conjugate ($\overline{\mathbf{N}}_\mathbf{c}$) representation are defined as

$\mathbf{N_c}$:  , $\overline{\mathbf{N}}_\mathbf{c}$: 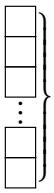 $N_c - 1$,

respectively. With this, the tensor product in Eq. (B.1) given in terms of Young diagrams reads

$\mathbf{N_c} \otimes \mathbf{N_c} \otimes \overline{\mathbf{N}}_\mathbf{c} \otimes \overline{\mathbf{N}}_\mathbf{c} =$ 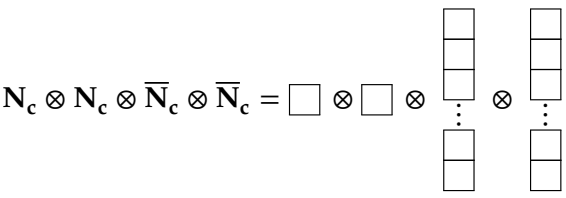 . (B.2)

This representation is all very nice, but the question is still, how do we actually carry out the tensor products. To illustrate this, we consider the direct product $\mathbf{8} \otimes \mathbf{8}$ of SU(3) and label the successive rows of the second diagrams with labels a_1, a_2, a_3 ..., with the

subscript labelling the row number from top to bottom:

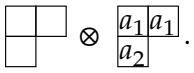

(B.3)

We then attach the labelled boxes from the right Young diagram one at a time to the end of the rows of the left diagram in all possible ways. After that, one needs to check if the obtained diagrams are actually valid Young diagrams. The rules to determine whether an obtained diagram is valid or not are:

1. Diagrams with more than one of each label a_j in the same column are discarded.
2. Generated Young diagrams with the same shape but different arrangement of the labels are kept, while the ones with identical arrangement of labels are discarded.
3. The labels are counted from right to left starting from the top row. The obtained diagram is only valid, if the number of label a_1 (N_{a_1}) is bigger or equal to the number of a_2 (N_{a_2}) etc., i.e., $N_{a_1} \geq N_{a_2} \geq N_{a_3} \geq \ldots$.
4. The number of rows cannot exceed the number of colours N_c.
5. The number of boxes of a row has to be less or equal to the number of boxes of the row above.

For the case given in Eq. (B.3) we start with the first box with a_1 in the top left of the right diagram and obtain:

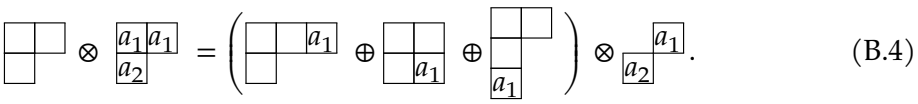

(B.4)

According to the rules above, all of the diagrams are valid for now. We continue by attaching the second box with label a_1 to the obtained result and get

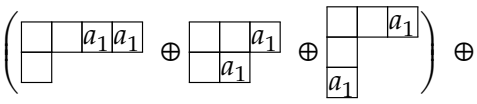

(B.5)

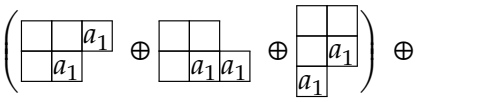

(B.6)

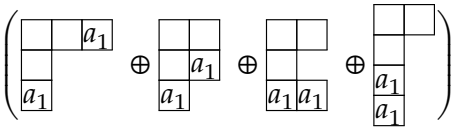

(B.7)

The results are grouped to correspond to the individual results from each of the three diagrams in Eq. (B.4). Before we attach the last box with label a_2 we need to check the validity of the diagrams. The diagrams in Eq. (B.5) are all valid according to the rules above. In Eq. (B.6), we discard the first diagram, as it violates *rule 2*, and the second diagram, which violates *rule 5*. In Eq. (B.7), we discard all diagrams: the first and second violate *rule 2*, the third violates *rule 5* and the last one disobeys *rules 1 and 4*. So in total we

retain only

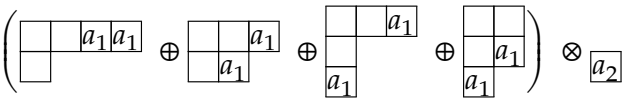

(B.8)

Finally, attaching the box with label a_2 we get

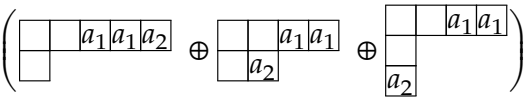

(B.9)

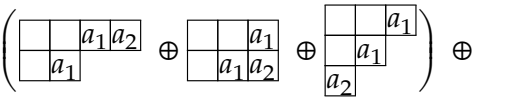

(B.10)

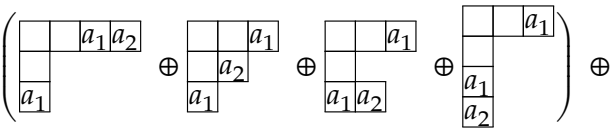

(B.11)

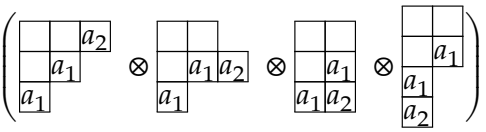

(B.12)

The grouping of results is done in a similar fashion to above. We now only need to check the validity of the individual diagrams to obtain the final result. The diagrams in Eq. (B.9) and Eq. (B.10) are all valid except for the first in each line as they violate *rule 3*. In Eq. (B.11), we discard diagram 1, 3 and 4: the first violates *rule 3*, the third *rule 5* and the last *rule 4*. And for Eq. (B.12) we discard diagrams 1, 2 and 4: the first disobeys *rule 3*, the second violates *rule 5* and the last again violates *rule 4*. The final result of the tensor product in Eq. (B.3) in terms of Young diagrams is then:

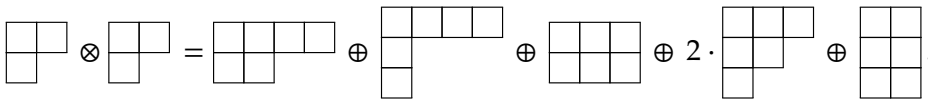

(B.13)

Now we know how to decompose the tensor product of irreducible representations into a direct sum of irreducible representation with the help of Young diagrams. However, we still do not know, how to obtain the dimension of the obtained representations. For this, we need to consider how one gets the dimension of the representation from the corresponding Young diagram. The dimension d of a Young diagram is obtained by the ratio $d = A/B$, with A and B specified in the following. For any SU(N) Young diagram λ, to calculate the factor A, we start filling the boxes by inserting the number N into the top left box. The rest of the diagram is filled by obeying two rules: when going to the right, the number of the previous box is *increased* by one and when moving to the bottom, the number of the previous box is *decreased* by one. The factor A is then calculated by the product of the box

entries, i.e.,

$$A = \prod_{s=1}^{N_\lambda} A_s \,, \tag{B.14}$$

with s the box index, N_λ the number of boxes in the diagram and A_s labelling the number in the respective box. The factor B is also calculated by filling the corresponding Young diagram with numbers. But in contrast to A, we now put the number of boxes *below*, also called **leg length** $l_\lambda(s)$, plus the number of boxes to the *right*, also called **arm length** $a_\lambda(s)$, of the current box s plus **one** into each box. This sum is also called the *hook length* $h_\lambda(s) = l_\lambda(s) + a_\lambda(s) + 1$. The factor B is then calculated as the product of the hook lengths:

$$B = \prod_{s=1}^{N_\lambda} h_\lambda(s) \,, \tag{B.15}$$

with s again labelling the boxes. The dimension d of a Young diagram is therefore obtained by

$$d = \prod_{s=1}^{N_\lambda} \frac{A_s}{h_\lambda(s)} \,. \tag{B.16}$$

As an example, we consider an arbitrary irreducible representation of SU(N). To calculate the numerator A we first fill the diagram as

N	$N+1$	$N+2$
$N-1$	N	
$N-2$		

, (B.17)

and obtain A in this case as

$$A = N \cdot (N+1) \cdot (N+2) \cdot (N-1) \cdot N \cdot (N-2) \,. \tag{B.18}$$

To obtain the denominator B, we fill the diagram with the hook lengths of the individual boxes, which for our case reads

5	3	1
3	1	
1		

, (B.19)

and determine B as

$$B = 5 \cdot 3 \cdot 3 \cdot 1 \cdot 1 \cdot 1 = 45 \,. \tag{B.20}$$

The dimension of our chosen Young diagram is therefore

$$d = \frac{N \cdot (N+1) \cdot (N+2) \cdot (N-1) \cdot N \cdot (N-2)}{45} \xrightarrow{N=3} 8\,. \tag{B.21}$$

Applying this to the obtained result in Eq. (B.13) of our SU(3) example of $\mathbf{8} \otimes \mathbf{8}$ in Eq. (B.3) we get

$$\mathbf{8} \otimes \mathbf{8} = \mathbf{27} \oplus \mathbf{10} \oplus \overline{\mathbf{10}} \oplus 2 \cdot \mathbf{8} \oplus \mathbf{1}\,, \tag{B.22}$$

where the second to last diagram is obtained twice during the tensor product decomposition.

Applying all of the above to the original direct product we wanted to consider for the four-quark states in Eq. (B.2), we get

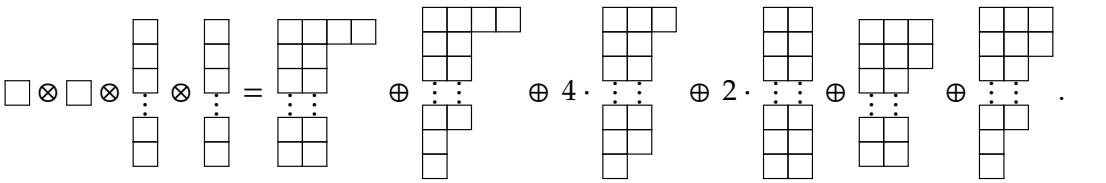

(B.23)

The individual obtained diagrams and the dimension of the associated irreducible representation are collected in Table B.1 for a general SU(N_c) as well as the special cases $N_c = 3$, $N_c = 4$ and $N_c = 5$. Numerical factors in front of the representations denote the multiplicity of that representation obtained during the decomposition of the direct products. Interestingly, the diagram in the last row of Table B.1 vanishes for the case of $N_c = 3$.

One can also first group Eq. (B.1) according to the internal diquark-antidiquark ($\mathcal{D}$) and meson-meson ($\mathcal{M}$) clusterings to get

$$\mathcal{D}: \quad (\mathbf{N_c} \otimes \mathbf{N_c}) \otimes (\overline{\mathbf{N}}_\mathbf{c} \otimes \overline{\mathbf{N}}_\mathbf{c})\,, \tag{B.24}$$

$$\mathcal{M}: \quad (\mathbf{N_c} \otimes \overline{\mathbf{N}}_\mathbf{c}) \otimes (\mathbf{N_c} \otimes \overline{\mathbf{N}}_\mathbf{c})\,. \tag{B.25}$$

Then one can first solve the direct products in the brackets and afterwards take the direct product of the terms in the brackets. Doing this, one can identify which direct product of representations produces the two singlet structures. We start with the diquark-antidiquark clustering. Using the Young diagram notation again, the direct products in the brackets evaluate to

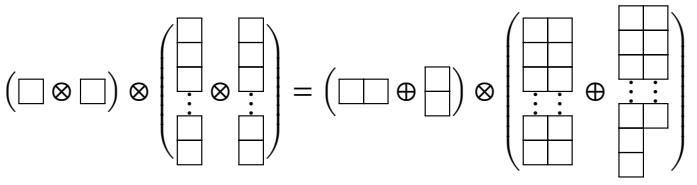

(B.26)

General N_c	d	$N_c = 3$	d	$N_c = 4$	d	$N_c = 5$	d
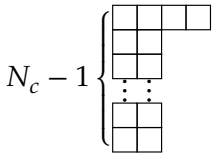	$\frac{N_c^2(N_c+3)(N_c-1)}{4}$	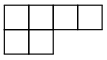	**27**	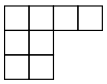	**84**	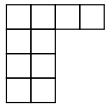	**200**
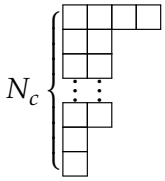	$\frac{(N_c^2-1)(N_c^2-4)}{4}$	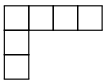	**10**	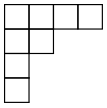	**45**	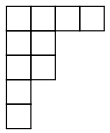	**126**
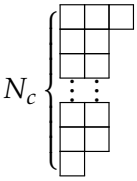	(N_c^2-1)		**8**	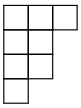	**15**	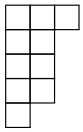	**24**
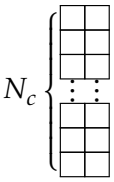	**1**		**1**	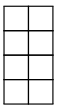	**1**	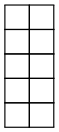	**1**
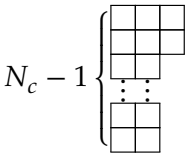	$\overline{\frac{(N_c^2-1)(N_c^2-4)}{4}}$		$\overline{\mathbf{10}}$		$\overline{\mathbf{45}}$	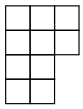	$\overline{\mathbf{126}}$
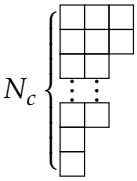	$\frac{N_c^2(N_c-3)(N_c+1)}{4}$	–	–	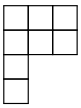	**20′** [a]	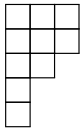	**75**

Table B.1: SU(N_c) Young diagrams and associated irreducible representations obtained from the tensor product in Eq. (B.1). We also show the specific Young diagrams and representations for the special cases $N_c = 3$, $N_c = 4$ and $N_c = 5$..

[a] This is a symmetric, traceless representation known as 20-prime representation.

This corresponds to the representations

$$\left(\frac{\mathbf{N_c(N_c+1)}}{\mathbf{2}} \oplus \frac{\mathbf{N_c(N_c-1)}}{\mathbf{2}}\right) \otimes \left(\frac{\mathbf{N_c(N_c+1)}}{\mathbf{2}} \oplus \frac{\mathbf{N_c(N_c-1)}}{\mathbf{2}}\right) . \tag{B.27}$$

We refrain from showing which of the representations is conjugate, as this is different for each N_c. Expanding the result from Eq. (B.26) we get

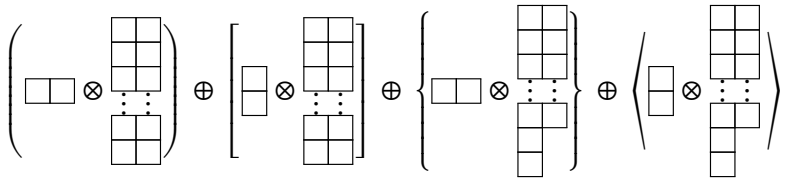

(B.28)

Evaluating the direct products in the brackets again, we get

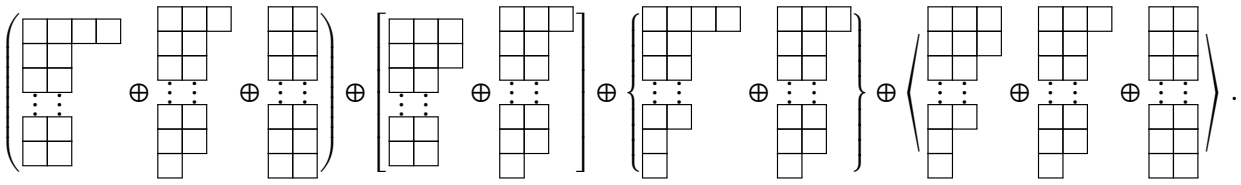

We see, that the two singlets are obtained from the direct products in the $(\ldots)$ and the last $\langle\ldots\rangle$ brackets. These direct products correspond to combining

$$\frac{\mathbf{N_c(N_c+1)}}{\mathbf{2}} \otimes \frac{\mathbf{N_c(N_c+1)}}{\mathbf{2}} = \mathbf{1}_c \oplus \ldots \quad \text{and} \quad \frac{\mathbf{N_c(N_c-1)}}{\mathbf{2}} \otimes \frac{\mathbf{N_c(N_c-1)}}{\mathbf{2}} = \mathbf{1}_c \oplus \ldots , \tag{B.29}$$

respectively. For the case $N_c = 3$ realized in nature, we therefore get

$$\mathbf{6} \otimes \bar{\mathbf{6}} = \mathbf{1}_c \oplus \ldots \quad \text{and} \quad \bar{\mathbf{3}} \otimes \mathbf{3} = \mathbf{1}_c \oplus \ldots . \tag{B.30}$$

This corresponds to the expression in Eq. (5.16).

Considering now the case of internal meson-meson clustering. Writing Eq. (B.25) in Young diagram notation and evaluating the direct products yields

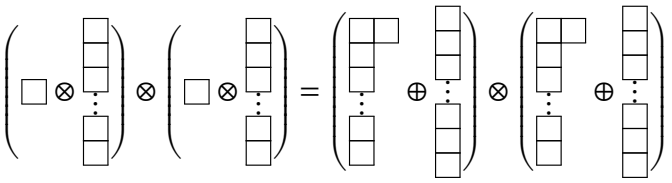

(B.31)

The result corresponds to the following combination of representations

$$\left((\mathbf{N_c^2-1}) \oplus \mathbf{1}_c\right) \otimes \left((\mathbf{N_c^2-1}) \oplus \mathbf{1}_c\right) . \tag{B.32}$$

Expanding the result from Eq. (B.31) we get

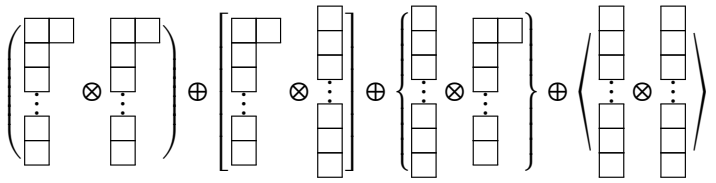

(B.33)

We can now evaluate the direct products in the different brackets to obtain

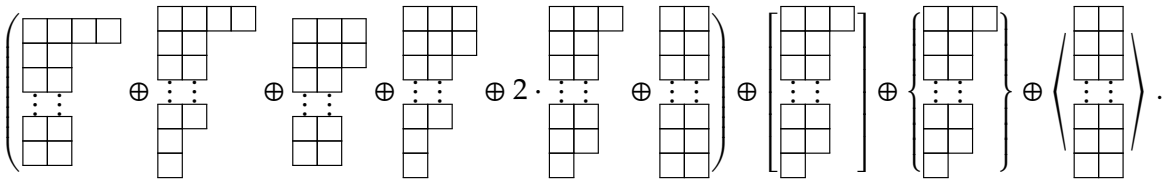

We see, that the singlets are obtained from the direct product in the $(\ldots)$ and $\langle\ldots\rangle$ brackets, which correspond to the direct products of the representations

$$(\mathbf{N_c^2-1})\otimes(\mathbf{N_c^2-1}) = \mathbf{1}_c \oplus \ldots \quad \text{and} \quad \mathbf{1}_c \otimes \mathbf{1}_c = \mathbf{1}_c\,, \tag{B.34}$$

respectively. For the case $N_c = 3$, the representation $(\mathbf{N_c^2-1}) = \mathbf{8_c}$. The expressions in Eq. (B.34) are the ones shown in Eq. (5.17).

B.1.1 Colour traces in the four-quark FYE

The basis elements for the colour part of the BSA are the colour singlet structures $\Gamma_C \in \{C_{\mathbf{11}}, C'_{\mathbf{11}}, C_{\bar{\mathbf{3}}\mathbf{3}}, C_{\mathbf{88}}, C'_{\mathbf{88}}, C_{\mathbf{6}\bar{\mathbf{6}}}\}$, which are given in Eqs. (5.18) and (5.19). In Section 5.2 we identified the colour projectors to be just the same singlets transposed $\mathbb{P}^C \in \{(C_{\mathbf{11}})^T, (C'_{\mathbf{11}})^T, (C_{\bar{\mathbf{3}}\mathbf{3}})^T, (C_{\mathbf{88}})^T, (C'_{\mathbf{88}})^T, (C_{\mathbf{6}\bar{\mathbf{6}}})^T\}$. Because $2/3$ of the colour singlets are just linear combinations of the two singlets $C_{\mathbf{11}}$ and $C'_{\mathbf{11}}$, it is sufficient to consider only these two elements in the following. All other results can be constructed by combining the results obtained using these two singlets. Acting with the projectors on the left-hand side of the four-quark FYE in Eq. (5.41), we get the following results of the trace

$$\mathrm{tr}\left\{\mathbb{P}_i^C \cdot \Gamma_C^j\right\}_{i,j\in\{0,1\}} = \begin{pmatrix} 1 & C_A - 2\cdot C_F \\ C_A - 2\cdot C_F & 1 \end{pmatrix} = \begin{pmatrix} 1 & \frac{1}{N_c} \\ \frac{1}{N_c} & 1 \end{pmatrix}, \tag{B.35}$$

with C_A and C_F the quadratic Casimir operators in the adjoint and fundamental representation, see Eqs. (A.35) and (A.37).

Moving on to the right-hand side of the four-quark FYE in Eq. (5.41), we find that for our two-body forces in the four-quark kernel, the traces we need to evaluate are of the form

$$M_2 = \mathrm{tr}\left\{\mathbb{P}_i^C \cdot t_a \cdot t^a \cdot \Gamma_C^j\right\}_{i,j\in\{0,1\}}, \tag{B.36}$$

where t_a are the SU(N_c) generators. We will again only display the results obtained using the singlets $C_{\mathbf{11}}$ and $C'_{\mathbf{11}}$, as the other results can be obtained by combining the matrix elements accordingly. The result of the traces in Eq. (B.36) differs, depending on the interaction topology of the diagram:

$$M_2^{(13)(24)} = \begin{pmatrix} C_F & \frac{C_F}{C_A} \\ \frac{C_F}{C_A} & 0 \end{pmatrix}, \quad M_2^{(14)(23)} = \begin{pmatrix} 0 & \frac{C_F}{C_A} \\ \frac{C_F}{C_A} & C_F \end{pmatrix}, \quad M_2^{(12)(34)} = \begin{pmatrix} 0 & \frac{C_F}{C_A} \\ \frac{C_F}{C_A} & 0 \end{pmatrix}. \tag{B.37}$$

The number in the brackets given as superscript denotes the quarks connected via the gluon exchanges. Using the explicit forms of C_A and C_F given in Eqs. (A.35) and (A.37) we can write the above matrices as

$$\begin{aligned} M_2^{(13)(24)} &= \begin{pmatrix} \frac{(N_c^2-1)}{2N_c} & \frac{(N_c^2-1)}{2N_c^2} \\ \frac{(N_c^2-1)}{2N_c^2} & 0 \end{pmatrix}, \quad M_2^{(14)(23)} = \begin{pmatrix} 0 & \frac{(N_c^2-1)}{2N_c^2} \\ \frac{(N_c^2-1)}{2N_c^2} & \frac{(N_c^2-1)}{2N_c} \end{pmatrix}, \\ M_2^{(12)(34)} &= \begin{pmatrix} 0 & \frac{(N_c^2-1)}{2N_c^2} \\ \frac{(N_c^2-1)}{2N_c^2} & 0 \end{pmatrix}. \end{aligned} \tag{B.38}$$

For completeness, one can also look at the traces on the right-hand side that one would need to evaluate if the three- and four-body forces in Fig. 5.1 were included. The following considerations are made using our physical BSA based on dominant internal two-body states. For the three- and four-body forces we get the following traces on the right-hand side

$$\begin{aligned} M_3 &= f^{abc} \mathrm{tr}\left\{ \mathbb{P}_i^{\mathrm{C}} \cdot t_a \cdot t_b \cdot t_c \cdot \Gamma_{\mathrm{C}}^j \right\}_{i,j\in\{0,1\}}, \\ M_4 &= \left(f^{xab} f_x{}^{cd} + f^{xac} f_x{}^{bd} + f^{xad} f_x{}^{bc} \right) \mathrm{tr}\left\{ \mathbb{P}_i^{\mathrm{C}} \cdot t_a \cdot t_b \cdot t_c \cdot t_d \cdot \Gamma_{\mathrm{C}}^j \right\}_{i,j\in\{0,1\}}, \end{aligned} \tag{B.39}$$

with f^{abc} denoting the SU(N_c) structure constants with the indices a, b, c, d, x the adjoint colour index. Evaluating the traces in Eq. (B.39), we get

$$M_3^{(123)4} = M_3^{(234)1} = \begin{pmatrix} 0 & -\frac{iC_F}{2} \\ \frac{iC_F}{2} & 0 \end{pmatrix}, \tag{B.40}$$

$$M_3^{(134)2} = M_3^{(124)3} = \begin{pmatrix} 0 & \frac{iC_F}{2} \\ -\frac{iC_F}{2} & 0 \end{pmatrix} \tag{B.41}$$

and

$$M_4^{(1234)} = \begin{pmatrix} 0 & -\frac{C_A C_F}{2} \\ -\frac{C_A C_F}{2} & -C_F \end{pmatrix}, \tag{B.42}$$

with the superscript again denoting the quarks connected via the three- and four-gluon vertices. Using the explicit forms of the Casimir operators again, we can write

$$M_3^{(123)4} = M_3^{(234)1} = \begin{pmatrix} 0 & -\frac{i\left(N_c^2-1\right)}{4N_c} \\ \frac{i\left(N_c^2-1\right)}{4N_c} & 0 \end{pmatrix}, \tag{B.43}$$

$$M_3^{(134)2} = M_3^{(124)3} = \begin{pmatrix} 0 & \frac{i\left(N_c^2-1\right)}{4N_c} \\ -\frac{i\left(N_c^2-1\right)}{4N_c} & 0 \end{pmatrix} \tag{B.44}$$

and

$$M_4^{(1234)} = \begin{pmatrix} 0 & -\frac{\left(N_c^2-1\right)}{4} \\ -\frac{\left(N_c^2-1\right)}{4} & -\frac{\left(N_c^2-1\right)}{2N_c} \end{pmatrix}. \tag{B.45}$$

In the above context, it is interesting to consider the large N_c limit of QCD [247], where one sends $N_c \to \infty$ but keeps the combination $g^2 N_c$ fixed. From this it immediately follows that the coupling has to go like $g \sim 1/\sqrt{N_c}$. The colour traces in Eq. (B.35) for the left-hand side of the FYE becomes diagonal in this limit. For the two-body interactions on the right-hand side, we add a factor of g^2 from the two quark-gluon vertices to M_2 in Eq. (B.38) and then consider the limit $N_c \to \infty$. Doing so, we find

$$\lim_{N_c\to\infty} g^2 M_2^{(13)(24)} = \lim_{N_c\to\infty} \begin{pmatrix} \frac{\left(N_c^2-1\right)}{2N_c^2} & \frac{\left(N_c^2-1\right)}{2N_c^3} \\ \frac{\left(N_c^2-1\right)}{2N_c^3} & 0 \end{pmatrix} = \lim_{N_c\to\infty} \begin{pmatrix} \frac{1}{2} & \frac{1}{2N_c} \\ \frac{1}{2N_c} & 0 \end{pmatrix}, \tag{B.46}$$

$$\lim_{N_c\to\infty} g^2 M_2^{(14)(23)} = \lim_{N_c\to\infty} \begin{pmatrix} 0 & \frac{1}{2N_c} \\ \frac{1}{2N_c} & \frac{1}{2} \end{pmatrix}, \tag{B.47}$$

$$\lim_{N_c\to\infty} g^2 M_2^{(12)(34)} = \lim_{N_c\to\infty} \begin{pmatrix} 0 & \frac{1}{2N_c} \\ \frac{1}{2N_c} & 0 \end{pmatrix}. \tag{B.48}$$

For the meson-meson diagrams, the traces evaluated using the corresponding native colour singlet in this interaction topology give a constant value of $\frac{1}{2}$ while every other combination is suppressed by $1/N_c$. Interestingly, the colour traces for the diquark-antidiquark type diagrams are completely suppressed in the large N_c limit.

Moving on to the three-body forces, which get a factor of g^4 due to the three quark-gluon (g^3) vertices and the three-gluon (g) vertex, we have

$$\lim_{N_c\to\infty} g^4 M_3^{(123)4} = \lim_{N_c\to\infty} \begin{pmatrix} 0 & -\frac{i\left(N_c^2-1\right)}{4N_c^3} \\ \frac{i\left(N_c^2-1\right)}{4N_c^3} & 0 \end{pmatrix} = \lim_{N_c\to\infty} \begin{pmatrix} 0 & -\frac{i}{4N_c} \\ \frac{i}{4N_c} & 0 \end{pmatrix}, \tag{B.49}$$

$$\lim_{N_c\to\infty} g^4 M_3^{(134)2} = \lim_{N_c\to\infty} \begin{pmatrix} 0 & \frac{i}{4N_c} \\ -\frac{i}{4N_c} & 0 \end{pmatrix}. \tag{B.50}$$

Therefore, the three-body forces are suppressed by $\frac{1}{N_c}$ in the large N_c limit.

Lastly, considering the four-body force, they get a factor g^6 from the four quark-gluon (g^4) vertices and the four-gluon (g^2) vertex. Therefore, Eq. (B.45) becomes

$$\lim_{N_c\to\infty} g^6 M_4(1234) = \lim_{N_c\to\infty} \begin{pmatrix} 0 & -\frac{(N_c^2-1)}{4N_c^3} \\ -\frac{(N_c^2-1)}{4N_c^3} & -\frac{(N_c^2-1)}{2N_c^4} \end{pmatrix} = \lim_{N_c\to\infty} \begin{pmatrix} 0 & -\frac{1}{4N_c} \\ -\frac{1}{4N_c} & -\frac{1}{N_c^2} \end{pmatrix}. \tag{B.51}$$

Similar to the three-body forces, also the four-body forces are suppressed by factors of $\frac{1}{N_c}$ or $\frac{1}{N_c^2}$ in the limit $N_c \to \infty$.

From the considerations above one might cautiously draw the following conclusion. Considering only gluon exchanges as a means of interaction between the quarks, the suppression of the three- and four-body forces in the large N_c limit supports the assumption that the two-body interactions might be dominant. Furthermore, the contributions coming from the diquark-antidiquark type interactions seem to vanish for large N_c.

	ϕ_j	$\psi^+_{1,2}$	ψ^-_1	ψ^-_2	ψ_3	ψ_4	ψ_5	ψ_6	ψ_7
(14)(23)	ϕ_j	$-\psi^+_{1,2}$	ψ^-_1	$-\psi^-_2$	$-\psi_3$	ψ_4	$-\psi_6$	$-\psi_5$	$-\psi_7$

Table B.2: Charge conjugation transformation in (14)(23) of the Dirac tensors in Table 5.2.

B.2 Physical BSA for four-quark states

In Section 5.1 we introduced and discussed the Dirac, colour and flavour parts of the Bethe-Salpeter amplitude in the case of a four-quark state. Furthermore, in Section 5.2 we introduced the physically motivated BSA and the approximations coming with it. We mentioned several times, that the Dirac part of the physical BSA consists of linear combinations of the tensors given in Table 5.2. The transformation properties of these tensors under charge conjugation symmetry in (14)(23) and Pauli antisymmetry under (12) or (34) are compiled in Tables B.2 and B.6. As in the main text, the numbers in the brackets label the quarks which are exchanged. In this section, we want to explicitly construct the physical four-quark BSAs for the states investigated in this work.

B.2.1 Hidden-flavour physical BSA

We will first consider the physical basis for the hidden-flavour heavy-light four-quark states $(Qq\bar{q}\bar{Q})$, with $Q \neq q$ and with quantum numbers $I\left(J^{PC}\right) = 0\,(1^{++})$, $1\,(1^{+-})$, $0\,(0^{++})$, $0\,(1^{--})$, $0\,(0^{-+})$. We know from the discussion above Eq. (5.22) that the colour singlets in Eqs. (5.18) and (5.19) as well as the flavour BSA in this case all have positive C-parity under (14)(23). Thus, the only BSA part which determines the correct C-parity transformation of the BSA is the Dirac part.

$0\,(1^{++})$

Starting out with the $0\,(1^{++})$ channel, we know from the main text, that the chosen sub-clusters in the respective topologies are: $(Q\bar{q})_{0^-} \otimes \left(q\bar{Q}\right)_{1^-}$ for the $\mathcal{M}_1$, $\left(Q\bar{Q}\right)_{1^{--}} \otimes (q\bar{q})_{1^{--}}$ for $\mathcal{M}_2$ and $(Qq)_{0^+} \otimes \left(\bar{q}\bar{Q}\right)_{1^+}$ for $\mathcal{D}$. We thus only need to look at Table 5.2 to see which tensors ψ_i match the chosen combinations in the sub-clusters and then look at Table B.2 which combination gives the correct sign under charge conjugation symmetry. For the present case, we need the final Dirac tensors to have positive C-parity. The tensors which match all the criteria from above for the present state are

$$\Xi_{\mathrm{D};0(1^{++})} = \left\{\psi^-_1,\, \psi_4,\, \psi_5 - \psi_6\right\}, \tag{B.52}$$

for the $\mathcal{M}_1$, $\mathcal{M}_2$ and $\mathcal{D}$ interaction topology respectively. The linear combination $\psi_5 - \psi_6$ is chosen here, as the individual tensors ψ_5 and ψ_6 transform into each other under charge conjugation symmetry in (14)(23). Only the linear combination has a definite C-parity with a positive sign.

$1\,(1^{+-})$

The procedure is the same for the rest of the hidden-flavour four-quark states. For the $1\,(1^{+-})$ channel, the sub-clusters which result in the overall quantum number of the four-quark state are:

- $\left\{(Q\bar{q})_{0^-} \otimes (q\bar{Q})_{1^-}\,,\, (Q\bar{q})_{1^-} \otimes (q\bar{Q})_{1^-}\right\}$ for $\mathcal{M}_1$,
- $\left\{(Q\bar{Q})_{1^{--}} \otimes (q\bar{q})_{0^{-+}}\,,\, (Q\bar{Q})_{0^{-+}} \otimes (q\bar{q})_{1^{--}}\right\}$ for $\mathcal{M}_2$ and
- $\left\{(Qq)_{0^+} \otimes (\bar{q}\bar{Q})_{1^+}\,,\, (Qq)_{1^+} \otimes (\bar{q}\bar{Q})_{1^+}\right\}$ for $\mathcal{D}$.

As mentioned in the main text in Section 5.2, we only take one internal two-body cluster for each topology into account. To decide, which of the ones given above will be chosen, we look at the combined masses of the two-body states involved in the sub-clusters. For each interaction topology, we then choose the one with the lower of the two combined masses, as it will affect the equation earlier and thus can be assumed as dominant. For the $1\,(1^{+-})$ with quark content $cn\bar{n}\bar{c}$, i.e., the $T_{c\bar{c}1}(3900)$, the above sets become $\left\{D\bar{D}^*, D^*\bar{D}^*\right\}$ for $\mathcal{M}_1$, $\left\{J/\psi\pi, \eta_c\rho\right\}$ for $\mathcal{M}_2$ and $\left\{S_{cn}A_{\bar{n}\bar{c}}, A_{cn}A_{\bar{n}\bar{c}}\right\}$ for $\mathcal{D}$. Taking the masses from Table 4.2, we see that the lowest thresholds are $D\bar{D}^*$, $J/\psi\pi$ and $S_{cn}A_{\bar{n}\bar{c}}$ for the three topologies respectively. Checking the tensors in Table 5.2 and the corresponding transformation property under charge conjugation, i.e., negative C-parity under $(14)(23)$, we find that the set

$$\Xi_{\mathrm{D};1(1^{+-})} = \left\{\psi_1^+,\, \psi_2^+ - \psi_2^-,\, \psi_5 + \psi_6\right\}\,, \tag{B.53}$$

correspond to the chosen internal structures from above. Forming the linear combinations $\psi_2^+ \pm \psi_2^-$, disentangles the two combinations within the $\psi_2^\pm$ tensor, i.e., $J/\psi\pi$ and $\eta_c\rho$. The combination $\psi_2^+ - \psi_2^-$ yields $2 \cdot \gamma_\perp^\mu \otimes \gamma^5$, which is the Dirac basis element describing the $J/\psi\pi$ combination.

$0\,(0^{++})$

Moving on to the scalar $0\,(0^{++})$ channel, we have the following possible sub-clusters:

- $\left\{(Q\bar{q})_{0^-} \otimes (q\bar{Q})_{0^-}\,,\, (Q\bar{q})_{1^-} \otimes (q\bar{Q})_{1^-}\right\}$ for $\mathcal{M}_1$,
- $\left\{(Q\bar{Q})_{0^{-+}} \otimes (q\bar{q})_{0^{-+}}\,,\, (Q\bar{Q})_{1^{--}} \otimes (q\bar{q})_{1^{--}}\right\}$ for $\mathcal{M}_2$ and
- $\left\{(Qq)_{0^+} \otimes (\bar{q}\bar{Q})_{0^+}\,,\, (Qq)_{1^+} \otimes (\bar{q}\bar{Q})_{1^+}\right\}$ for $\mathcal{D}$.

Considering the $cn\bar{n}\bar{c}$ state again, we chose the two heavy-light pseudoscalar states $(D\bar{D})$ for the $\mathcal{M}_1$ topology, the heavy-heavy vector and light-light vector $(J/\psi\omega)$ for the $\mathcal{M}_2$ topology and the heavy-light scalar diquark-antidiquark pair $(S_{cn}S_{\bar{n}\bar{c}})$. Even though the $\eta_c\eta$ combination is the lightest one in the $\mathcal{M}_2$ topology, we did not choose it, as the η is mass degenerate with the π in this work (cf. caption of Table 4.2). Thus, the threshold where the singularity enters the integration domain is not representative of the physical one. Once the η mass can be determined more accurately in our framework, this combination should definitely be included. Again, checking Table B.2 for the C-parity of the basis tensors in

d	$J^P = 0^-$	$J^P = 1^-$
$\mathcal{M}_1$	$\tilde{\phi}_1 = \delta_{\alpha_1\alpha_3}\gamma^5_{\alpha_2\alpha_4}$	$\tilde{\psi}_1^{\pm} = \left(\gamma^5_{\alpha_1\alpha_3}(\gamma^5\gamma_\perp^\mu)_{\alpha_2\alpha_4} \pm (\gamma^5\gamma_\perp^\mu)_{\alpha_1\alpha_3}\gamma^5_{\alpha_2\alpha_4}\right)$
$\mathcal{M}_1$	$\tilde{\phi}_2 = \gamma^5_{\alpha_1\alpha_3}\delta_{\alpha_2\alpha_4}$	$\tilde{\psi}_2^{\pm} = \left(\delta_{\alpha_1\alpha_3}(\gamma_\perp^\mu)_{\alpha_2\alpha_4} \pm (\gamma_\perp^\mu)_{\alpha_1\alpha_3}\delta_{\alpha_2\alpha_4}\right)$
$\mathcal{M}_2$	$\tilde{\phi}_3 = \delta_{\alpha_1\alpha_4}\gamma^5_{\alpha_2\alpha_3}$	$\tilde{\psi}_3^{\pm} = \left(\gamma^5_{\alpha_1\alpha_4}(\gamma^5\gamma_\perp^\mu)_{\alpha_2\alpha_3} \pm (\gamma^5\gamma_\perp^\mu)_{\alpha_1\alpha_4}\gamma^5_{\alpha_2\alpha_3}\right)$
$\mathcal{M}_2$	$\tilde{\phi}_4 = \gamma^5_{\alpha_1\alpha_4}\delta_{\alpha_2\alpha_3}$	$\tilde{\psi}_4^{\pm} = \left(\delta_{\alpha_1\alpha_4}(\gamma_\perp^\mu)_{\alpha_2\alpha_3} \pm (\gamma_\perp^\mu)_{\alpha_1\alpha_4}\delta_{\alpha_2\alpha_3}\right)$
$\mathcal{M}_1$	$\tilde{\phi}_5 = (\gamma_\perp^\mu)_{\alpha_1\alpha_3}(\gamma^5\gamma_\mu^\perp)_{\alpha_2\alpha_4}$	$\tilde{\psi}_5 = \varepsilon^{\mu\nu\rho\sigma}\hat{P}_\nu(\gamma_\rho)_{\alpha_1\alpha_3}(\gamma^5\gamma_\sigma)_{\alpha_2\alpha_4}$
$\mathcal{M}_1$	$\tilde{\phi}_6 = (\gamma^5\gamma_\perp^\mu)_{\alpha_1\alpha_3}(\gamma_\mu^\perp)_{\alpha_2\alpha_4}$	$\tilde{\psi}_6 = \varepsilon^{\mu\nu\rho\sigma}\hat{P}_\nu(\gamma^5\gamma_\rho)_{\alpha_1\alpha_3}(\gamma_\sigma)_{\alpha_2\alpha_4}$
$\mathcal{M}_2$	$\tilde{\phi}_7 = (\gamma_\perp^\mu)_{\alpha_1\alpha_4}(\gamma^5\gamma_\mu^\perp)_{\alpha_2\alpha_3}$	$\tilde{\psi}_7 = \varepsilon^{\mu\nu\rho\sigma}\hat{P}_\nu(\gamma_\rho)_{\alpha_1\alpha_4}(\gamma^5\gamma_\sigma)_{\alpha_2\alpha_3}$
$\mathcal{M}_2$	$\tilde{\phi}_8 = (\gamma^5\gamma_\perp^\mu)_{\alpha_1\alpha_4}(\gamma_\mu^\perp)_{\alpha_2\alpha_3}$	$\tilde{\psi}_8 = \varepsilon^{\mu\nu\rho\sigma}\hat{P}_\nu(\gamma^5\gamma_\rho)_{\alpha_1\alpha_4}(\gamma_\sigma)_{\alpha_2\alpha_3}$
$\mathcal{D}$	$\tilde{\phi}_9 = (\mathbb{I}C)_{\alpha_1\alpha_2}(C^T\gamma^5)_{\alpha_3\alpha_4}$	$\tilde{\psi}_9 = (\mathbb{I}C)_{\alpha_1\alpha_2}(C^T\gamma_\perp^\mu)_{\alpha_3\alpha_4}$
$\mathcal{D}$	$\tilde{\phi}_{10} = (\gamma^5C)_{\alpha_1\alpha_2}(C^T\mathbb{I})_{\alpha_3\alpha_4}$	$\tilde{\psi}_{10} = (\gamma_\perp^\mu C)_{\alpha_1\alpha_2}(C^T\mathbb{I})_{\alpha_3\alpha_4}$
$\mathcal{D}$	$\tilde{\phi}_{11} = (\gamma^5\gamma_\perp^\mu C)_{\alpha_1\alpha_2}(C^T\gamma_\mu^\perp)_{\alpha_3\alpha_4}$	$\tilde{\psi}_{11} = (\gamma^5C)_{\alpha_1\alpha_2}(C^T\gamma^5\gamma_\perp^\mu)_{\alpha_3\alpha_4}$
$\mathcal{D}$	$\tilde{\phi}_{12} = (\gamma_\perp^\mu C)_{\alpha_1\alpha_2}(C^T\gamma^5\gamma_\mu^\perp)_{\alpha_3\alpha_4}$	$\tilde{\psi}_{12} = (\gamma^5\gamma_\perp^\mu C)_{\alpha_1\alpha_2}(C^T\gamma^5)_{\alpha_3\alpha_4}$

Table B.3: The relevant Dirac basis elements corresponding to the quantum numbers $J^P = 0^-$ and 1^- are collected. The interaction topology is indicated in the column labelled d. The transversal gamma matrices are defined as $\gamma_\perp^\mu = T^{\mu\nu}(P)\gamma_\nu$, with $\hat{P}$ representing the normalized total hadron momentum .

Table 5.2 corresponding to the chosen internal components, we find that

$$\Xi_{\mathrm{D};0(0^{++})} = \{\phi_1, \phi_4, \phi_5\}\ , \tag{B.54}$$

are the Dirac basis elements chosen for the $0(0^{++})$ state.

$0(1^{--})$

To investigate the Dirac basis elements for four-quark states with quantum numbers 0^{-+} and 1^{--}, we first need to construct a set of suitable Dirac basis tensors. To do this, we take the leading tensors for 0^+ and 1^+ in Table 5.2 and flip the parity by individually multiplying the internal elements by γ^5. The resulting tensors are compiled in Table B.3. Regarding the s-wave diquark-antidiquark pairings for these quantum numbers, they always contain either a pseudoscalar or a vector (anti)diquark. These are notoriously unreliable when using the MT interaction and thus we will refrain from using these components. Furthermore, they are also heavier than the scalar/axialvector diquarks respectively and therefore constitute a higher threshold. It would be possible to achieve the desired four-quark quantum numbers by a p-wave pairing of scalar or axialvector (anti)diquarks, but that would involve angular momentum and is beyond the scope of

	$\tilde{\phi}_{1,2}$	$\tilde{\phi}_{3,4}$	$\tilde{\phi}_{5,6}$	$\tilde{\phi}_{7,8}$	$\tilde{\phi}_{9,10}$	$\tilde{\phi}_{11,12}$
(14)(23)	$\tilde{\phi}_{2,1}$	$\tilde{\phi}_{3,4}$	$-\tilde{\phi}_{6,5}$	$-\tilde{\phi}_{7,8}$	$\tilde{\phi}_{10,9}$	$-\tilde{\phi}_{12,11}$

	$\tilde{\psi}^+_{1,3}$	$\tilde{\psi}^+_{2,4}$	$\tilde{\psi}^-_1$	$\tilde{\psi}_2$	$\tilde{\psi}^-_3$	$\tilde{\psi}^-_4$	$\tilde{\psi}_{5,6}$	$\tilde{\psi}_{7,8}$	$\tilde{\psi}_{9,10}$	$\tilde{\psi}_{11,12}$
(14)(23)	$\tilde{\psi}^+_{1,3}$	$-\tilde{\psi}^+_{2,4}$	$-\tilde{\psi}^-_1$	$\tilde{\psi}^-_2$	$\tilde{\psi}^-_3$	$-\tilde{\psi}^-_4$	$-\tilde{\psi}_{6,5}$	$-\tilde{\psi}_{7,8}$	$-\tilde{\psi}_{10,9}$	$-\tilde{\psi}_{12,11}$

Table B.4: Charge conjugation transformation in (14)(23) of the Dirac tensors in Table B.3. The notation $\psi_{i,j} \to \pm\psi_{i,j}$ denotes that the tensors ψ_i and ψ_j transform into themselves up to a possible sign, i.e., $\psi_i \to \pm\psi_i$ and $\psi_j \to \pm\psi_j$. The $\psi_{i,j} \to \pm\psi_{j,i}$ means the tensors transform into each other ($\psi_i \to \psi_j$, $\psi_j \to \psi_i$) with a possible sign.

this work.

Having introduced the leading Dirac tensors for the pseudoscalar and vector four-quark states in Table B.4, we can proceed with the possible sub-clusters for the $0(1^{--})$. These are:

- $\left\{(Q\bar{q})_{0^-} \otimes (q\bar{Q})_{1^+}\,,\, (Q\bar{q})_{0^+} \otimes (q\bar{Q})_{1^-}\right\}$ for $\mathcal{M}_1$,
- $\left\{ (Q\bar{Q})_{1^{--}} \otimes (q\bar{q})_{0^{++}}, (Q\bar{Q})_{1^{+-}} \otimes (q\bar{q})_{0^{-+}} \right\}$ and
- $\left\{ (Q\bar{Q})_{0^{++}} \otimes (q\bar{q})_{1^{--}}, (Q\bar{Q})_{0^{-+}} \otimes (q\bar{q})_{1^{+-}} \right\}$ for $\mathcal{M}_2$.

Considering the $cn\bar{n}\bar{c}$ state, i.e., the $\psi(4230)$ in this channel, the above combinations are $D\bar{D}_1$ and $D_0\bar{D}^*$ for $\mathcal{M}_1$ and $J/\psi f_0(1370)$, $h_c\eta$, $\chi_{c0}\omega$ and $\eta_c h_1$ for $\mathcal{M}_2$. In the combination $J/\psi f_0(1370)$, we refrain from using the σ meson as the companion state, because of its four-quark state nature [69, 248]. In addition, the σ has a huge decay width, making it too broad to form a bound state. For the reason mentioned above, we neglect the diquark-antidiquark combinations. In the $\mathcal{M}_1$ interaction topology, we choose the $D\bar{D}_1$ combination over the $D_0\bar{D}^*$, as the decay width of the D_0 is much to broad to form a molecular bound state, which was already argued in [56, 194]. In the $\mathcal{M}_2$ topology, we choose the $\chi_{c0}\omega$ and the $J/\psi f_0(1370)$. Checking the tables in Table B.4 for combination of tensors that transform negatively under C-parity, we find that the Dirac basis tensors corresponding to the chosen internal components are:

$$\Xi_{\mathrm{D};0(1^{--})} = \left\{\tilde{\psi}^-_1,\, \tilde{\psi}^+_4 + \tilde{\psi}^-_4,\, \tilde{\psi}^+_4 - \tilde{\psi}^-_4\right\}. \tag{B.55}$$

$0(0^{-+})$

Last but not least for the hidden-flavour four-quark states, we need to construct the physical basis for the $0(0^{-+})$ channel. The possible internal sub-clusters in this channel are:

- $\left\{(Q\bar{q})_{0^-} \otimes (q\bar{Q})_{0^+}\,,\, (Q\bar{q})_{1^-} \otimes (q\bar{Q})_{1^+}\right\}$ for $\mathcal{M}_1$,
- $\left\{ (Q\bar{Q})_{0^{++}} \otimes (q\bar{q})_{0^{-+}}, (Q\bar{Q})_{0^{-+}} \otimes (q\bar{q})_{0^{++}} \right\}$ and
- $\left\{ (Q\bar{Q})_{1^{+-}} \otimes (q\bar{q})_{1^{--}}, (Q\bar{Q})_{1^{--}} \otimes (q\bar{q})_{1^{+-}} \right\}$ for $\mathcal{M}_2$.

Again considering the 0^{-+} four-quark state with quark content $cn\bar{n}\bar{c}$, the above combinations amount to $D\bar{D}_0$ and $D^*\bar{D}_1$ for the $\mathcal{M}_1$ topology and $\chi_{c0}\pi$, $\eta_c f_0(1370)$, $h_c\omega$ and $J/\psi h_1$

for the $\mathcal{M}_2$ topology. For the physical basis, we choose the $D^*\bar{D}_1$ in the $\mathcal{M}_1$ topology and the combinations $\chi_{c0}\pi$ and $\eta_c f_0(1370)$ in the $\mathcal{M}_2$ topology. Also here, we neglect the combination containing the D_0 because of its broad decay width [56, 194]. The combinations containing axialvector and vector components in the $\mathcal{M}_2$ topology constitute higher threshold than the scalar-pesudoscalar combinations and are therefore neglected. Checking the Table B.4 again, we find the Dirac basis for the 0^{-+} four-quark state to be:

$$\Xi_{\mathrm{D};0(0^{-+})} = \left\{\tilde{\phi}_5 - \tilde{\phi}_6,\, \tilde{\phi}_3,\, \tilde{\phi}_4\right\}. \tag{B.56}$$

Since we want to investigate the effects from the attractive and repulsive combination of each internal clustering, we multiply each element in the sets Ξ_{D} with the attractive and repulsive colour singlets in the corresponding topology. This yields the combined Dirac-colour BSA, which is then multiplied with the flavour part of the BSA to get the full physical four-quark BSA.

ss	*aa*	*sa*	*as*
$QQ\bar{n}\bar{n}$ $(I=1)$ $QQ\bar{q}\bar{q}$ $(I=0)$		$QQ\bar{n}\bar{n}$ $(I=0)$	
$QQ'\bar{n}\bar{n}$ $(I=1)$ $QQ'\bar{q}\bar{q}$ $(I=0)$	$QQ'\bar{n}\bar{n}$ $(I=0)$	$QQ'\bar{n}\bar{n}$ $(I=0)$	$QQ'\bar{n}\bar{n}$ $(I=1)$ $QQ\bar{q}\bar{q}$ $(I=0)$
$QQ\bar{q}\bar{q}'$		$QQ\bar{q}\bar{q}'$	

Table B.5: Flavour BSAs Γ_{F} with definite Pauli symmetry .

B.2.2 Open-flavour physical BSA

In this section we will consider the physical BSA for the open-flavour four-quark states $(QQ'\bar{q}\bar{q}')$ with quantum numbers $I(J^P) = I(0^+), I(1^+)$ with $I = 0, 1/2, 1$. We know from Eq. (5.23), that the physical BSA needs to have a definite Pauli antisymmetry in either (12) or (34), if $Q = Q'$ or $\bar{q} = \bar{q}'$ respectively. We will start out with these cases and later on move to cases with $Q \neq Q'$ or $\bar{q} \neq \bar{q}'$, where there is no strict symmetry under the respective quark exchanges. For the open-flavour states, the symmetry of the flavour BSA under (12) and (34) dictates the transformation properties of the Dirac and colour tensors. We will therefore first determine the transformation of the flavour part of the BSA and then of the combined Dirac-colour tensors.

Before we come to the construction of the physical BSAs, we will investigate the symmetries of the flavour BSA outlined in Section 5.1.3 more closely. Considering a four-quark state with quark content

$$\Gamma_{\mathrm{F}} = \Gamma^1_{\mathrm{F}}\,\Gamma^2_{\mathrm{F}} = QQ\bar{q}\bar{q}\,, \tag{B.57}$$

the isospin can either be $I = 0, 1$. The first part of Γ_{F} features only heavy quarks $Q \in \{b, c\}$, which automatically has isospin $I = 0$. Furthermore, because the two heavy quarks are equal, the flavour BSA reads $\Gamma^1_{\mathrm{F}} = \{QQ\}$ and is symmetric (s) under quark exchange (12). We therefore write $\Gamma^{s\cdots}_{\mathrm{F}}$, with the ... denoting the, as of yet, undetermined transformation property of the second part of the flavour BSA. For the second part, i.e., Γ^2_{F}, the situation depends on whether $\bar{q} = \bar{n}$ or $\bar{q} \neq \bar{n}$, with $n = u/d$. In the first case, the flavour BSA can either be $\Gamma^2_{\mathrm{F}} = [\bar{u}\bar{d}]$ for the case $I = 0$, which transforms antisymmetric (a), or $\Gamma^2_{\mathrm{F}} = \{\bar{u}\bar{d}\}$ for the case $I = 1$, which transforms symmetric (s) under (34). In the second case $(\bar{q} \neq \bar{n})$, the flavour BSA can only have isospin $I = 0$ and read $\Gamma^2_{\mathrm{F}} = \{\bar{q}\bar{q}\}$, which is again symmetric under (34). We therefore have the following combinations:

$$\bar{q} \neq \bar{n}: \quad I = 0: \quad \Gamma^{ss}_{\mathrm{F}}\,, \qquad \bar{q} = \bar{n}: \quad \begin{cases} I = 0: & \Gamma^{sa}_{\mathrm{F}}\,, \\ I = 1: & \Gamma^{ss}_{\mathrm{F}}\,, \end{cases} \tag{B.58}$$

Continuing this with a four-quark state with quark content

$$\Gamma_{\mathrm{F}} = \Gamma_{\mathrm{F}}^{1}\,\Gamma_{\mathrm{F}}^{2} = QQ'\bar{q}\bar{q}\,, \tag{B.59}$$

with $Q \neq Q'$, we find that the symmetry under (12) is not fixed, as we can have both $\Gamma_{\mathrm{F}}^{1} = \{QQ'\}$ and $\Gamma_{\mathrm{F}}^{1} = [QQ']$. The considerations regarding Γ_{F}^{2} are the same as above. Therefore, we have the following combinations:

$$\bar{q} \neq \bar{n}: \quad I = 0: \quad \Gamma_{\mathrm{F}}^{(s/a)s}\,, \qquad \bar{q} = \bar{n}: \quad \begin{cases} I = 0: & \Gamma_{\mathrm{F}}^{(s/a)a}\,, \\ I = 1: & \Gamma_{\mathrm{F}}^{(s/a)s}\,, \end{cases} \tag{B.60}$$

The last case important for the present thesis, is the case where

$$\Gamma_{\mathrm{F}} = \Gamma_{\mathrm{F}}^{1}\,\Gamma_{\mathrm{F}}^{2} = QQ\bar{q}\bar{q}'\,, \tag{B.61}$$

with $\bar{q} \neq \bar{q}'$. This is also the only case where we can have isospin $I = 1/2$. Here the Γ_{F}^{1} is symmetric again, while the definite symmetry in (34) is lost. This means, regardless whether one of the antiquarks $\bar{q}$, $\bar{q}' = \bar{n}$, we can have both $\Gamma_{\mathrm{F}}^{2} = \{\bar{q}\bar{q}'\}$ and $\Gamma_{\mathrm{F}}^{2} = [\bar{q}\bar{q}']$. Thus, we find the following combinations:

$$\bar{q} \neq \bar{n}: \quad I = 0: \quad \Gamma_{\mathrm{F}}^{s(s/a)}\,, \qquad \bar{q} = \bar{n}: \quad \begin{cases} I = 0: & \Gamma_{\mathrm{F}}^{s(s/a)}\,, \\ I = 1/2: & \Gamma_{\mathrm{F}}^{s(s/a)}\,, \end{cases} \tag{B.62}$$

We have collected the transformation properties of the different flavour BSAs in Table B.5.

To get an overall antisymmetric BSA, one now needs to combine the flavour BSA $\Gamma_{\mathrm{F}}^{(s/a)(s/a)}$ with a corresponding Dirac-colour tensor which features the opposite transformation properties in (12) or (34), i.e., $\Gamma_{\mathrm{DC}}^{(a/s)(a/s)}$, such that the overall BSA has the desired antisymmetry under Pauli transformation. E.g., for a $QQ\bar{q}\bar{q}$ state, one needs to combine the tensors, such that the physical BSA has $\Gamma_{\mathrm{phys.}}^{aa}$.

For the construction of the physical basis below, we need to specify what we mean by saying we multiply the Dirac tensors for the meson-meson components in Table B.6 with the corresponding colour singlet. It means, each tensor in the linear combination is individually combined with the respective colour singlet. E.g., the ss tensor $\phi_1 + \phi_2$ multiplied with the colour singlets yields $\phi_1 \cdot C_{\mathbf{11}} + \phi_2 \cdot C'_{\mathbf{11}}$. Since these singlets transform into each other under Pauli symmetry (cf. Eq. (5.24) and above), the transformation properties of the combined Dirac-colour tensor are the same as for the Dirac tensor for the meson-meson components. For the diquark-antidiquark tensors, the situation differs depending on the colour structure.

$I(0^+)$

Let us apply this to the quantum numbers of open-flavour four-quark states investigated in this thesis. The first channel is the $I(J^P) = I(0^+)$. Considering first the state with isospin $I = 0$ and quark content $QQ\bar{q}\bar{q}$, with $\bar{q} = \bar{n}$. We know from Eq. (B.58), that the flavour part

ss	*aa*	*sa*	*as*
$\phi_1 + \phi_2$	$\phi_1 - \phi_2$		
$\phi_3 + \phi_4$	$\phi_3 - \phi_4$		
ϕ_6	ϕ_5		
$\psi_1^+ + \psi_2^+$	$\psi_1^+ - \psi_2^+$	$\psi_1^- - \psi_2^-$	$\psi_1^- + \psi_2^-$
ψ_7		$\psi_3 - \psi_4$	$\psi_3 + \psi_4$
		ψ_6	ψ_5
$\tilde{\phi}_{(1+2)} + \tilde{\phi}_{(3+4)}$	$\tilde{\phi}_{(1+2)} - \tilde{\phi}_{(3+4)}$	$\tilde{\phi}_{(1-2)} - \tilde{\phi}_{(3-4)}$	$\tilde{\phi}_{(1-2)} + \tilde{\phi}_{(3-4)}$
$\tilde{\phi}_{(5+6)} + \tilde{\phi}_{(7+8)}$	$\tilde{\phi}_{(5+6)} - \tilde{\phi}_{(7+8)}$	$\tilde{\phi}_{(5-6)} - \tilde{\phi}_{(7-8)}$	$\tilde{\phi}_{(5-6)} + \tilde{\phi}_{(7-8)}$
	$\tilde{\phi}_9$	$\tilde{\phi}_{12}$	$\tilde{\phi}_{11}$
	$\tilde{\phi}_{10}$		
$\tilde{\psi}_1^+ + \tilde{\psi}_3^+$	$\tilde{\psi}_1^+ - \tilde{\psi}_3^+$	$\tilde{\psi}_1^- - \tilde{\psi}_3^-$	$\tilde{\psi}_1^- + \tilde{\psi}_3^-$
$\tilde{\psi}_{(5-6)} + \tilde{\psi}_{(7-8)}$	$\tilde{\psi}_{(5-6)} - \tilde{\psi}_{(7-8)}$	$\tilde{\psi}_{(5+6)} - \tilde{\psi}_{(7+8)}$	$\tilde{\psi}_{(5+6)} + \tilde{\psi}_{(7+8)}$
	$\tilde{\psi}_{11}$	$\tilde{\psi}_{10}$	$\tilde{\psi}_9$
	$\tilde{\psi}_{12}$		

Table B.6: Dirac tensors with definite Pauli symmetry. We have introduced the shorthand $x_{(i\pm j)} = x_i \pm x_j$ with $x \in \{\tilde{\phi}, \tilde{\psi}\}$. Multiplying the tensors with their respective colour singlets from Eqs. (5.18) and (5.19) does not change the table significantly. The only change affects the tensors in the $\mathcal{D}$ topology, which upon multiplication with the $C_{\bar{3}\bar{3}}$ singlet exactly flips the transformation properties.

of the BSA transforms as Γ_{F}^{sa} in this case. This means, that we need to pair it with a Dirac-colour tensor which transforms according to $\Gamma_{\mathrm{DC}}^{as}$. Looking at the first row in Table B.6, we find that such a Dirac tensor does not exist. We therefore have to conclude, that such a state is not realized. However, when we consider the case $I = 1$ with $\bar{q} = \bar{n}$ or $I = 0$ with $\bar{q} \neq \bar{n}$, we have a flavour BSA which transforms symmetric under both (12) and (34), i.e., Γ_{F}^{ss}. This needs to be paired with the Dirac-colour tensors transforming antisymmetric under both quark exchanges $\Gamma_{\mathrm{DC}}^{aa}$. For the meson-meson interaction topologies, the Dirac tensors in the *aa* column in Table B.6 can be read of directly as the multiplication with the respective colour singlets does not change anything. For the tensors in the diquark topology, one needs to combine the transformation property of the Dirac tensors, given in Table B.6, with the ones of the colour BSA, given in Table 5.1, to form the desired $\Gamma_{\mathrm{DC}}^{aa}$. For the $\Gamma_{\mathrm{C}} = C_{\bar{3}\bar{3}}$, which transforms antisymmetric (Γ_{C}^{aa}), one needs to combine it with $\Gamma_{\mathrm{D}} = \phi_6$, transforming symmetric under both quark exchanges, i.e., Γ_{D}^{ss}. On the contrary,

one needs to combine the totally symmetric $\Gamma_{\mathrm{C}}^{ss} = C_{\mathbf{6}\bar{\mathbf{6}}}$ with the totally antisymmetric $\Gamma_{\mathrm{D}}^{aa} = \phi_5$ to get an overall antisymmetric BSA. In total, we find:

$$\Gamma_{\mathrm{F}}^{ss} \to \Gamma_{\mathrm{DC}}^{aa} = \begin{cases} \Gamma_{\mathrm{D}}^{ss} \otimes \Gamma_{\mathrm{C}}^{aa}\,, & \text{for} \quad \Gamma_{\mathrm{C}} = C_{\bar{\mathbf{3}}\mathbf{3}} \;\to\; \text{attractive}\, A_{QQ} A_{\bar{q}\bar{q}} \\ \Gamma_{\mathrm{D}}^{aa} \otimes \Gamma_{\mathrm{C}}^{ss}\,, & \text{for} \quad \Gamma_{\mathrm{C}} = C_{\mathbf{6}\bar{\mathbf{6}}} \;\to\; \text{repulsive}\, S_{QQ} S_{\bar{q}\bar{q}} \end{cases} . \tag{B.63}$$

With this, we conclude that for the $I(0^+)$ channel a $QQ\bar{q}\bar{q}$ four-quark state has the physical Dirac basis

$$\Xi_{\mathrm{D};I(0^+)} = \{\phi_1 - \phi_2,\, \phi_3 - \phi_4,\, \underbrace{\phi_6}_{\text{att.}},\, \underbrace{\phi_5}_{\text{rep.}}\}\,, \tag{B.64}$$

with the addition that the isospin $I = 0$ state is not realized for $\bar{q} = \bar{n}$. The meson-meson tensors are the same for the attractive and repulsive colour channels, whereas the first diquark-antidiquark tensor (ϕ_6) is for the attractive and the second one (ϕ_5) is for the repulsive colour channel.

This then corresponds to the combinations

- $(Q\bar{q})_{0^-} \otimes (Q\bar{q})_{0^-}$ attractive and repulsive $\mathcal{M}_1$ component,
- $(Q\bar{q})_{1^-} \otimes (Q\bar{q})_{1^-}$ for the attractive and repulsive $\mathcal{M}_2$ component and
- $(QQ)_{1^+} \otimes (\bar{q}\bar{q})_{1^+}$ for the attractive and
- $(QQ)_{0^+} \otimes (\bar{q}\bar{q})_{0^+}$ for the repulsive $\mathcal{D}$ components.

Taking the special case of $cc\bar{n}\bar{n}$ with quantum numbers $I(J^P) = 1(0^+)$, this amounts to DD and D^*D^* for the attractive and repulsive $\mathcal{M}_1$ and $\mathcal{M}_2$ topologies respectively and $A_{cc}A_{\bar{n}\bar{n}}$ as the attractive and $S_{cc}S_{\bar{n}\bar{n}}$ as the repulsive component in the $\mathcal{D}$ topology. Looking closely at the flavour combinations in Table B.5, we realize that the Dirac basis for the 0^+ channel given in Eq. (B.64) is also valid for the four-quark states with quark content $QQ'\bar{q}\bar{q}$ and $QQ\bar{q}\bar{q}'$. The only exception is the $QQ'\bar{n}\bar{n}$ state with isospin $I = 0$. Here the flavour part transforms antisymmetric under both (12) and (34). Therefore the Dirac-colour part needs to transform symmetric under both quark exchanges. For the meson-meson topologies, one needs to take the Dirac tensors in the *ss* column in Table B.6 and combine them with the appropriate colour singlets. For the diquark-antidiquark cluster, the corresponding combinations are then:

$$\Gamma_{\mathrm{F}}^{aa} \to \Gamma_{\mathrm{DC}}^{ss} = \begin{cases} \Gamma_{\mathrm{D}}^{aa} \otimes \Gamma_{\mathrm{C}}^{aa}\,, & \text{for} \quad \Gamma_{\mathrm{C}} = C_{\bar{\mathbf{3}}\mathbf{3}} \;\to\; \text{attractive}\, S_{QQ} S_{\bar{q}\bar{q}} \\ \Gamma_{\mathrm{D}}^{ss} \otimes \Gamma_{\mathrm{C}}^{ss}\,, & \text{for} \quad \Gamma_{\mathrm{C}} = C_{\mathbf{6}\bar{\mathbf{6}}} \;\to\; \text{repulsive}\, A_{QQ} A_{\bar{q}\bar{q}} \end{cases} . \tag{B.65}$$

Thus, the physical Dirac basis in this case reads

$$\Xi_{\mathrm{D};0(0^+)}^{QQ'\bar{n}\bar{n}} = \{\phi_1 + \phi_2,\, \phi_3 + \phi_4,\, \underbrace{\phi_5}_{\text{att.}},\, \underbrace{\phi_6}_{\text{rep.}}\}\,, \tag{B.66}$$

Compared to Eq. (B.64), the linear combinations have a different sign and the two diquark-antidiquark tensors for the attractive and repulsive components are switched. This means, in this case we get a scalar-scalar diquark-antidiquark attractive and axialvector-axialvector

diquark-antidiquark repulsive component.

$I(1^+)$

The second open-flavour channel investigated in this work is the $I(J^P) = I(1^+)$. We again start with the isospin $I = 0$ state with quark content $QQ\bar{q}\bar{q}$. For the case where $\bar{q} = \bar{n}$, we know from Table B.5 that the flavour BSA transforms as Γ_{F}^{sa}. Therefore, we would need a Dirac-colour tensor transforming as $\Gamma_{\mathrm{DC}}^{as}$. Consulting the $J^P = 1^+$ Dirac tensors (ψ_i) in Table B.6, we find the Dirac tensors with the correct transformation properties under Pauli symmetry in the last column. The Dirac tensors for the meson-meson topologies can again be read off directly. When we consider the diquark-antidiquark tensors, we need to check which combination yields the correct (as) transformation properties. Here, we can either have

$$\Gamma_{\mathrm{F}}^{sa} \to \Gamma_{\mathrm{DC}}^{as} = \begin{cases} \Gamma_{\mathrm{D}}^{sa} \otimes \Gamma_{\mathrm{C}}^{aa}\,, & \text{for} \quad \Gamma_{\mathrm{C}} = C_{\bar{\mathbf{33}}} \;\to\; \text{attractive}\, A_{QQ} S_{\bar{n}\bar{n}} \\ \Gamma_{\mathrm{D}}^{as} \otimes \Gamma_{\mathrm{C}}^{ss}\,, & \text{for} \quad \Gamma_{\mathrm{C}} = C_{\mathbf{6}\bar{\mathbf{6}}} \;\to\; \text{repulsive}\, S_{QQ} A_{\bar{n}\bar{n}} \end{cases} . \tag{B.67}$$

From this, we find that the physical Dirac basis reads

$$\Xi_{\mathrm{D};0(1^+)} = \{\psi_1^- + \psi_2^-,\, \psi_3 + \psi_4,\, \underbrace{\psi_6}_{\text{att.}},\, \underbrace{\psi_5}_{\text{rep.}}\}\,. \tag{B.68}$$

We therefore have the following internal clusters for $0(1^+)$ with $QQ\bar{n}\bar{n}$:

- $(Q\bar{n})_{0^-} \otimes (Q\bar{n})_{1^-}$ for $\mathcal{M}_1$ attractive and repulsive,
- $(Q\bar{n})_{1^-} \otimes (Q\bar{n})_{1^-}$ for $\mathcal{M}_2$ attractive and repulsive,
- $(QQ)_{1^+} \otimes (\bar{n}\bar{n})_{0^+}$ for the attractive and
- $(QQ)_{0^+} \otimes (\bar{n}\bar{n})_{1^+}$ for the repulsive $\mathcal{D}$ topology.

As an example, consider the case $cc\bar{n}\bar{n}$, i.e., the T_{cc}^+. The physical components stated above are here attractive and repulsive DD^* and D^*D^* for the $\mathcal{M}_1$ and $\mathcal{M}_2$ respectively and $A_{cc}S_{\bar{n}\bar{n}}$ in the attractive and $S_{cc}A_{\bar{n}\bar{n}}$ in the repulsive $\mathcal{D}$ topology.

As is evident from Table B.5, the flavour BSA in the isospin $I = 1$ case of $QQ\bar{n}\bar{n}$ and the case for $QQ\bar{q}\bar{q}$ with $\bar{q} \neq \bar{n}$ have the same symmetries under Pauli symmetry, i.e., Γ_{F}^{ss}. Therefore, the corresponding Dirac-colour tensors need to be the same and transform as $\Gamma_{\mathrm{DC}}^{aa}$ under Pauli symmetry. Checking Table B.6 for the corresponding Dirac tensors, we find only a meson-meson tensor in the *aa* column, which can of course again be taken directly. For the diquark-antidiquark tensors, we need to combine the possible tensors of the *ss* and the *aa* column with the attractive and repulsive colour singlets to get

$$\Gamma_{\mathrm{F}}^{ss} \to \Gamma_{\mathrm{DC}}^{aa} = \begin{cases} \Gamma_{\mathrm{D}}^{ss} \otimes \Gamma_{\mathrm{C}}^{aa}\,, & \text{for} \quad \Gamma_{\mathrm{C}} = C_{\bar{\mathbf{33}}} \;\to\; \text{attractive}\, A_{QQ} A_{\bar{q}\bar{q}} \\ \Gamma_{\mathrm{D}}^{aa} \otimes \Gamma_{\mathrm{C}}^{ss}\,, & \text{for} \quad \Gamma_{\mathrm{C}} = C_{\mathbf{6}\bar{\mathbf{6}}} \;\to\; \text{not possible with } J^P = 1^+ \end{cases} . \tag{B.69}$$

Since the *aa* column of Table B.6 does not feature any Dirac tensors, the only valid combination is combining the totally symmetric ψ_7 tensor with the total antisymmetric attractive

colour singlet $C_{\bar{3}3}$. The physical Dirac basis thus reads

$$\Xi_{\mathrm{D};1(1^+)} = \{\psi_1^+ - \psi_2^+,\, \psi_7\} \quad \left(= \Xi^{QQ\bar{q}\bar{q}}_{\mathrm{D};0(1^+)}\right). \tag{B.70}$$

The corresponding internal clusters are

- $(Q\bar{q})_{0^-} \otimes (Q\bar{q})_{1^-}$ for the attractive and repulsive $\mathcal{M}_1$ and
- $(QQ)_{1^+} \otimes (\bar{q}\bar{q})_{1^+}$ for the attractive $\mathcal{D}$ topology.

We do not have a $\mathcal{M}_2$ component and also the repulsive $\mathcal{D}$ component is missing. Considering again the example case of $cc\bar{n}\bar{n}$, we have an attractive and repulsive DD^* component in $\mathcal{M}_1$ and an attractive $A_{cc}S_{\bar{q}\bar{q}}$ component in $\mathcal{D}$.

We now have to consider the case of $J^P = 1^+$ with quark content $QQ'\bar{q}\bar{q}$ and $QQ\bar{q}\bar{q}'$ with $Q \neq Q'$ and $\bar{q} \neq \bar{q}'$ respectively. In both of these cases, the flavour BSA does not have a fixed definite Pauli symmetry under (12) for the $QQ'\bar{q}\bar{q}$ or (34) for the $QQ\bar{q}\bar{q}'$, but rather can transform both symmetric or antisymmetric under the respective quark exchange. This is also reflected in Table B.5. For the case of $QQ'\bar{q}\bar{q}$, the flavour BSAs can transform as

$$\Gamma_{\mathrm{F}}^{(s/a)a} \text{ for } I = 0 \text{ with } \bar{q} = \bar{n} \quad \text{or} \quad \Gamma_{\mathrm{F}}^{(s/a)s} \begin{cases} \text{for } I = 1 \text{ with } \bar{q} = \bar{n} \\ \text{for } I = 0 \text{ with } \bar{q} \neq \bar{n} \end{cases} \tag{B.71}$$

The corresponding Dirac-colour tensors are

$$\Gamma_{\mathrm{F}}^{(s/a)a} \to \Gamma_{\mathrm{DC}}^{(a/s)s} \quad \text{and} \quad \Gamma_{\mathrm{F}}^{(s/a)s} \to \Gamma_{\mathrm{DC}}^{(a/s)a} \tag{B.72}$$

In the case of $QQ\bar{q}\bar{q}'$, the flavour BSAs transform as $\Gamma_{\mathrm{F}}^{s(s/a)}$. The corresponding Dirac-colour BSA therefore has to transform as $\Gamma_{\mathrm{DC}}^{a(a/s)}$. The different combinations will impact the existence of certain diquark-antidiquark components, which will be discussed in the following. Before we do that, we need to consider the possible meson-meson combinations based on the tensors in Table B.6. Here we have the combinations $\psi_1^\pm \pm \psi_2^\pm$ and $\psi_3 \pm \psi_4$. Taking now the special case for $QQ'\bar{q}\bar{q} = bc\bar{n}\bar{n}$, we see that the physical components these linear combinations correspond to are

$$\begin{aligned} \psi_1^\pm \pm \psi_2^\pm &\sim \left(\bar{B} \otimes D^* \pm \bar{B}^* \otimes D\right) \pm \left(\bar{B} \otimes D^* \pm \bar{B}^* \otimes D\right), \\ \psi_3 \pm \psi_4 &\sim \bar{B}^* \otimes D^* \pm \bar{B}^* \otimes D^*. \end{aligned} \tag{B.73}$$

We see, that the tensors $\psi_1^\pm$ and $\psi_2^\pm$ mix the $\bar{B}D^*$ and $\bar{B}^*D$ components. This is obviously not the case for equal heavy quarks. Similarly, for the case $QQ\bar{q}\bar{q}' = bb\bar{n}\bar{s}$, we have

$$\begin{aligned} \psi_1^\pm \pm \psi_2^\pm &\sim \left(\bar{B} \otimes \bar{B}_s^* \pm \bar{B}^* \otimes \bar{B}_s\right) \pm \left(\bar{B}_s \otimes \bar{B}^* \pm \bar{B}_s^* \otimes \bar{B}\right), \\ \psi_3 \pm \psi_4 &\sim \bar{B}^* \otimes \bar{B}_s^* \pm \bar{B}_s^* \otimes \bar{B}^*. \end{aligned} \tag{B.74}$$

where the $\bar{B}\bar{B}_s^*$ and $\bar{B}^*\bar{B}_s$ components are mixed in the tensors $\psi_{1,2}^\pm$. In these cases, the two components need to be disentangled. For this, we look at where the flavour BSA has a

fixed definite Pauli symmetry, i.e., s or a in (34) for $QQ'\bar{q}\bar{q}$ and s in (12) for $QQ\bar{q}\bar{q}'$, and form a linear combination of the corresponding tensors with s and a under the other quark exchange. That is

$$\begin{aligned}
\Gamma_{\mathrm{F}}^{(s/a)a} &\to \Psi^{(s\pm a)s} = (\psi_1^+ - \psi_2^+) \pm (\psi_1^- - \psi_2^-)\,, \\
\Gamma_{\mathrm{F}}^{(s/a)s} &\to \Psi^{(s\pm a)a} = (\psi_1^+ + \psi_2^+) \pm (\psi_1^- + \psi_2^-)\,, \\
\Gamma_{\mathrm{F}}^{s(s/a)} &\to \Psi^{a(s\pm a)} = (\psi_1^+ - \psi_2^+) \pm (\psi_1^- + \psi_2^-)\,,
\end{aligned} \tag{B.75}$$

with $\Psi^{\cdots}$ denoting the linear combinations of Dirac tensors. This effectively disentangles the two physical components from the $\psi_{1,2}^{\pm}$ tensors in Eq. (B.73), as the linear combinations in Eq. (B.75) correspond to

$$\Psi^{(s+a)a} \sim \bar{B} \otimes D^*\,, \qquad \Psi^{(s-a)a} \sim \bar{B}^* \otimes D\,, \tag{B.76}$$

$$\Psi^{(s+a)s} \sim \bar{B} \otimes D^*\,, \qquad \Psi^{(s-a)s} \sim \bar{B}^* \otimes D\,, \tag{B.77}$$

$$\Psi^{a(s+a)} \sim \bar{B} \otimes \bar{B}_s^*\,, \qquad \Psi^{a(s-a)} \sim \bar{B}^* \otimes \bar{B}_s\,. \tag{B.78}$$

The combinations $\psi_3 \pm \psi_4$ in Eqs. (B.73) and (B.74) need not be changed, as they are still valid for these cases.

Starting out with the case of $QQ'\bar{n}\bar{n}$ and isospin $I = 0$, the flavour BSA transforms under Pauli as $\Gamma_{\mathrm{F}}^{(s/a)a}$. It has a definite antisymmetry in (34), but can transform symmetric or antisymmetric under (12) as $Q \neq Q'$. The corresponding Dirac-colour tensor needs to transform as $\Gamma_{\mathrm{DC}}^{(a/s)s}$. It is interesting to take a closer look at the diquark-antidiquark tensors. Here we find

$$\begin{aligned}
\Gamma_{\mathrm{F}}^{sa} \to \Gamma_{\mathrm{DC}}^{as} &= \begin{cases} \Gamma_{\mathrm{D}}^{sa} \otimes \Gamma_{\mathrm{C}}^{aa}\,, & \text{for} \quad \Gamma_{\mathrm{C}} = C_{\bar{\mathbf{33}}} \;\to\; \text{attractive}\, A_{QQ'} S_{\bar{n}\bar{n}} \\ \Gamma_{\mathrm{D}}^{as} \otimes \Gamma_{\mathrm{C}}^{ss}\,, & \text{for} \quad \Gamma_{\mathrm{C}} = C_{\mathbf{6}\bar{\mathbf{6}}} \;\to\; \text{repulsive}\, S_{QQ'} A_{\bar{n}\bar{n}} \end{cases}, \\
\Gamma_{\mathrm{F}}^{aa} \to \Gamma_{\mathrm{DC}}^{ss} &= \begin{cases} \Gamma_{\mathrm{D}}^{aa} \otimes \Gamma_{\mathrm{C}}^{aa}\,, & \text{for} \quad \Gamma_{\mathrm{C}} = C_{\bar{\mathbf{33}}} \;\to\; \text{not possible with } J^P = 1^+ \\ \Gamma_{\mathrm{D}}^{ss} \otimes \Gamma_{\mathrm{C}}^{ss}\,, & \text{for} \quad \Gamma_{\mathrm{C}} = C_{\mathbf{6}\bar{\mathbf{6}}} \;\to\; \text{repulsive}\, A_{QQ'} A_{\bar{n}\bar{n}} \end{cases}.
\end{aligned} \tag{B.79}$$

Since the *aa* column in Table B.6 does not feature any $\mathcal{D}$ Dirac tensors, this attractive component is not realized for $J^P = 1^+$. The chosen physical Dirac basis elements in this case are

$$\Xi_{\mathrm{D};\,0(1^+)}^{QQ'\bar{n}\bar{n}} = \{\Psi^{(s+a)s},\, \Psi^{(s-a)s},\, \psi_6,\, \psi_5\}\,. \tag{B.80}$$

We have neglected the repulsive $A_{QQ'}A_{\bar{n}\bar{n}}$ as it constitutes the highest threshold of the diquark-antidiquark components. The internal clusters we choose are therefore

- $(Q\bar{n})_{0^-} \otimes (Q'\bar{n})_{1^-}$ for $\mathcal{M}_1$ attractive and repulsive,
- $(Q\bar{n})_{1^-} \otimes (Q'\bar{n})_{0^-}$ for the attractive and repulsive $\mathcal{M}_2$,
- $(QQ')_{1^+} \otimes (\bar{n}\bar{n})_{0^+}$ for the attractive $\mathcal{D}$ and
- $(QQ')_{0^+} \otimes (\bar{n}\bar{n})_{1^+}$ for the repulsive $\mathcal{D}$ topology.

For the special case $QQ'\bar{n}\bar{n} = bc\bar{n}\bar{n}$ we have an attractive and repulsive $\bar{B}D^*$ component in $\mathcal{M}_1$, an attractive and repulsive $\bar{B}^*D$ in $\mathcal{M}_2$ and an attractive $A_{bc}S_{\bar{n}\bar{n}}$ and repulsive $S_{bc}A_{\bar{n}\bar{n}}$ component in $\mathcal{D}$.

As was the case before, for the $QQ'\bar{n}\bar{n}$ with isospin $I = 1$ and the $QQ'\bar{q}\bar{q}$ with $\bar{q} \neq \bar{n}$ the flavour BSAs have a definite Pauli symmetry under (34) and both possible symmetries in (12), i.e., $\Gamma_{\mathrm{F}}^{(s/a)s}$. Similar as before, we want to construct a Dirac-colour tensor with $\Gamma_{\mathrm{DC}}^{(a/s)a}$. For the diquark-antidiquark tensors, we have

$$\begin{aligned}
\Gamma_{\mathrm{F}}^{ss} \to \Gamma_{\mathrm{DC}}^{aa} &= \begin{cases} \Gamma_{\mathrm{D}}^{ss} \otimes \Gamma_{\mathrm{C}}^{aa}, & \text{for} \quad \Gamma_{\mathrm{C}} = C_{\bar{\mathbf{3}}\mathbf{3}} \;\to\; \text{attractive}\, A_{QQ'}A_{\bar{q}\bar{q}} \\ \Gamma_{\mathrm{D}}^{aa} \otimes \Gamma_{\mathrm{C}}^{ss}, & \text{for} \quad \Gamma_{\mathrm{C}} = C_{\mathbf{6}\bar{\mathbf{6}}} \;\to\; \text{not possible with}\, J^P = 1^+ \end{cases}, \\
\Gamma_{\mathrm{F}}^{as} \to \Gamma_{\mathrm{DC}}^{sa} &= \begin{cases} \Gamma_{\mathrm{D}}^{as} \otimes \Gamma_{\mathrm{C}}^{aa}, & \text{for} \quad \Gamma_{\mathrm{C}} = C_{\bar{\mathbf{3}}\mathbf{3}} \;\to\; \text{attractive}\, S_{QQ'}A_{\bar{q}\bar{q}} \\ \Gamma_{\mathrm{D}}^{sa} \otimes \Gamma_{\mathrm{C}}^{ss}, & \text{for} \quad \Gamma_{\mathrm{C}} = C_{\mathbf{6}\bar{\mathbf{6}}} \;\to\; \text{repulsive} A_{QQ'}S_{\bar{q}\bar{q}} \end{cases}.
\end{aligned} \tag{B.81}$$

The chosen physical Dirac basis reads

$$\Xi_{\mathrm{D};1(1^+)} = \{\Psi^{(s+a)a}, \Psi^{(s-a)a}, \psi_5, \psi_3 - \psi_4, \psi_6\} \quad \left(= \Xi_{0(1^+)}^{QQ'\bar{q}\bar{q}}\right) \tag{B.82}$$

We again neglect the $A_{QQ'}A_{\bar{q}\bar{q}}$ component as it is again the highest diquark-antidiquark threshold and can therefore be assumed to be subleading compared to the other combinations. Thus, the chosen internal clusters are

- $(Q\bar{n})_{0^-} \otimes (Q'\bar{n})_{1^-}$ for $\mathcal{M}_1$ attractive and repulsive,
- $(Q\bar{n})_{1^-} \otimes (Q'\bar{n})_{0^-}$ for the attractive $\mathcal{M}_2$,
- $(QQ')_{0^+} \otimes (\bar{n}\bar{n})_{1^+}$ for the attractive $\mathcal{D}$,
- $(Q\bar{n})_{1^-} \otimes (Q'\bar{n})_{1^-}$ for the repulsive $\mathcal{M}_2$ and
- $(QQ')_{1^+} \otimes (\bar{n}\bar{n})_{0^+}$ for the repulsive $\mathcal{D}$ topology.

For the $\mathcal{M}_2$ topology, we choose the repulsive vector-vector meson pairing, because we found that the inclusion of this repulsive component significantly affects the four-quark mass in the $1(1^+)$ channel. Considering the special case of $QQ'\bar{q}\bar{q} = bc\bar{n}\bar{n}$, we have a $\bar{B}D^*$ for the attractive and repulsive $\mathcal{M}_1$ topology, an attractive $\bar{B}^*D$ and repulsive $\bar{B}^*D^*$ component in $\mathcal{M}_2$ and an attractive $S_{bc}A_{\bar{n}\bar{n}}$ and repulsive $A_{bc}S_{\bar{n}\bar{n}}$ component in the $\mathcal{D}$ topology.

The last case investigated in this work, is for the flavour combination $QQ\bar{q}\bar{q}'$. Here, we do not need to make a distinction between the different isospins $I = 0$ and $I = 1/2$, because the flavour BSAs have the same symmetries under Pauli, i.e., $\Gamma_{\mathrm{F}}^{s(s/a)}$. The needed Dirac-colour tensor in this case therefore needs to transform as $\Gamma_{\mathrm{DC}}^{a(a/s)}$. Investigating the

possible diquark-antidiquark clusters, we find

$$\begin{aligned}\Gamma_{\mathrm{F}}^{ss} \to \Gamma_{\mathrm{DC}}^{aa} &= \begin{cases}\Gamma_{\mathrm{D}}^{ss} \otimes \Gamma_{\mathrm{C}}^{aa}\,, & \text{for} \quad \Gamma_{\mathrm{C}} = C_{\bar{\mathbf{3}}\mathbf{3}} \;\to\; \text{attractive}\, A_{QQ}A_{\bar{q}\bar{q}'} \\ \Gamma_{\mathrm{D}}^{aa} \otimes \Gamma_{\mathrm{C}}^{ss}\,, & \text{for} \quad \Gamma_{\mathrm{C}} = C_{\mathbf{6}\bar{\mathbf{6}}} \;\to\; \text{not possible with } J^P = 1^+\end{cases}, \\ \Gamma_{\mathrm{F}}^{sa} \to \Gamma_{\mathrm{DC}}^{as} &= \begin{cases}\Gamma_{\mathrm{D}}^{sa} \otimes \Gamma_{\mathrm{C}}^{aa}\,, & \text{for} \quad \Gamma_{\mathrm{C}} = C_{\bar{\mathbf{3}}\mathbf{3}} \;\to\; \text{attractive}\, A_{QQ}S_{\bar{q}\bar{q}'} \\ \Gamma_{\mathrm{D}}^{as} \otimes \Gamma_{\mathrm{C}}^{ss}\,, & \text{for} \quad \Gamma_{\mathrm{C}} = C_{\mathbf{6}\bar{\mathbf{6}}} \;\to\; \text{repulsive}\, S_{QQ}A_{\bar{q}\bar{q}'}\end{cases}.\end{aligned} \tag{B.83}$$

Similar to Eq. (B.81), we only get one possible repulsive component for $J^P = 1^+$. The chosen physical Dirac basis is

$$\Xi_{\mathrm{D};I(1^+)}^{QQ\bar{q}\bar{q}'} = \{\Psi^{a(s+a)},\, \Psi^{a(s-a)},\, \psi_6,\, \psi_3 + \psi_4,\, \psi_5\}\,. \tag{B.84}$$

Similar to the cases before, we again neglect the $A_{QQ}A_{\bar{q}\bar{q}'}$ diquark-antidiquark component, as it is the highest threshold in this topology. The chosen internal clusters are

- $(Q\bar{q})_{0^-} \otimes (Q\bar{q}')_{1^-}$ for $\mathcal{M}_1$ attractive and repulsive,
- $(Q\bar{q}')_{0^-} \otimes (Q\bar{q})_{1^-}$ for the attractive $\mathcal{M}_2$,
- $(QQ)_{0^+} \otimes (\bar{q}\bar{q}')_{1^+}$ for the attractive $\mathcal{D}$,
- $(Q\bar{q}')_{1^-} \otimes (Q\bar{q})_{1^-}$ for the repulsive $\mathcal{M}_2$ and
- $(QQ)_{1^+} \otimes (\bar{q}\bar{q}')_{0^+}$ for the repulsive $\mathcal{D}$ topology.

Concretely for the case $QQ\bar{q}\bar{q}' = bb\bar{n}\bar{s}$ we get the following physical internal components. An attractive and repulsive $\bar{B}\bar{B}_s^*$ in the $\mathcal{M}_1$ topology, an attractive $\bar{B}_s\bar{B}^*$ and a repulsive $\bar{B}^*\bar{B}_s^*$ in the $\mathcal{M}_2$ topology and finally an attractive $A_{bb}S_{\bar{n}\bar{s}}$ and repulsive $S_{bb}A_{\bar{n}\bar{s}}$ component in the $\mathcal{D}$ topology.

Rest of this page intentionally left blank.

Appendix C

More on BSEs

C.1 Properties of BSEs

C.1.1 Transformations

Here we collect the transformation properties of a generic n-body BSE under parity and charge conjugation. With the charge conjugation matrices defined in Eq. (A.23) we obtain the charge conjugated BSA for the cases of spin $J = 0$ and $J = 1$ as

$$\bar{\Gamma}^{\mu}(\{p_i\}, P) = (-1)^J C\, \Gamma^{\mu}(-\{p_i\}, -P)^T\, C^T\,, \tag{C.1}$$

which reduces to

$$\bar{\Gamma}^{\mu}(\{p_i\}, P) = (-1)^J c\, \Gamma^{\mu}(\{p_i\}, -P)\,, \tag{C.2}$$

if the state is an eigenstate of C-parity with eigenvalues $c = \pm 1$. Upon acting with the parity transformation operator $\mathcal{P}$ upon the generic BSA, we get

$$\mathcal{P}\Big(\Gamma^{\mu}(\{p_i\}, P)\Big) = (-1)^J\, \Pi^{\mu\sigma}\, \gamma^4\, \Gamma_{\sigma}(\{\Pi p_i\}, \Pi P)\, \gamma^4\,, \tag{C.3}$$

with $\Pi = \mathrm{diag}(-1, -1, -1, 1)$.

C.1.2 Charge conjugation symmetry of four-quark basis elements

As we have seen in Section 5.1.3, the definite C-parity of a hidden-flavour four-quark state $(Qq\bar{q}\bar{Q})$ is the main construction principle for a correct physical BSA for this state. In this section, we will explicitly calculate the charge conjugation transformation under quark exchange $(14)(23)$, as given in Eq. (5.22), of some example tensors of Tables 5.2 and B.3. The flavour and colour BSAs both transform positively under this C-parity.

We start with the $J^P = 0^+$ tensors. Consider the ϕ_1 tensor in Table 5.2. Following the rule given in Eq. (5.22), we have

$$\begin{aligned} &C_{\alpha_1\alpha_1'}\, C_{\alpha_2\alpha_2'}\, C_{\alpha_3\alpha_3'}\, C_{\alpha_4\alpha_4'}\, (\phi_1)_{\alpha_4'\alpha_3'\alpha_2'\alpha_1'} = \\ &C_{\alpha_1\alpha_1'}\, C_{\alpha_2\alpha_2'}\, C_{\alpha_3\alpha_3'}\, C_{\alpha_4\alpha_4'}\, (\gamma^5)_{\alpha_4'\alpha_2'}\, (\gamma^5)_{\alpha_3'\alpha_1'} = \left(C\gamma^5 C^T\right)_{\alpha_4\alpha_2} \left(C\gamma^5 C^T\right)_{\alpha_3\alpha_1}\,. \end{aligned}$$

We then use the charge conjugation of the γ^5 matrix in Eq. (A.24) and get

$$\left(\gamma^5\right)^T_{\alpha_4\alpha_2}\left(\gamma^5\right)^T_{\alpha_3\alpha_1} = \gamma^5_{\alpha_2\alpha_4}\gamma^5_{\alpha_1\alpha_3} = \phi_1\,.$$

To also demonstrate the transformation of a tensor belonging to the $\mathcal{M}_2$ topology, we choose the ϕ_4 tensor. Applying Eq. (5.22), we have

$$\begin{aligned}
&C_{\alpha_1\alpha_1'}\,C_{\alpha_2\alpha_2'}\,C_{\alpha_3\alpha_3'}\,C_{\alpha_4\alpha_4'}\,\left(\phi_1\right)_{\alpha_4'\alpha_3'\alpha_2'\alpha_1'} = \\
&C_{\alpha_1\alpha_1'}\,C_{\alpha_2\alpha_2'}\,C_{\alpha_3\alpha_3'}\,C_{\alpha_4\alpha_4'}\,\left(\gamma^\mu_\perp\right)_{\alpha_4'\alpha_1'}\left(\gamma^\perp_\mu\right)_{\alpha_3'\alpha_2'} = \left(C\gamma^\mu_\perp C^T\right)_{\alpha_4\alpha_1}\left(C\gamma^\perp_\mu C^T\right)_{\alpha_3\alpha_2}\,.
\end{aligned}$$

Using the C-parity of the γ^μ matrix in Eq. (A.24), the above reads

$$\left(-\gamma^\mu_\perp\right)^T_{\alpha_4\alpha_1}\left(-\gamma^\perp_\mu\right)^T_{\alpha_3\alpha_2} = \left(\gamma^\mu_\perp\right)_{\alpha_1\alpha_4}\left(\gamma^\perp_\mu\right)_{\alpha_2\alpha_3} = \phi_4\,.$$

For tensors in the $\mathcal{D}$ topology, we choose the ϕ_5 tensor. The charge conjugation for this tensor reads

$$\begin{aligned}
&C_{\alpha_1\alpha_1'}\,C_{\alpha_2\alpha_2'}\,C_{\alpha_3\alpha_3'}\,C_{\alpha_4\alpha_4'}\,\left(\phi_5\right)_{\alpha_4'\alpha_3'\alpha_2'\alpha_1'} = \\
&C_{\alpha_1\alpha_1'}\,C_{\alpha_2\alpha_2'}\,C_{\alpha_3\alpha_3'}\,C_{\alpha_4\alpha_4'}\,\left(\gamma^5C\right)_{\alpha_4'\alpha_3'}\left(C^T\gamma^5\right)_{\alpha_2'\alpha_1'} = \left(C\left[\gamma^5C\right]C^T\right)_{\alpha_4\alpha_3}\left(C\left[C^T\gamma^5\right]C^T\right)_{\alpha_2\alpha_1}\,.
\end{aligned}$$

We insert a $\mathbb{I} = C^TC$ between the tensors in the square brackets and get

$$\begin{aligned}
&\left(C\left[\gamma^5C^TCC\right]C^T\right)_{\alpha_4\alpha_3}\left(C\left[C^TC^TC\gamma^5\right]C^T\right)_{\alpha_2\alpha_1} = \Big(\left(\gamma^5\right)^T C\underbrace{CC^T}_{=\mathbb{I}}\Big)_{\alpha_4\alpha_3}\Big(\underbrace{CC^T}_{=\mathbb{I}}C^T\left(\gamma^5\right)^T\Big)_{\alpha_2\alpha_1} = \\
&\left(C^T\gamma^5\right)^T_{\alpha_4\alpha_3}\left(\gamma^5C\right)^T_{\alpha_2\alpha_1} = \left(C^T\gamma^5\right)_{\alpha_3\alpha_4}\left(\gamma^5C\right)_{\alpha_1\alpha_2} = \phi_5\,.
\end{aligned}$$

Carrying out this procedure for all the $J^P = 0^+$ tensors in Table 5.2, one can show, that they each transform according to $\phi_i \to +\phi_i$, with $i = 1, 2, \ldots, 6$. This confirms the first column of Table B.2.

We apply the same technique also to some example tensors in the $J^P = 1^+$ channel. First, we consider the $\psi_1^\pm$ tensor.

$$\begin{aligned}
&C_{\alpha_1\alpha_1'}\,C_{\alpha_2\alpha_2'}\,C_{\alpha_3\alpha_3'}\,C_{\alpha_4\alpha_4'}\,\left(\psi_1^\pm\right)_{\alpha_4'\alpha_3'\alpha_2'\alpha_1'} = \\
&C_{\alpha_1\alpha_1'}\,C_{\alpha_2\alpha_2'}\,C_{\alpha_3\alpha_3'}\,C_{\alpha_4\alpha_4'}\left(\left(\gamma^5\right)_{\alpha_4'\alpha_2'}\left(\gamma^\mu_\perp\right)_{\alpha_3'\alpha_1'} \pm \left(\gamma^\mu_\perp\right)_{\alpha_4'\alpha_2'}\left(\gamma^5\right)_{\alpha_3'\alpha_1'}\right) = \\
&\left(\left(C\gamma^5C^T\right)_{\alpha_4\alpha_2}\left(C\gamma^\mu_\perp C^T\right)_{\alpha_3\alpha_1} \pm \left(C\gamma^\mu_\perp C^T\right)_{\alpha_4\alpha_2}\left(C\gamma^5C^T\right)_{\alpha_3\alpha_1}\right)
\end{aligned}$$

Using the C-parity of the gamma matrices in Eq. (A.24) again, we get

$$\begin{aligned}
&\left(\left(\gamma^5\right)^T_{\alpha_4\alpha_2}\left(-\gamma^\mu_\perp\right)^T_{\alpha_3\alpha_1} \pm \left(-\gamma^\mu_\perp\right)^T_{\alpha_4\alpha_2}\left(\gamma^5\right)^T_{\alpha_3\alpha_1}\right) = \\
&\left(-\left(\gamma^5\right)_{\alpha_2\alpha_4}\left(\gamma^\mu_\perp\right)_{\alpha_1\alpha_3} \mp \left(\gamma^\mu_\perp\right)_{\alpha_2\alpha_4}\left(\gamma^5\right)_{\alpha_1\alpha_3}\right) =
\end{aligned}$$

$$\left(\mp (\gamma^5)_{\alpha_1\alpha_3} (\gamma_\perp^\mu)_{\alpha_2\alpha_4} - (\gamma_\perp^\mu)_{\alpha_1\alpha_3} (\gamma^5)_{\alpha_2\alpha_4} \right) = \mp \psi_1^\pm \,.$$

Therefore, the tensor ψ_1^+ has negative and ψ_1^- positive C-parity under $(14)(23)$. As a last example for the 1^+ tensors, we will look at the ψ_5 tensor in the $\mathcal{D}$ topology. Applying Eq. (5.22) to ψ_5 we get

$$\begin{aligned}
&C_{\alpha_1\alpha_1'} C_{\alpha_2\alpha_2'} C_{\alpha_3\alpha_3'} C_{\alpha_4\alpha_4'} \, (\psi_5)_{\alpha_4'\alpha_3'\alpha_2'\alpha_1'} = \\
&C_{\alpha_1\alpha_1'} C_{\alpha_2\alpha_2'} C_{\alpha_3\alpha_3'} C_{\alpha_4\alpha_4'} \, (\gamma^5 C)_{\alpha_4'\alpha_3'} (C^T \gamma_\perp^\mu)_{\alpha_2'\alpha_1'} = \left(C \left[\gamma^5 C\right] C^T\right)_{\alpha_4\alpha_3} \left(C \left[C^T \gamma_\perp^\mu\right] C^T\right)_{\alpha_2\alpha_1} \,.
\end{aligned}$$

As done before, we insert $C^T C = \mathbb{I}$ between the tensors in the square brackets. Doing so, we get

$$\begin{aligned}
&\left(C \left[\gamma^5 C^T C C\right] C^T\right)_{\alpha_4\alpha_3} \left(C \left[C^T C^T C \gamma_\perp^\mu\right] C^T\right)_{\alpha_2\alpha_1} = \left((\gamma^5)^T C \underbrace{C C^T}_{\mathbb{I}} \right)_{\alpha_4\alpha_3} \left(\underbrace{C C^T}_{\mathbb{I}} C^T (-\gamma_\perp^\mu)^T \right)_{\alpha_2\alpha_1} = \\
&= \left(C^T \gamma^5\right)^T_{\alpha_4\alpha_3} \left(-\gamma_\perp^\mu C\right)^T_{\alpha_2\alpha_1} = -\left(\gamma_\perp^\mu C\right)_{\alpha_1\alpha_2} \left(C^T \gamma^5\right)_{\alpha_3\alpha_4} = -\psi_6 \,.
\end{aligned}$$

So, under charge conjugation under quark exchange $(14)(23)$ the tensor ψ_5 transforms into $-\psi_6$.

As a last example, we look at the C-parity of the $\tilde{\psi}_1^\pm$ tensor in the $J^P = 1^-$ basis elements in Table B.3. Using Eq. (5.22) on $\tilde{\psi}_1^\pm$ we get

$$\begin{aligned}
&C_{\alpha_1\alpha_1'} C_{\alpha_2\alpha_2'} C_{\alpha_3\alpha_3'} C_{\alpha_4\alpha_4'} \, (\tilde{\psi}_1^\pm)_{\alpha_4'\alpha_3'\alpha_2'\alpha_1'} = \\
&C_{\alpha_1\alpha_1'} C_{\alpha_2\alpha_2'} C_{\alpha_3\alpha_3'} C_{\alpha_4\alpha_4'} \left((\gamma^5)_{\alpha_4'\alpha_2'} (\gamma^5 \gamma_\perp^\mu)_{\alpha_3'\alpha_1'} \pm (\gamma^5 \gamma_\perp^\mu)_{\alpha_4'\alpha_2'} (\gamma^5)_{\alpha_3'\alpha_1'} \right) = \\
&\left((C\gamma^5 C^T)_{\alpha_4\alpha_2} (C[\gamma^5 \gamma_\perp^\mu] C^T)_{\alpha_3\alpha_1} \pm (C[\gamma^5 \gamma_\perp^\mu] C^T)_{\alpha_4\alpha_2} (C\gamma^5 C^T)_{\alpha_3\alpha_1} \right)
\end{aligned}$$

We again insert unity as $C^T C = \mathbb{I}$ between the tensors in the square brackets and get

$$\begin{aligned}
&\left(\left(C\gamma^5 C^T\right)_{\alpha_4\alpha_2} \left(C[\gamma^5 C^T C \gamma_\perp^\mu] C^T\right)_{\alpha_3\alpha_1} \pm \left(C[\gamma^5 C^T C \gamma_\perp^\mu] C^T\right)_{\alpha_4\alpha_2} \left(C\gamma^5 C^T\right)_{\alpha_3\alpha_1} \right) = \\
&\left(\left(\gamma^5\right)^T_{\alpha_4\alpha_2} \left((\gamma^5)^T (-\gamma_\perp^\mu)^T \right)_{\alpha_3\alpha_1} \pm \left((\gamma^5)^T (-\gamma_\perp^\mu)^T \right)_{\alpha_4\alpha_2} \left(\gamma^5\right)^T_{\alpha_3\alpha_1} \right) = \\
&\left(\left(\gamma^5\right)^T_{\alpha_4\alpha_2} \left(-\gamma_\perp^\mu \gamma^5 \right)^T_{\alpha_3\alpha_1} \pm \left(-\gamma_\perp^\mu \gamma^5 \right)^T_{\alpha_4\alpha_2} \left(\gamma^5\right)^T_{\alpha_3\alpha_1} \right) = \\
&\left(\mp \left(\gamma^5\right)_{\alpha_1\alpha_3} \left(\gamma_\perp^\mu \gamma^5\right)_{\alpha_2\alpha_4} - \left(\gamma_\perp^\mu \gamma^5\right)_{\alpha_1\alpha_3} \left(\gamma^5\right)_{\alpha_2\alpha_4} \right)
\end{aligned}$$

Using the anticommutation relation of the γ^5 matrix given in Eq. (A.22), we get

$$\left(\pm \left(\gamma^5\right)_{\alpha_1\alpha_3} \left(\gamma^5 \gamma_\perp^\mu\right)_{\alpha_2\alpha_4} + \left(\gamma^5 \gamma_\perp^\mu\right)_{\alpha_1\alpha_3} \left(\gamma^5\right)_{\alpha_2\alpha_4} \right) = \pm \tilde{\psi}_1^\pm \,.$$

Here, the tensor $\tilde{\psi}_1^+$ has positive and $\tilde{\psi}_1^-$ negative C-parity under $(14)(23)$.

C.1.3 Pauli antisymmetry of four-quark basis elements

While the main construction principle for the physical BSA of hidden-flavour four-quark states with quark content $Qq\bar{q}\bar{Q}$ is the charge conjugation symmetry given in Eq. (5.22), for the open-flavour four-quark states with quark content $QQ'\bar{q}\bar{q}'$ the main symmetry the physical BSA has to fulfil is either or both of the Pauli antisymmetries in Eq. (5.23). As an example, we will show how to calculate the Pauli (anti)symmetry of some Dirac tensors of Tables 5.2 and B.3 under quark exchange (12) and (34).

First, we want to consider the $J^P = 0^+$ tensors. As an example, we look at the ϕ_1 tensor under quark exchange (12) and (34). Applying the transformations in Eq. (5.23) we get

$$\begin{aligned} (12): &\qquad \left(\phi_1\right)_{\alpha_2\alpha_1\alpha_3\alpha_4} = (\gamma^5)_{\alpha_2\alpha_3}(\gamma^5)_{\alpha_1\alpha_4} = \phi_2\,, \\ (34): &\qquad \left(\phi_1\right)_{\alpha_1\alpha_2\alpha_4\alpha_3} = (\gamma^5)_{\alpha_1\alpha_4}(\gamma^5)_{\alpha_2\alpha_3} = \phi_2\,. \end{aligned}$$

We see, that the tensor ϕ_1 transforms into the tensor ϕ_2 under quark exchanges (12) and (34) with a positive sign. The transformation $\phi_2 \to \phi_1$ under Pauli (anti)symmetry follows straightforwardly. Forming the linear combination $\Phi^+ = \phi_1 + \phi_2$, the resulting tensor transforms symmetric (s) under both (12) and (34). We will denote this behaviour as subscripts on the name of the combined tensor, i.e., Φ^+_{ss}. The first and second subscript correspond to the transformation under (12) and (34) correspondingly. Forming the other possible linear combination, i.e., $\Phi^- = \phi_1 - \phi_2$, we find that this tensor transforms antisymmetric (a) under both (12) and (34). We denote the transformation properties of this tensor as Φ^-_{aa}. These two linear combinations then denote Dirac tensors with a definite Pauli (anti)symmetry and are given in the first line of the first two columns of Table B.6.

Next, it is useful to consider a $J^P = 0^+$ tensor in the $\mathcal{D}$ topology. We choose ϕ_5 as an example. Again applying Eq. (5.23), we find

$$\begin{aligned} (12): &\quad \left(\phi_5\right)_{\alpha_2\alpha_1\alpha_3\alpha_4} = (\gamma^5 C)_{\alpha_2\alpha_1}(C^T\gamma^5)_{\alpha_3\alpha_4} = (\gamma^5 C)^T_{\alpha_1\alpha_2}(C^T\gamma^5)_{\alpha_3\alpha_4} \\ &\qquad = (C^T(\gamma^5)^T)_{\alpha_1\alpha_2}(C^T\gamma^5)_{\alpha_3\alpha_4} \overset{(A.24)}{=} -(\gamma^5 C)_{\alpha_1\alpha_2}(C^T\gamma^5)_{\alpha_3\alpha_4} = -\phi_5 \\ (34): &\quad \left(\phi_5\right)_{\alpha_1\alpha_2\alpha_4\alpha_3} = (\gamma^5 C)_{\alpha_1\alpha_2}(C^T\gamma^5)_{\alpha_4\alpha_3} = (\gamma^5 C)_{\alpha_1\alpha_2}(C^T\gamma^5)^T_{\alpha_3\alpha_4} \\ &\qquad = (\gamma^5 C)_{\alpha_1\alpha_2}((\gamma^5)^T C)_{\alpha_3\alpha_4} \overset{(A.24)}{=} -(\gamma^5 C)_{\alpha_1\alpha_2}(C^T\gamma^5)_{\alpha_3\alpha_4} = -\phi_5\,. \end{aligned}$$

Hence the tensor $\Phi = \phi_5$ has a definite Pauli antisymmetry under the quark exchanges (12) and (34), i.e., Φ_{aa}. Thus, it is classified in the second column, first row in Table B.6.

One can carry out the same procedure as written above for all the Dirac basis tensors given in Table 5.2, i.e., check whether the tensors have definite Pauli (anti)symmetry and if not, form linear combinations of the tensors that do. Having done so, they can be classified according to the respective transformation properties as shown in Table B.6.

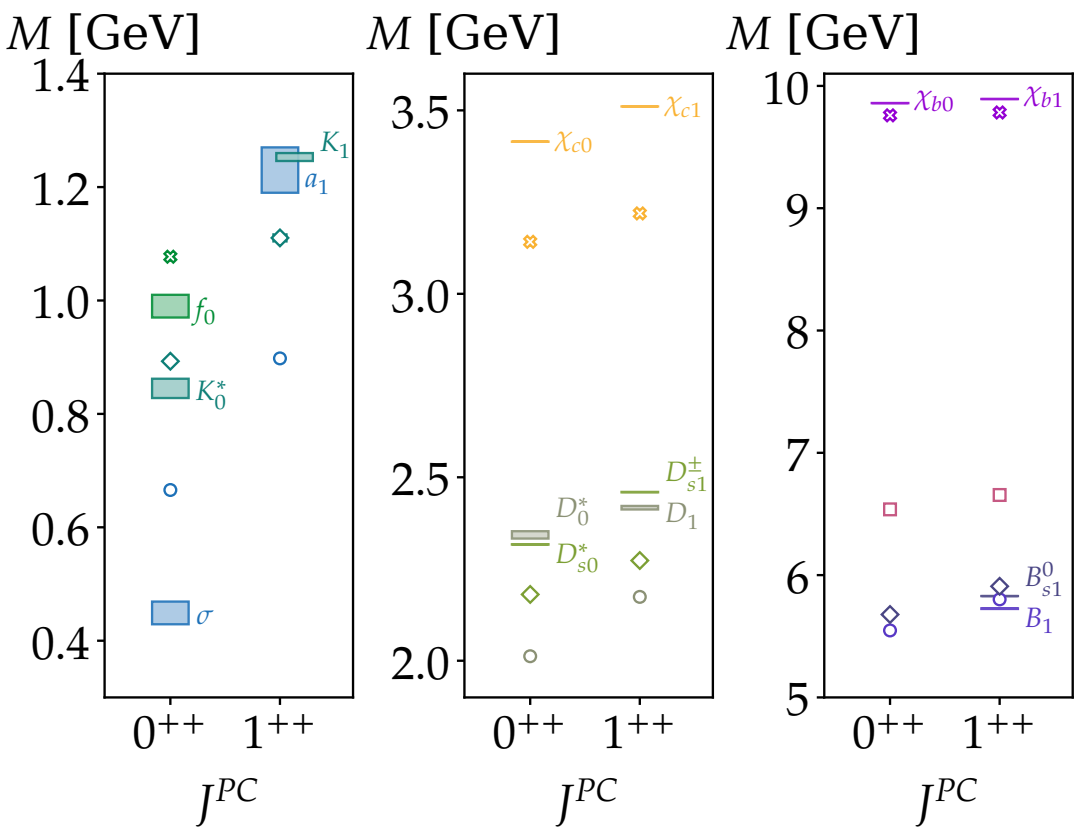

Figure C.1: Similar meson mass spectrum as in Fig. 4.9 but for the scalar and axialvector states using the rainbow-ladder truncation together with the MT interaction.

C.2 Scalar and axialvector two-body spectrum

Here we show the masses of the scalar and axialvector mesons. As can be seen from Fig. C.1 and Table C.1 the states obtained using the rainbow-latter truncation plus Maris-Tandy interaction deviate greatly from their corresponding experimental counterparts [20]. This is known to be the case for the MT interaction, see, e.g., [69]. The only exception are the states involving a bottom quark. There the obtained numerical results match with the experimental values.

In Fig. C.1 we show the obtained results for the scalar $q\bar{q}' = n\bar{n}$, $s\bar{n}$ and $s\bar{s}$ mesons. However, as the scalar states below 1 GeV are known to be of four-quark state nature [66, 248], we fix the meson masses for the states with the quark configurations mentioned above to the masses of the scalar nonet above 1 GeV.

	0^{++}			1^{++}		
	PDG	m_{RL}	$\Delta m^{\mathrm{rel.}}$	PDG	m_{RL}	$\Delta m^{\mathrm{rel.}}$
$n\bar{n}$	$f_0(1370)$	1370	‡	a_1	898	27.0%
$s\bar{n}$	$K_0^*(1430)$	1425	‡	K_1	1110	11.4%
$s\bar{s}$	$f_0(1500)$	1522	‡	–	1248	–
$c\bar{n}$	D_0^*	2012	14.1%	D_1	2174	10.1%
$c\bar{s}$	D_{s0}^*	2181	5.9%	D_{s1}	2273	7.6%
$c\bar{c}$	χ_{c0}	3142	8.0%	χ_{c1}	3154	8.3%
$b\bar{n}$	–	5550	–	B_1	5802	1.3%
$b\bar{s}$	–	5680	–	B_{s1}	5909	1.4%
$b\bar{c}$	–	6538	–	–	6655	–
$b\bar{b}$	χ_{b0}	9759	1.0%	χ_{b1}	9768	1.1%

Table C.1: Quark-antiquark ($Q\bar{q}$) mesons with quantum numbers $J^{PC} = \{0^{++}, 1^{++}\}$ are organized according to their quark model classification. We present the experimental candidates identified by [20], the masses m_{RL} calculated using our rainbow-ladder approach, and the relative errors of these values compared to those listed by the PDG (when the experimental state has been identified). All masses are provided in MeV. ‡: The lightest scalar meson nonet, known to be of four-quark nature [66, 248], is not considered as potential internal components. Instead, we refer to the scalar nonet with masses above 1 GeV .

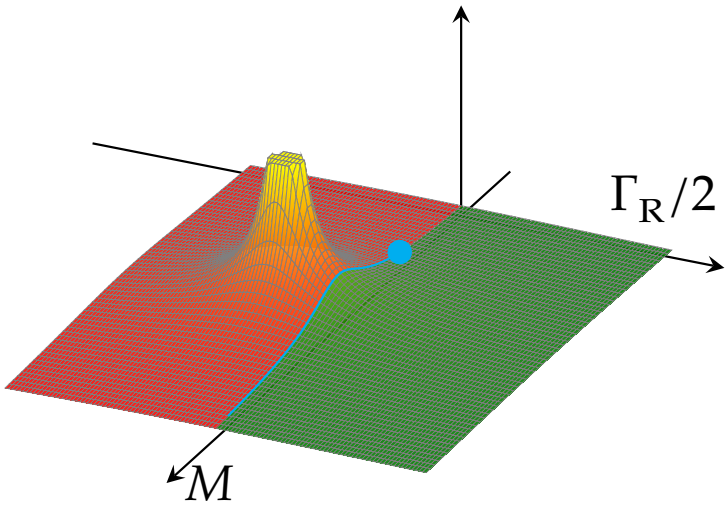

Figure C.2: Visualization of the complex energy plane spanned by the mass M and the decay width Γ_R on the x- and y-axis respectively. The green zone represents the physical or first Riemann sheet and the red zone corresponds to an unphysical Riemann sheet where a resonance pole is located. The cyan point represents the branch point and the cyan line is the branch cut which connects the Riemann sheets.

C.3 Contour deformation and solution in the complex plane

Recall from Chapter 4, that the homogeneous Bethe-Salpeter equation is an eigenvalue equation of the form

$$\lambda(P^2)\Gamma = KG_0\,\Gamma\,, \tag{C.4}$$

with Γ the Bethe-Salpeter amplitude, K the interaction kernel, G_0 denoting the product of full quark propagators and P the total hadron momentum. The solution of this equation is obtained when the condition $\lambda = 1$ is fulfilled. Throughout this thesis, we obtained the masses of hadrons by considering the hadron in its rest frame and choosing $P^\mu = iM \cdot \hat{e}_4^\mu$, with $\hat{e}_4^\mu$ denoting the unit vector in Euclidean 4-direction. Using this, the condition $\lambda = 1$ is fulfilled, when $P^2 = -M^2$ is at the mass M of the hadron.

However, since most of the known hadrons are resonances and decay via the strong interactions, they only have a (often very short) finite lifetime τ. This can be expressed in terms of the decay width $\Gamma_R = \frac{\hbar}{\tau}$, which has units of energy. In scattering theory, one usually identifies bound states, resonances and virtual states via the location of the corresponding pole structure in the complex energy plane of the s-channel or s-plane. This is spanned by the mass and the decay width as $\sqrt{s} = M - i\Gamma_R/2$. Bound states are stable and hence are found as poles on the real $\sqrt{s}$ axis on the first Riemann sheet below the energies of any hadronic decay channels. The hadronic decay channels introduce branch points, above which the energy plane splits into different Riemann sheets. Note, that

only the first Riemann sheet is directly accessible from the physical region. The poles of resonances are found above these branching points on the unphysical Riemann sheets. A visualization of this is presented in Fig. C.2. For a more detailed discussion about this topic, we refer the reader to [16] and the section "Resonances" in [20].

In principle, it is also possible to solve the homogeneous BSE in Eq. (C.4) for complex values of P^2 by choosing $P^\mu = (iM - \Gamma_R/2) \cdot \hat{e}_4^\mu$ in analogy to the $\sqrt{s}$ plane introduced above. The solution of Eq. (C.4) is then obtained at the point where $\mathrm{Re}(\lambda(P^2)) = 1$ and $\mathrm{Im}(\lambda(P^2)) = 0$. The naive determination of eigenvalues is only possible in the first Riemann sheet, after which one needs to use analytic continuation to go into the higher Riemann sheets where the poles of the resonances are located. To utilize this, one needs to calculate the eigenvalues above the thresholds of hadronic decay channels, which introduce pole structures into the integration domain, see discussion around Fig. 5.2 for a visualization of this. To directly calculate the eigenvalues, one needs to employ path deformation techniques to ensure that these singularity structures are not hit.

A technique implementing the above to investigate the light scalar mesons using the DSE/BSE framework has been developed and applied in the two-body approach to four-quark states [79, 164]. In contrast to the approach presented in this work, which consists of quarks interacting via gluon exchange, the two-body approach deals with meson and diquark degrees of freedom interacting via quark exchange. Here, the two-body pole structures appearing in the integration are of the form

$$P_a \cdot P_{a'} = \frac{1}{b^2 + \eta z + (\eta P)^2 + m_a^2} \cdot \frac{1}{b^2 - (1-\eta) z + ((1-\eta)P)^2 + m_{a'}^2}\,, \tag{C.5}$$

with m_a and $m_{a'}$ denoting the masses of the two particles a and a', b is the relative (integration) momentum, η is the corresponding momentum partitioning parameter and $z = \hat{b} \cdot \hat{P}$. With P and η fixed, one needs to find a suitable path for the radial variable b^2 which depends on z such that the conditions

$$b^2 + \eta z + (\eta P)^2 \neq -m_a^2\,, \tag{C.6}$$

$$b^2 - (1-\eta) z + ((1-\eta)P)^2 \neq -m_{a'}^2 \tag{C.7}$$

are fulfilled. This can be done relatively straightforward and the first results presented in [79] look very promising.

Using the four-body approach presented in this work, we also have the internal two-body poles as given in Eq. (5.37). In contrast to the two-body approach, the phase space of the four-body approach is more elaborate and therefore the expressions for the poles in the denominator are more complex. They are mostly of the form

$$P_a \cdot P_{a'} = \frac{1}{b^2 + f_a(S_0, z, y, \alpha) + m_a^2} \cdot \frac{1}{b^2 + f_{a'}(S_0, z, y, \alpha) + m_{a'}^2}\,, \tag{C.8}$$

with functions f_a and $f_{a'}$ depending on the singlet variable S_0 and the three angles appearing in Eq. (5.28). The y and α are printed in grey, as they do not appear in all pole structures.

The appearance of the singlet S_0 variable comes from considering the relative momenta in the central limit, which is the modus operandi of this thesis.

Upon inserting the physical BSA in Eq. (5.41) into the diagrams in Fig. 5.1, one needs to find a path deformation for each pole in Eq. (5.41) such that the conditions

$$b^2 + f_a(S_0, z, y, \alpha) \neq -m_a^2\,, \tag{C.9}$$

$$b^2 + f_{a'}(S_0, z, y, \alpha) \neq -m_{a'}^2\,, \tag{C.10}$$

are satisfied. In the best cases, the path deformation depends only on two variables (S_0, z), in the worst cases on four variables (S_0, z, y, α). Inserting BSA elements of a specific interaction topology into diagrams of that topology on the right-hand side of Fig. 5.1, the poles get cancelled by the projectors, e.g., Eq. (5.46). Only when the interaction topology of the BSA element and the diagram are different, the poles remain in the integration and a path deformation is needed. Take the case of the σ meson: considering the BSA element corresponding to $\pi - \pi$ in one of the diquark-antidiquark topologies shown in Fig. 5.1 the $\pi - \pi$ poles are not cancelled by the corresponding projectors.

What makes the path deformation particularly complicated is the dependence on the external radial momentum variable S_0. This introduces an additional dynamic, as the path needs to change with the external energy scale S_0. After trying for some time, we managed to perform the path deformation only by setting $S_0 = 0$ in the functions f_a and $f_{a'}$. This effectively removes the additional dynamic of the external variable. For the σ meson, we observed the emergence of a branch cut in the eigenvalues above the $2m_\pi$ threshold, which is expected. However, since we are in the central limit (see Fig. 5.2), setting $S_0 = 0$ corresponds to setting the relative momenta between the internal clusters to zero, which is a questionable approximation.

Due to the sheer complexity of the phase space and the enormous effort of finding a dynamic path deformation in four variables, we decided not to pursue this endeavour further in this thesis and relegate it to future work. There are interesting recent developments considering path deformations in the DSE/BSE framework of up to three variables [244, 249, 250], which gives us hope that the above problem might be feasible in the near future.

C.4 Attempt to access the internal spatial structure

Towards the end of the introduction in Section 6.2 we discussed that it is difficult to directly access the spatial structure of the internal components of hadrons using the BSE formulated in momentum space, as is the case for this work. From our mathematics lectures, we know that we can use a Fourier transform to switch between momentum to position space. Generally, for a QFT in four spacetime dimensions, the Fourier transform of a function $g(E, \vec{p})$ reads

$$g(t, \vec{x}) = \int \frac{\mathrm{d}^4 p}{(2\pi)^4}\, \mathrm{e}^{i(\vec{p}\cdot\vec{x} - Et)}\, g(E, \vec{p})\,, \tag{C.11}$$

with E the energy, t the time, $\vec{p}$ and $\vec{x}$ the momentum and position three-vectors. The Fourier transform including the e^{-iEt} factor transforms from energy to time, which is not what we are after there. Therefore, we will neglect this integral and consider only the three-dimensional Fourier transform

$$g(\vec{r}) = \int \frac{\mathrm{d}^3 p}{(2\pi)^3} \, \mathrm{e}^{i\vec{p}\cdot\vec{r}} \, g(\vec{p}) \,, \tag{C.12}$$

where we have relabelled $\vec{x}$ to $\vec{r}$.

Upon solving a BSE, one obtains the mass and the associated dressing functions $f_j(p^2, \dots)$ depending on a generic (squared) relative momentum p^2 and some angles. The angular dependence of the dressing functions is usually not overly strong and will therefore be neglected. The idea is now, to use a Fourier transform with respect to the relative momentum between two constituents, to obtain the spatial distance between them. Setting $g(\vec{p}) = f_j(p^2)$ in Eq. (C.12) we have

$$f_j(r) = \frac{1}{(2\pi)^3} \int_0^\infty \mathrm{d}p \; p^2 \int_{-1}^{1} \mathrm{d}z \, \bar{z} \int_0^{2\pi} \mathrm{d}\phi \, \mathrm{e}^{iprz} f_j(p^2) \,, \tag{C.13}$$

with z the angle between $\vec{p}$ and $\vec{r}$ and $\bar{z} = \sqrt{1 - z^2}$. Since we want the distance between the constituents, we consider only the radius r as an argument of the Fourier transformed function $f_j(r)$. The last integral is trivial and evaluates to 2π. With this Eq. (C.13) becomes

$$f_j(r) = \frac{1}{(2\pi)^2} \int_0^\infty \mathrm{d}p \, p^2 \int_{-1}^{1} \mathrm{d}z \, \bar{z} \, \mathrm{e}^{iprz} f_j(p^2) \,. \tag{C.14}$$

The dressing functions do not depend on the angle z and can be pulled out of the z-integral. Evaluating this integral, the expression reads

$$f_j(r) = \frac{1}{(2\pi)^2} \int_0^\infty \mathrm{d}p \, p^2 \, \frac{2\sin(pr)}{pr} f_j(p^2) \,. \tag{C.15}$$

Rearranging and cancelling some terms we have the final integral, which reads

$$f_j(r) = \frac{1}{(2\pi)^2} \int_0^\infty \mathrm{d}p \, \frac{\sin(\sqrt{p}r)}{r} f_j(p) \,, \tag{C.16}$$

where we have used the variable transformation $p^2 \to p$ such that the dressing function depends linearly on the integration variable.[1]

Once the Fourier transformed function $f_j(r)$ is obtained, one can build the absolute square $|f_j(r)|^2 = f_j^*(r) \cdot f_j(r)$ where the star denotes complex conjugation. In analogy to the radial distribution of an electron in an atom, one can think of $|f_j(r)|^2$ as the radial

[1] To make the argument of the sinus dimensionless, one needs to transform the r, which has dimension femtometre (fm) to GeV^{-1} by using the relation in Eq. (A.3), i.e., doing $r' = 5.068 \cdot r$.

'probability' density for a certain component corresponding to the dressing function f_j. Thus, one can extract the mean radial distance $\langle r^m \rangle$ between the two components in a subcluster j via the formula

$$\langle r^m \rangle_j = \frac{\int \mathrm{d}^3 r \cdot |f_j(r)|^2 \cdot r^m}{\int \mathrm{d}^3 r \, |f_j(r)|^2}, \tag{C.17}$$

where the term in the denominator serves as a normalization such that we do not need to normalize the dressing functions in the BSA. The m is usually chosen $m = 1$ or $m = 2$. The angular integrals are trivial and the remaining integral reads

$$\langle r^m \rangle_j = \frac{\int_0^\infty \mathrm{d}r \, r^2 \cdot |f_j(r)|^2 \cdot r^m}{\int_0^\infty \mathrm{d}r \, r^2 |f_j(r)|^2}. \tag{C.18}$$

In our test calculations, we found that it is numerically advantageous to introduce a radial cutoff function in the integral

$$h(r) = \begin{cases} 1 & \text{, for } r < 3 \text{ fm} \\ \mathrm{e}^{-100 \cdot r} & \text{, for } r > 3 \text{ fm} \end{cases} \tag{C.19}$$

This effectively cancels out numerical noise coming from the dressing functions at large distances r.

To see whether the method described above yields plausible results, we consider the $n\bar{n}$, $c\bar{c}$ and $b\bar{b}$ pseudoscalar mesons as a test system. Applying the Fourier transform to the (on-shell) dressing function $f_0(p^2)$, which corresponds to the leading tensor basis element, i.e., γ^5, for pseudoscalar mesons and neglecting the angular dependence yields the radial distributions shown in Fig. C.3. We see that going from $n\bar{n}$ to $b\bar{b}$, the peak wanders towards smaller distances r and the curve gets narrower and has a larger magnitude. We used Eq. (C.17) to calculate the average distances $\langle r \rangle$ ($m = 1$), the location of which are shown by the vertical dotted lines in the respective colours. Also here, it is observed that for increasing quark pair mass, the average distance decreases:

$$\langle r \rangle_{n\bar{n}} = 0.356 \text{ fm}, \qquad \langle r \rangle_{c\bar{c}} = 0.243 \text{ fm}, \qquad \langle r \rangle_{b\bar{b}} = 0.147 \text{ fm}, \tag{C.20}$$

$$\langle r^2 \rangle_{n\bar{n}}^{1/2} = 0.394 \text{ fm}, \qquad \langle r^2 \rangle_{c\bar{c}}^{1/2} = 0.270 \text{ fm}, \qquad \langle r^2 \rangle_{b\bar{b}}^{1/2} = 0.171 \text{ fm}. \tag{C.21}$$

In the second line, we show the results for $\langle r^2 \rangle^{1/2}$ ($m = 2$), which we do not show in Fig. C.3. With the charge radius of the π known to be $\approx 0.659(4)$ fm [20], the mean distance between the $n\bar{n}$ is indeed a plausible result. It would be interesting to explore this idea further in the future.

When we want to investigate the radial distance between the internal clusters of a four-quark state, we need to identify the relative momenta needed to apply the Fourier

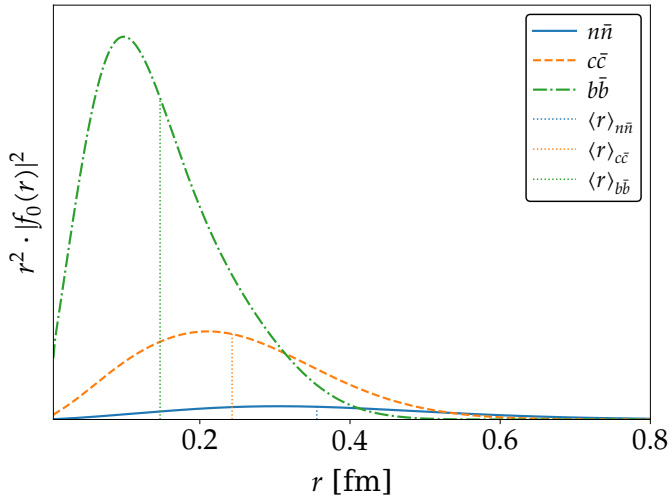

Figure C.3: Radial distribution of the quark-antiquark pair in a $n\bar{n}$ (*blue, solid*), $c\bar{c}$ (*orange, dashed*) and $b\bar{b}$ (*green, dash-dotted*) pseudoscalar meson. The vertical line represents the location of $\langle r \rangle$ for the different mesons.

transform. Remember that, because we consider everything in the central limit, the dressing functions depend only on the singlet S_0. Since $S_0 = (k^2 + q^2 + p^2)/4$ (see Eq. (5.29)), the relative momenta can be expressed in terms of the singlet in the central limit as $k^2 = q^2 = p^2 = 4S_0/3$. Thus, one would need to make the Fourier transform in Eq. (C.16) with respect to $p^2 = 4S_0/3$. We need to mention a caveat here. To make statements about the distance between the internal components, one has to consider the dressing functions at the physical point for a given hadron. This fact makes it difficult to investigate the distances between the internal clusters for four-quark states where the mass is not directly obtainable but relies on extrapolation and the extraction from the QMECs (cf. Appendix C.6). Of course, one could also calculate the radial distance for every eigenvalue in the eigenvalue curve and use extrapolation to get the values at the physical point. It is very difficult to gauge the accuracy of the obtained results for the mean distance at the present moment, which is why we relegated the further investigation of this matter to future studies.

C.5 Extrapolation and error analysis

In this section we want to systematically introduce the extrapolation procedure and error analysis for the eigenvalue curves of the four-quark states investigated in this thesis. The eigenvalues $\lambda(P^2)$ of a given four-quark state can be calculated directly, up to a certain value of $P^2_{\text{max}} = -M^2_{\text{max}}$. In Section 5.2 we saw that above this threshold value, certain singularity structures from the internal two-body poles or the quark poles enter into the integration domain and obstruct the direct calculation. In those cases, the condition for the eigenvalue $\lambda(P^2 = -M^2) = 1$ cannot be reached directly. The first option is to resort to contour deformation techniques as done in [79, 251], to circumvent the poles and directly calculate the eigenvalues. However, as shown in Appendix C.3, the contour deformation

needed in the case of the four-body FYE investigated in this thesis is a little more involved because of the complicated phase space. We therefore resorted to the second option, which is calculating the eigenvalue curve (EVC) up to the maximal mass M^2_{max} and extrapolate to the point where $\lambda(P^2 = -M^2) = 1$ is fulfilled.

In the past, it has been customary in the functional DSE/BSE framework to use quadratic or cubic polynomials or the Schlessinger-Point-Method (SPM) [179] for extrapolating the eigenvalue curves. The error for the resulting masses was usually given by the estimate for the systematic error of our model MT interaction. This in turn is achieved, by calculating and extrapolating the eigenvalue curve for a varying η_{MT} parameter in a range of $\{1.6, 2.0\}$. The four-quark states turn out to be remarkably stable under this variation [74, 78], which is why we neglect this estimate of the systematic error. We will, however, take into account the error coming from the extrapolation. This is important, as the extrapolation range can at times be quite large.

To achieve this, we employ an extrapolation procedure based on the SPM, which works as follows. Having calculated a set of N eigenvalues $\mathcal{E}_N = \left\{\lambda_r(P^2)\right\}_{r=1}^{N}$, up to the threshold P^2_{max}, we use a polynomial $p_n(P^2)$ of degree n to extrapolate the full EVC, involving all N eigenvalues, to the value where $\lambda(P^2 = -M^2) = 1$ is fulfilled. For the actual extrapolation, we use the tuple $\left(M_r, \lambda_r\right)$, with $r = 1, 2, \dots, N$ and $\lambda_r = \lambda(-M_r^2)$. Thereby, we obtain a first mass estimate M_{base} in the region where the mass of the investigated four-quark state is located. In principle one can test out different orders of polynomials and find which fits the EVC best. We found, that in most cases a cubic polynomial is sufficient, with higher orders not changing much. The quadratic polynomial, however, often does not agree well with the EVC and overshoots the relevant mass region significantly. The reason we use a polynomial to obtain the first mass estimate, instead of directly using the SPM, is because the SPM is known to at times produce spurious singularities, which would result in an unreasonably low first mass estimate. A pedagogical description of this behaviour and other features of the SPM is given in Appendix D of [164]. Using a polynomial is simply more stable and provides a more reliable first estimate. After determining the M_{base}, we choose a 5% (error) region around this mass and use the SPM to extrapolate the eigenvalues in $\mathcal{E}_N$ again. When using the SPM to extrapolate, it is actually advantageous to transform our input tuple $\left(M_r, \lambda_r\right)$ into $\left(M_r, \frac{1}{1-\lambda_r}\right)$ and search for the solution by looking for poles in the error region. We then repeat this extrapolation/pole search about 300 times and add each of the obtained values, which is located within the error region, to a set $\mathcal{B}_N$. After that, we choose a random subset of eigenvalues $\mathcal{E}_m \subset \mathcal{E}_N$, where $m \in \{N-1, N-2, N-3, N-4, N-5, N-6\}$ and repeat the same pole search as before. We repeat this about 300 times for each m and put every accepted mass, i.e., the values within the chosen error region, into a set $\mathcal{B}_m$ respectively. At the end of this, we have seven sets, $\mathcal{B}_N$, $\mathcal{B}_{N-1}$, ..., $\mathcal{B}_{N-6}$ containing about 300 mass values (depending on how many got accepted).

In Fig. C.4, we show example EVCs with their respective cubic fits in green. The histograms are the masses from the sets $\mathcal{B}_N$, $\mathcal{B}_{N-1}$, ..., $\mathcal{B}_{N-6}$ obtained by the SPM. One can distinguish two cases here: one where the mass values obtained by the SPM agree very nicely with the base estimate from the polynomial extrapolation (shown on the left),

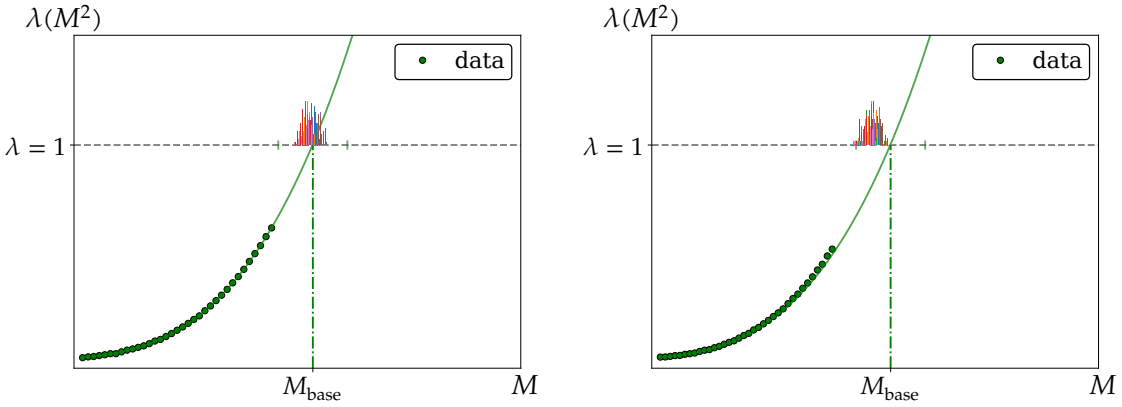

Figure C.4: Example eigenvalue curves with cubic fits and the obtained base mass estimate M_{base}. The histogram show the values in the sets $\mathcal{B}_m$ obtained by the SPM. On the left, we show the case where the masses from the SPM are in good agreement with the base estimate. On the right, we display the case, where the masses obtained from the SPM differ from the cubic fit.

and one where the polynomial fit does not fit the EVC perfectly and therefore yields an inaccurate base estimate (see right panel in Fig. C.4). In cases, where the extrapolation range in M is very large, one can up the error range to 10% around the M_{base}. One just needs to be careful not to make the error range too big, because of the spurious singularities of the SPM, which would then also get accepted as valid mass values.

In order to obtain the masses and corresponding error coming from the extrapolation, we first determine the arithmetic mean ($\overline{M}$) and standard deviation (σ) of the masses in each of the obtained sets $\mathcal{B}_m$ and add them to the sets $\mathcal{A}$ and $\mathcal{S}$, i.e.,

$$\mathcal{A} := \left\{ \overline{M}_{\mathcal{B}_m} \,\middle|\, m = N, N-1, \ldots, N-6 \right\}, \tag{C.22}$$

$$\mathcal{S} := \left\{ \sigma_{\mathcal{B}_m} \,\middle|\, m = N, N-1, \ldots, N-6 \right\}. \tag{C.23}$$

After that, we take the average of the values in the sets $\mathcal{A}$ and $\mathcal{S}$ to get the final mass plus error respectively: $M \pm \Delta M$. These masses then serve as an input for the quark mass evolution curves of the four-quark states compiled in Appendix C.6.

C.6 Four-quark state QMECs

We have already mentioned in Section 4.3.1, that the investigation of the current-quark mass evolution curve (QMEC) is crucial especially for the extraction of the heavy-light meson systems at physical u/d-quark masses. In the following, we will show the QMECs for the ground and first radial excited four-quark states investigated in this thesis using only the attractive colour channels (black crosses) and the attractive plus repulsive colour channels (green dots). The masses and error ($M + \Delta M$) going into the QMEC are obtained via the extrapolation scheme described in Appendix C.5. Additionally, we plot the behaviour of the two-body thresholds with varying current-quark mass. The closer the mass of the

four-quark state gets to the threshold, the more the state is affected by the poles of this threshold. In most cases this results in a strong upwards bending of the QMEC when approaching or crossing the threshold. Having identified the data points in the QMEC not affected by thresholds, we then apply a fit of the form Eq. (4.56), or more fits with varying degree in the polynomial if the fit range is large. The data points not taken into account by the fits are shown in opaque in the following plots. The final masses plotted in the spectra in Section 6.1 and stated in Appendix C.7 are then obtained from the fit function at the corresponding current-quark mass. The error is a combination of the error coming from the extrapolation and an error coming from the fits, i.e., $\Delta M = \Delta M^{\text{fits}} + \Delta M^{\text{extrap.}}$.

C.6.1 Hidden-flavour QMECs

In this section, we show the calculated QMECs used to extract the masses for the ground and excited states shown in Figs. 6.1 and 6.2. We always show the QMECs for the ground state in the top row and for the first radial excited state in the bottom row.

In Fig. C.5, we see that the inclusion of the repulsive colour channels has a huge effect on the QMECs for the $0(1^{++})$ channel, increasing the masses especially for $m_q > 350$ MeV for both the $cq\bar{q}\bar{c}$ and $bq\bar{q}\bar{b}$ systems. This results in the QMECs for the attractive plus repulsive colour channels (green dots) to be closer to the lowest two-body threshold and steeper. It also leads to the threshold coming into effect earlier than for the attractive only QMECs.

For the QMECs in the $1(1^{+-})$ and $0(1^{--})$ channels, the effect of the repulsive colour channels is not that big, as can be seen from the corresponding QMECs in Figs. C.6 and C.8.

For the $0(0^{++})$ channel, we observe a significant increase in mass of the QMECs in Fig. C.7 when including the repulsive colour forces in the physical BSA.

The $0(0^{-+})$ channel, the QMECs for the attractive only and the full physical BSA show no deviation for $m_q \to m_b$ and start to deviate around $m_q \approx m_c$, going to a much higher mass for the $cn\bar{n}\bar{c}$ and $bn\bar{n}\bar{b}$ states in the case of attractive + repulsive colour forces.

Generally, we observe a similar behaviour of the QMECs for the ground and first excited states for the different channels upon the inclusion of the repulsive colour forces.

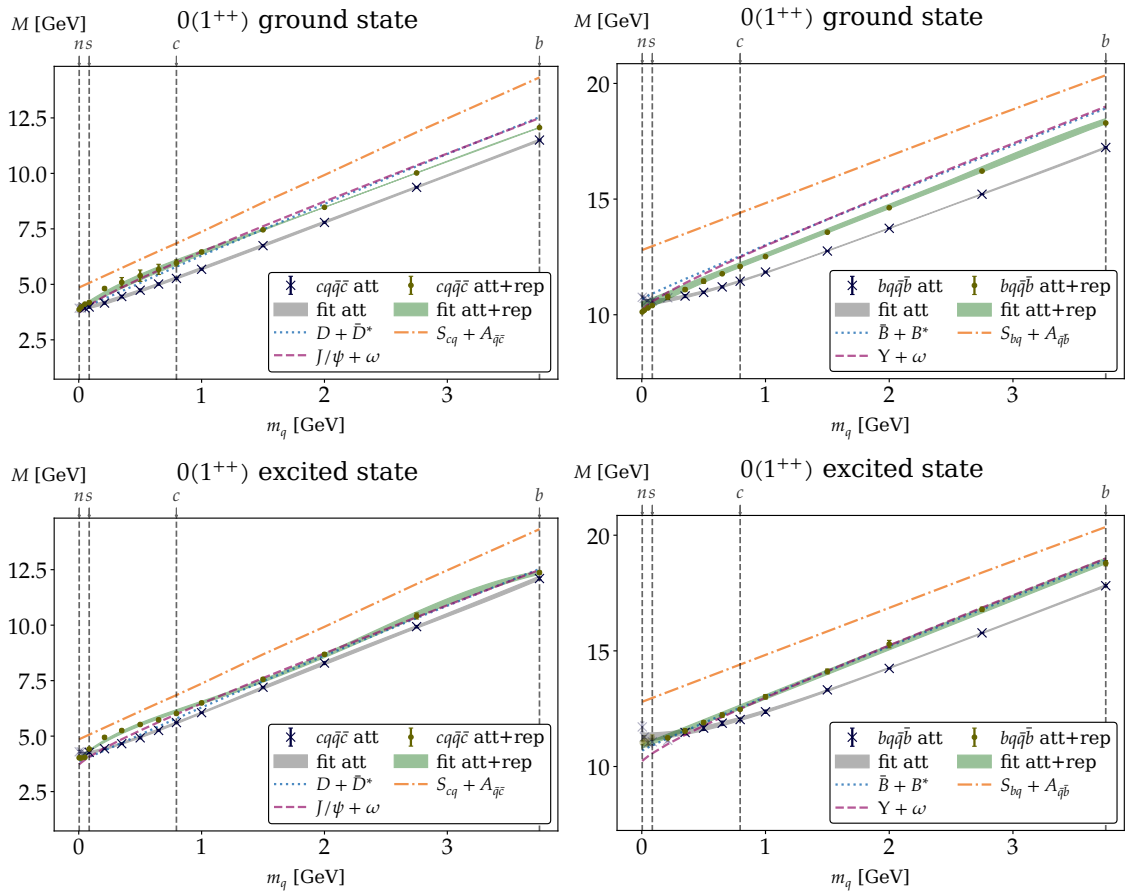

Figure C.5: Quark mass evolution curve for the $0(1^{++})$ ground and excited states for the hidden-charm (*left panel*) and hidden-bottom (*right panel*) quark configuration. The black crosses denote the results with only attractive colour forces, the green dots are the results with attractive plus repulsive colour channels. The grey and green bands are the respective fits to the data, with the opaque data not taken into account into the fit. Additionally, we show the quark mass evolution of the relevant two-body thresholds.

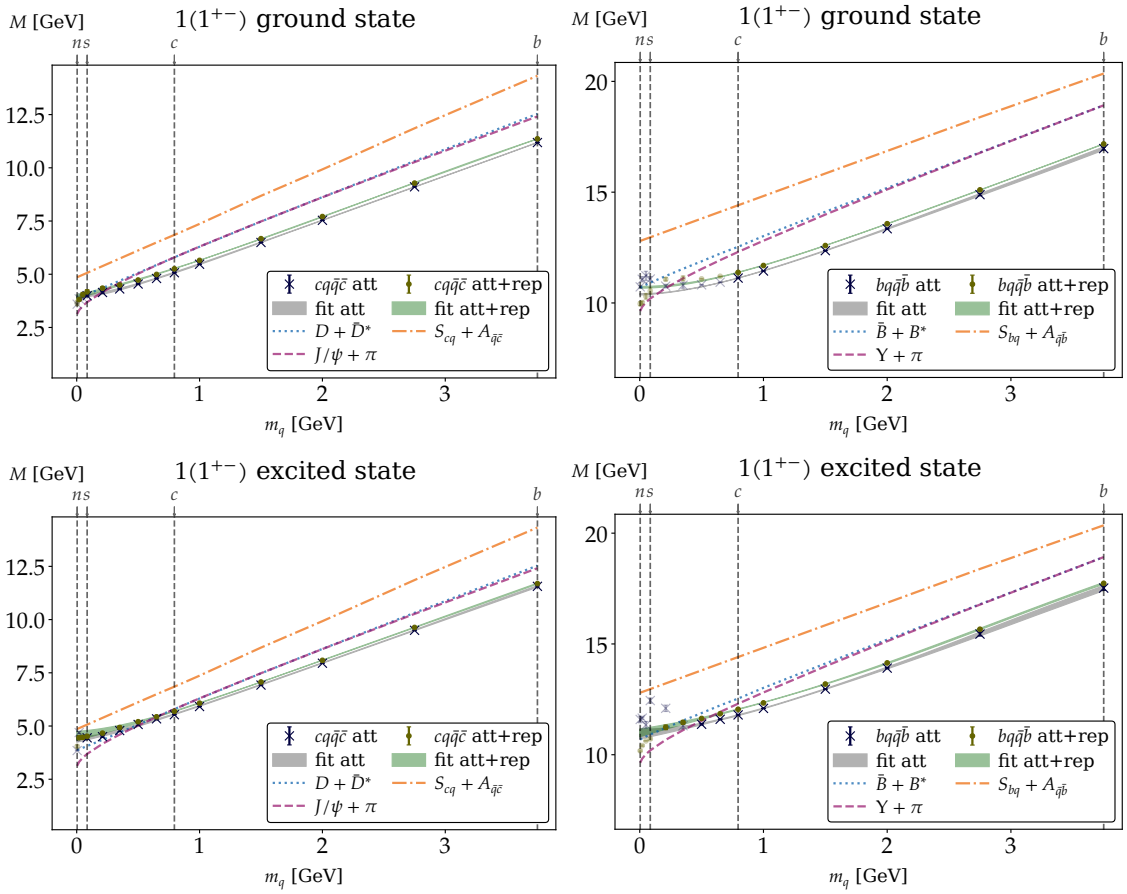

Figure C.6: Same as in Fig. C.5 but for the hidden-charm and hidden-bottom ground states in the $1(1^{+-})$ channel.

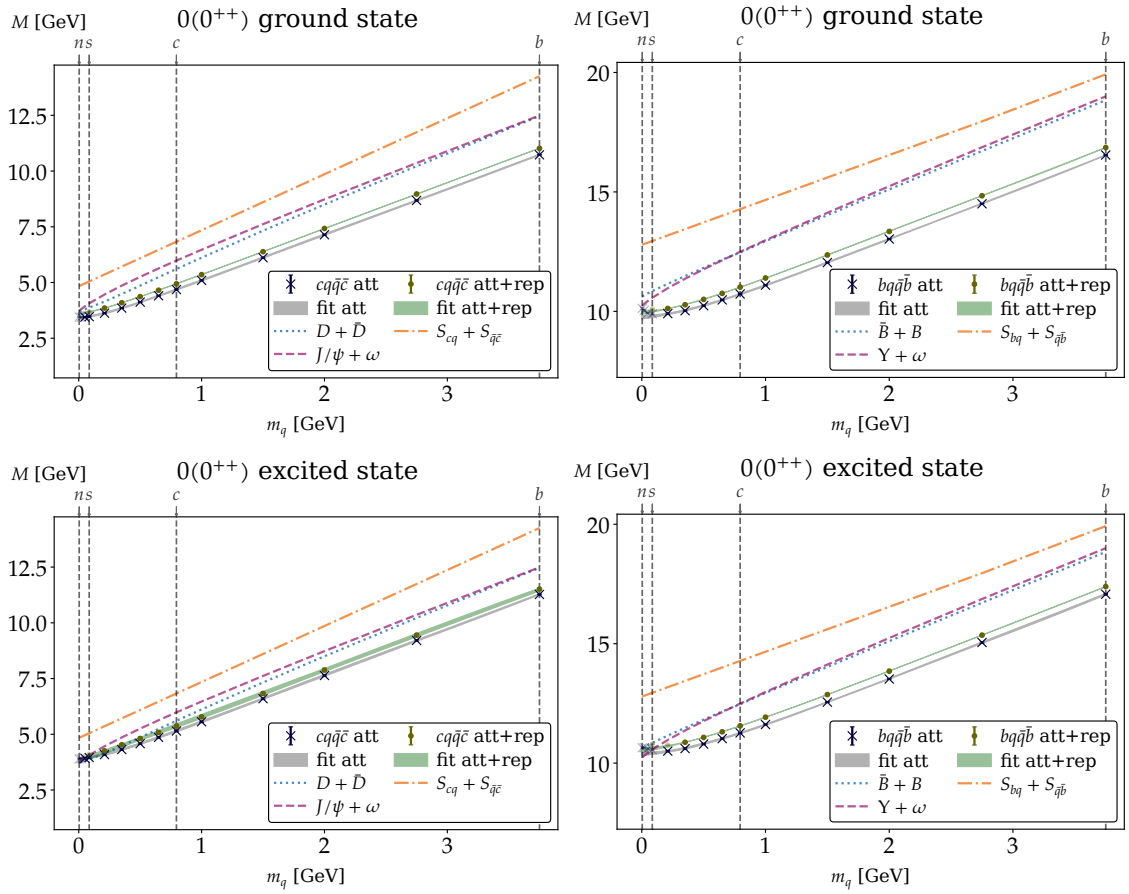

Figure C.7: Same as in Fig. C.5 but for the ground states in the $0(0^{++})$ channel.

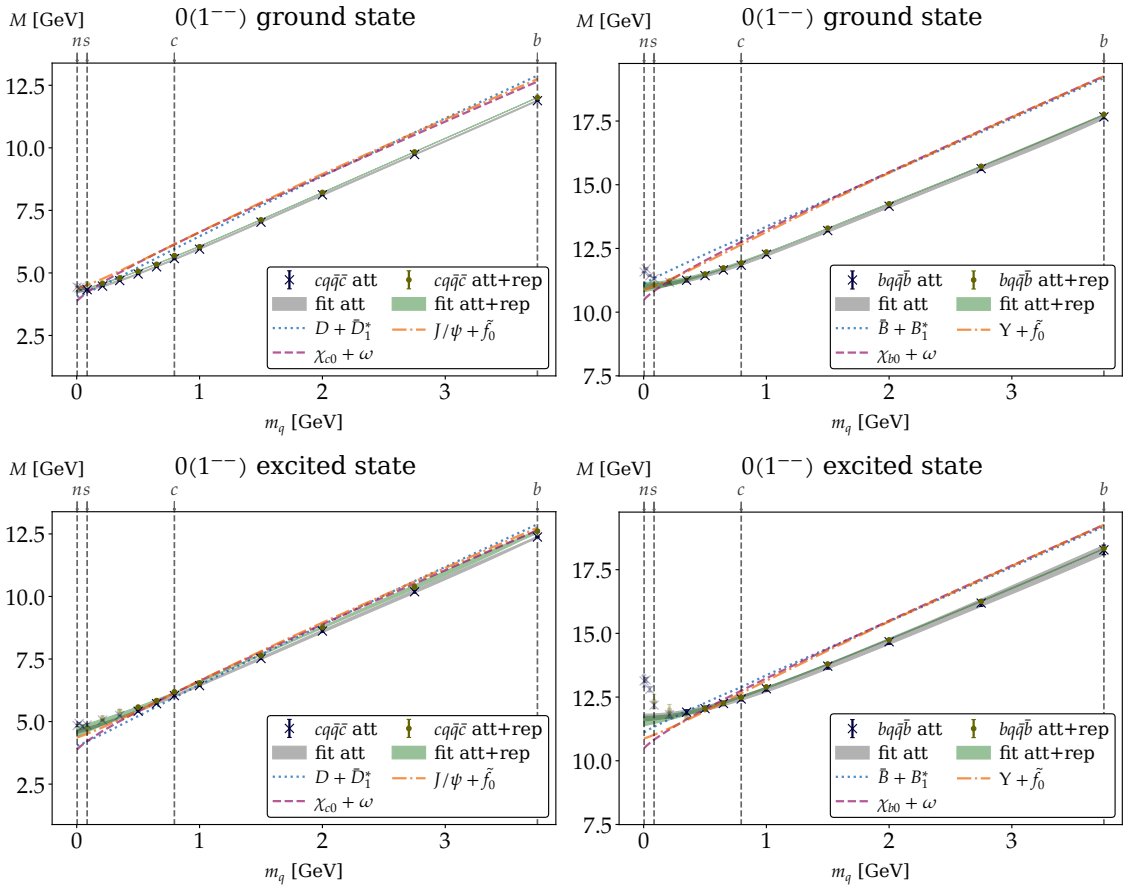

Figure C.8: Same as in Fig. C.5 but for the ground states in the $0(1^{--})$ channel.

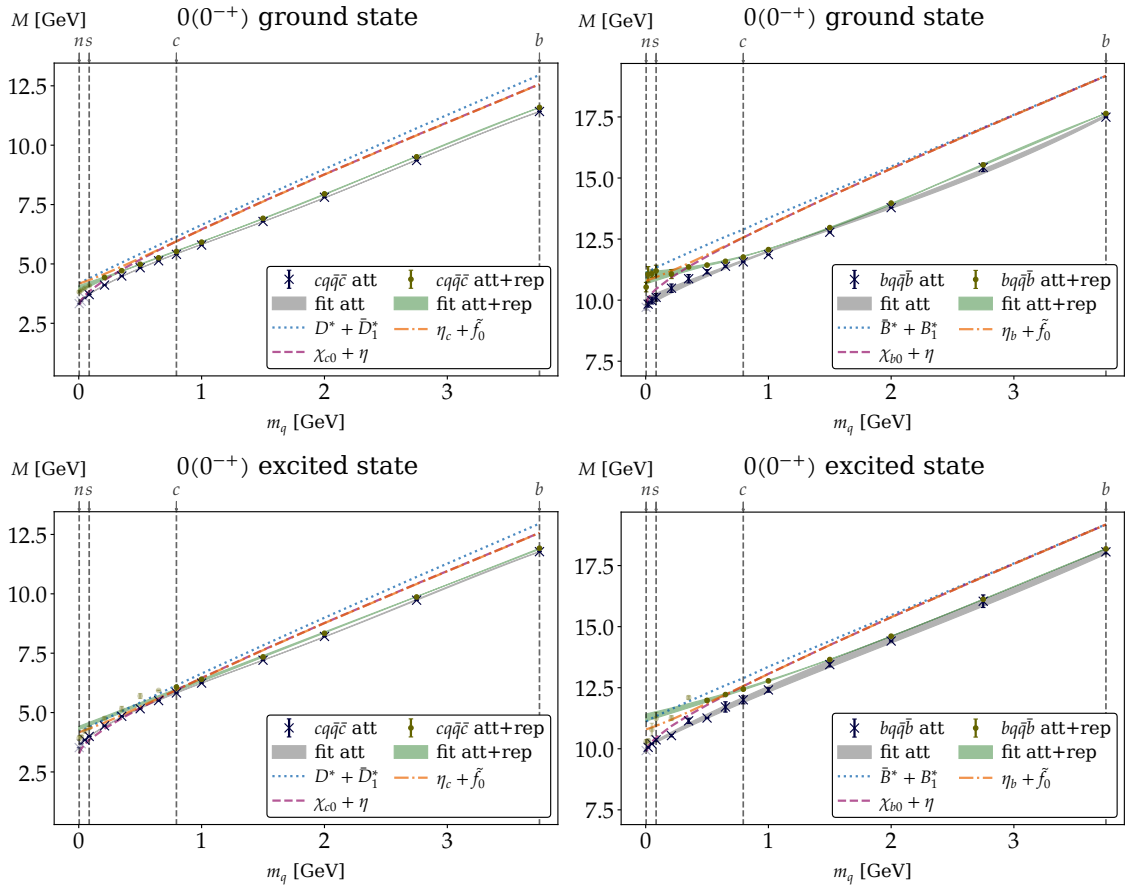

Figure C.9: Same as in Fig. C.5 but for the ground states in the $0(0^{-+})$ channel.

C.6.2 Open-flavour QMECs

In this section, we display the QMECs for the open-flavour four-quark states investigated in this work. These were used to extract the masses (and binding energies) shown in Figs. 6.3 and 6.6 with the associated numerical values given in Tables C.4 and C.6 to C.8.

As discussed in the main text, we see that for the open-charm ($cc\bar{q}\bar{q}$)and open-bottom ($bb\bar{q}\bar{q}$) ground states in the $0(1^+)$ channel, the inclusion of the repulsive channels yields a significant increase in the four-quark state masses, cf. Fig. C.10. The masses are closer to the threshold and the QMECs are more linear in nature, which also changes the behaviour when going to $m_q \to m_{u/d}$. The same is also observed for the open-bottom-charm ($bc\bar{q}\bar{q}$) ground state.

For the isospin partner channel, the $1(1^+)$, we do not observe this behaviour at least for the ground states with $bb\bar{q}\bar{q}$ and $cc\bar{q}\bar{q}$ quark configurations. The $bc\bar{q}\bar{q}$ ground states exhibit also a very strong increase in mass upon inclusion of the repulsive colour forces.

For the corresponding excited states, we find a very similar picture. For the $bb\bar{q}\bar{q}$ excited state with quantum numbers $1(1^+)$ (bottom right in Fig. C.11), we observe that for $m_q \to m_b$ the QMEC shows some strange behaviour for the attractive only case. This is due to the appearance of complex conjugate eigenvalues, which thwart a precise determination of the mass via the extrapolation method (cf. Appendix C.5) and results in a large extrapolation error. This situation improves drastically when we include the repulsive channels, yielding a QMEC with linear behaviour over the whole current-quark mass span.

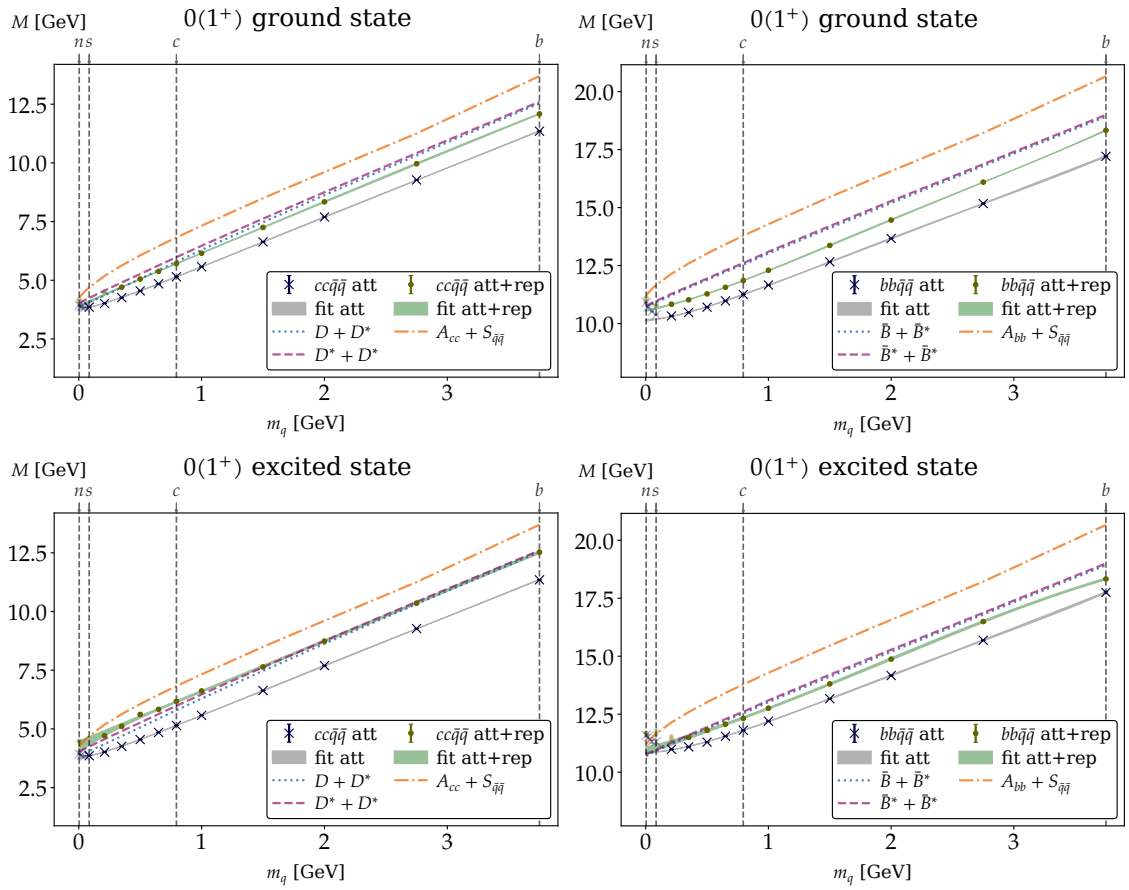

Figure C.10: Quark mass evolution curve for the $0(1^+)$ ground and excited states for the open-charm (*left panel*) and open-bottom (*right panel*) quark configuration. The black crosses denote the results with only attractive colour forces, the green dots are the results with attractive plus repulsive colour channels. The grey and green bands are the respective fits to the data, with the opaque data not taken into account into the fit. Additionally, we show the quark mass evolution of the relevant two-body thresholds.

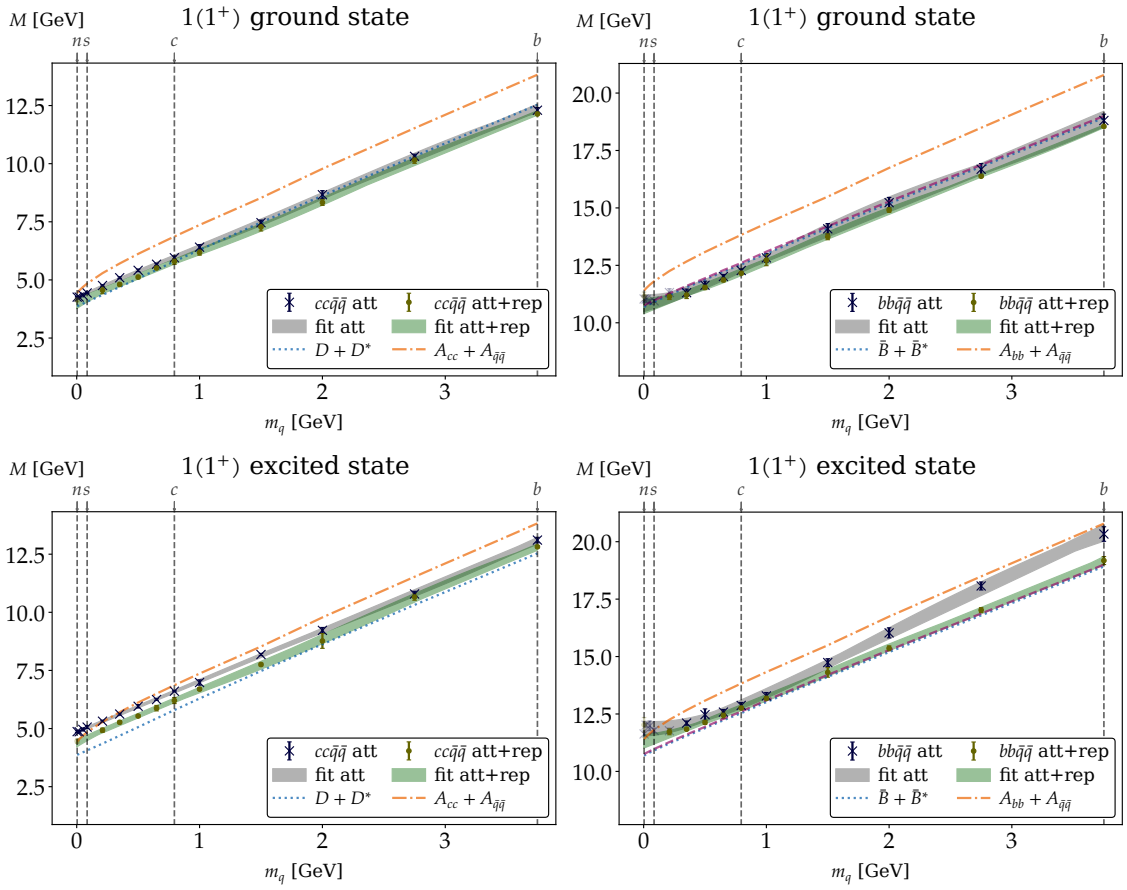

Figure C.11: Same as in Fig. C.10 but for the $1(1^+)$ channel .

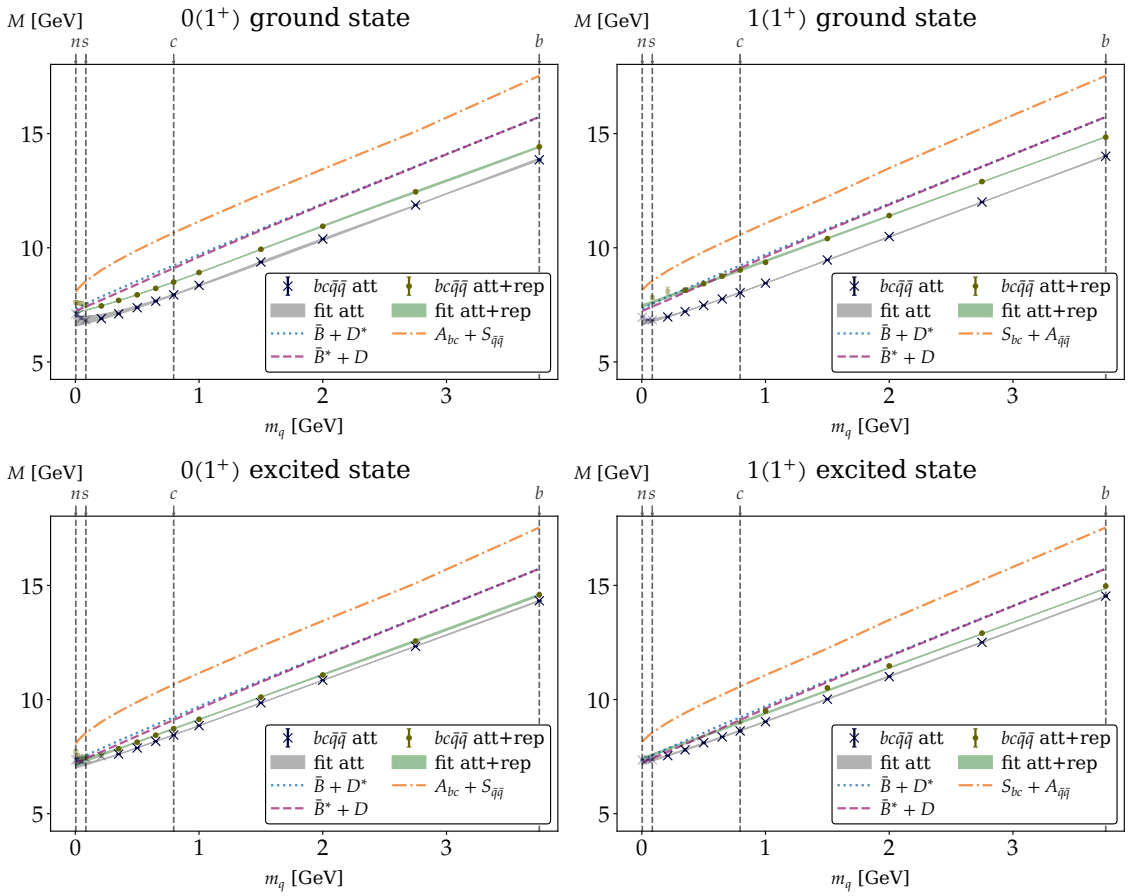

Figure C.12: Same as in Fig. C.10 but for the open-bottom-charm $bc\bar{q}\bar{q}$ states in the $0(1^+)$ (*left*) and $1(1^+)$ (*right*) channel .

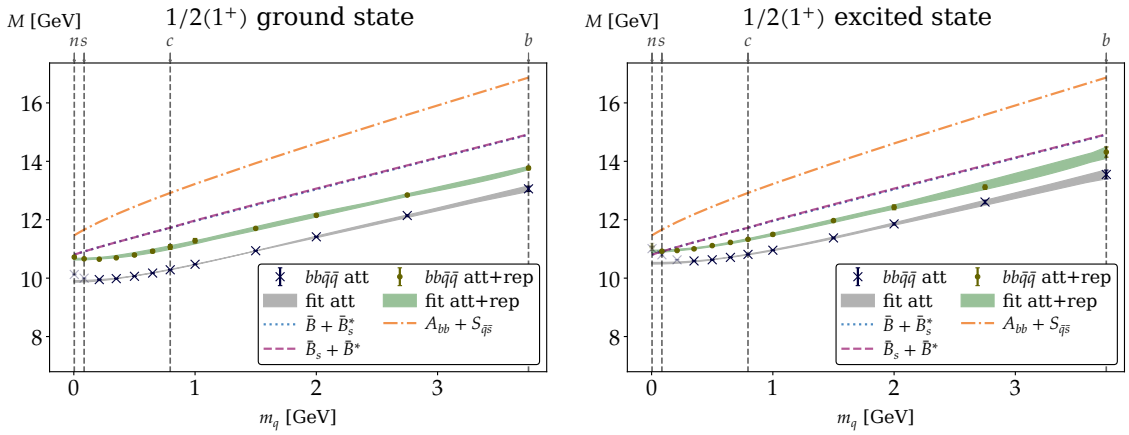

Figure C.13: Same as in Fig. C.10 but for the open-bottom-strange $bb\bar{q}\bar{s}$ ground (*left*) and excited states (*right*) .

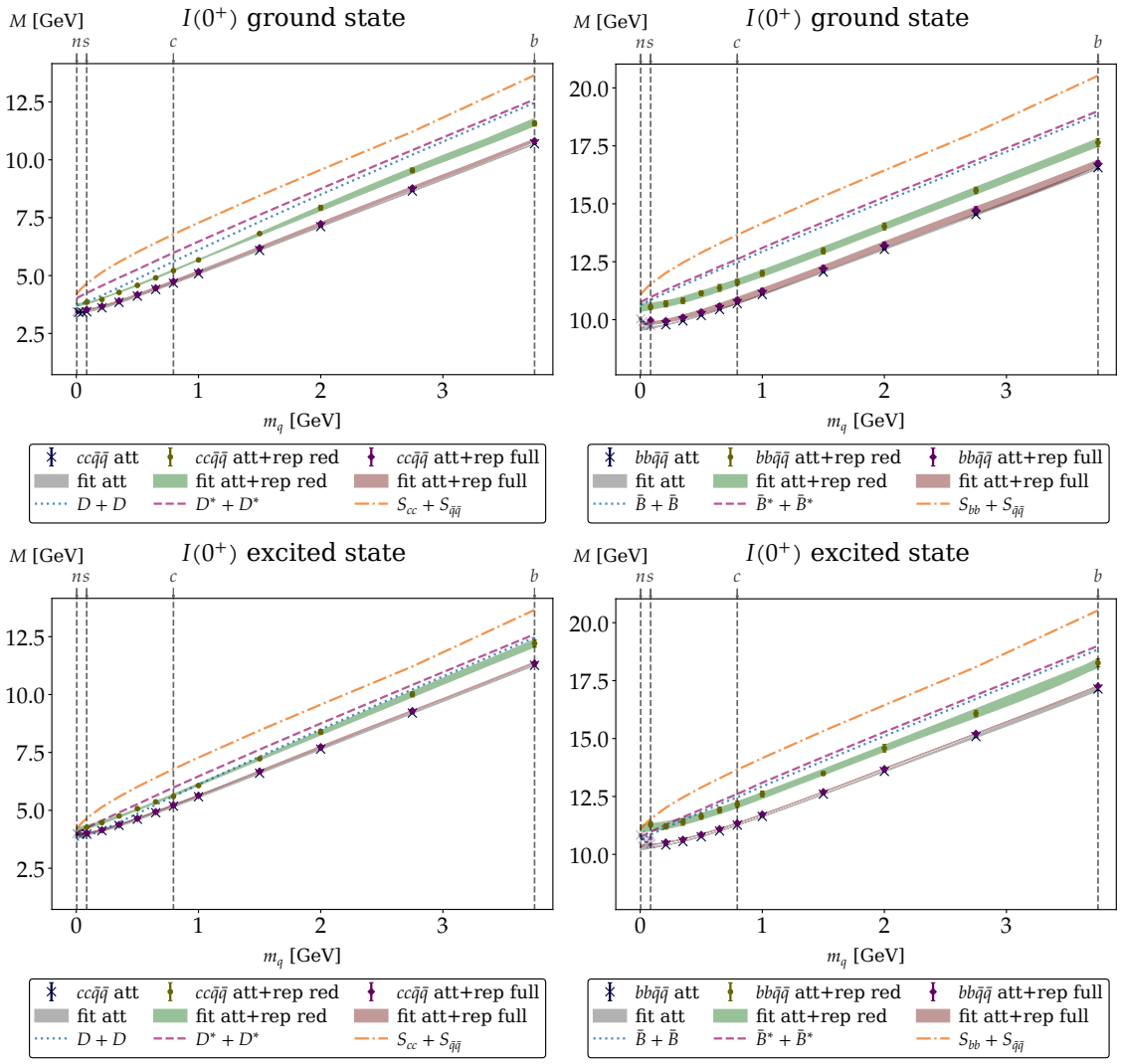

Figure C.14: Same as in Fig. C.10 but for the $J^P = 0^+$ channel.

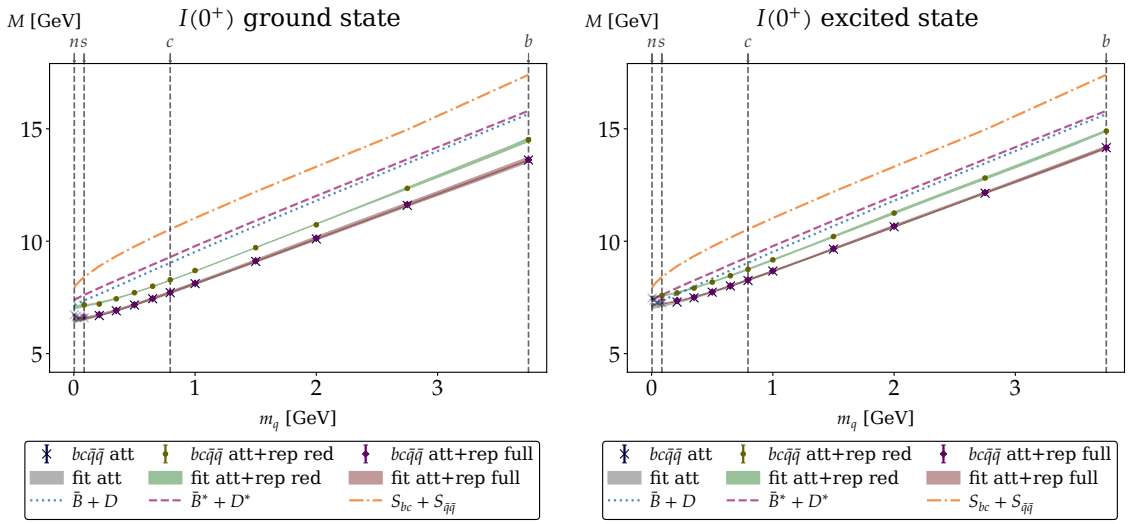

Figure C.15: Same as in Fig. C.14 but for the open-bottom-charm $bc\bar{q}\bar{q}$ ground (*left*) and excited states (*right*) .

C.7 Four-quark masses and binding energies

In this section, we compile the numerical values for the mass spectra of the hidden- and open-flavour four-quark states shown and discussed in Section 6.1. These values are obtained from the QMECs shown in Appendix C.6. Additionally, we give the values for the binding energies (E_B) with respect to the lowest heavy-light meson-meson threshold for the corresponding channels.

C.7.1 Hidden-flavour masses and binding energies

In Table C.2 we state the numerical values for the masses and binding energies (plus the obtained error) for the hidden-flavour ground states shown in Figs. 6.1 and 6.2. Correspondingly, in Table C.3 we state the values for the associated first radial excited states

	$0(0^{-+})$		$0(1^{--})$		$0(0^{++})$		$1(1^{+-})$		$0(1^{++})$	
	M	E_B	M	E_B	M	E_B	M	E_B	M	E_B
$cn\bar{n}\bar{c}$	3.37(0)	−0.81(0)	4.27(2)	0.23(2)	3.41(1)	−0.31(1)	3.94(2)	0.07(2)	3.89(4)	0.02(4)
$cn\bar{n}\bar{c}$	3.96(22)	−0.23(22)	4.28(1)	0.25(1)	3.60(7)	−0.12(7)	3.94(6)	0.07(6)	3.91(3)	0.04(3)
$cs\bar{s}\bar{c}$	3.68(0)	−0.71(0)	4.33(2)	0.12(2)	3.47(1)	−0.40(1)	3.99(2)	−0.07(2)	3.98(4)	−0.08(4)
$cs\bar{s}\bar{c}$	4.14(15)	−0.25(15)	4.39(1)	0.18(1)	3.68(3)	−0.19(3)	4.07(4)	0.01(4)	4.18(7)	0.12(7)
$bn\bar{n}\bar{b}$	9.93(19)	−1.24(19)	11.00(5)	−0.11(5)	9.77(2)	−0.85(2)	10.40(1)	−0.28(1)	10.52(6)	−0.17(6)
$bn\bar{n}\bar{b}$	11.01(35)	−0.17(35)	10.91(12)	−0.20(12)	9.95(6)	−0.67(6)	10.66(6)	−0.03(6)	10.34(15)	−0.34(15)
$bs\bar{s}\bar{b}$	10.13(16)	−1.27(16)	11.03(5)	−0.30(5)	9.80(2)	−1.05(2)	10.42(1)	−0.49(1)	10.55(6)	−0.36(6)
$bs\bar{s}\bar{b}$	11.07(25)	−0.33(25)	10.98(9)	−0.35(9)	10.00(3)	−0.85(3)	10.67(5)	−0.24(5)	10.54(13)	−0.37(13)
$bc\bar{c}\bar{b}$	11.61(3)	−1.35(3)	11.89(3)	−1.00(3)	10.72(2)	−1.74(2)	11.13(0)	−1.41(0)	11.45(2)	−1.08(2)
$bc\bar{c}\bar{b}$	11.78(1)	−1.17(1)	11.97(0)	−0.92(0)	11.01(0)	−1.45(0)	11.37(1)	−1.16(1)	12.13(6)	−0.41(6)

Table C.2: Masses for the hidden-charm ($cq\bar{q}\bar{c}$) and hidden-bottom ($bq\bar{q}\bar{b}$) ground states in GeV. Additionally, we display the obtained binding energies E_B with respect to the lightest heavy-light meson-meson thresholds (masses obtained by the two-body BSE). The error in the brackets is a combination of extrapolation error of the EVCs and the error coming from the fit of the QMECs. The colourless rows denote the values obtained by using only the attractive colour channels while the rows highlighted in green display the values obtained for the attractive plus repulsive colour channels. Resonant particles found above threshold haver their "binding energy" shown in grey.

	$0(0^{-+})$		$0(1^{--})$		$0(0^{++})$		$1(1^{+-})$		$0(1^{++})$	
	M	E_B	M	E_B	M	E_B	M	E_B	M	E_B
$cn\bar{n}\bar{c}$	3.69(0)	−0.50(0)	4.64(4)	0.60(4)	3.89(2)	0.17(2)	4.36(4)	0.49(4)	4.19(3)	0.32(3)
$cn\bar{n}\bar{c}$	4.35(6)	0.17(6)	4.52(7)	0.48(7)	3.85(10)	0.13(10)	4.30(12)	0.43(12)	4.26(3)	0.39(3)
$cs\bar{s}\bar{c}$	4.00(1)	−0.40(1)	4.71(3)	0.50(3)	3.95(2)	0.08(2)	4.42(4)	0.36(4)	4.26(3)	0.20(3)
$cs\bar{s}\bar{c}$	4.52(6)	0.12(6)	4.69(6)	0.48(6)	4.00(9)	0.12(9)	4.46(10)	0.40(10)	4.51(4)	0.45(4)
$bn\bar{n}\bar{b}$	10.09(3)	−1.09(3)	11.71(8)	0.60(8)	10.38(2)	−0.24(2)	10.97(5)	0.29(5)	11.27(9)	0.58(9)
$bn\bar{n}\bar{b}$	11.22(13)	0.05(13)	11.55(17)	0.44(17)	10.56(9)	−0.06(9)	10.99(18)	0.31(18)	10.84(9)	0.16(9)
$bs\bar{s}\bar{b}$	10.30(4)	−1.09(4)	11.73(7)	0.40(7)	10.41(2)	−0.44(2)	11.02(5)	0.11(5)	11.30(9)	0.39(9)
$bs\bar{s}\bar{b}$	11.35(12)	−0.05(12)	11.60(14)	0.27(14)	10.61(6)	−0.24(6)	11.10(14)	0.18(14)	11.00(7)	0.09(7)
$bc\bar{c}\bar{b}$	12.00(11)	−0.96(11)	12.46(6)	−0.43(6)	11.26(2)	−1.21(2)	11.78(1)	−0.75(1)	12.06(5)	−0.48(5)
$bc\bar{c}\bar{b}$	12.44(4)	−0.51(4)	12.51(3)	−0.38(3)	11.56(0)	−0.91(0)	12.05(1)	−0.48(1)	12.53(7)	−0.00(7)

Table C.3: Same as in Table C.2 but for the first radial excited states.

C.7.2 Open-flavour masses and binding energies

Similar to above, we compiled the masses and binding energies corresponding to the $J^P = 1^+$ open-flavour ground and excited states shown in Fig. 6.3 in Tables C.4 and C.6. Correspondingly, the masses and binding energies of the investigated $J^P = 0^+$ ground and excited states (shown in Fig. 6.6) are compiled in Tables C.7 and C.8. We show the masses and binding energy for the $^1/_2(1^+)$ $bb\bar{q}\bar{s}$ state in Table C.5.

	$QQ\bar{q}\bar{q}$					$QQ'\bar{q}\bar{q}$			
	$0(1^+)$		$1(1^+)$			$0(1^+)$		$1(1^+)$	
	M	E_B	M	E_B		M	E_B	M	E_B
$cc\bar{n}\bar{n}$	3.78(5)	−0.09(5)	4.25(3)	0.38(3)	$bc\bar{n}\bar{n}$	6.61(4)	−0.63(4)	6.65(2)	−0.58(2)
$cc\bar{n}\bar{n}$	3.89(5)	0.02(5)	4.03(12)	0.16(12)	$bc\bar{n}\bar{n}$	7.24(3)	0.00(3)	7.45(5)	0.22(5)
$cc\bar{s}\bar{s}$	4.45(2)	0.39(2)	–	–	$bc\bar{s}\bar{s}$	6.77(2)	−0.65(2)	–	–
$cc\bar{s}\bar{s}$	4.23(10)	0.17(10)	–	–	$bc\bar{s}\bar{s}$	7.61(5)	0.19(5)	–	–
$bb\bar{n}\bar{n}$	10.14(4)	−0.54(4)	10.90(25)	0.21(25)	$bc\bar{c}\bar{c}$	8.04(0)	−1.07(0)	–	–
$bb\bar{n}\bar{n}$	10.57(4)	−0.11(4)	10.71(11)	0.03(11)	$bc\bar{c}\bar{c}$	9.02(1)	−0.09(1)	–	–
$bb\bar{s}\bar{s}$	10.96(20)	0.05(20)	–	–	$bc\bar{b}\bar{b}$	14.01(1)	−1.72(1)	–	–
$bb\bar{s}\bar{s}$	10.83(10)	−0.08(10)	–	–	$bc\bar{b}\bar{b}$	14.86(1)	−0.88(1)	–	–
$bb\bar{c}\bar{c}$	12.35(13)	−0.19(13)	–	–					
$bb\bar{c}\bar{c}$	12.20(9)	−0.33(9)	–	–					

Table C.4: Ground state masses for the $J^P = 1^+$ open-charm ($cc\bar{q}\bar{q}$) and open-bottom ($bb\bar{q}\bar{q}$) states (*left*) and the open-bottom-charm ($bc\bar{q}\bar{q}$) states (*right*) in GeV. For completeness we also display the binding energies E_B with respect to the lightest (calculated) heavy-light meson-meson threshold in each channel $\big((Q\bar{q})_{1^-} \otimes (Q'\bar{q})_{0^-}$ for $QQ'\bar{q}\bar{q}\big)$; the "binding energies" for resonant particles above the threshold are shown in grey. The colourless rows denote the values obtained by using only the attractive colour channels while the rows highlighted in green display the values obtained for the attractive plus repulsive colour channels. The error given in the brackets is the combination of the extrapolation error and the error of the fit to the quark mass evolution curve. Table adapted from [190].

	$\frac{1}{2}(1^+)$ ground		$\frac{1}{2}(1^+)$ excited	
	M	E_B	M	E_B
$bb\bar{n}\bar{s}$	9.89(2)	−0.91(2)	10.51(3)	−0.29(3)
$bb\bar{n}\bar{s}$	10.68(5)	−0.12(5)	11.01(9)	0.22(9)
$bb\bar{c}\bar{s}$	10.30(1)	−1.42(1)	10.81(1)	−0.91(1)
$bb\bar{c}\bar{s}$	11.05(5)	−0.67(5)	11.31(2)	−0.41(2)
$bb\bar{b}\bar{s}$	13.07(7)	−1.84(7)	13.56(11)	−1.35(11)
$bb\bar{b}\bar{s}$	13.78(4)	−1.13(4)	14.30(15)	−0.61(15)

Table C.5: Masses and binding energies of the $bb\bar{q}\bar{s}$ ground (*left*) and first excited state (*right*).

	$QQ\bar{q}\bar{q}$					$QQ'\bar{q}\bar{q}$			
	$0(1^+)$		$1(1^+)$			$0(1^+)$		$1(1^+)$	
	M	E_B	M	E_B		M	E_B	M	E_B
$cc\bar{n}\bar{n}$	4.25(9)	0.37(9)	4.87(4)	0.99(4)	$bc\bar{n}\bar{n}$	7.02(2)	−0.22(2)	7.18(2)	−0.06(2)
$cc\bar{n}\bar{n}$	4.43(3)	0.56(3)	4.41(9)	0.54(9)	$bc\bar{n}\bar{n}$	7.38(3)	0.15(3)	7.52(8)	0.29(8)
$cc\bar{s}\bar{s}$	5.04(3)	0.97(3)	–	–	$bc\bar{s}\bar{s}$	7.32(2)	−0.10(2)	–	–
$cc\bar{s}\bar{s}$	4.61(8)	0.55(8)	–	–	$bc\bar{s}\bar{s}$	7.68(8)	0.26(8)	–	–
$bb\bar{n}\bar{n}$	10.84(3)	0.15(3)	11.84(27)	1.16(27)	$bc\bar{c}\bar{c}$	8.64(1)	−0.46(1)	–	–
$bb\bar{n}\bar{n}$	10.92(15)	0.24(15)	11.27(10)	0.58(10)	$bc\bar{c}\bar{c}$	9.09(6)	−0.01(6)	–	–
$bb\bar{s}\bar{s}$	11.85(25)	0.94(25)	–	–	$bc\bar{b}\bar{b}$	14.53(1)	−1.20(1)	–	–
$bb\bar{s}\bar{s}$	11.40(8)	0.49(8)	–	–	$bc\bar{b}\bar{b}$	14.94(0)	−0.79(0)	–	–
$bb\bar{c}\bar{c}$	12.93(15)	0.40(15)	–	–					
$bb\bar{c}\bar{c}$	12.77(7)	0.23(7)	–	–					

Table C.6: Same as in Table C.4 but for the first radial excited states.

	$QQ\bar{q}\bar{q}$					$QQ'\bar{q}\bar{q}$			
	$0(0^+)$		$1(0^+)$			$0(0^+)$		$1(0^+)$	
	M	E_B	M	E_B		M	E_B	M	E_B
$cc\bar{n}\bar{n}$	–	–	3.39(4)	−0.33(4)	$bc\bar{n}\bar{n}$	–	–	6.52(5)	−0.65(5)
$cc\bar{n}\bar{n}$	–	–	3.47(0)	−0.26(0)	$bc\bar{n}\bar{n}$	–	–	6.53(2)	−0.64(8)
$cc\bar{n}\bar{n}$	–	–	3.73(4)	0.00(4)	$bc\bar{n}\bar{n}$	–	–	7.07(2)	−0.10(2)
$cc\bar{s}\bar{s}$	3.45(2)	−0.42(2)	–	–	$bc\bar{s}\bar{s}$	6.57(2)	−0.79(2)	–	–
$cc\bar{s}\bar{s}$	3.53(0)	−0.34(0)	–	–	$bc\bar{s}\bar{s}$	6.58(2)	−0.78(658)	–	–
$cc\bar{s}\bar{s}$	3.81(3)	−0.06(3)	–	–	$bc\bar{s}\bar{s}$	7.13(2)	−0.23(2)	–	–
$bb\bar{n}\bar{n}$	–	–	9.60(7)	−1.02(7)	$bc\bar{c}\bar{c}$	7.71(2)	−1.33(2)	–	–
$bb\bar{n}\bar{n}$	–	–	9.86(3)	−0.76(3)	$bc\bar{c}\bar{c}$	7.72(3)	−1.31(2)	–	–
$bb\bar{n}\bar{n}$	–	–	10.56(13)	−0.06(13)	$bc\bar{c}\bar{c}$	8.26(0)	−0.77(0)	–	–
$bb\bar{s}\bar{s}$	9.65(4)	−1.20(4)	–	–	$bc\bar{b}\bar{b}$	13.61(1)	−2.04(1)	–	–
$bb\bar{s}\bar{s}$	9.89(3)	−0.96(3)	–	–	$bc\bar{b}\bar{b}$	13.63(7)	−2.02(733)	–	–
$bb\bar{s}\bar{s}$	10.61(13)	−0.24(13)	–	–	$bc\bar{b}\bar{b}$	14.51(5)	−1.15(5)	–	–
$bb\bar{c}\bar{c}$	10.69(0)	−1.77(0)	–	–					
$bb\bar{c}\bar{c}$	10.84(7)	−1.63(7)	–	–					
$bb\bar{c}\bar{c}$	11.66(13)	−0.80(13)	–	–					

Table C.7: Same as in Table C.4 but for the $J^P = 0^+$ states. The white rows are the masses obtained with using only the attractive colour forces, the red highlighted rows are obtained by using the full attractive plus repulsive component basis in Table 5.4. The green rows are the masses obtained by using the 'reduced' physical component basis, see Section 6.1.2 for details.

	$QQ\bar{q}\bar{q}$					$QQ'\bar{q}\bar{q}$			
	$0(0^+)$		$1(0^+)$			$0(0^+)$		$1(0^+)$	
	M	E_B	M	E_B		M	E_B	M	E_B
$cc\bar{n}\bar{n}$	–	–	3.92(7)	0.20(7)	$bc\bar{n}\bar{n}$	–	–	7.09(8)	−0.08(8)
$cc\bar{n}\bar{n}$	–	–	3.95(2)	0.23(2)	$bc\bar{n}\bar{n}$	–	–	7.18(0)	0.01(8)
$cc\bar{n}\bar{n}$	–	–	4.19(3)	0.47(3)	$bc\bar{n}\bar{n}$	–	–	7.47(1)	0.30(1)
$cc\bar{s}\bar{s}$	3.99(3)	0.11(3)	–	–	$bc\bar{s}\bar{s}$	7.15(5)	−0.21(5)	–	–
$cc\bar{s}\bar{s}$	4.01(2)	0.14(2)	–	–	$bc\bar{s}\bar{s}$	7.22(0)	−0.14(722)	–	–
$cc\bar{s}\bar{s}$	4.28(3)	0.40(3)	–	–	$bc\bar{s}\bar{s}$	7.54(1)	0.18(1)	–	–
$bb\bar{n}\bar{n}$	–	–	10.26(6)	−0.36(6)	$bc\bar{c}\bar{c}$	8.27(2)	−0.77(2)	–	–
$bb\bar{n}\bar{n}$	–	–	10.50(1)	−0.11(1)	$bc\bar{c}\bar{c}$	8.28(1)	−0.76(0)	–	–
$bb\bar{n}\bar{n}$	–	–	11.06(1)	0.45(1)	$bc\bar{c}\bar{c}$	8.75(1)	−0.28(1)	–	–
$bb\bar{s}\bar{s}$	10.30(3)	−0.55(3)	–	–	$bc\bar{b}\bar{b}$	14.16(1)	−1.49(1)	–	–
$bb\bar{s}\bar{s}$	10.51(1)	−0.34(1)	–	–	$bc\bar{b}\bar{b}$	14.17(4)	−1.48(746)	–	–
$bb\bar{s}\bar{s}$	11.13(1)	0.28(1)	–	–	$bc\bar{b}\bar{b}$	14.90(2)	−0.75(2)	–	–
$bb\bar{c}\bar{c}$	11.26(0)	−1.21(0)	–	–					
$bb\bar{c}\bar{c}$	11.36(4)	−1.10(4)	–	–					
$bb\bar{c}\bar{c}$	12.21(11)	−0.25(11)	–	–					

Table C.8: Same as in Table C.7 but for the first radial excited states with $J^P = 0^+$.

C.8 Four-quark state NCQMECs

In this section we show the norm contribution (current-)quark mass evolution curves (NCQMECs) and the corresponding fits used to extract the norm contributions shown in Figs. 6.8 and 6.9. We always show the obtained NCQMEC using only the attractive colour components on the left and using the attractive plus repulsive colour channels on the right. The colour coding of the data corresponds to the matrix entries in Fig. 6.7 and to the results displayed in Figs. 6.8 and 6.9. Data points plotted in opaque are not taken into account by the fits as they correspond to the omitted data points in the fits for the corresponding quark mass evolution curves in Appendix C.6.

C.8.1 Hidden-flavour NCQMECs

In Fig. C.16 and Fig. C.17 we show the obtained norm contribution quark mass evolution curves for the investigated hidden-flavour four-quark states with total spin $J = 1$ and $J = 0$, respectively. For each quantum number we show the $cq\bar{q}\bar{c}$ in the top panel and the $bq\bar{q}\bar{b}$ in the bottom panel.

We see, that most of the NCQMECs are well behaved across the whole range of current-quark masses. For the $1(1^{+-})$ states, the data towards the quark mass $m_q \to m_n$ is not really trustworthy as the internal two-body poles restrict the calculations in this channel. Therefore, the range that needs to be fitted is quite large here. The only channel, where the norm contributions vary largely with changing quark mass is for the $cq\bar{q}\bar{c}$ state in the 0^{-+} channel.

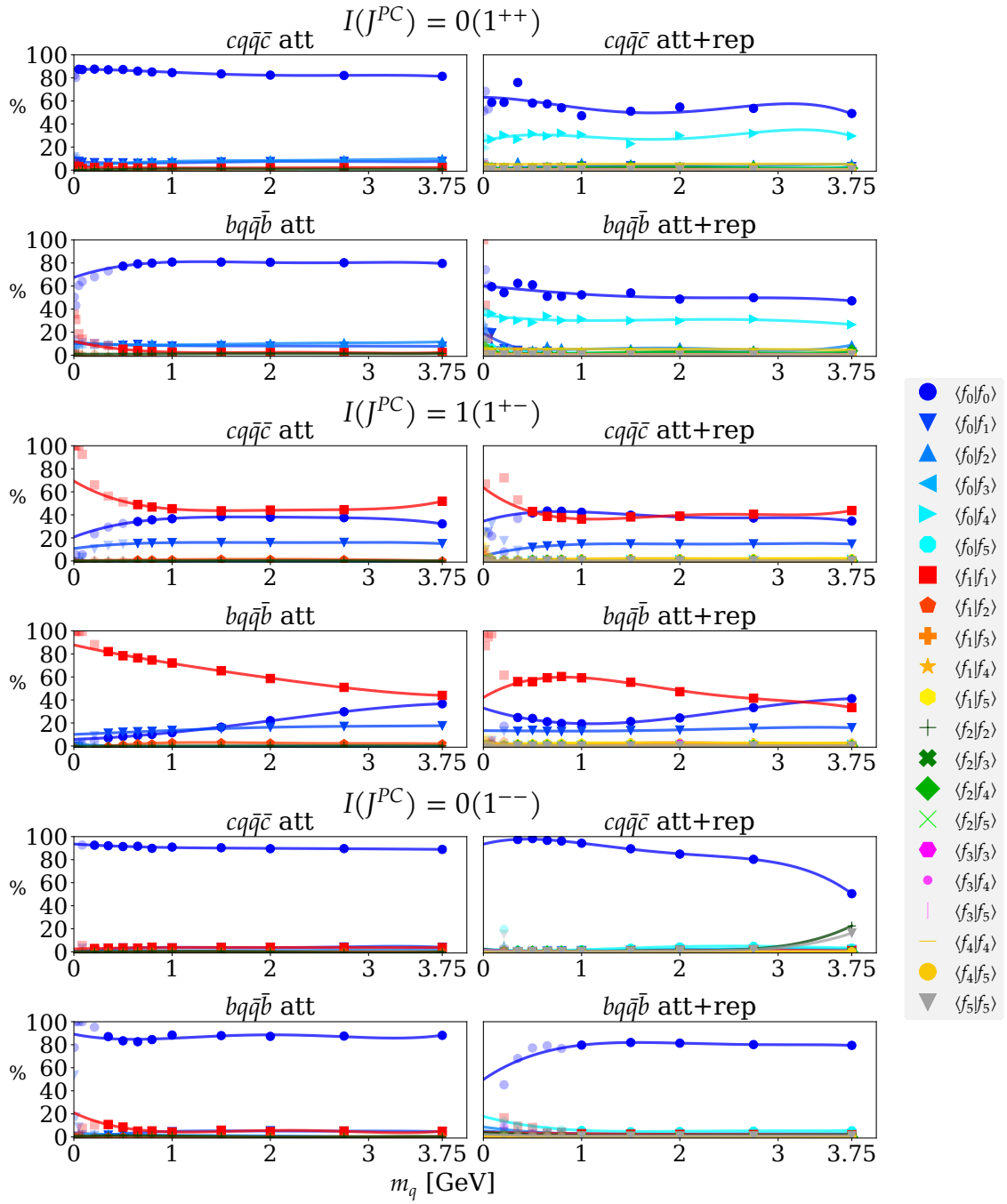

Figure C.16: Norm contribution quark mass evolution curve of the hidden-bottom and hidden-charm four-quark candidates with total spin $J = 1$. The colour coding is according to the results displayed in Fig. 6.8.

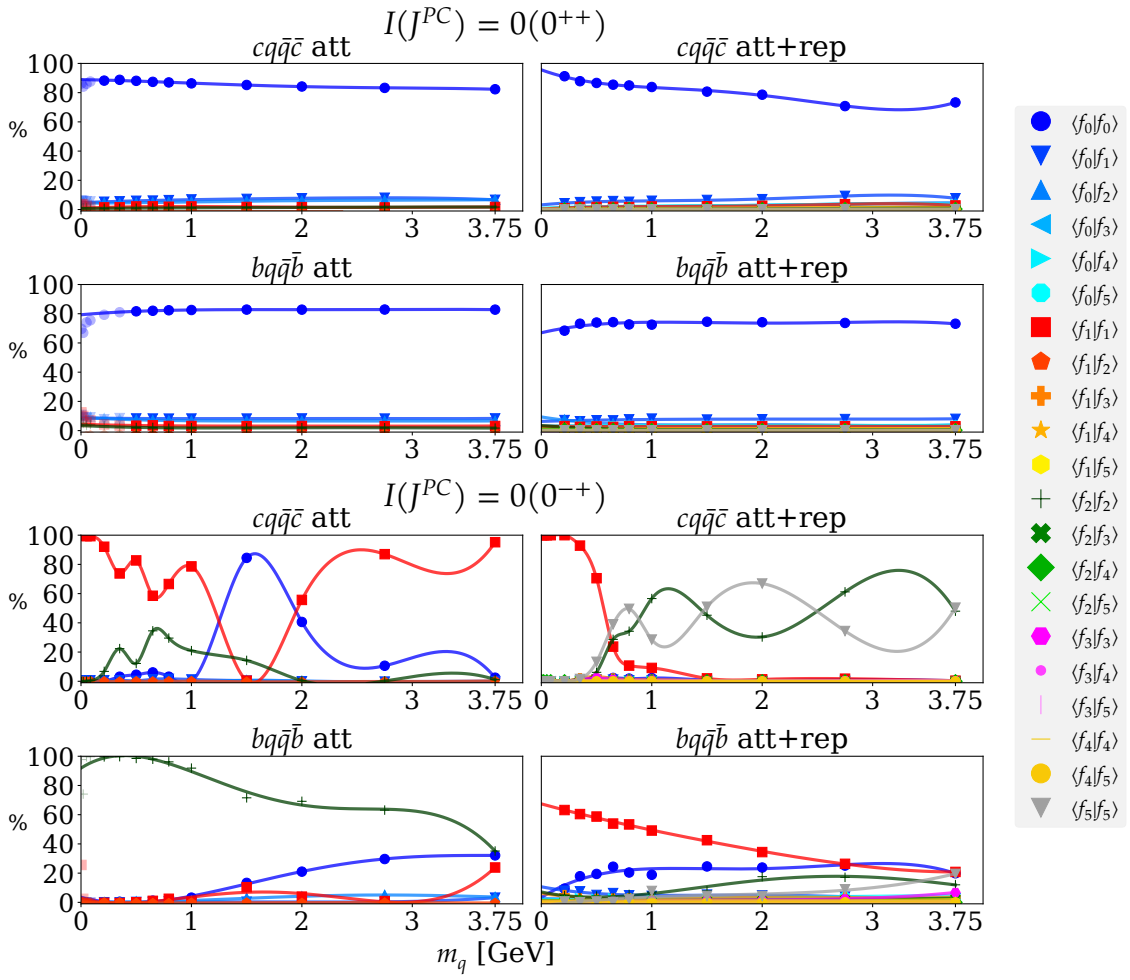

Figure C.17: Same as in Fig. C.16 but for the investigated hidden-flavour four-quark states with total spin $J = 0$.

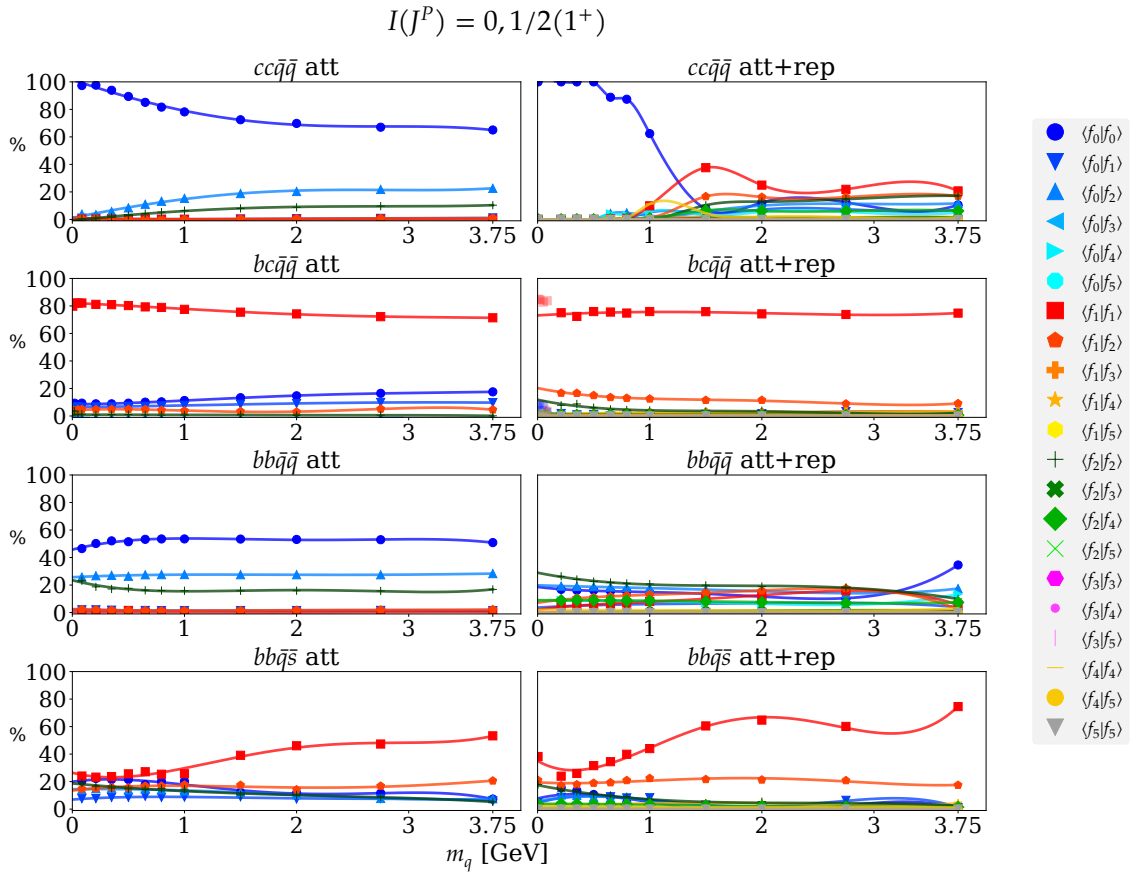

Figure C.18: Norm contribution quark mass evolution curve of the open-flavour four-quark candidates with quantum numbers $I(J^P) = 0, 1/2(1^+)$. The colour coding is according to the results displayed in Fig. 6.9.

C.8.2 Open-flavour NCQMECs

In Figs. C.18 to C.20 we display the obtained norm contribution quark mass evolution curves for the open-flavour four-quark states investigated in this work.

Also here, most of the NCQMECs do not show too drastic changes across the whole range of current-quark masses. Exceptions to this would be the $cc\bar{q}\bar{q}$ and the $bb\bar{q}\bar{s}$ states with $J = 1$ using the attractive and repulsive channels. The strong change in the $cc\bar{q}\bar{q}$ NCQMEC for $J = 0$ (the top left in Fig. C.20) is a numerical error.

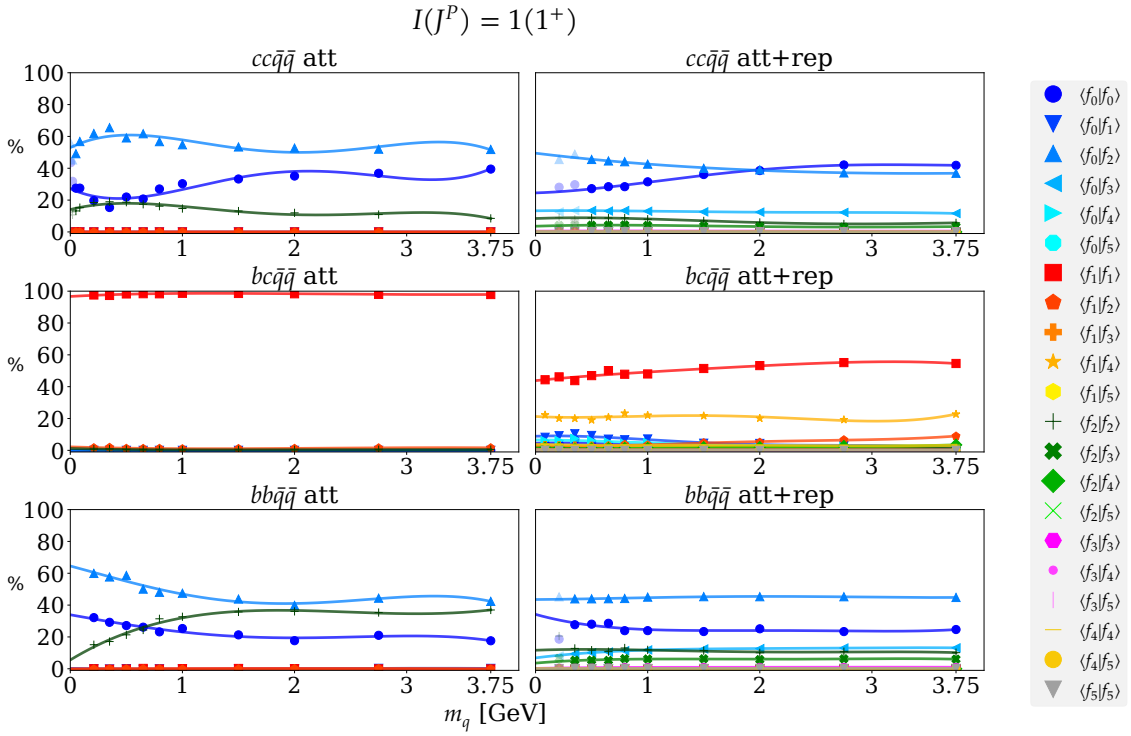

Figure C.19: Same as in Fig. C.18 but for states with $I(J^P) = 1(1^+)$.

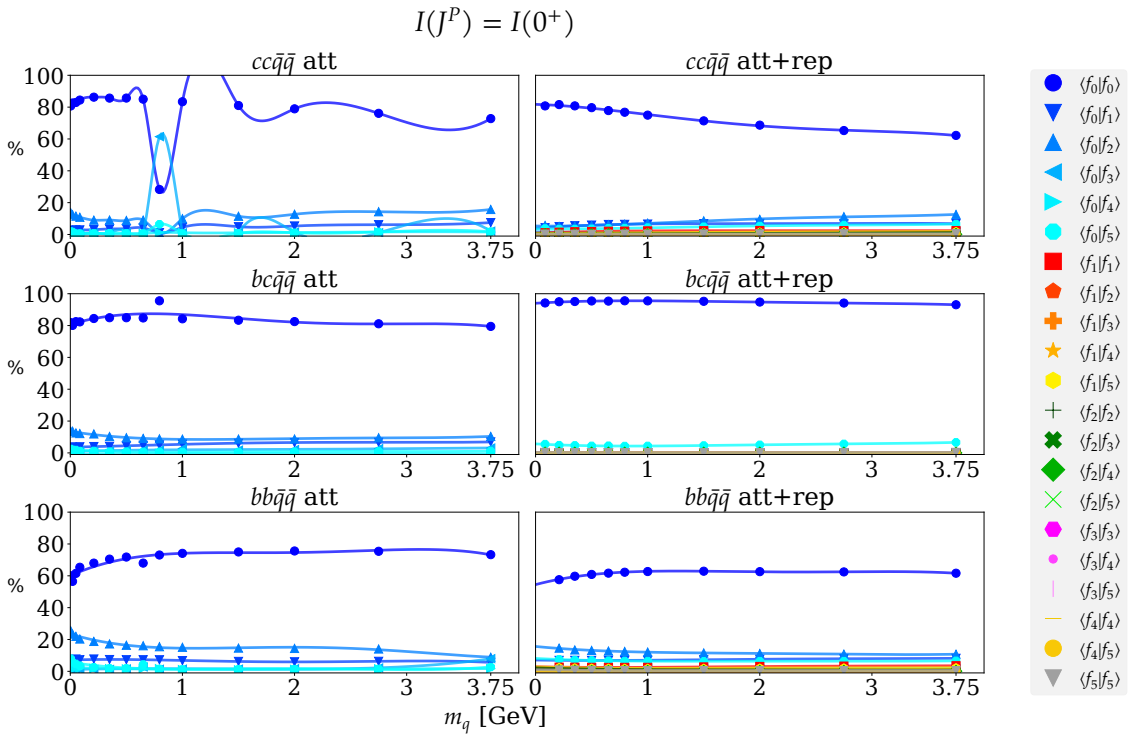

Figure C.20: Same as in Fig. C.18 but for states with total spin $J = 0$.

Rest of this page intentionally left blank.

Appendix D

Numerical methods

Numerical integration

To evaluate the integrals appearing in this work numerically, we used two different methods: Gaussian Quadrature and Monte Carlo integration.

Gaussian Quadrature

The Gaussian Quadrature was used to evaluate the integrals appearing the the quark DSE and the two- and four-body BSE. Originally formulated such that a function $f(x)$ integrated in the interval $[-1,1]$ can be well approximated by

$$\int_{-1}^{1} \mathrm{d}x\, f(x) \approx \sum_{i=1}^{n} w_i \cdot f(x_i)\,, \tag{D.1}$$

with w_i the quadrature weights and x_i the nodes. One can reformulate this to arbitrary boundaries $[a,b]$ by introducing a positive weight function $w(x)$ into the integral and write

$$\int_{a}^{b} \mathrm{d}x\; w(x) f(x)\,. \tag{D.2}$$

The specific form of the weight function depends on the chosen quadrature and its polynomials, see, e.g., [252]. We choose Legendre polynomials for almost all integrals except the ones where the measure comes with a factor of $dz\sqrt{1-z^2}$. In these cases the use of Chebyshev polynomials is more suitable, as the wight function $w_{\text{cheby}} = (1-z^2)^{-1/2}$ cancels this factor. The nodes for the integration of the polynomial $p(x)$ are given by its zeros

$$\{x_i \,|\, p(x_i) = 0\}\,, \tag{D.3}$$

with the weights calculated as [253]

$$w_i = \frac{a_n}{a_{n-1}} \cdot \frac{\int_a^b \mathrm{d}x\; w(x) p_{n-1}(x)^2}{p_n'(x) p_{n-1}(x_i)}\,. \tag{D.4}$$

p_n denotes a polynomial of degree n, p' denotes a derivative with respect to x. The a_m denotes the coefficient belonging to the highest order term of a polynomial p_m. For the numerical implementation of the Gauß-Legendre and Gauß-Chebyshev integrations, we used the **C++** routines provided by the **GNU Scientific Library** [254].

Monte Carlo integration

To compute the norm contributions, one needs to solve three integrals of the form given in Eq. (A.18), which makes for twelve integrals in total. In this case, the appropriate choice is the Monte Carlo integration rather than the Gaussian quadrature, as the former is simply more efficient when dealing with large number of integrals. The idea behind it is the following. Consider a multidimensional integral

$$I = \int \mathrm{d}^n x \, f(x_1, \dots, x_n) \,, \tag{D.5}$$

with $x_1, \dots, x_n$ denoting the integration variables. One then uniformly samples sets of N points for each integration variable x_i in the respective integral boundaries $\Omega_i = [a_i, b_i]$. The integral in Eq. (D.5) can then be approximated by

$$I \approx I_N \equiv \frac{V}{N} \sum_{j=1}^{N} f(x_{1_j}, \dots, x_{n_j}) \,, \tag{D.6}$$

where x_{i_j} denote the sampled data points and V is the volume

$$V = \prod_{i=1}^{n} (b_i - a_i) \,. \tag{D.7}$$

The error coming from the integration is then given by

$$\delta I_N = \sigma_N = V \sqrt{\frac{\langle f^2 \rangle - \langle f \rangle^2}{N-1}} \,. \tag{D.8}$$

For the actual calculation, we use a variant of the Monte Carlo integration known as VEGAS Monte Carlo [255], which essentially first determines the areas of the integrand which make the greatest contribution to the final integral and in a second step uses importance sampling to focus the sampling of points in these areas. We again use the routines provided by the **GNU Scientific Library**.

Solution of Eigenvalues

The homogeneous Bethe-Salpeter equations can be viewed as an eigenvalue equation of the form

$$K \cdot \vec{v} = \lambda \, \vec{v} \,, \tag{D.9}$$

with K the (kernel) matrix, $\vec{v}$ denoting the eigenvector and λ is the eigenvalue. In the following, we will shortly outline the two algorithms used to numerically solve eigenvalue equations.

Power method

The power method (or Von Mises iteration [256]) is a method to compute the eigenvalue λ with the largest absolute value and its associated eigenvector v of a diagonalizable matrix K. The idea is the following. Let $\vec{b}_0$ be an approximation to the dominant eigenvector. Assuming the matrix K to have one dominant eigenvalue whose absolute value $|\lambda_{\max}|$ is strictly greater than all other eigenvalues and that the vector $\vec{b}_0$ has a non-zero component in the direction of the eigenvector associated to λ_0, the recurrence relation

$$\vec{b}_{k+1} = \frac{K^{k+1} \cdot \vec{b}_0}{||K^{k+1} \cdot \vec{b}_0||}\,, \tag{D.10}$$

converges to an eigenvector $\vec{b}_{\max}$, associated to the dominant eigenvalue. The eigenvalue can then be obtained, e.g., via the Rayleigh quotient [257, 258] $R(K, \vec{b}_{\max}) = \lambda_{\max}$.

One caveat of this method is, that it is limited to extracting only the largest eigenvalue and its eigenvector. For our case, this is useful when we only want to investigate the ground state of a hadron, which is associated to the largest eigenvalue of K. But the radial excited states are associated to the next lower eigenvalues of the matrix K.

Arnoldi iteration

The Arnoldi iteration [259], can be used to extract more than just the largest eigenvalue. It makes use of the *Krylov subspace*, which is a linear subspace generated by applying powers of a matrix K onto a vector $\vec{b}$, starting from $K^0 = \mathbb{I}$. The resulting space of some order r reads

$$\mathcal{K}_r(K, \vec{b}) = \text{span}\{\vec{b},\, K \cdot \vec{b}, \dots,\, K^{r-1} \cdot \vec{b}\}\,. \tag{D.11}$$

Let n be the number of iterations needed to converge to the eigenvector associated to the eigenvalue with the largest absolute value. One can then use the elements of the $\mathcal{K}_n$ Krylov subspace to form the so-called *Krylov matrix*:

$$K_n = [\vec{b},\, K \cdot \vec{b}, \dots,\, K^{n-1} \cdot \vec{b}]\,. \tag{D.12}$$

By, e.g., using the Gram-Schmidt orthogonalization, one can extract an orthogonal basis from the columns of the matrix and the resulting set of vectors forms an orthogonal basis of the Krylov subspace $\mathcal{K}_n$. These basis vectors then span good approximations to the eigenvectors corresponding to the n largest eigenvalues.

Note, that for Hermitian matrices, the Arnoldi iteration reduces to the Lanczos algorithm [260]. For the numerical implementation of this algorithm, we use the open source

package **ARPACK** [261], originally written in FORTRAN77, made compatible with **C** and **C++** via the packages [262, 263].

Interpolation

Regarding the necessary interpolations, we mostly used one- and two-dimensional linear interpolation, as it was sufficient for most cases. In those few cases, where the linear interpolation did not suffice, we used the cubic Hermite spline interpolation provided by the **GNU Scientific Library**.

Appendix E

Technical Toolkit

Programming

The numerical solution of the four-quark FYE requires efficient and fast computer programs, which for this work were written in the **C++** programming language using the *GNU Compiler Collection* (GCC) [264]. Various scripts to analyse the obtained data were written in **Python 3** [265]. Various routines for integration and interpolation were taken from the **GNU Scientific Library** [254].

Algebra Calculus

Before the numerical solution of the BSE, there is much algebra to be done. Most of the algebraic calculus was done using **FORM** [266] as a basis in combination with **Wolfram Mathematica** [267], in particular the **FeynCalc** package [268, 269].

Typesetting

This work was written in LaTeX [270] and rendered in LuaTeX [271] using the TeXLive setup [272]. The template for this thesis is based on the excellent **LaTeX Cookbook** template written (mainly) by Alex Povel [273].

Plotting and Graphics

All the data plots in this thesis were done in **Python 3**. The schematic plots serving as illustrations were exclusively done using the **PGF/TikZ** packages for LaTeX [274].

Rest of this page intentionally left blank.

Bibliography

[1]S. Tomonaga, "On a Relativistically Invariant Formulation of the Quantum Theory of Wave Fields.", Progress of Theoretical Physics **1**, 27–42, ISSN: 0033-068X (1946) (cit. on p. 11).

[2]J. Schwinger, "On Quantum-Electrodynamics and the Magnetic Moment of the Electron", Physical Review **73**, 416–417, ISSN: 0031-899X (1948) (cit. on p. 11).

[3]R. P. Feynman, "Space-Time Approach to Non-Relativistic Quantum Mechanics", Reviews of Modern Physics **20**, 367–387, ISSN: 0034-6861 (1948) (cit. on p. 11).

[4]F. J. Dyson, "The Radiation Theories of Tomonaga, Schwinger, and Feynman", Physical Review **75**, 486–502, ISSN: 0031-899X (1949) (cit. on p. 11).

[5]S. L. Glashow, "Partial-symmetries of weak interactions", Nuclear Physics **22**, 579–588, ISSN: 0029-5582 (1961) (cit. on p. 11).

[6]S. Weinberg, "A Model of Leptons", Physical Review Letters **19**, 1264–1266, ISSN: 0031-9007 (1967) (cit. on p. 11).

[7]A. Salam, "Weak and electromagnetic interactions", in, *Selected papers of abdus salam* (WORLD SCIENTIFIC, May 1994), pp. 244–254 (cit. on p. 11).

[8]H. Fritzsch, M. Gell-Mann, and H. Leutwyler, "Advantages of the color octet gluon picture", Physics Letters B **47**, 365–368, ISSN: 0370-2693 (1973) (cit. on p. 11).

[9]D. J. Gross and F. Wilczek, "Ultraviolet Behavior of Non-Abelian Gauge Theories", Physical Review Letters **30**, 1343–1346, ISSN: 0031-9007 (1973) (cit. on p. 11).

[10]H. D. Politzer, "Reliable Perturbative Results for Strong Interactions?", Physical Review Letters **30**, 1346–1349, ISSN: 0031-9007 (1973) (cit. on p. 11).

[11]M. Gell-Mann, "A schematic model of baryons and mesons", Physics Letters **8**, 214–215, ISSN: 0031-9163 (1964) (cit. on pp. 12, 13).

[12]G. Zweig, "An SU_3 model for strong interaction symmetry and its breaking. Version 1", 10.17181/CERN-TH-401, 10.17181/CERN-TH-401 (1964) (cit. on pp. 12, 13).

[13]G. Zweig, "An SU_3 model for strong interaction symmetry and its breaking. Version 2", 10.17181/CERN-TH-412, 10.17181/CERN-TH-401 (1964) (cit. on pp. 12, 13).

[14]O. W. Greenberg, "Spin and Unitary-Spin Independence in a Paraquark Model of Baryons and Mesons", Physical Review Letters **13**, 598–602, ISSN: 0031-9007 (1964) (cit. on p. 12).

[15]M. Y. Han and Y. Nambu, "Three-Triplet Model with Double SU(3) Symmetry", Physical Review **139**, B1006–B1010, ISSN: 0031-899X (1965) (cit. on p. 12).

[16]F.-K. Guo et al., "Hadronic molecules", Reviews of Modern Physics **90**, 015004 (2018) (cit. on pp. 13, 15, 18, 115, 119, 168).

[17]A. Esposito, A. Pilloni, and A. Polosa, "Multiquark resonances", Physics Reports **668**, 1–97, ISSN: 0370-1573 (2017) (cit. on pp. 13, 15, 65).

[18]A. Ali, L. Maiani, and A. D. Polosa, *Multiquark Hadrons* (Cambridge University Press, Apr. 2019), ISBN: 9781107171589 (cit. on p. 13).

[19]J. Basdevant, C. Froggatt, and J. Petersen, "$\pi\pi$ phenomenology below 1100 MeV", Physics Letters B **41**, 178–182, ISSN: 0370-2693 (1972) (cit. on p. 13).

[20]S. Navas et al., "Review of Particle Physics", Physical Review D **110**, 030001, ISSN: 2470-0029 (2024) (cit. on pp. 13, 14, 16, 28, 30, 32, 70, 73, 74, 80, 91, 101–104, 107, 118, 119, 165, 166, 168, 171).

[21]R. J. Jaffe, "Multiquark hadrons. I. Phenomenology of $Q_2\bar{Q}_2$ mesons", Physical Review D **15**, 267–280, ISSN: 0556-2821 (1977) (cit. on pp. 14, 15, 115).

[22]S.-K. Choi *et al.* (Belle), "Observation of a Narrow Charmoniumlike State in Exclusive $B^{\pm} \to K^{\pm}\pi^{+}\pi^{-}J/\psi$ Decays", Physical Review Letters **91**, 262001 (2003) (cit. on pp. 14, 16).

[23]R. Aaij et al., "Determination of the X(3872) Meson Quantum Numbers", Physical Review Letters **110**, 222001, ISSN: 1079-7114 (2013) (cit. on pp. 14, 16).

[24]R. Aaij et al., "Quantum numbers of the X(3872) state and orbital angular momentum in its $\rho_0 J/\psi$ decay", Physical Review D **92**, 011102, ISSN: 1550-2368 (2015) (cit. on pp. 14, 16).

[25]J. Ballot and J. Richard, "Four quark states in additive potentials", Physics Letters B **123**, 449–451, ISSN: 0370-2693 (1983) (cit. on p. 14).

[26]S. Zouzou et al., "Four-quark bound states", Zeitschrift für Physik C Particles and Fields **30**, 457–468, ISSN: 1434-6052 (1986) (cit. on p. 14).

[27]H. J. Lipkin, "A model-independent approach to multiquark bound states", Physics Letters B **172**, 242–247, ISSN: 0370-2693 (1986) (cit. on p. 14).

[28]L. Heller and J. A. Tjon, "On the existence of stable dimesons", Physical Review D **35**, 969–974, ISSN: 0556-2821 (1987) (cit. on p. 14).

[29]A. V. Manohar and M. B. Wise, "Exotic states in QCD", Nuclear Physics B **399**, 17–33, ISSN: 0550-3213 (1993) (cit. on p. 14).

[30]R. Aaij *et al.* (LHCb Collaboration), "Study of the doubly charmed tetraquark T_{cc}^{+}", Nature Communications **13**, 10.1038/s41467-022-30206-w, ISSN: 2041-1723 (2022) (cit. on pp. 14, 16, 108, 110).

[31]R. Aaij *et al.* (LHCb Collaboration), "Observation of an exotic narrow doubly charmed tetraquark", Nature Physics **18**, 751–754, ISSN: 1745-2481 (2022) (cit. on pp. 14, 16, 108, 110).

[32]A. Francis et al., "Lattice Prediction for Deeply Bound Doubly Heavy Tetraquarks", Physical Review Letters **118**, 142001 (2017) (cit. on pp. 14, 108, 111).

[33]E. J. Eichten and C. Quigg, "Heavy-Quark Symmetry Implies Stable Heavy Tetraquark Mesons $Q_iQ_j\bar{q}_k\bar{q}_l$", Physical Review Letters **119**, 202002, ISSN: 1079-7114 (2017) (cit. on pp. 14, 108, 111).

[34]P. Junnarkar, N. Mathur, and M. Padmanath, "Study of doubly heavy tetraquarks in lattice QCD", Physical Review D **99**, 034507, ISSN: 2470-0029 (2019) (cit. on pp. 14, 108, 111, 113).

[35]E. Braaten, L.-P. He, and A. Mohapatra, "Masses of doubly heavy tetraquarks with error bars", Physical Review D **103**, 016001, ISSN: 2470-0029 (2021) (cit. on pp. 14, 108, 111).

[36]R. J. Hudspith and D. Mohler, "Exotic tetraquark states with two $\bar{b}$-quarks and $J^P = 0^+$ and 1^+ B_s states in a nonperturbatively tuned lattice NRQCD setup", Physical Review D **107**, 114510, ISSN: 2470-0029 (2023) (cit. on pp. 14, 108, 111).

[37]C. Alexandrou et al., "Shallow Bound States and Hints for Broad Resonances with Quark Content $\bar{b}\bar{c}ud$ in $B-\bar{D}$ and $B*-\bar{D}$ Scattering from Lattice QCD", Physical Review Letters **132**, 151902, ISSN: 1079-7114 (2024) (cit. on pp. 14, 108, 110, 111, 113).

[38]X.-K. Dong, F.-K. Guo, and B.-S. Zou, "A survey of heavy-antiheavy hadronic molecules", 10.13725/j.cnki.pip.2021.02.001 (2021) (cit. on p. 15).

[39]M. Voloshin, "Charmonium", Progress in Particle and Nuclear Physics **61**, 455–511 (2008) (cit. on pp. 15, 115).

[40]A. Ali, J. S. Lange, and S. Stone, "Exotics: Heavy pentaquarks and tetraquarks", Progress in Particle and Nuclear Physics **97**, 123–198 (2017) (cit. on pp. 15, 16).

[41]G. Barucca et al., "PANDA Phase One: PANDA collaboration", The European Physical Journal A **57**, 10.1140/epja/s10050-021-00475-y, ISSN: 1434-601X (2021) (cit. on pp. 15, 17).

[42]S.-K. Choi et al., "Observation of a Near-Threshold $\omega J/\psi$ Mass Enhancement in Exclusive $B \to K\omega J/\psi$ Decays", Physical Review Letters **94**, 182002, ISSN: 1079-7114 (2005) (cit. on p. 16).

[43]A. Bondar et al., "Observation of Two Charged Bottomoniumlike Resonances in $\Upsilon(5S)$ Decays", Physical Review Letters **108**, 122001, ISSN: 1079-7114 (2012) (cit. on p. 16).

[44]Belle2 collaboration, https://belle2.jp/the-collaboration/ (cit. on p. 16).

[45]A. A. Alves et al., "The LHCb Detector at the LHC", Journal of Instrumentation **3**, S08005–S08005, ISSN: 1748-0221 (2008) (cit. on p. 16).

[46]R. Aaij et al., "Observation of $J/\psi p$ Resonances Consistent with Pentaquark States in $\Lambda_b^0 \to J/\psi K^- p$ Decays", Physical Review Letters **115**, 072001, ISSN: 1079-7114 (2015) (cit. on p. 16).

[47]R. Aaij et al., "Model-Independent Evidence for $J/\psi p$ Contributions to $\Lambda_b^0 \to J/\psi p K^-$ Decays", Physical Review Letters **117**, 082002, ISSN: 1079-7114 (2016) (cit. on p. 16).

[48]R. Aaij et al., "Observation of $J/\psi\phi$ Structures Consistent with Exotic States from Amplitude Analysis of $B^+ \to J/\psi\phi K^+$ Decays", Physical Review Letters **118**, 022003, ISSN: 1079-7114 (2017) (cit. on p. 16).

[49]R. Aaij et al., "Observation of New Resonances Decaying to $J/\psi K^+$ and $J/\psi\phi$", Physical Review Letters **127**, 082001, ISSN: 1079-7114 (2021) (cit. on p. 16).

[50]R. Aaij *et al.* (LHCb Collaboration), "Observation of structure in the J/ψ-pair mass spectrum", Science Bulletin **65**, 1983–1993, ISSN: 2095-9273 (2020) (cit. on p. 16).

[51]LHCb collaboration, `https://lhcb-outreach.web.cern.ch/collaboration/` (cit. on p. 16).

[52]M. Ablikim et al., "Observation of a Charged Charmoniumlike Structure in $e^+e^- \to \pi^+\pi^- J/\psi$ at $s = 4.26$ GeV", Physical Review Letters **110**, 252001, ISSN: 1079-7114 (2013) (cit. on p. 16).

[53]BESIII collaboration, `http://bes3.ihep.ac.cn/` (cit. on p. 16).

[54]T. Aaltonen et al., "Evidence for a Narrow Near-Threshold Structure in the $J/\psi\varphi$ Mass Spectrum in $B^+ \to J/\psi\phi K^+$ Decays", Physical Review Letters **102**, 242002, ISSN: 1079-7114 (2009) (cit. on p. 17).

[55]V. M. Abazov et al., "Evidence for a $B_s^0\pi^\pm$ State", Physical Review Letters **117**, 022003, ISSN: 1079-7114 (2016) (cit. on p. 17).

[56]N. Brambilla et al., "The XYZ states: Experimental and theoretical status and perspectives", Physics Reports **873**, 1–154, ISSN: 0370-1573 (2020) (cit. on pp. 17, 18, 119, 149, 150).

[57]J.-M. Richard, "An introduction to the quark model", `10.48550/ARXIV.1205.4326` (2012) (cit. on p. 17).

[58]P.-P. Shi, F. Huang, and W.-L. Wang, "Hidden charm tetraquark states in a diquark model", Physical Review D **103**, 094038, ISSN: 2470-0029 (2021) (cit. on p. 17).

[59]H. Huang et al., "Tetraquarks and Pentaquarks from Quark Model Perspective", Symmetry **15**, 1298, ISSN: 2073-8994 (2023) (cit. on p. 17).

[60]R. N. Faustov, V. O. Galkin, and E. M. Savchenko, "Heavy Tetraquarks in the Relativistic Quark Model", Universe **7**, 94, ISSN: 2218-1997 (2021) (cit. on p. 17).

[61]C. Gattringer and C. B. Lang, *Quantum Chromodynamics on the Lattice: An Introductory Presentation* (Springer Berlin Heidelberg, 2010), ISBN: 9783642018503 (cit. on pp. 17, 23, 34).

[62]P. Bicudo, "Tetraquarks and pentaquarks in lattice QCD with light and heavy quarks", Physics Reports **1039**, 1–49 (2023) (cit. on pp. 17, 19).

[63]A. Francis, "Lattice perspectives on doubly heavy tetraquarks", Progress in Particle and Nuclear Physics **140**, 104143, ISSN: 0146-6410 (2025) (cit. on pp. 17, 19, 108, 110, 111).

[64]P. Maris, C. D. Roberts, and P. C. Tandy, "Pion mass and decay constant", Physics Letters B **420**, 267–273, ISSN: 0370-2693 (1998) (cit. on pp. 18, 61).

[65]G. Eichmann et al., "Nucleon Mass from a Covariant Three-Quark Faddeev Equation", Physical Review Letters **104**, 201601, ISSN: 1079-7114 (2010) (cit. on p. 18).

[66]G. Eichmann, C. S. Fischer, and W. Heupel, "The light scalar mesons as tetraquarks", Physics Letters B **753**, 282–287, ISSN: 0370-2693 (2016) (cit. on pp. 18, 88, 89, 165, 166).

[67]P. C. Wallbott, G. Eichmann, and C. S. Fischer, "X(3872) as a four-quark state in a Dyson-Schwinger/Bethe-Salpeter approach", Physical Review D **100**, 014033, ISSN: 2470-0029 (2019) (cit. on pp. 18, 19, 80, 89, 90, 93, 108, 113–115, 117, 126).

[68]M. Q. Huber, C. S. Fischer, and H. Sanchis-Alepuz, "Spectrum of scalar and pseudoscalar glueballs from functional methods", The European Physical Journal C **80**, 10.1140/epjc/s10052-020-08649-6, ISSN: 1434-6052 (2020) (cit. on pp. 18, 47).

[69]G. Eichmann et al., "Baryons as relativistic three-quark bound states", Progress in Particle and Nuclear Physics **91**, 1–100, ISSN: 0146-6410 (2016) (cit. on pp. 18, 39, 46, 47, 62, 149, 165).

[70]G. Eichmann et al., "Four-Quark States from Functional Methods", Few-Body Systems **61**, 10.1007/s00601-020-01571-3, ISSN: 1432-5411 (2020) (cit. on pp. 18, 78).

[71]S. Weinberg, "Elementary Particle Theory of Composite Particles", Physical Review **130**, 776–783, ISSN: 0031-899X (1963) (cit. on p. 18).

[72]S. Weinberg, "Evidence That the Deuteron Is Not an Elementary Particle", Physical Review **137**, B672–B678, ISSN: 0031-899X (1965) (cit. on p. 18).

[73]R. M. Albuquerque et al., "QCD sum rules approach to the X, Y and Z states", Journal of Physics G: Nuclear and Particle Physics **46**, 093002, ISSN: 1361-6471 (2019) (cit. on p. 18).

[74]P. C. Wallbott, G. Eichmann, and C. S. Fischer, "Disentangling different structures in heavy-light four-quark states", Physical Review D **102**, 051501, ISSN: 2470-0029 (2020) (cit. on pp. 19, 84, 91–93, 108, 113–115, 119, 126, 173).

[75]N. Santowsky and C. S. Fischer, "Light scalars: Four-quark versus two-quark states in the complex energy plane from Bethe-Salpeter equations", Physical Review D **105**, 034025, ISSN: 2470-0029 (2022) (cit. on pp. 19, 94, 108, 114, 115, 117, 119, 126).

[76]J. Bulava et al., "Hadron Spectroscopy with Lattice QCD", 10.48550/ARXIV.2203.03230 (2022) (cit. on p. 19).

[77]W. Heupel, "Light tetraquarks and mesons in a DSE/BSE approach", PhD thesis (Justus Liebig University Giessen, 2015) (cit. on pp. 19, 87–89, 125).

[78]P. C. Wallbott, "Heavy-light four-quark states in the charmonium region in a Bethe-Salpeter and Dyson-Schwinger approach", PhD thesis (Justus Liebig University Giessen, 2019) (cit. on pp. 19, 90, 125, 173).

[79]N. Santowsky and C. S. Fischer, "Four-quark states with charm quarks in a two-body Bethe–Salpeter approach", The European Physical Journal C **82**, 10.1140/epjc/s10052-022-10272-6, ISSN: 1434-6052 (2022) (cit. on pp. 19, 93, 94, 127, 168, 172).

[80]S. Weinberg, *The Quantum Theory of Fields. Vol. 1: Foundations.* (Cambridge University Press, June 1995), ISBN: 9781139644167 (cit. on p. 21).

[81]S. Weinberg, *The Quantum Theory of Fields. Volume 2, Modern Applications* (Cambridge University Press, Aug. 1996), ISBN: 9781139644174 (cit. on pp. 21, 24, 28, 51).

[82]J. Zinn-Justin, *Quantum Field Theory and Critical Phenomena* (Oxford University Press, June 2002), ISBN: 9780198509233 (cit. on pp. 21, 37).

[83]M. E. Peskin and D. V. Schroeder, *An Introduction To Quantum Field Theory* (CRC Press, May 1995), ISBN: 9780429972102 (cit. on pp. 21, 51).

[84]M. D. Schwartz, *Quantum Field Theory and the Standard Model* (Cambridge University Press, Dec. 2013), ISBN: 9781107034730 (cit. on pp. 21, 27, 33, 37, 51).

[85]M. Srednicki, *Quantum Field Theory* (Cambridge University Press, 2007), ISBN: 9780511813917 (cit. on pp. 21, 24, 37, 51).

[86]B. S. DeWitt, "Quantum Theory of Gravity. II. The Manifestly Covariant Theory", Physical Review **162**, 1195–1239, ISSN: 0031-899X (1967) (cit. on p. 23).

[87]L. Faddeev and V. Popov, "Feynman diagrams for the Yang-Mills field", Physics Letters B **25**, 29–30, ISSN: 0370-2693 (1967) (cit. on p. 23).

[88]L. D. Faddeev, "The Feynman integral for singular Lagrangians", Theoretical and Mathematical Physics **1**, 1–13, ISSN: 1573-9333 (1969) (cit. on p. 23).

[89]P. Silva and O. Oliveira, "Gribov copies, lattice QCD and the gluon propagator", Nuclear Physics B **690**, 177–198, ISSN: 0550-3213 (2004) (cit. on p. 23).

[90]A. Sternbeck et al., "Towards the infrared limit in SU(3) Landau gauge lattice gluodynamics", Physical Review D **72**, 014507, ISSN: 1550-2368 (2005) (cit. on p. 23).

[91]I. Bogolubsky et al., "Lattice gluodynamics computation of Landau-gauge Green's functions in the deep infrared", Physics Letters B **676**, 69–73, ISSN: 0370-2693 (2009) (cit. on p. 23).

[92]M. Blank, A. Krassnigg, and A. Maas, "ρ meson, Bethe-Salpeter equation, and the far infrared", Physical Review D **83**, 034020, ISSN: 1550-2368 (2011) (cit. on p. 23).

[93]J. Bernhardt, "Quark Mass and Volume Dependence of the QCD Phase Diagram with DSEs", PhD thesis (Justus Liebig University Giessen, 2023) (cit. on pp. 23, 41).

[94]M. Fierz, "Über die relativistische Theorie kräftefreier Teilchen mit beliebigem Spin", 10.5169/SEALS-110930 (1939) (cit. on p. 24).

[95]W. Pauli, "The Connection Between Spin and Statistics", Physical Review **58**, 716–722, ISSN: 0031-899X (1940) (cit. on p. 24).

[96]G. 'tHooft, "Renormalization of massless Yang-Mills fields", Nuclear Physics B **33**, 173–199, ISSN: 0550-3213 (1971) (cit. on p. 25).

[97]G. 't Hooft and M. Veltman, "Regularization and renormalization of gauge fields", Nuclear Physics B **44**, 189–213, ISSN: 0550-3213 (1972) (cit. on p. 25).

[98]B. W. Lee and J. Zinn-Justin, "Spontaneously Broken Gauge Symmetries. I. Preliminaries", Physical Review D **5**, 3121–3137, ISSN: 0556-2821 (1972) (cit. on p. 25).

[99]B. W. Lee and J. Zinn-Justin, "Spontaneously Broken Gauge Symmetries. II. Perturbation Theory and Renormalization", Physical Review D **5**, 3137–3155, ISSN: 0556-2821 (1972) (cit. on p. 25).

[100]B. W. Lee and J. Zinn-Justin, "Spontaneously Broken Gauge Symmetries. IV. General Gauge Formulation", Physical Review D **7**, 1049–1056, ISSN: 0556-2821 (1973) (cit. on p. 25).

[101]W. Celmaster and R. J. Gonsalves, "Renormalization-prescription dependence of the quantum-chromodynamic coupling constant", Physical Review D **20**, 1420–1434, ISSN: 0556-2821 (1979) (cit. on p. 25).

[102]J. Taylor, "Ward identities and charge renormalization of the Yang-Mills field", Nuclear Physics B **33**, 436–444, ISSN: 0550-3213 (1971) (cit. on p. 25).

[103]A. A. Slavnov, "Ward identities in gauge theories", Theoretical and Mathematical Physics **10**, 99–104, ISSN: 1573-9333 (1972) (cit. on p. 25).

[104]J. C. Ward, "An Identity in Quantum Electrodynamics", Physical Review **78**, 182–182, ISSN: 0031-899X (1950) (cit. on p. 25).

[105]Y. Takahashi, "On the generalized ward identity", Il Nuovo Cimento **6**, 371–375, ISSN: 1827-6121 (1957) (cit. on p. 25).

[106]R. Alkofer and L. von Smekal, "The infrared behaviour of QCD Green's functions Confinement, dynamical symmetry breaking, and hadrons as relativistic bound states", Physics Reports **353**, 281–465, ISSN: 0370-1573 (2001) (cit. on pp. 25, 37).

[107]E. Noether, "Invariante Variationsprobleme", Nachrichten von der Gesellschaft der Wissenschaften zu Göttingen, Mathematisch-Physikalische Klasse **1918**, 235–257 (1918), http://eudml.org/doc/59024 (cit. on p. 25).

[108]J. Goldstone, "Field theories with « Superconductor » solutions", Il Nuovo Cimento **19**, 154–164, ISSN: 1827-6121 (1961) (cit. on p. 26).

[109]J. Goldstone, A. Salam, and S. Weinberg, "Broken Symmetries", Physical Review **127**, 965–970, ISSN: 0031-899X (1962) (cit. on p. 26).

[110]Y. Nambu, "Quasi-Particles and Gauge Invariance in the Theory of Superconductivity", Physical Review **117**, 648–663, ISSN: 0031-899X (1960) (cit. on p. 26).

[111]A. Beekman, L. Rademaker, and J. van Wezel, "An introduction to spontaneous symmetry breaking", SciPost Physics Lecture Notes, 10.21468/scipostphyslectnotes.11, ISSN: 2590-1990 (2019) (cit. on p. 26).

[112]R. F. Streater and A. S. Wightman, *PCT, Spin and Statistics, and All That* (Princeton University Press, Dec. 2001), ISBN: 9781400884230 (cit. on p. 26).

[113]S.-S. Chern and J. Simons, "Characteristic Forms and Geometric Invariants", The Annals of Mathematics **99**, 48, ISSN: 0003-486X (1974) (cit. on p. 27).

[114]C. Abel et al., "Measurement of the Permanent Electric Dipole Moment of the Neutron", Physical Review Letters **124**, 081803, ISSN: 1079-7114 (2020) (cit. on p. 27).

[115]C. Becchi, A. Rouet, and R. Stora, "Renormalization of the abelian Higgs-Kibble model", Communications in Mathematical Physics **42**, 127–162, ISSN: 1432-0916 (1975) (cit. on p. 27).

[116]C. Becchi, A. Rouet, and R. Stora, "Renormalization of gauge theories", Annals of Physics **98**, 287–321, ISSN: 0003-4916 (1976) (cit. on p. 27).

[117]I. V. Tyutin, "Gauge Invariance in Field Theory and Statistical Physics in Operator Formalism", Lebedev Physics Institute preprint 39 (1975), 10.48550/ARXIV.0812.0580 (1975) (cit. on p. 27).

[118]T. Kugo and I. Ojima, "Local Covariant Operator Formalism of Non-Abelian Gauge Theories and Quark Confinement Problem", Progress of Theoretical Physics Supplement **66**, 1–130, ISSN: 0375-9687 (1979) (cit. on pp. 28, 34).

[119]D. Tong, "Lectures on Gauge Theory", http://www.damtp.cam.ac.uk/user/tong/gaugetheory.html (cit. on p. 29).

[120]S. Weinberg, "Approximate Symmetries and Pseudo-Goldstone Bosons", Physical Review Letters **29**, 1698–1701, ISSN: 0031-9007 (1972) (cit. on p. 31).

[121]M. Shifman, A. Vainshtein, and V. Zakharov, "Remarks on Higgs-boson interactions with nucleons", Physics Letters B **78**, 443–446, ISSN: 0370-2693 (1978) (cit. on p. 31).

[122]J. C. Collins, A. Duncan, and S. D. Joglekar, "Trace and dilatation anomalies in gauge theories", Physical Review D **16**, 438–449, ISSN: 0556-2821 (1977) (cit. on p. 31).

[123]N. Nielsen, "The energy-momentum tensor in a non-Abelian quark gluon theory", Nuclear Physics B **120**, 212–220, ISSN: 0550-3213 (1977) (cit. on p. 31).

[124]M. Gell-Mann, R. J. Oakes, and B. Renner, "Behavior of Current Divergences under $SU(3) \times SU(3)$", Physical Review **175**, 2195–2199, ISSN: 0031-899X (1968) (cit. on pp. 31, 71).

[125]S. L. Adler, "Axial-Vector Vertex in Spinor Electrodynamics", Physical Review **177**, 2426–2438, ISSN: 0031-899X (1969) (cit. on p. 31).

[126]J. S. Bell and R. Jackiw, "A PCAC puzzle: $\pi^0 \to \gamma\gamma$ in the σ-model", Il Nuovo Cimento A **60**, 47–61, ISSN: 1826-9869 (1969) (cit. on p. 31).

[127]K. Fujikawa, "Path-Integral Measure for Gauge-Invariant Fermion Theories", Physical Review Letters **42**, 1195–1198, ISSN: 0031-9007 (1979) (cit. on p. 31).

[128]ATLAS Collaboration, "A precise determination of the strong-coupling constant from the recoil of Z bosons with the ATLAS experiment at $\sqrt{s} = 8$ TeV", 10.48550/ARXIV.2309.12986 (2023) (cit. on p. 32).

[129]J. Greensite, *An Introduction to the Confinement Problem* (Springer Berlin Heidelberg, 2011), ISBN: 9783642143823 (cit. on p. 34).

[130]K. G. Wilson, "Confinement of quarks", Physical Review D **10**, 2445–2459, ISSN: 0556-2821 (1974) (cit. on p. 34).

[131]S. Elitzur, "Impossibility of spontaneously breaking local symmetries", Physical Review D **12**, 3978–3982, ISSN: 0556-2821 (1975) (cit. on p. 34).

[132]H. Hata, "Restoration of the Local Gauge Symmetry and Color Confinement in Non-Abelian Gauge Theories", Progress of Theoretical Physics **67**, 1607–1618, ISSN: 1347-4081 (1982) (cit. on p. 34).

[133]T. Kugo, "The Universal Renormalization Factors Z_1/Z_3 and Color Confinement Condition in Non-Abelian Gauge Theory", 10.48550/ARXIV.HEP-TH/9511033 (1995) (cit. on p. 34).

[134]N. Nakanishi and I. Ojima, *Covariant Operator Formalism of Gauge Theories and Quantum Gravity* (WORLD SCIENTIFIC, Nov. 1990), ISBN: 9789812799340 (cit. on p. 34).

[135]V. Gribov, "Quantization of non-Abelian gauge theories", Nuclear Physics B **139**, 1–19, ISSN: 0550-3213 (1978) (cit. on p. 34).

[136]D. Zwanziger, "Vanishing of zero-momentum lattice gluon propagator and color confinement", Nuclear Physics B **364**, 127–161, ISSN: 0550-3213 (1991) (cit. on p. 34).

[137]D. Zwanziger, "Renormalization in the Coulomb gauge and order parameter for confinement in QCD", Nuclear Physics B **518**, 237–272, ISSN: 0550-3213 (1998) (cit. on p. 34).

[138]D. Zwanziger, "Renormalizability of the critical limit of lattice gauge theory by BRS invariance", Nuclear Physics B **399**, 477–513, ISSN: 0550-3213 (1993) (cit. on p. 34).

[139]K.-I. Kondo, "Kugo–Ojima color confinement criterion and Gribov–Zwanziger horizon condition", Physics Letters B **678**, 322–330, ISSN: 0370-2693 (2009) (cit. on p. 34).

[140]R. J. Rivers, *Path Integral Methods in Quantum Field Theory* (Cambridge University Press, Nov. 1987), ISBN: 9780511564055 (cit. on p. 37).

[141]M. Böhm, A. Denner, and H. Joos, *Gauge Theories of the Strong and Electroweak Interaction* (Vieweg+Teubner Verlag, 2001), ISBN: 9783322801609 (cit. on p. 37).

[142]C. D. Roberts and A. G. Williams, "Dyson-Schwinger equations and their application to hadronic physics", Progress in Particle and Nuclear Physics **33**, 477–575, ISSN: 0146-6410 (1994) (cit. on p. 37).

[143]M. Q. Huber and M. Mitter, "CrasyDSE: A framework for solving Dyson–Schwinger equations", Computer Physics Communications **183**, 2441–2457, ISSN: 0010-4655 (2012) (cit. on p. 38).

[144]M. Q. Huber, A. K. Cyrol, and J. M. Pawlowski, "DoFun 3.0: Functional equations in mathematica", Computer Physics Communications **248**, 107058, ISSN: 0010-4655 (2020) (cit. on p. 38).

[145]J. M. Cornwall, R. Jackiw, and E. Tomboulis, "Effective action for composite operators", Physical Review D **10**, 2428–2445, ISSN: 0556-2821 (1974) (cit. on p. 39).

[146]R. W. Haymaker, "Variational methods for composite operators", La Rivista del Nuovo Cimento **14**, 1–89, ISSN: 1826-9850 (1991) (cit. on p. 39).

[147]J. Berges, "*n*-particle irreducible effective action techniques for gauge theories", Physical Review D **70**, 105010, ISSN: 1550-2368 (2004) (cit. on p. 39).

[148]M. E. Carrington and Y. Guo, "Techniques forn-particle irreducible effective theories", Physical Review D **83**, 016006, ISSN: 1550-2368 (2011) (cit. on p. 39).

[149]C. S. Fischer, "Infrared properties of QCD from Dyson–Schwinger equations", Journal of Physics G: Nuclear and Particle Physics **32**, R253–R291, ISSN: 1361-6471 (2006) (cit. on p. 42).

[150]C. S. Fischer, "QCD at finite temperature and chemical potential from Dyson–Schwinger equations", Progress in Particle and Nuclear Physics **105**, 1–60, ISSN: 0146-6410 (2019) (cit. on p. 43).

[151]H. J. Munczek and A. M. Nemirovsky, "Regularization and renormalization of four-fermion theories", Physical Review D **22**, 2001–2005, ISSN: 0556-2821 (1980) (cit. on p. 45).

[152]H. J. Munczek and A. M. Nemirovsky, "Ground-state $q\bar{q}$ mass spectrum in quantum chromodynamics", Physical Review D **28**, 181–186, ISSN: 0556-2821 (1983) (cit. on p. 45).

[153]Y. Nambu and G. Jona-Lasinio, "Dynamical Model of Elementary Particles Based on an Analogy with Superconductivity. I", Physical Review **122**, 345–358, ISSN: 0031-899X (1961) (cit. on p. 45).

[154]Y. Nambu and G. Jona-Lasinio, "Dynamical Model of Elementary Particles Based on an Analogy with Superconductivity. II", Physical Review **124**, 246–254, ISSN: 0031-899X (1961) (cit. on p. 45).

[155]P. Jain and H. J. Munczek, "Calculation of the pion decay constant in the framework of the Bethe-Salpeter equation", Physical Review D **44**, 1873–1879, ISSN: 0556-2821 (1991) (cit. on p. 46).

[156]H. J. Munczek and P. Jain, "Relativistic pseudoscalar $q\bar{q}$ bound states: Results on Bethe-Salpeter wave functions and decay constants", Physical Review D **46**, 438–445, ISSN: 0556-2821 (1992) (cit. on p. 46).

[157]M. R. Frank and C. D. Roberts, "Model gluon propagator and pion and ρ-meson observables", Physical Review C **53**, 390–398, ISSN: 1089-490X (1996) (cit. on p. 46).

[158]R. Alkofer and C. D. Roberts, "Calculation of the anomalous form factor", Physics Letters B **369**, 101–107, ISSN: 0370-2693 (1996) (cit. on p. 46).

[159]P. Maris and C. D. Roberts, "π- and K-meson Bethe-Salpeter amplitudes", Physical Review C **56**, 3369–3383, ISSN: 1089-490X (1997) (cit. on p. 46).

[160]P. Maris and P. C. Tandy, "Bethe-Salpeter study of vector meson masses and decay constants", Physical Review C **60**, 055214, ISSN: 1089-490X (1999) (cit. on p. 46).

[161]C. S. Fischer and R. Alkofer, "Nonperturbative propagators, running coupling, and the dynamical quark mass of Landau gauge QCD", Physical Review D **67**, 094020, ISSN: 1089-4918 (2003) (cit. on p. 47).

[162]R. Alkofer, C. Fischer, and F. Llanes-Estrada, "Erratum to: "vertex functions and infrared fixed point in landau gauge su(n) yang–mills theory" [phys. lett. b 611 (2005) 279]", Physics Letters B **670**, 460–461, ISSN: 0370-2693 (2009) (cit. on p. 47).

[163]R. Williams, C. S. Fischer, and W. Heupel, "Light mesons in QCD and unquenching effects from the 3PI effective action", Physical Review D **93**, 034026, ISSN: 2470-0029 (2016) (cit. on p. 47).

[164]N. G. Santowsky, "The Role of Four-Quark States in the Nature of Exotic Hadrons from Bethe-Salpeter Equations", PhD thesis (Justus Liebig University Giessen, 2021) (cit. on pp. 47, 50, 64, 75, 76, 94, 168, 173).

[165]R. Alkofer et al., "Analytic properties of the Landau gauge gluon and quark propagators", Physical Review D **70**, 014014, ISSN: 1550-2368 (2004) (cit. on p. 49).

[166]A. Windisch, "Analytic properties of the quark propagator from an effective infrared interaction model", Physical Review C **95**, 045204, ISSN: 2469-9993 (2017) (cit. on p. 49).

[167]G. Eichmann et al., "A covariant view on the nucleons' quark core", Annals of Physics **323**, 2505–2553, ISSN: 0003-4916 (2008) (cit. on p. 50).

[168]C. S. Fischer, D. Nickel, and R. Williams, "On Gribov's supercriticality picture of quark confinement", The European Physical Journal C **60**, 47–61, ISSN: 1434-6052 (2008) (cit. on p. 50).

[169]E. E. Salpeter and H. A. Bethe, "A Relativistic Equation for Bound-State Problems", Physical Review **84**, 1232–1242, ISSN: 0031-899X (1951) (cit. on p. 51).

[170]G. Eichmann, "QCD and Hadron Physics", Lecture notes, `https://homepage.uni-graz.at/de/gernot.eichmann/teaching/` (cit. on pp. 52, 53).

[171]K. Huang and H. A. Weldon, "Bound-state wave functions and bound-state scattering in relativistic field theory", Physical Review D **11**, 257–278, ISSN: 0556-2821 (1975) (cit. on pp. 53, 78).

[172]L. D. Faddeev, " Mathematical aspects of the three-body problem in the quantum scattering theory", PhD thesis (1965) (cit. on p. 54).

[173]L. D. Faddeev, "SCATTERING THEORY FOR A THREE-PARTICLE SYSTEM", in, *Fifty years of mathematical physics* (WORLD SCIENTIFIC, Feb. 2016), pp. 37–42, ISBN: 9789814340960 (cit. on p. 54).

[174]Yakubovsky, "On the Integral equations in the theory of N particle scattering", Sov.J.Nucl.Phys. 5 (1967) 937, Yad.Fiz. 5 (1967) 1312-1320, 9 (1967) (cit. on p. 55).

[175]R. E. Cutkosky and M. Leon, "Normalization of Bethe-Salpeter Wave Functions and Bootstrap Equations", Physical Review **135**, B1445–B1446, ISSN: 0031-899X (1964) (cit. on p. 56).

[176]N. Nakanishi, "Normalization Condition and Normal and Abnormal Solutions of the Bethe-Salpeter Equation", Physical Review **138**, B1182–B1192, ISSN: 0031-899X (1965) (cit. on p. 57).

[177]R. Williams, "Bethe–Salpeter studies of mesons beyond rainbow-ladder", EPJ Web of Conferences **3**, 03005, ISSN: 2100-014X (2010) (cit. on pp. 62, 64).

[178]C. S. Fischer, S. Kubrak, and R. Williams, "Spectra of heavy mesons in the Bethe-Salpeter approach", The European Physical Journal A **51**, `10.1140/epja/i2015-15010-7`, ISSN: 1434-601X (2015) (cit. on p. 70).

[179]L. Schlessinger, "Use of Analyticity in the Calculation of Nonrelativistic Scattering Amplitudes", Physical Review **167**, 1411–1423, ISSN: 0031-899X (1968) (cit. on pp. 73, 173).

[180]M. Neubert, "Heavy-quark symmetry", Physics Reports **245**, 259–395, ISSN: 0370-1573 (1994) (cit. on p. 73).

[181] A. N. Kvinikhidze and A. M. Khvedelidze, "Pair-interaction approximation in the equations of quantum field theory for a four-body system", Theoretical and Mathematical Physics **90**, 62–74, ISSN: 1573-9333 (1992) (cit. on p. 78).

[182] W. Heupel, G. Eichmann, and C. S. Fischer, "Tetraquark bound states in a Bethe–Salpeter approach", Physics Letters B **718**, 545–549, ISSN: 0370-2693 (2012) (cit. on p. 78).

[183] A. N. Kvinikhidze and B. Blankleider, "Unified tetraquark equations", Physical Review D **107**, 094014, ISSN: 2470-0029 (2023) (cit. on p. 78).

[184] G. Eichmann, C. S. Fischer, and W. Heupel, "Four-point functions and the permutation group S_4", Physical Review D **92**, 056006, ISSN: 1550-2368 (2015) (cit. on pp. 78, 80, 87, 90).

[185] L. H. Ryder, *Quantum field theory*, Second edition, 14th printing (Cambridge University Press, Cambridge, 2014), 487 pp., ISBN: 9780521478144 (cit. on p. 80).

[186] T. Ohlsson, *Relativistic quantum physics, From advanced quantum mechanics to introductory quantum field theory*, Includes bibliographical references and index (Cambridge University Press, Cambridge, UK, 2011), 1297 pp., ISBN: 9781139032681 (cit. on p. 80).

[187] J. Lubański, "Sur la theorie des particules élémentaires de spin quelconque. I", Physica **9**, 310–324, ISSN: 0031-8914 (1942) (cit. on p. 80).

[188] J. Lubanski, "Sur la théorie des particules élémentaires de spin quelconque. II", Physica **9**, 325–338, ISSN: 0031-8914 (1942) (cit. on p. 80).

[189] J. Hoffer, G. Eichmann, and C. S. Fischer, "Hidden-flavor four-quark states in the charm and bottom region", Physical Review D **109**, 074025, ISSN: 2470-0029 (2024) (cit. on pp. 89, 93, 98, 102, 103).

[190] J. Hoffer, G. Eichmann, and C. S. Fischer, "The structure of open-flavour four-quark states in the charm and bottom region", 10.48550/ARXIV.2409.05779 (2024) (cit. on pp. 93, 108, 109, 189).

[191] R. Aaij et al., "Observation of a Resonant Structure near the $D_s^+ D_s^-$ Threshold in the $B^+ \to D_s^+ D_s^- K^+$ Decay", Physical Review Letters **131**, 071901, ISSN: 1079-7114 (2023) (cit. on p. 104).

[192] Q. Wang et al., "Y(4260): Hadronic molecule versus hadro-charmonium interpretation", Physical Review D **89**, 034001, ISSN: 1550-2368 (2014) (cit. on p. 105).

[193] T. Ji et al., "Prediction of a Narrow Exotic Hadronic State with Quantum Numbers $J^{PC} = 0^{--}$", Physical Review Letters **129**, 102002, ISSN: 1079-7114 (2022) (cit. on p. 105).

[194] M. Cleven et al., "Employing spin symmetry to disentangle different models for the XYZ-states", Physical Review D **92**, 014005, ISSN: 1550-2368 (2015) (cit. on pp. 105, 149, 150).

[195] V. Baru et al., "Spin partners W_{bJ} from the line shapes of the $Z_b(10610)$ and $Z_b(10650)$", Physical Review D **99**, 094013 (2019) (cit. on pp. 106, 107).

[196] P. Bicudo et al., "Study of I=0 bottomonium bound states and resonances in S , P , D , and F waves with lattice QCD static-static-light-light potentials", Physical Review D **107**, 094515, ISSN: 2470-0029 (2023) (cit. on p. 107).

[197]Z.-Y. Yang et al., "Investigation of the stability for fully-heavy $bc\bar{b}\bar{c}$ tetraquark states", Physical Review D **104**, 014003 (2021) (cit. on p. 108).

[198]A. Jalili et al., "Rotation and Vibration in Tetraquarks", Few-Body Systems **64**, 10.1007/s00601-023-01847-4 (2023) (cit. on p. 108).

[199]Gang Yang and Jialun Ping and Jorge Segovia, "Exotic resonances of fully-heavy tetraquarks in a lattice-QCD insipired quark model", Physical Review D **104**, 014006 (2021) (cit. on p. 108).

[200]A. Francis et al., "Evidence for charm-bottom tetraquarks and the mass dependence of heavy-light tetraquark states from lattice QCD", Physical Review D **99**, 054505 (2019) (cit. on pp. 108, 111).

[201]L. Leskovec et al., "Lattice QCD investigation of a doubly-bottom $\bar{b}\bar{b}ud$ tetraquark with quantum numbers $I(J^P) = 0(1^+)$", Physical Review D **100**, 014503 (2019) (cit. on pp. 108, 111).

[202]Y. Lyu et al., "Doubly Charmed Tetraquark T_{cc}^+ from Lattice QCD near Physical Point", Physical Review Letters **131**, 161901, ISSN: 1079-7114 (2023) (cit. on pp. 108, 111).

[203]T. Aoki, S. Aoki, and T. Inoue, "Lattice study on a tetra-quark state T_{bb} in the HAL QCD method", 10.48550/ARXIV.2306.03565 (2023) (cit. on pp. 108, 111).

[204]M. Padmanath, A. Radhakrishnan, and N. Mathur, "Bound isoscalar axial-vector $bc\bar{u}\bar{d}$ tetraquark T_{bc} from lattice QCD using two-meson and diquark-antidiquark variational basis", 10.48550/ARXIV.2307.14128 (2023) (cit. on pp. 108, 110, 111).

[205]C. Alexandrou et al., "$\bar{b}\bar{b}ud$ and $\bar{b}\bar{b}us$ tetraquarks from lattice QCD using symmetric correlation matrices with both local and scattering interpolating operators", 10.48550/ARXIV.2404.03588 (2024) (cit. on pp. 108, 111).

[206]S. Sakai, L. Roca, and E. Oset, "Charm-beauty meson bound states from $B(B*)D(D*)$ and $B(B*)\bar{D}(\bar{D}*)$ interaction", Physical Review D **96**, 054023, ISSN: 2470-0029 (2017) (cit. on pp. 108, 111).

[207]W. Park, S. Noh, and S. Lee, "Masses of the Doubly-heavy Tetraquarks in a Constituent Quark Model", Acta Physica Polonica B **50**, 1151, ISSN: 1509-5770 (2019) (cit. on pp. 108, 111).

[208]T. F. Caramés, J. Vijande, and A. Valcarce, "Exotic $bc\bar{q}\bar{q}$ four-quark states", Physical Review D **99**, 014006, ISSN: 2470-0029 (2019) (cit. on pp. 108, 111).

[209]L. Maiani, A. D. Polosa, and V. Riquer, "Hydrogen bond of QCD in doubly heavy baryons and tetraquarks", Physical Review D **100**, 074002, ISSN: 2470-0029 (2019) (cit. on pp. 108, 111).

[210]P. Mohanta and S. Basak, "Construction of $bb\bar{u}\bar{d}$ tetraquark states on lattice with NRQCD bottom and HISQ up and down quarks", Physical Review D **102**, 094516, ISSN: 2470-0029 (2020) (cit. on pp. 108, 111).

[211]Q. Meng et al., "Stable double-heavy tetraquarks: Spectrum and structure", Physics Letters B **814**, 136095, ISSN: 0370-2693 (2021) (cit. on pp. 108, 111).

[212]S. Noh, W. Park, and S. H. Lee, "Doubly heavy tetraquarks, $qq'\bar{Q}\bar{Q}'$, in a nonrelativistic quark model with a complete set of harmonic oscillator bases", Physical Review D **103**, 114009, ISSN: 2470-0029 (2021) (cit. on pp. 108, 111).

[213]Q. Meng et al., "Doubly heavy tetraquark resonant states", Physics Letters B **824**, 136800, ISSN: 0370-2693 (2022) (cit. on pp. 108, 111).

[214]M. Albaladejo, "T_{cc}^+ coupled channel analysis and predictions", Physics Letters B **829**, 137052, ISSN: 0370-2693 (2022) (cit. on pp. 108, 111).

[215]H.-W. Ke, X.-H. Liu, and X.-Q. Li, "Possible molecular states of $D^{(*)}D^{(*)}$ and $B^{(*)}B^{(*)}$ within the Bethe–Salpeter framework", The European Physical Journal C **82**, 10.1140/epjc/s10052-022-10092-8, ISSN: 1434-6052 (2022) (cit. on pp. 108, 111).

[216]P. Ortega et al., "Nature of the doubly-charmed tetraquark T_{cc}^+ in a constituent quark model", Physics Letters B **841**, 137918, ISSN: 0370-2693 (2023) (cit. on pp. 108, 111).

[217]Y.-X. Song and D.-J. Jia, "Mass spectra of doubly heavy tetraquarks in diquark−antidiquark picture*", Communications in Theoretical Physics **75**, 055201, ISSN: 1572-9494 (2023) (cit. on pp. 108, 111).

[218]D. Wang et al., "Spectrum of S- and P-wave $cc\bar{q}\bar{q}'$ ($\bar{q}, \bar{q}' = \bar{u}, \bar{d}, \bar{s}$) systems in a chiral SU(3) quark model", 10.48550/ARXIV.2403.15187 (2024) (cit. on pp. 108, 111).

[219]M. Kucab and M. Praszalowicz, "Heavy Quarkonia, Heavy-Light Tetraquarks and the Chiral Quark-Soliton Model", 10.48550/ARXIV.2402.04169 (2024) (cit. on pp. 108, 111).

[220]R. J. Hudspith et al., "Lattice investigation of exotic tetraquark channels", Physical Review D **102**, 114506, ISSN: 2470-0029 (2020) (cit. on p. 111).

[221]S. Meinel, M. Pflaumer, and M. Wagner, "Search for $\bar{b}\bar{b}us$ and $\bar{b}\bar{c}ud$ tetraquark bound states using lattice QCD", Physical Review D **106**, 034507, ISSN: 2470-0029 (2022) (cit. on pp. 111, 113).

[222]A. Radhakrishnan, M. Padmanath, and N. Mathur, "Study of isoscalar scalar $bc\bar{u}\bar{d}$ tetraquark T_{bc} from lattice QCD", 10.48550/ARXIV.2404.08109 (2024) (cit. on p. 111).

[223]M. Padmanath and S. Prelovsek, "Signature of a Doubly Charm Tetraquark Pole in DD* Scattering on the Lattice", Phys. Rev. Lett. **129**, 032002 (2022) (cit. on p. 111).

[224]G. K. C. Cheung et al. (Hadron Spectrum), "Tetraquark operators in lattice QCD and exotic flavour states in the charm sector", JHEP **11**, 033 (2017) (cit. on p. 111).

[225]P. Bicudo et al., "Evidence for the existence of $ud\bar{b}\bar{b}$ and the non-existence of $ss\bar{b}\bar{b}$ and $cc\bar{b}\bar{b}$ tetraquarks from lattice QCD", Phys. Rev. D **92**, 014507 (2015) (cit. on pp. 111, 112, 114).

[226]P. Bicudo et al., "BB interactions with static bottom quarks from Lattice QCD", Phys. Rev. D **93**, 034501 (2016) (cit. on p. 111).

[227]G. Eichmann, "Theory Introduction to Baryon Spectroscopy", Few-Body Systems **63**, 10.1007/s00601-022-01756-y (2022) (cit. on pp. 115, 122).

[228]A. Torcato et al., "Heavy Baryon Spectroscopy in a Quark–Diquark Approach", Few-Body Systems **64**, 10.1007/s00601-023-01826-9 (2023) (cit. on pp. 115, 122).

[229]L. Liu, C. Chen, and C. D. Roberts, "Wave functions of $(I, J^P) = (\frac{1}{2}, \frac{3}{2}^{\mp})$ baryons", Physical Review D **107**, 014002, ISSN: 2470-0029 (2023) (cit. on pp. 115, 122).

[230]M. Ablikim *et al.* (BESIII Collaboration), "Observation of a charged $(D\bar{D}^*)^{\pm}$ mass peak in $e^+e^- \to \pi D\bar{D}^*$ at $\sqrt{s} = 4.26$ GeV", Physical Review Letters **112**, 022001 (2014) (cit. on p. 119).

[231]Y. Ikeda et al., "Fate of the Tetraquark Candidate $Z_c(3900)$ from Lattice QCD", Physical Review Letters **117**, 242001 (2016) (cit. on pp. 119, 122).

[232]Y. I. and, "The tetraquark candidate $Z_c(3900)$ from dynamical lattice QCD simulations", Journal of Physics G: Nuclear and Particle Physics **45**, 024002 (2018) (cit. on pp. 119, 122).

[233]Y.-H. Chen, M.-L. Du, and F.-K. Guo, "Precise determination of the pole position of the exotic $Z_c(3900)$", 10.48550/ARXIV.2310.15965 (2023) (cit. on pp. 119, 122).

[234]L.-W. Yan et al., "Reconciling experimental and lattice data of $Z_c(3900)$ in a $J/\psi\pi$-$D\bar{D}^*$ coupled-channel analysis", 10.48550/ARXIV.2307.12283 (2023) (cit. on pp. 119, 122).

[235]R. Aaij *et al.* (LHCb Collaboration), "Observation of a resonant structure near the $D_s^+D_s^-$ threshold in the $B^+ \to D_s^+D_s^-K^+$ decay", Phys. Rev. Lett. 131, 071901 (2023), 10.1103/PhysRevLett.131.071901 (2022) (cit. on p. 119).

[236]L. von Detten, C. Hanhart, and V. Baru, "The $Y(4230)$ as a $D_1\bar{D}$ molecule", 10.48550/ARXIV.2309.11970 (2023) (cit. on p. 119).

[237]L. von Detten et al., "How many vector charmonium(-like) states sit in the energy range from 4.2 to 4.35 GeV?", 10.48550/ARXIV.2402.03057 (2024) (cit. on p. 119).

[238]C. Hanhart, "Theory of hadronic molecules applied to the XYZ states", 10.48550/ARXIV.1709.09920 (2017) (cit. on p. 119).

[239]F.-K. Guo, C. Hanhart, and U.-G. Meißner, "Evidence that the $Y(4660)$ is an $f_0(980)\psi'$ bound state", Physics Letters B **665**, 26–29 (2008) (cit. on p. 119).

[240]F.-L. Wang and X. Liu, "Exotic double-charm molecular states with hidden or open strangeness and around 4.5 ∼ 4.7 GeV", Physical Review D **102**, 094006 (2020) (cit. on p. 119).

[241]J.-R. Zhang, "$Y(4626)$ as a P-wave $[cs][\bar{c}\bar{s}]$ tetraquark state", Physical Review D **102**, 054006 (2020) (cit. on p. 119).

[242]H. Garcilazo and A. Valcarce, "Hidden and Open Heavy-Flavor Hadronic States", Few-Body Systems **61**, 10.1007/s00601-020-01557-1, ISSN: 1432-5411 (2020) (cit. on p. 121).

[243]C. Deng and S.-L. Zhu, "T_{cc}^+ and its partners", Physical Review D **105**, 054015, ISSN: 2470-0029 (2022) (cit. on p. 121).

[244]M. Q. Huber, W. J. Kern, and R. Alkofer, "How to Determine the Branch Points of Correlation Functions in Euclidean Space II: Three-Point Functions", Symmetry **15**, 414, ISSN: 2073-8994 (2023) (cit. on pp. 126, 169).

[245]G. C. Wick, "Properties of Bethe-Salpeter Wave Functions", Physical Review **96**, 1124–1134, ISSN: 0031-899X (1954) (cit. on p. 131).

[246]A. Young, "On Quantitative Substitutional Analysis", Proceedings of the London Mathematical Society **s1-33**, 97–145, ISSN: 0024-6115 (1900) (cit. on p. 135).

[247]G. Hooft, "A planar diagram theory for strong interactions", Nuclear Physics B **72**, 461–473, ISSN: 0550-3213 (1974) (cit. on p. 144).

[248]J. R. Peláez, "From controversy to precision on the sigma meson: A review on the status of the non-ordinary $f_0(500)$ resonance", Physics Reports **658**, 1–111, ISSN: 0370-1573 (2016) (cit. on pp. 149, 165, 166).

[249]A. Windisch, M. Q. Huber, and R. Alkofer, "How to determine the branch points of correlation functions in Euclidean space", 10.48550/ARXIV.1304.3642 (2013) (cit. on p. 169).

[250]M. Q. Huber, W. J. Kern, and R. Alkofer, "Analytic structure of three-point functions from contour deformations", Physical Review D **107**, 074026, ISSN: 2470-0029 (2023) (cit. on p. 169).

[251]G. Eichmann et al., "Scattering amplitudes and contour deformations", Physical Review D **100**, 094001, ISSN: 2470-0029 (2019) (cit. on p. 172).

[252]M. Abramowitz and I. A. Stegun, eds., *Handbook of mathematical functions, With formulas, graphs, and mathematical tables*, 9. Dover print.; [Nachdr. der Ausg. von 1972], Dover books on mathematics, This ninth Dover printing conforms to the tenth (December 1972) printing by the Government Printing Office, except that additional corrections have been made (Dover Publ., New York, NY, 2013), 1046 pp., ISBN: 9780486612720 (cit. on p. 199).

[253]Gaussian quadrature, https://en.wikipedia.org/wiki/Gaussian_quadrature (cit. on p. 199).

[254]M. Galassi, *GNU scientific library reference manual, For gsl version 1.12*, edited by B. Gough, 3. ed. (Network Theory, Bristol, 2009), 573 pp., ISBN: 0954612078 (cit. on pp. 200, 203).

[255]G. Peter Lepage, "A new algorithm for adaptive multidimensional integration", Journal of Computational Physics **27**, 192–203, ISSN: 0021-9991 (1978) (cit. on p. 200).

[256]R. V. Mises and H. Pollaczek-Geiringer, "Praktische Verfahren der Gleichungsauflösung", ZAMM - Journal of Applied Mathematics and Mechanics / Zeitschrift für Angewandte Mathematik und Mechanik **9**, 152–164, ISSN: 1521-4001 (1929) (cit. on p. 201).

[257]B. N. Parlett, *The symmetric eigenvalue problem, "this siam edition is an unabridged, corrected republication of the work first published by prentice-hall, inc., englewood cliffs, new jersey, 1980"–t.p. verso*, Classics in applied mathematics 20, Restricted to subscribers or individual electronic text purchasers (Society for Industrial and Applied Mathematics (SIAM, 3600 Market Street, Floor 6, Philadelphia, PA 19104), Philadelphia, Pa, 1998), 1398 pp., ISBN: 9781611971163 (cit. on p. 201).

[258]R. A. Horn, *Matrix analysis*, edited by C. R. Johnson, 23rd printing (Cambridge University Press, Cambridge, 2010), 1561 pp., ISBN: 9780511810817 (cit. on p. 201).

[259]W. E. Arnoldi, "The principle of minimized iterations in the solution of the matrix eigenvalue problem", Quarterly of Applied Mathematics **9**, 17–29, ISSN: 1552-4485 (1951) (cit. on p. 201).

[260]C. Lanczos, "An iteration method for the solution of the eigenvalue problem of linear differential and integral operators", Journal of Research of the National Bureau of Standards **45**, 255, ISSN: 0091-0635 (1950) (cit. on p. 201).

[261]R. B. Lehoucq, *Arpack users' guide, Solution of large-scale eigenvalue problems with implicitly restarted arnoldi methods*, edited by D. C. Sorensen and C. Yang, Software, environments, tools 6 (Society for Industrial and Applied Mathematics, Philadelphia, Pa., 1998), 142 pp., ISBN: 0898714079 (cit. on p. 202).

[262]ARPACK-NG, https://github.com/opencollab/arpack-ng (cit. on p. 202).

[263]ARPACK++, https://github.com/m-reuter/arpackpp (cit. on p. 202).

[264]GNU Compiler Collection (GCC), https://gcc.gnu.org/ (cit. on p. 203).

[265]G. Rossum, *Python documentation manual*, edited by F. L. Drake, Release 3.0.1 [Repr.], Vol. Pt. 2, Documentation for Python, Enth. außerdem Bonus-Dokumente zu Python Release 3.0.1 (SoHo Books, [Redwood City, Calif.], 2010), 109126 pp., ISBN: 9781441412690 (cit. on p. 203).

[266]J. A. M. Vermaseren, "New features of FORM", 10.48550/ARXIV.MATH-PH/0010025 (2000) (cit. on p. 203).

[267]Wolfram Research, Inc., *Mathematica, Version 14.1*, Champaign, IL, 2024, https://www.wolfram.com/mathematica (cit. on p. 203).

[268]R. Mertig, M. Böhm, and A. Denner, "Feyn calc - computer-algebraic calculation of feynman amplitudes", Computer Physics Communications **64**, 345–359, ISSN: 0010-4655 (1991) (cit. on p. 203).

[269]FeynCalc, https://feyncalc.github.io/ (cit. on p. 203).

[270]L. Lamport, *LATEX: a document preparation system*, [*user's guide & reference manual*], 25. [print.] (Addison-Wesley Publishing Company, Reading, Massachusetts [u.a.], 1993), 242 pp., ISBN: 020115790X (cit. on p. 203).

[271]LuaTeX, https://www.luatex.org/ (cit. on p. 203).

[272]https://tug.org/texlive/ (cit. on p. 203).

[273]Alex Povel, *LaTeX Cookbook*, https://github.com/alexpovel/latex-cookbook (cit. on p. 203).

[274]PGF plots and TikZ, https://ctan.org/pkg/pgf (cit. on p. 203).

Acknowledgements

First and foremost, I want to express my deep gratitude to my supervisor Prof. Dr. Christian Fischer, who introduced me to the world of functional methods and gave me the opportunity to work on such a fascinating topic. He always had an open ear for technical as well as physical questions and provided me with guidance whenever needed. Secondly, I would like to thank Prof. Dr. Marc Wagner, for taking on the role as my second advisor in the context of the doctoral program of HGS-HIRe and for all the fruitful discussions throughout my doctoral project. Furthermore, I want to especially thank Prof. Dr. Gernot Eichmann for the many discussions on technical intricacies, the continued competent support and collaboration over the years.

I want to thank the Helmholtz Graduate School for Hadron and Ion Research (HGS-HIRe) for FAIR for their access to useful courses and providing me with the opportunity of spending a few months abroad. Related to that, I would like to thank Prof. Dr. Antonio Polosa and Dr. Angelo Esposito from the Sapienza Università di Roma for the very interesting discussions during my time in Rome.

Many thanks go out to my office mate Dr. Nico Santowsky for his patient guidance and support in the beginning of my doctoral project and also for proof-reading parts of this work. Additionally, I am indebted to Milad Ghanbarpour, Dr. Julian Bernhardt and Jonathan Yigzaw for carefully proof-reading parts of this thesis.

Coming to the institute in Gießen from Austria, I want to thank my past and present colleagues for the warm welcome and for the very pleasant work atmosphere. Especially, I want to thank Dr. Julian Bernhardt for our many discussions on various topics and for always providing me with good advice on computing problems and mathematics. I want to thank Dr. Philipp Isserstedt for the extended coffee breaks and for his insights on the intricacies of writing good code. Many thanks go out to Milad Ghanbarpour for his friendship over the years and our interesting discussions during our shared walks back into the city. Furthermore, I want to thank Franziska Münster for our time as office mates and our memorable conversations. I also want to thank PD Dr. Markus Huber for initially indicating the open doctoral position with Prof. Fischer and for the always helpful and interesting discussions. Additionally, I want to thank the institute's secretaries – Monika Weingärtner and Ilka Sproates – who were always quick to help in bureaucratic and organizational matters.

I would like to especially thank my family and my friends for their continued support and for always having an open ear for problems whenever needed. Especially, I want to give thanks to Stephan Schauberger for his continued friendship and for our discussions which never fail to brighten my mood. Thank you also to the (former) physics students of the Einheitskreis group, our weekly Skype meetings is always something I look forward too.

Lastly, probably the biggest thanks goes out to my girlfriend Sara, for enduring the four years of long-distance relationship such that I could follow my passion and for the continued emotional support. Thank you for always being there for me and for being the most reliable constant in my life.

This work was supported by the Helmholtz Graduate School for Hadron and Ion Re-

search (HGS-HIRe) for FAIR, the GSI Helmholtzzentrum für Schwerionenforschung and the Bundesministerium für Bildung und Forschung (BMBF) und Contract number 05P2021 and the Deutsche Forschungsgesellschaft (DFG) under grant number FI 970/11-2. Furthermore, this work contributes to the aims of the U.S. Department of Energy ExoHad Topical Collaboration, contract DE-SC0023598. I also acknowledge computational resources provided by the HPC Core Facility and the HRZ of the Justus-Liebig- Universität Gießen.

Selbstständigkeitserklärung

Ich erkläre: Ich habe die vorgelegte Dissertation selbstständig und ohne unerlaubte fremde Hilfe und nur mit den Hilfen angefertigt, die ich in der Dissertation angegeben habe. Alle Textstellen, die wörtlich oder sinngemäß aus veröffentlichten Schriften entnommen sind, und alle Angaben, die auf mündlichen Auskünften beruhen, sind als solche kenntlich gemacht. Ich stimme einer evtl. Überprüfung meiner Dissertation durch eine Antiplagiat-Software zu. Bei den von mir durchgeführten und in der Dissertation erwähnten Untersuchungen habe ich die Grundsätze guter wissenschaftlicher Praxis, wie sie in der "Satzung der Justus-Liebig-Universität Gießen zur Sicherung guter wissenschaftlicher Praxis" niedergelegt sind, eingehalten.

Graz, den 28.01.2025

(Joshua Hoffer)